Chip-Scale Quadrupole Mass Filters for a Micro-Gas Analyzer

by

Kerry Cheung

B.S., Applied and Engineering Physics
Cornell University, 2003
S.M., Electrical Engineering and Computer Science
Massachusetts Institute of Technology, 2005

Submitted to the Department of Electrical Engineering and Computer Science
in partial fulfillment of the requirements for the degree of

Doctor of Philosophy in Electrical Engineering and Computer Science

at the

MASSACHUSETTS INSTITUTE OF TECHNOLOGY

June 2009

Author_____
Department of Electrical Engineering and Computer Science
May 22, 2009

Certified by_____
Akintunde I. Akinwande
Professor of Electrical Engineering and Computer Science
Thesis Supervisor

Accepted by_____
Terry P. Orlando
Professor of Electrical Engineering and Computer Science
Chairman, Department Committee on Graduate Students

Chip-Scale Quadrupole Mass Filters
for a Micro-Gas Analyzer

by

Kerry Cheung

Submitted to the Department of Electrical Engineering and Computer Science
on May 22, 2009 in partial fulfillment of the requirements for the degree of
Doctor of Philosophy in Electrical Engineering and Computer Science

Abstract

Mass spectrometers are powerful analytical instruments that serve as the gold standard for chemical analysis. This tool has numerous applications ranging from national security, industrial processing, environmental monitoring, space exploration, and healthcare to name a few. These systems are typically large, heavy, power-hungry, and expensive, constraining its usage to a laboratory setting. In recent years, there has been a growing interest in utilizing mass spectrometers outside the lab.

Microelectromechanical systems (MEMS) technology holds the promise of making devices smaller, faster, better, and cheaper. The Micro-Gas Analyzer (MGA) project attempts to leverage MEMS capabilities to create a low-cost, high-performance, portable mass spectrometer. Batch-fabrication of various components for the MGA has been demonstrated to date, but the mass filter component still has room for exploration.

Chip-scale quadrupole mass filters achieved entirely through wafer-scale processing have been designed, fabricated, and characterized. The device integrates the quadrupole electrodes, ion optics, and housing into a single monolithic block, eliminating the electrode-to-housing misalignments inherent in other quadrupoles. To achieve this integration, unconventional square electrode geometry was utilized. This concept formed the basis of the micro-square electrode quadrupole mass filter (MuSE-QMF).

The MuSE-QMF demonstrated mass filtering with a maximum mass range of 650 amu and a minimum peak-width of 0.5 amu at mass 40, corresponding to a resolution of 80. More importantly, the design concept can be extended to complex architectures that were previously unachievable. Batch-fabricated quadrupoles in arrays, in tandem, or with integrated pre-filters can have significant impact on the future of portable mass spectrometry. Additionally, the MuSE-QMF makes a case for operation in the second stability region, and motivates new studies on quadrupole ion dynamics.

Thesis Supervisor: Akintunde I. Akinwande
Title: Professor of Electrical Engineering and Computer Science

Acknowledgements

As an applied and engineering physics major with little to no real world experience, graduate school seemed like the next logical step. Frank Wise, my undergraduate advisor, gave me fair warning of what to expect but it was still quite the journey. These past six years have been filled with challenges, struggles, and emotional turmoil, but I was fortunate enough to have an equal amount of rewards and accomplishments. I've learned so much and grown personally and professionally within this time, and I owe it all to the people who have supported me throughout the experience.

First and foremost, I would like to thank my advisor, Tayo Akinwande, for giving me the opportunity to work under his guidance. His faith in me and my abilities is what got me through the lows of my doctoral work. He sometimes pushed me when it was needed but was always supportive. Additionally, his compassion and understanding throughout life's many ups and downs is something I am extremely grateful for. Next, I would like to thank my other committee members, Marty Schmidt and Forest White. Marty supervised my masters but he has never stopped providing excellent advice and feedback since. He has been a source of knowledge and I've learned many lessons from him, especially the importance of simple fabrication. I am also very grateful to have Forest onboard who was always enthusiastic about my research and helped me gauge the relevance of my work in the greater community.

Outside of my committee, there have been others who have given me excellent advice and assistance with issues that I encountered throughout this thesis work. I want to thank Luis Velásquez-García for many fruitful discussions and his experience with fabrication techniques. My work would not have been possible without some of his insights. Randy Pedder is another who has been instrumental in my work, and I am extremely thankful for his advice and patience. He has been a tremendous asset towards getting me caught up to speed on the field of mass spectrometry and the experimental work involved. I would also like to thank Thomas Hogan and Steve Taylor who have contributed a substantial amount of their time and resources to conduct simulations on my behalf. Appreciation goes to Hanqing Li for helpful feedback on fabrication issues as well.

I want to thank Vicky Diadiuk and the Microsystems Technology Laboratories staff for their training and assistance which were vital for my success in the cleanroom. I want to acknowledge Dennis Ward, Bob Bicchieri, Eric Lim, and Donal Jamieson for maintaining the tools needed to complete my devices and for their understanding when I caused tools to go down. I also want to thank Kurt Broderick, Paul Tierney, Dave Terry, Pat Varley, Pat Burkhart, Acia Adams, Debb Hodges-Pabon, Sam Crooks, Carolyn Collins, Anne Wasserman, and others members of the MTL community for their smiles and friendship through the years. Additionally, I want to thank the fab users of past and present – Annie Wang, Kevin Ryu, Orit Shamir, Nan Yang, Vikas Sharma, Ole Nielsen, Kishori Desphande, Andrea Adamo, Ivan Nausieda, Darius Golda, Linhvu, and others who made time in the cleanroom much more enjoyable.

Table of Contents

List of Figures

List of Tables

Chapter

1

Introduction

1.1 Motivation

As technology advances, there has been an increasing desire to know what is occurring in our surroundings. The ability to extract information from our environment is a great asset in making our machines, tools, and appliances smarter and better. From temperature sensors that regulate the heating and cooling of our homes and vehicles, to accelerometers and gyroscopes used in navigation, personal safety, and entertainment, sensors have become a part of our everyday lives.

If we draw a comparison to the five human senses, we have achieved the ability to "touch" (physical sensors), "see" (optical sensors), and "hear" (acoustic sensors). These sensors are able to provide us with sensitivities that surpass what is humanly possible. The capability to "taste" and "smell" lie within the domain of chemical sensors, which has limited developments to date. Chemical sensing of a few known species such as carbon monoxide, alcohol, or carbon dioxide can be readily accomplished, but the detectors are usually very specific and limited in speed, sensitivity, and lifetime.

Selective detectors operate through a reaction activated by absorption onto another compound or structure. These sensors are not very reliable since they are susceptible to contamination, saturation, and can be fooled by altering the specificity of a potentially hazardous compound. We would like to go beyond the limitations of selective detection, and provide fast, reliable chemical sensing for a wide range of substances. Developing such a sensor will have applications in war zones to alert our soldiers of complex

chemical and biological warfare agents, or possibly at airports and public spaces to monitor for explosives and other forms of terrorist threats. These sensors will also be extremely useful in the environment for the detection and regulation of pollutants or toxins that are introduced into our land, air, and water. Overall, the ability to detect and analyze known and unknown compounds is extremely beneficial, ensuring that many more applications will be discovered.

1.2   Mass Spectrometers

Mass spectrometers are powerful analytical instruments that serve as the gold standard for chemical analysis. The first mass spectrometer was reported in 1910 and was followed by 40 years of sporadic, but modest innovations [1]. Before the 1950's, mass spectrometers only had a few applications in physics but this was soon changed with the growth of the petroleum industry. Commercialization of the mass spectrometer for chemical analysis pushed the rapid development of this tool. In turn, emphasis shifted from the physics of the device to finding new applications. Today, mass spectrometers are utilized in industrial processing, environmental monitoring, national security, space exploration, and healthcare to name a few.

1.2.1   Overview

A typical mass spectrometer is comprised of four main components – the ionizer, the mass filter, the detector, and the pump. The ionizer takes the gas sample to be analyzed, and turns them into ions by putting a charge on them. This enables the molecules to be directed and manipulated since they are neutral by nature. The ions then enter the mass filter, the core of the system, where they are sorted depending on their mass to charge ratios (m/e). Conditions are set so that only ions with a specific m/e are allowed to pass onto the detector where they are collected and counted. If we plot the detector count as a function of the specified m/e, we will generate a mass spectrum for the analyte. This spectrum will provide information on the relative quantities of each m/e within the sample, and serves as a chemical "finger print". The last major component is the pump which keeps the other three components under vacuum. It is vital to have the gas mean

free path larger than the largest dimension of the mass spectrometer in order to prevent ions colliding with neutrals. Collisions will lead to discharging or the formation of complexes which negatively affect the analysis. Usually there are ion optics utilized between the ionizer, mass filter, and detector. These electrostatic lenses help couple ions into the mass filter and the filtered ions out to the detector. A schematic of typical mass spectrometer operation is shown in Figure 1-1.
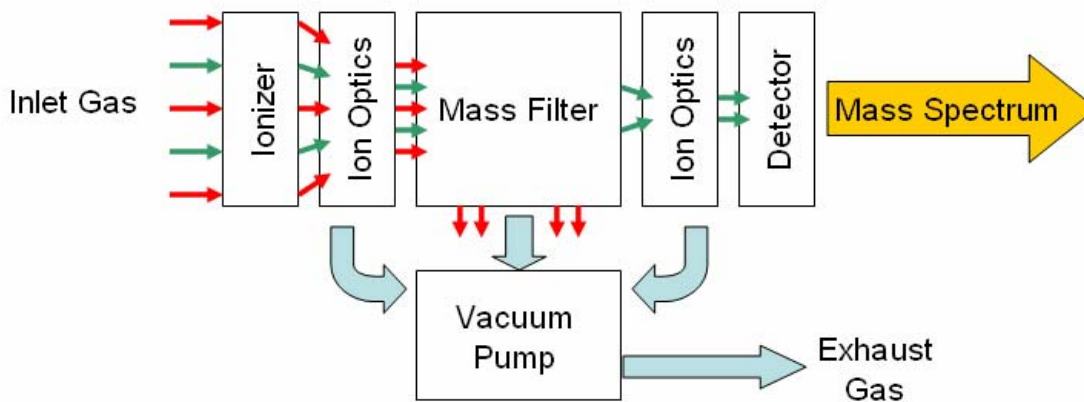
Figure 1-1: Schematic of mass spectrometer operation

1.2.2   Mass Filters

Of the four major components that constitute a mass spectrometer, the one that determines the capabilities of the device is the mass filter. There are several methods to perform mass filtering, each with their advantages and disadvantages. Depending on the application, one method might be better suited than the others. Several of the more popular types of mass filters are the cross-field, the quadrupole, the ion trap, the time-of-flight, and the Fourier-transform ion cyclotron resonance [2].

The cross-field type relies on the Lorentz force exerted on a moving charge by an external magnetic field to perform the filtering. This mass filter is capable of very high resolution but is usually very large and heavy due to the magnets required. Additional disadvantages of this device are the associated cost, the non-linearity of the filtering mechanism, and the susceptibility of the performance to changes in pressure or the inlet conditions.

15

The quadrupole mass filter utilizes four parallel electrodes that are driven with a combination of d.c. and a.c. voltages to control the ion trajectories. Mass filtering is accomplished by scanning the voltages to produce stable and unstable trajectories for a given m/e. The main advantages of this type of mass filter are the device simplicity, the light weight, and the relative tolerance that the performance has to changes in pressure or ion energies. Additionally, mass scanning is linear and the sensitivity is high, but the key disadvantage is the limited resolution.

The ion trap is comprised of a ring electrode with ends caps and operates on the same principles as the quadrupole, namely the utilization of d.c. and a.c. voltages to control ion trajectories. The main advantages of this device are the compact size, and the ability to store the ions to be analyzed. Mass filtering is achieved by varying the voltage on an end cap to eject the desired m/e towards the detector. This mass filter is useful when the ion samples are limited, but there are potential issues with space-charge effects, storage efficiency, and limitations in resolution.

The time-of-flight mass filter operates on the principle of varying velocities for ions with different masses and the same kinetic energy. A burst of ions is released at the inlet, accelerated to the same potential, and allowed to separate in a long tube. Larger masses will fly slower, resulting in a later arrival time at the detector. The advantages of this device are the simplicity, the high sensitivity, the speed, and the ability to analyze very large masses. The disadvantages are the susceptibility to changes in the inlet condition, the need for very fast electronics to resolve light masses, and the non-linearity of the filtering mechanism.

The Fourier-transform ion cyclotron resonance type is quite complex and uses an interesting method for analysis. Ions are trapped within a cubic cell, and exposed to a magnetic field. Cyclotron motion is induced with an external pulse, and the resulting signal is detected and amplified. Performing a Fourier-transform on the amplified signal will produce a spectrum where the frequency is inversely related to m/e and the intensity is proportional to the number of ions with the same m/e. The key advantages of this device are the very high resolution, the ability to measure all the ions at once in a non-destructive manner, and the fact that there is an ion trap to hold limited samples. The

main disadvantages are the size, the cost, and potential issues with space-charge effects and storage efficiencies.

1.3   Miniaturization

If we are able to miniaturize a mass spectrometer and make it cheap enough, we will have the chemical sensor that we desire. With the growing demand for chemical analysis outside the laboratory, other researchers have identified the potential for scaled-down mass spectrometers. Substantial progress on the miniaturization of ion sources, mass filters, and detectors have been made but advances in small-scale pumps and valves are still limited. There is the option of implementing passive getter pumps, but this is not practical for long term usage. Other than the scaled-down components, appropriate drive electronics are needed before a fully miniaturized system can be realized. Ultimately, the performance may not match laboratory versions but there are applications where portable low-resolution devices are useful.

1.3.1   Benefits

Mass spectrometers are generally large, heavy, expensive, and power hungry due to the pumping requirements needed for proper operation. The main advantage of scaling-down is the relaxation on operational pressure [3]. Reduced dimensions will allow for higher pressures, enabling smaller, lighter, and cheaper vacuum pumps to be used. Once bulky, expensive pumps are removed from the system, portability becomes a viable option. Other benefits are the general reduction in size and weight of the mass filter component itself, the reductions in overall costs, and the increase in sensitivity associated with operation at higher pressures.

Portable mass spectrometers will have major contributions towards environmental monitoring, national security, and space exploration [4]. Field applications of mass spectrometers typically require samples to be obtained on-site and then taken back to a lab for analysis. This is highly inefficient, leading to delays and potential errors. In the case of national security, monitoring of explosives and other threats are limited to checkpoints that can be easily circumvented. In terms of space exploration, mission costs

are directly related to payloads so launching a conventional mass spectrometer into space will be very expensive. Development of a miniaturized mass spectrometer will address all these issues.

1.3.2   Scaled-Down Components

One direction for miniaturization is taking conventional machining technologies and using them to manufacture scaled-down components. Significant progress has been made by several groups on various types of mass filters using this method. Smith and Cromey reported making a small, inexpensive quadrupole from machined ceramics and stainless steel rods [5]. Ferran and Boumsellek demonstrated a quadrupole array formed from precision electrodes mounted into a glass base [6], [7]. Orient et al. also produced a quadrupole array but utilized precisions stainless steel electrodes and machineable ceramics [8]. Quadrupoles with hyperbolic electrodes have been reported by Holkeboer [9] and Wang [10]. Holkeboer et al. utilized electrical discharge machining to create the electrodes while Wang et al. machined a ceramic tube and coated the hyperbolic surfaces with a thin metal. Thorleaf Research Inc. (Santa Barbara, CA) demonstrated a miniature Paul ion trap used in conjunction with gas chromatography [11], while Oak Ridge National Laboratory (Oak Ridge, TN) reported a simple cylindrical ion trap [12]. Diaz et al. created an impressive double-focusing sector-field mass spectrometer [13], and Cooks' group at Purdue University reported remarkable progress with a rectilinear ion trap [14], [15].

Another popular method for the miniaturization of mass spectrometers is the use of microfabrication technologies associated with microelectromechanical systems (MEMS) [16]. Microfabrication techniques allows for complex structures to be formed on a small scale with high precision. Most of the literature focuses on microfabricated mass filters and other individual components, but there are several reports that demonstrated fully integrated systems. For the mass filter, researchers have demonstrated cylindrical ion traps [17]-[19], a Wien filter [20], time-of-flight [21], and quadrupoles [22]-[27]. Novel concepts using traveling waves [28], and planar electrodes to form a Paul trap potential [29] have also been reported. Other microfabricated components such as hot filament ion sources [30], [31], electrospray ionizers [32], and micro-leak valves [33] have been

demonstrated successfully. Impressive work from Müller's group from the Hamburg University of Technology (Hamburg, Germany) demonstrated an integrated system with a plasma ionizer, a time-of-flight mass filter, an energy filter, as well as a detector [34], [35]. A modification using a traveling wave mass filter has also been demonstrated [36]. Recently, the NASA Goddard Space Flight Center (Greenbelt, MD) reported a time-of-flight mass spectrometer assembled from various microfabricated components [37], [38].

1.4   Micro-Gas Analyzer Project

MEMS technology has become a reliable method for constructing complex geometries, and serves as a key enabler for the development of many small, low-cost, high-performance sensors [39]. The Micro-Gas Analyzer (MGA) project attempts to leverage the benefits of MEMS technology to develop a miniature mass spectrometer for portable chemical sensing. The system concept is shown in Figure 1-2 along with several images of microfabricated components that have been achieved to date by collaborators on the project.
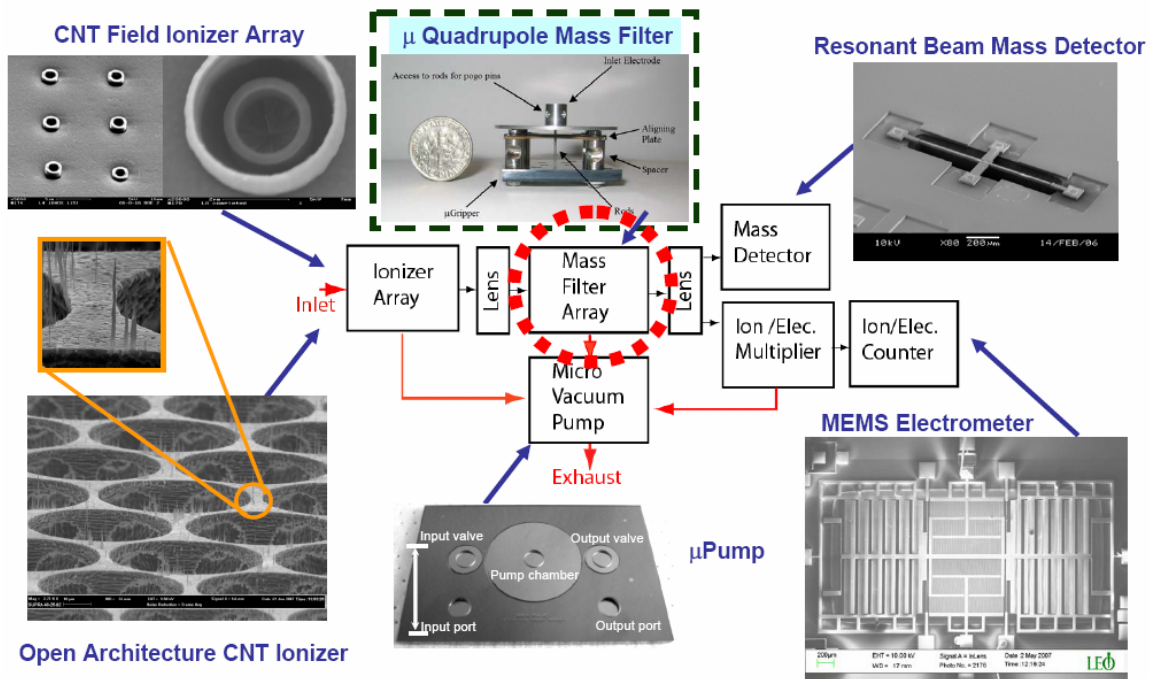
Figure 1-2: Overview of the Micro-Gas Analyzer

19

For the ionizer, Chen et al. developed double-gated carbon nano-tube (CNT) field ionizer arrays capable of generating ions at very low powers [40], [41]. An open architecture CNT ionizer has also been fabricated by Velásquez-García [42], [43], where the design facilitates gas transport to the ionizer tips. For the detector, Zhu et al. reported an electrometer made from SOI technology that demonstrated an extremely low noise floor [44], [45]. Additionally, a silicon resonant beam mass detector can be fabricated alongside the electrometer for parallel detection [46]. Unpublished work by Vikas Sharma at the Massachusetts Institute of Technology demonstrated a micro-displacement vacuum pump that was able to pull down 220 Torr from atmosphere.

Out-of-plane quadrupole mass filters assembled using silicon deflection springs in a MEMS platform has been demonstrated as well [47]. Quadrupoles were implemented because of their simplicity, and robustness under operation. Figure 1-3 shows three popular types of mass filters that were considered for microfabrication due to their simple construction. From the fundamental equation of operation provided under each type of device, we can clearly see that the quadrupole is the best suited for scaling-down.

Magnetic Sector

$$\frac{m}{e} = \frac{B^2 r^2}{2V_{ion}}$$

Time-of-Flight

$$\frac{m}{e} = \frac{2V_{ion}\tau^2}{L^2}$$

Quadrupole Field

$$\frac{m}{e} = \frac{4V}{q\omega^2 r_0^2}$$
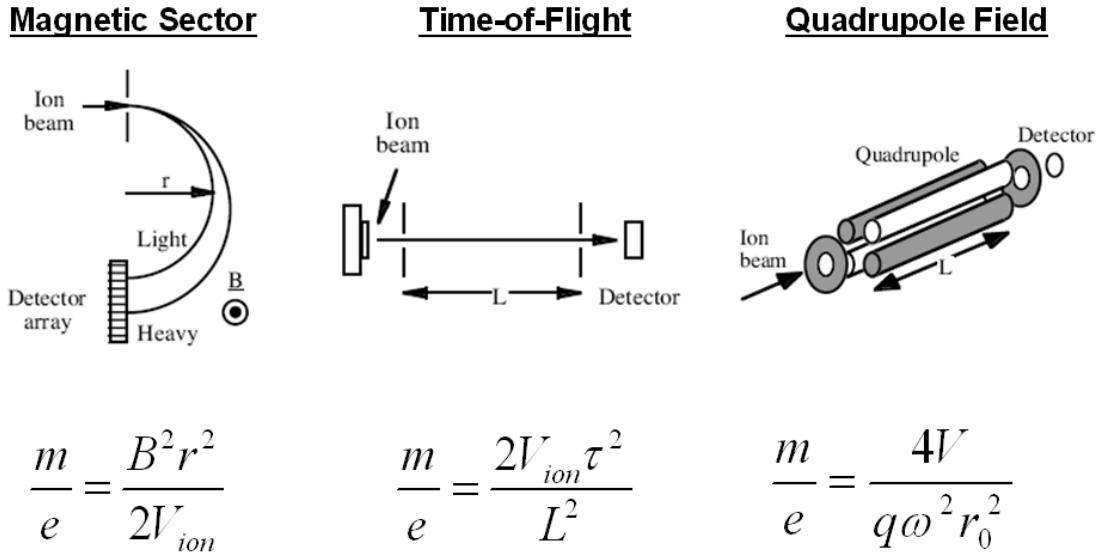
Figure 1-3: Popular types of mass filters [48]

If we make the magnetic sector device smaller (decrease *r*), an increase in the magnetic field *B* will be needed to maintain operation (*m/e* unchanged). This will require

larger and heavier magnets which is undesirable for miniaturization. If we scale-down the time-of-flight device (decrease L), then the ion flight times, τ, will also decrease to maintain operation. As a result, very fast electronics will be needed to detect light ions which might not be achievable. For the quadrupole field device, as the mass filter scales-down (smaller r_0), the drive voltage V reduces quite substantially. An additional benefit of this device is that the equation of operation has no dependence on the ion energy V_{ion}. Ion energy can be difficult to maintain accurately and will significantly impact the performance of the other types of mass filters.

For the MGA to become a ubiquitous gas sensor, the total system must be affordable. The low costs associated with MEMS sensors are achieved through batch-fabrication and economy of scale. Currently, the only component of the MGA that is not entirely batch-fabricated is the mass filter. The post-fabrication electrode assembly needed for the out-of-plane quadrupoles will serve as a bottleneck to mass production. This issue should be addressed, forming the basis of this thesis.

1.5   Thesis Organization

In this chapter, we identified several applications that are in need of fast, reliable chemical sensors. Mass spectrometers have the potential to fulfill this need if they can be miniaturized. The Micro-Gas Analyzer project aims to leverage MEMS technology to develop a low-cost, high-performance chemical sensor. Current limitations with the mass filter component prompts further exploration. The goal of this thesis was to address these limitations through the development of a chip-scale quadrupole mass filter.

The rest of this thesis is organized as follows – Chapter 2 introduces the theory behind quadrupole mass filter operation, and provides definitions for several relevant performance metrics. A summary of prior work on MEMS-based quadrupole mass filters is also included to put this thesis into perspective. Chapter 3 outlines the scaling considerations, and the optimization process used to arrive at the final device design. Chapter 4 covers the fabrication steps and experimental characterization for the first generation of chip-scale quadrupole mass filters. Chapter 5 details the design, construction, and calibration of a quadrupole testing facility assembled for in-house

device characterization. Chapter 6 covers the improvements made to our initial device design, and outlines a modified fabrication process flow. Extensive characterization of the improved devices using the in-house testing facility is also reported. Chapter 7 investigates several interesting phenomena encountered during the testing of our new devices, while Chapter 8 summarizes the work in this thesis and makes recommendations for future directions.

Chapter

2

Quadrupole Mass Filters

2.1 Quadrupole Physics

To fully appreciate the power and simplicity of a quadrupole mass filter (QMF), a review of the underlying physics of operation is provided. As the name implies, the fundamental principle behind this type of mass filter is the quadrupole field. When four hyperbolic electrodes are placed symmetrically in space with the electric potentials shown in Figure 2-1, an ideal quadrupole field is established. This field can be expressed in Cartesian coordinates as

$$\Phi(x, y) = \frac{\Phi_0 (x^2 - y^2)}{2 r_0^2} \tag{2-1}$$

where r_0 is the radius of the circle that is tangent to all four electrodes, and Φ_0 is the potential across adjacent electrodes.
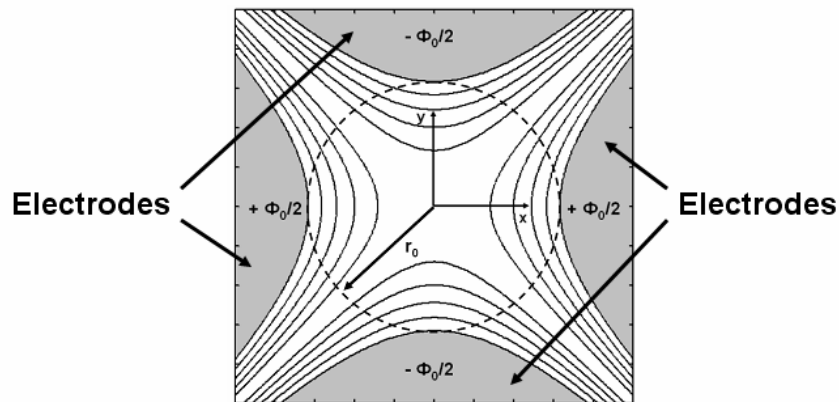
Figure 2-1: Ideal quadrupole field with hyperbolic electrodes

If the applied potential to each electrode is a combination of d.c. and a.c. voltages, $|\Phi_0/2| = U - V \cos(\omega t)$, the equations of motion for an ion in the field will be

$$\frac{d^2x}{dt^2} + \left(\frac{2e}{mr_0^2}\right)[U - V\cos(\omega t)]x = 0 \tag{2-2}$$

$$\frac{d^2y}{dt^2} - \left(\frac{2e}{mr_0^2}\right)[U - V\cos(\omega t)]y = 0 \tag{2-3}$$

where e and m are the charge and the mass of the ion, U is the amplitude of the d.c. drive component, and V and ω are the amplitude and frequency of the a.c. component respectively. Typically, ω is in the range of radio frequencies (r.f.) for most practical applications so "a.c." will be referred to as "r.f." throughout this thesis.

From Equations 2-2 and 2-3, we see that ion motion in the x and y directions are independent of one another, decoupling the problem and allowing it to be solved more readily. By making the substitutions $u_x = x/r_0$, $u_y = y/r_0$, and $\xi = \omega t/2$, we obtain the Mathieu-like equations

$$\frac{d^2u_{x,y}}{d\xi^2} \pm [a - 2q\cos(2(\xi - \xi_0))]u_{x,y} = 0 \tag{2-4}$$

$$a = \frac{8eU}{m\omega^2 r_0^2} \tag{2-5}$$

$$q = \frac{4eV}{m\omega^2 r_0^2} \tag{2-6}$$

where a and q are known as the Mathieu parameters, and ξ_0 corresponds to the initial r.f. phase in which the ion enters the field. Equation 2-4 has a general solution in the form

$$u = \alpha' e^{\mu\xi} \sum_{n=-\infty}^{\infty} C_{2n} e^{2in\xi} + \alpha'' e^{-\mu\xi} \sum_{n=-\infty}^{\infty} C_{2n} e^{-2in\xi} \tag{2-7}$$

where α' and α'' are constants that depend on the initial conditions, and the constants C_{2n} and μ depend only on the Mathieu parameters [1]. This fundamental property of the Mathieu equation means the nature of ion motion in the quadrupole will depend only on a and q, and not on the initial conditions.

Looking at Equation 2-7, we see that if μ is complex or real and non-zero, the solutions will be unstable due to the $e^{\mu\xi}$ and $e^{-\mu\xi}$ terms. When $\mu = i\beta$ and is purely imaginary, the solutions will be periodic and stable for non-integer values of β, and will be periodic but unstable for integer values [1]. The periodic and stable solutions are the ones that are useful in a QMF, highlighting the true power of this type of mass filter. The filtering property is defined only by trajectory stabilities that are governed by the Mathieu parameters, independent of initial conditions. Filtering will only be affected by initial conditions in the sense that trajectories with amplitudes greater or equal to the confines of the device (r_0) will not be transmitted.

The stable and unstable solutions of the Mathieu equation can be mapped as a function of the Mathieu parameters. The boundaries defining the regions shown in Figure 2-2 correspond to the integer values for β. From Equation 2-4, we see that the stability diagram will be symmetric about the a-axis, and that the boundaries stemming from positive a values correspond to the motion in the x-axis. Boundaries stemming from negative a values correspond to motion in the y-axis, so regions in which both stability diagrams overlap denote values of a and q in which ion motion is stable in both x and y. These sets of a and q form stability regions that are shaded and labeled in Figure 2-2. If the quadrupole is operated at an (a, q) near the corner of a stability region, mass filtering is achieved.
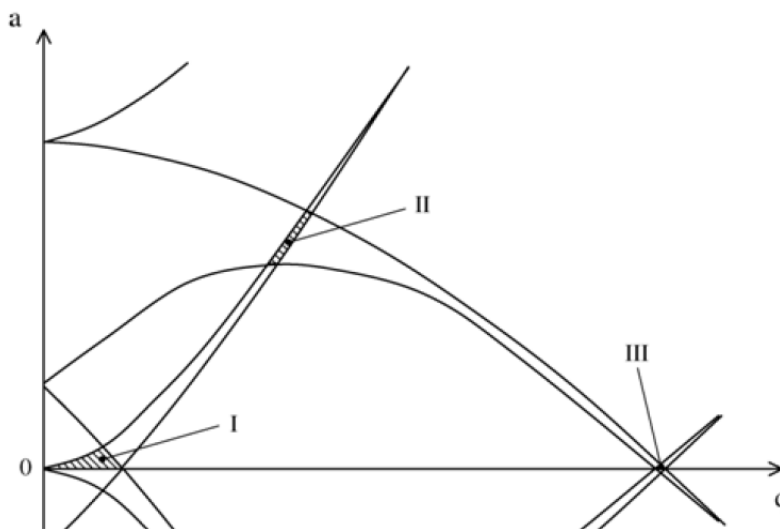
Figure 2-2: Mathieu stability diagram

2.2   Mass Filtering

Given an operating frequency and characteristic device dimension (r_0), we can use Equation 2-5, 2-6, and the Mathieu stability diagram to calculate the range of U and V that will produce stable trajectories for a specific m/e. If the quadrupole is operated at a point near the corner of a stability region, there will be a small range of U and V that will transmit the specified ions. This range of voltages will be proportional to the peak-width of the detected signal, so a higher resolution mass peak is associated with a smaller range. A mass spectrum can be generated if the d.c. and r.f. voltages are scanned in a fixed ratio $a/q = 2U/V$, and the number of transmitted ions for each m/e is recorded. Figure 2-3 depicts the mass filtering principle for operation in the first stability region. Assuming an ion with $m/z = 219$ and the scan-line shown, the points along the scan-line that are within the stability region (green) will produce stable trajectories that transmit through the quadrupole and into the detector. Points that lie outside the stability region (red) will produce unstable trajectories that collide into the electrodes and discharge. The quantity m/z is often used interchangeably with m/e, where z corresponds to the number of charges on an ion of mass m.
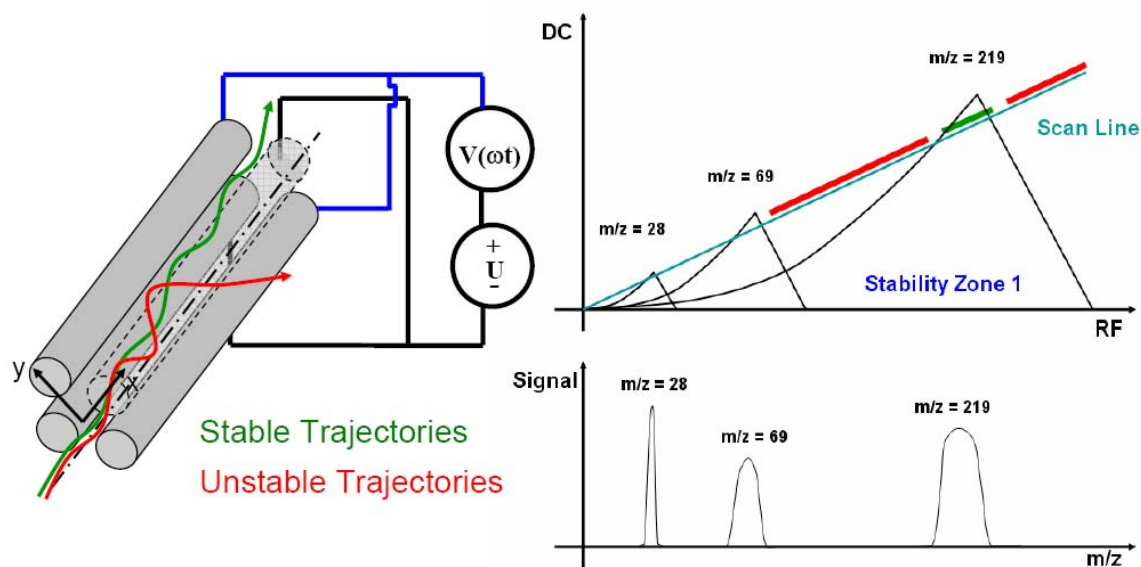
Figure 2-3: Schematic of mass filtering

Most commercial quadrupoles utilize cylindrical electrodes instead of hyperbolic ones due to the manufacturing simplicity. Researchers have found that cylindrical electrodes with radius r serve as a good approximation to ideal hyperbolic electrodes if the r-to-r_0 ratio is 1.148 [49]. This number corresponds to the ratio needed to eliminate the dodecapole term associated with using cylindrical electrodes, and was later revised to 1.145 [50]. Recent work using advanced simulations involving actual ion flight report an optimal value of 1.128 [51], [52]. Despite these approximations, there are still non-idealities that degrade performance and will be addressed in Section 2.3.

From Figure 2-3, we see that the peak-width of the detected signal becomes wider at larger masses. This is a direct result of the linear scan-line used, and is often referred to as the constant resolution mode since every peak has the same resolution. Commercial systems typically utilize a constant peak-width mode where the peak-width stays the same for every peak. This mode is more useful since it ensures proper mass separation throughout the range of the scanned masses. In turn, the resolution will be increasing for larger and larger masses, and the detected signals will decrease. The relative abundance of the analyte may be skewed, but proper calibration and tuning can address this issue. Ideally, mass spectra with constant peak-widths are produced by using a non-linear scan-line (dashed line) as depicted in Figure 2-4. An approximation to this curved scan-line can be achieved by assuming a linear scan-line with a non-zero intercept called Δm, and a slope called Δres [53]. For each system, these values are determined empirically through calibration with a low-mass ion and a high-mass ion simultaneously.
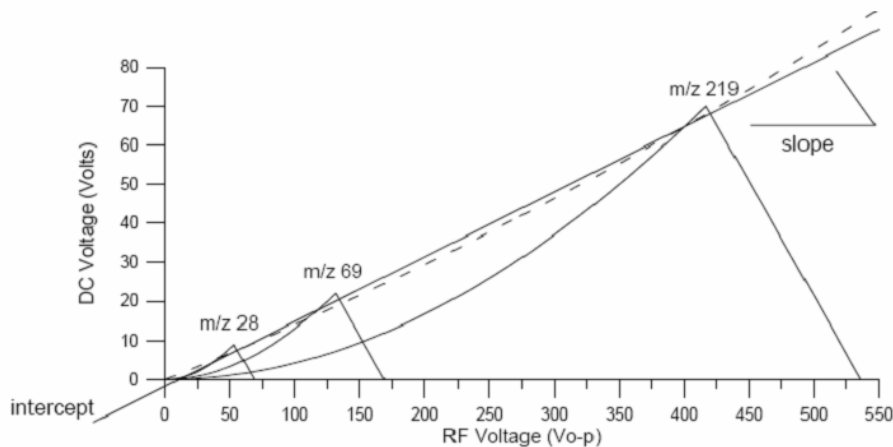
Figure 2-4: Scan-line for constant peak-width operation [53]

27

2.3   Quadrupole Performance

The performance of a QMF can be characterized by two key metrics, the mass range and the resolution. The mass range is the maximum mass resolvable with a quadrupole of radius r_0 given a set of operating conditions. The operating point (a, q), the drive frequency, and the maximum applied voltage will affect this metric, but it is ultimately constrained by the electrical breakdown of the QMF and the voltages that can be supplied by the drive electronics. The resolution is the more important performance metric, and is an indicator of how well the quadrupole can distinguish between ions with m/e that are close in value. Resolution is expressed as the ratio $R = m/\Delta m$, where m is the mass corresponding to the peak detected and Δm is the peak full-width at half the maximum signal intensity (FWHM). Other researchers use different definitions for the peak-width (10% or 25% signal intensity) but this thesis will use the FWHM definition. The closer the quadrupole is operated to the corner of a stability region, the smaller the peak-width and the higher the resolution. Theoretically, the resolution can be infinite but in a real device with finite length, the maximum resolution attainable is limited by n, the number of r.f. cycles that an ion spends in the QMF [1].

Since the filtering mechanism of the quadrupole is based on ion trajectories with an oscillatory nature dictated by the drive frequency, we would expect the resolution to have a dependence on the value of n. Experimental data has shown that the resolution can be related to n by

$$R = \frac{m}{\Delta m} \approx \frac{1}{h} n^p \tag{2-8}$$

where h is a constant that reflects the operating point (a, q) as well as how the ionizer is coupled to the quadrupole, and p has been empirically determined to be about 2. A good approximation for n can be given by fL/v_z where f is the drive frequency, L is the quadrupole length, and v_z is the axial ion velocity. If the ion is accelerated with a potential V_z, then the resolution can be expressed as

$$R \cong \frac{n^2}{h} \approx \frac{1}{h}\left(f\frac{L}{v_z} \right)^2 = \frac{1}{h} f^2 L^2 \left(\frac{m}{2V_z e} \right) \tag{2-9}$$

Combining Equation 2-8 and 2-9 and solving for Δm, we get

$$\Delta m = h \frac{2V_z e}{f^2 L^2} \tag{2-10}$$

which means the peak-width achievable is independent of mass. This result supports the constant peak-width mode of operation, but Equation 2-10 does not factor in field imperfections that limit the maximum resolution attainable.

Field imperfections can arise from either (1) misalignment of the electrodes, (2) the use of non-hyperbolic electrodes, (3) imbalances in the drive signals, or (4) static charges resulting from electrode contamination [1], [54]. The impact of each of these reasons on the resolution is not very well understood, but there have been reports which estimate the maximum resolving power as a function of misalignments [1], [54]. Since the filtering mechanism of a quadrupole (stable ion trajectories) depends on the established electric fields, distortions arising from construction errors such as electrode misalignments or variations in electrode diameters will degrade performance. A first-order approximation for the maximum resolution attainable from a QMF with construction error ε can be given by $R_{max} \sim 2r_0/\varepsilon$, where r_0 is the characteristic dimension of the device. The other reasons listed for field imperfections have been reported to have a direct impact on peak-shape. The formation of a precursor peak in the low-mass tails of the mass spectrum has been attributed to the use of circular electrodes [55], [56], while imbalances in the drive signals and contamination issues have been reported to cause peak-splitting [54], [57]. These undesirable features stem from non-linear resonances that will be discussed more extensively in Section 2.4.

Other performance metrics for a quadrupole are the abundance sensitivity and the transmission, but these quantities are not well understood. The abundance sensitivity is a measure of how "clean" a peak is, namely how much signal from mass M overlaps onto masses M-1 or M+1. Typically, this value is calculated by taking the ratio of the signal at mass M and the signal at M-0.5 or M+0.5. Larger values correspond to better abundance sensitivities since adjacent peaks will be more distinct. Ion energies, field imperfections, and fringing-fields arising from the finite length of the quadrupole electrodes will all impact this quantity in different ways that is not very predictable [56], [58]-[61]. These factors will affect the ion trajectories which ultimately determine peak-shapes and thus,

abundance sensitivity. The transmission is measured as the percentage of incoming ions that make it through the device after filtering. This quantity is proportional to the quadrupole acceptance which is an electronically controlled aperture that depends on the ion dynamics. For a given operating condition, the acceptance signifies the area of the quadrupole inlet which allows ions to pass for all initial r.f. phases [62]. It is important to keep in mind that there are points that lie outside the quadrupole acceptance which can transmit ions for certain phases but not all. To further confuse things, the acceptance is affected by fringing-fields, the drive frequency, and the operating point (a, q) [60], [62], [63]. General trends are that fringing-fields and increased drive frequencies will decrease acceptance, and operation at higher resolution will decrease transmission.

Aside from the factors mentioned above, the ionizer, detector, ion lenses, and drive electronics also impact the performance of a quadrupole. For the ionizer, the ion energy used and the ionizer emittance will affect the transmission, abundance sensitivity, as well as peak-shapes. Large ion energies usually improve transmission but degrade abundance sensitivity and peak-shape since ions spend less time being filtered [59]. Typically, ion lenses are utilized to match the ionizer emittance to the quadrupole acceptance in order to improve overall performance. The same concept can be applied to the detector end of the device to couple filtered ions into the detector. Drive electronic stability is another key factor that impacts resolution [54]. Since the operating point (a, q) is set by the drive voltages, fluctuations in the $2U/V$ ratio during scanning can cause severe limitations in the maximum resolution attainable. Care should be taken during the drive circuit design to ensure signal precision and invariance to heating or drifts.

2.4 Non-linear Resonances

In an ideal QMF, the equations of motion for the x-axis and y-axis are independent from one another. Field imperfections arising from the factors mentioned in Section 2.3 will couple the equations of motion, changing the solutions of the Mathieu equation. The coupling will manifest as non-linear resonances that degrade peak-shape by introducing precursor peaks and peak-splitting. Substantial research has been conducted with Paul traps that demonstrated non-linear resonances with a good match to theory [64]-[67].

30

Linear Paul traps were later investigated and displayed the existence of non-linear resonances as well [68], [69]. These resonances effectively introduce lines of instability within the stability diagram as depicted in Figure 2-5. These new lines correspond to values of *a* and *q* that produce unstable ion trajectories that normally should be stable without the presence of the field imperfections.
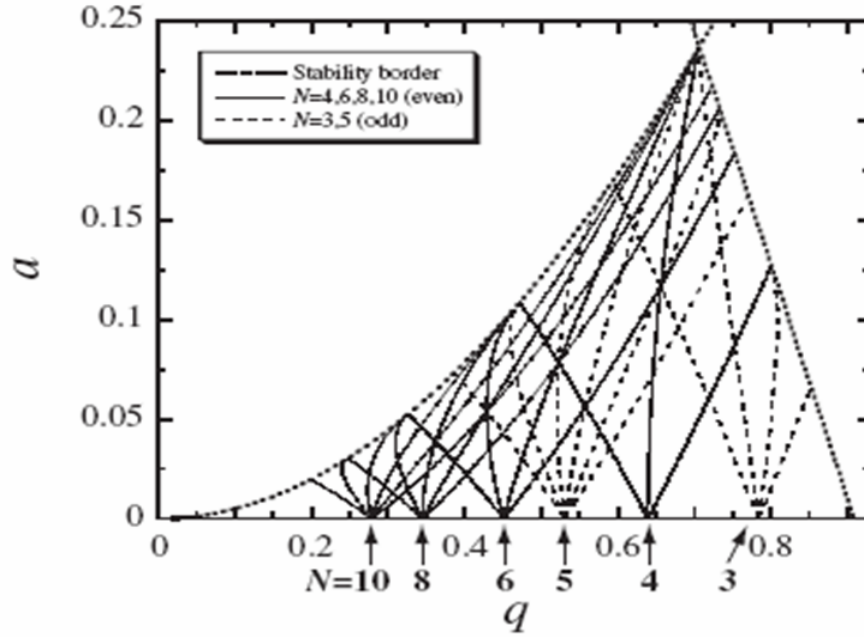
Figure 2-5: Non-linear resonances in the first stability region [69]

The location of the instability lines shown in Figure 2-5 follows the theory that has been laid out by Wang et al. [70]. The resonance conditions of the coupled ion motion in a linear quadrupole are given by

$$\frac{\beta_x}{2} n_x + \frac{\beta_y}{2} n_y = v \tag{2-11}$$

$$|n_x| + |n_y| = N \tag{2-12}$$

where n_x, n_y, v, N are integers, and β_x, β_y are the characteristic exponents of the Mathieu equation that depends on *a* and *q*. The integer *N* corresponds to the order of the non-ideal field components arising from field imperfections, and are only considered for values greater than 2 since $N = 2$ is the ideal quadrupole term. $N = 3$ corresponds to the hexapole term, $N = 4$ is the octopole term, and so on and so forth.

If we imagine a scan-line that passes through the modified stability region shown in Figure 2-5, it is clear that several of these non-linear resonance lines will be crossed. As a result, the mass spectrum will have noding and peak-splitting that correspond to the unstable ion trajectories along the scan. Interestingly, the peak-splitting associated with these non-linear resonances are not as pronounced for low-resolution scans [71]. This result is due to the fact that the transmission is high and abundance sensitivity is small at low resolutions. The effects of the non-linear resonances are essentially smeared and hidden within the spectrum. Conversely, the peak-splitting and noding will be much more dramatic at high resolutions leading to a substantial degradation in peak-shape.

2.5   Higher Stability Regions

In Section 2.2, we introduced the Mathieu stability diagram which maps the stable and unstable solutions of the Mathieu equation. The boundaries shown in Figure 2-2 correspond to integer values of β, and provide information on the oscillatory nature of the ion trajectories in the quadrupole. Stable trajectories with a larger value of β will have a higher fundamental frequency of ion motion. From Figure 2-2, we can identify the three stability regions where ion motion will be stable in both x and y. Theoretically, there are a large number of these stability regions but only operation in the labeled three makes sense. The others regions are located at much larger a and q values which translates to significantly higher voltages that are not practical to implement. Operation in the first stability region correspond to $0 < \beta < 1$, while operation in the third stability region correspond to $1 < \beta < 2$. The second stability region is essentially a combination of the first and third stability regions with $0 < \beta < 1$ and $1 < \beta < 2$, and if often referred to as the intermediate stability region.

Most studies on quadrupole mass filters are conducted in the first stability region, but there have been reports of improved performance with operation in the second stability region [72]-[75]. Resolution is improved due to the higher fundamental frequency of ion motion associated with the higher stability region. An ion effectively experiences more r.f. cycles, and thus filtering is improved. Operation in the third stability region has also been proposed [76] but the large associated q and the fact that operation in this region

will require the scan-line to pass through the first stability region make it less desirable [77]. The trade-offs of utilizing the higher stability regions for improved resolution is the decrease in transmission and the need for larger operating voltages. This trade-off might be acceptable for applications where the decrease in transmission can be compensated for with a more sensitive detector or a more abundant ion source.

The second stability region is a rectangular zone centered about $(a, q) = (2.9, 3.0)$ with the corners located at the values portrayed in Figure 2-6. Reported values for h in this region are between 0.73 and 1.43, as opposed to 10 and 20 for the first stability region [1]. If we assume operation in the first stability region is centered around $(a, q) = (0.23, 0.7)$, operating in the second stability region will require a 12.6 fold increase in d.c. voltage, and a 4.3 fold increase in r.f. voltage. This selection would provide a 7 to 20 fold increase in resolution with all else constant [47]. There have also been reports that the transmission decreases less rapidly as a function of resolution in the second stability region than in the first stability region [78]. Operation in the second stability region promises high resolution devices with a moderate decrease in transmission.
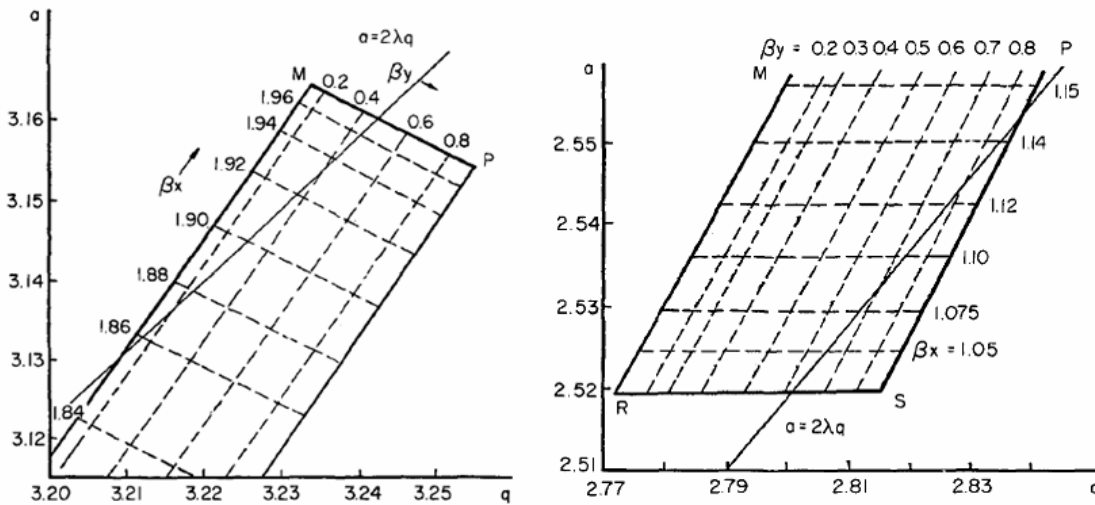
Figure 2-6: Upper and lower corners of the second stability region [78]

Other than the improvement in resolution, there have been reports of improved peak-shape associated with operation in the second stability region [47]. Detected peaks are more symmetric, precursor peaks and peak-splitting from non-ideal field components are

drastically reduced, and abundance sensitivity increases. These effects can be explained by the fact that ions are much more defocusing in this stability region [77]. Ions that enter the quadrupole farther away from the central axis of the device will have trajectories that quickly grow [79]. The large amplitudes associated with this motion will cause the ions to collide with the electrodes, effectively decreasing the acceptance and lowering transmission. Additionally, ions that are able to transmit will have trajectories confined near the central axis of the device [80], thus minimizing the effects of imperfect fields that produce poor peak-shape.

2.6   MEMS-based Quadrupoles

Miniaturization of quadrupoles has been introduced in Chapter 1, but an extensive summary of MEMS-based quadrupoles is included to expand on relevant work to this thesis. There has been significant progress made from several groups that demonstrated functional devices, while other researchers have reported fabricated devices without experimental data.

Taylor et al. reported a QMF made from metalized glass fibers that were aligned in V-shaped grooves etched into silicon by KOH, and mounted with solder [22]-[24]. The electrodes measured 500 μm in diameter and 30 mm in length, and were assembled utilizing the popular r-to-r_0 ratio of 1.148. Larger cylindrical spacer rods were used to separate the two silicon substrates as shown in Figure 2-7. The device was operated at 6 MHz in the first stability region, demonstrating a mass range of 50 amu and a peak-width of 1.3 amu at mass 40. This result corresponds to a resolution of ~31, which is quite good for the first report of a MEMS-based quadrupole. The limited mass range was due to capacitive coupling of the electrodes to the silicon, leading to excessive heating during operation. The heating caused the solder to melt, ultimately leading to the delamination of the electrodes. Follow-up work by Syms et al. incorporated an Einzel lens into the design that demonstrated one-dimensional focusing [81]. The lens elements were assembled in a similar manner as the electrodes as depicted in Figure 2-8.
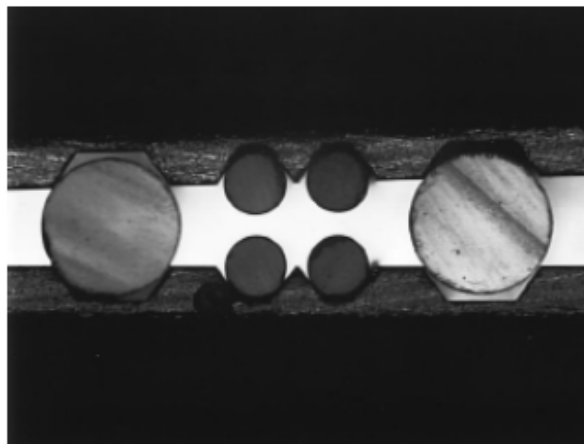
Figure 2-7: V-shaped groove MEMS QMF [23]
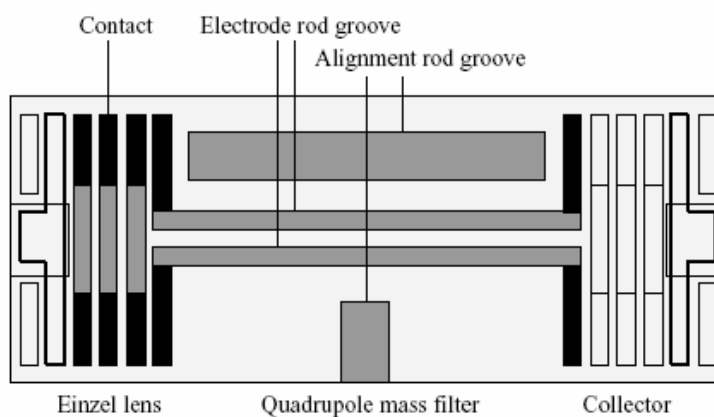
Figure 2-8: Integrated Einzel lens for V-shaped groove MEMS QMF [81]

Geear et al. proposed a new design in which the quadrupole electrodes are held and align with deflection springs etched into a monolithic silicon block [27]. The device was made from two bonded SOI wafers, and contained integrated ion optics that were astigmatic (Figure 2-9). The reported device comprised of cylindrical metal electrodes 500 μm in diameter and 30 mm long that were positioned with an r-to-r_0 ratio of 1.148. Device operation at 6 MHz demonstrated a mass range of 400 amu and a peak-width of 0.8 amu at mass 69, corresponding to a resolution of ~86. An enhanced spectrum using only a single peak achieved a maximum resolution of ~115 but this number is not indicative of performance during normal operation. Overall, Geear's work presented a substantial improvement over the QMF reported by Taylor.
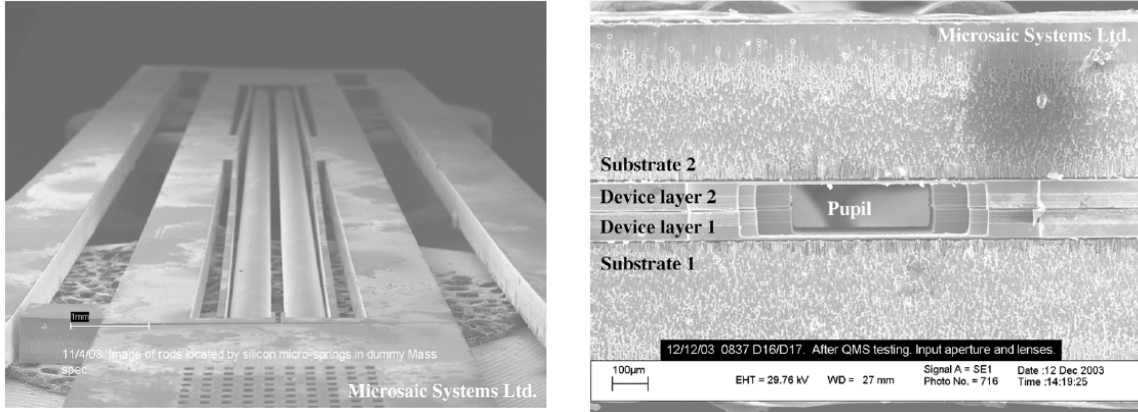
Figure 2-9: Monolithic MEMS QMF [27]

More recently, Velásquez-García reported an out-of-plane quadrupole that utilized deflection springs to precisely align the electrodes during assembly [47]. The springs were fabricated into a MEMS platform called the μ-Gripper that implemented an r-to-r_0 ratio of 1.148 (Figure 2-10). The technology used commercially available dowel pins as electrodes and was able to accommodate a wide range of rod diameters. An assembled quadrupole with electrodes 1.58 mm in diameter and 90 mm long demonstrated fairly good performance. A mass range of 650 amu was achieved when driven at 1.44 MHz, and a minimum peak-width of 0.4 amu at mass 28 was obtained when driven at 2.0 MHz in the second stability region. This result corresponds to a resolution of ~70 and was the first report of a miniaturized device operating in a higher stability region. Data was also shown for a device with electrodes 1.0 mm in diameter and 37 mm long, but only a resolution of ~17 was achieved.
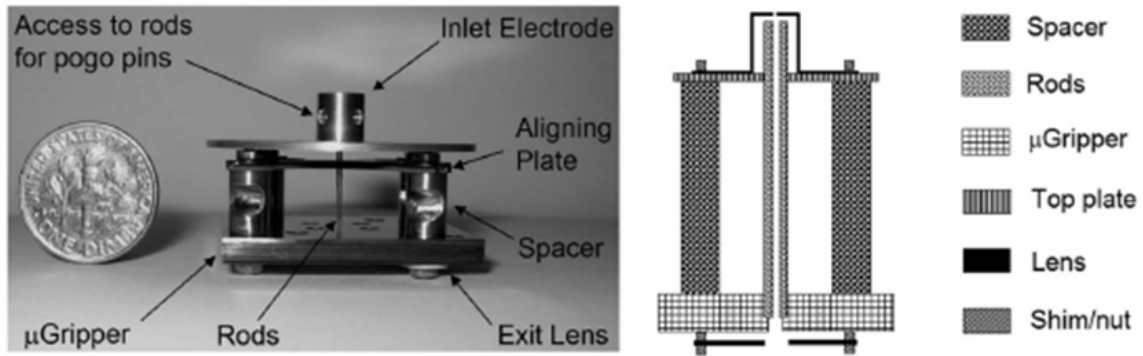
Figure 2-10: Out-of-plane MEMS QMF [47]

The MEMS-based quadrupoles described so far demonstrated good performance but they all share a major limitation – the quadrupole electrodes were assembled after the microfabrication was completed. This post-fabrication assembly can lead to potential issues in terms of performance repeatability between different devices, as well as the extra costs associated with serial assembly. Wiberg et al. reported a QMF array with hyperbolic electrodes defined using LIGA [25], while Deshmukh et al. proposed utilizing semiconducting cantilevers to establish a quadrupole field [26]. Both of these devices demonstrated batch-fabrication of the quadrupole electrodes (Figure 2-11), addressing the issues mentioned above. Unfortunately, despite the innovations in electrode construction, functionality was not shown.
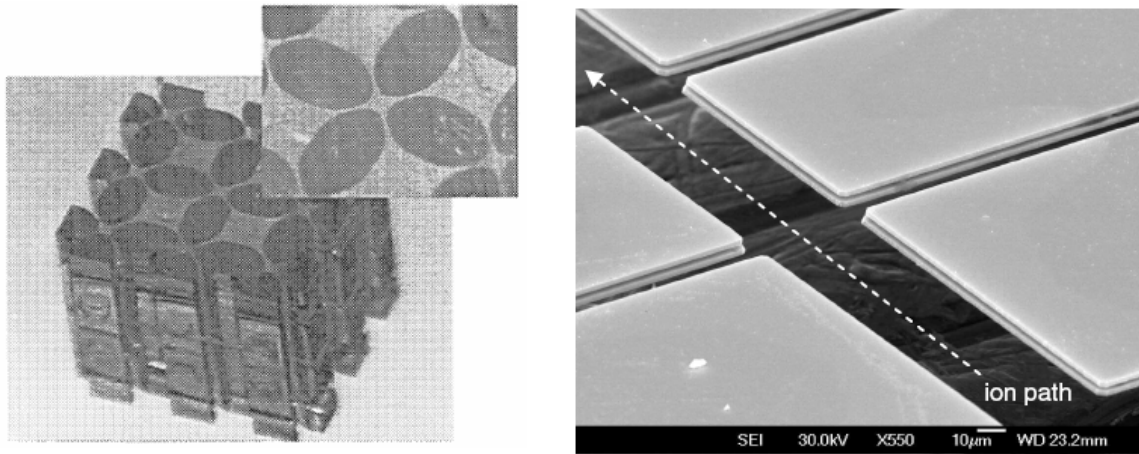
Figure 2-11: Other MEMS-based QMFs [25], [26]

2.7   Summary

In this chapter, we covered the fundamentals of quadrupole mass filter operation and introduced some interesting capabilities associated with these powerful devices. The physics behind the ion dynamics and discussion on the quadrupole performance metrics were included to familiarize the reader with terminologies and concepts that are discussed throughout this thesis. Issues with non-linear resonances were mentioned and operation in a higher stability region was presented as a means to improve performance and peak-

shape. Finally, a review of prior work conducted in the field of MEMS-based quadrupole mass filters was provided to put this thesis into context.

Chapter

3

Device Design

3.1 Scaling Considerations

When designing a miniature quadrupole mass filter (QMF), an important step is to evaluate how the general characteristics of the device will be affected by scaling-down. Characteristics to consider are the device performance, the device capacitance, and the maximum operational pressure. The performance is guided by the fundamental equations of operation presented in Chapter 2, which are directly affected by size. The quadrupole capacitance and associated parasitic capacitances are also important because they have implications for drive electronics and power considerations. Finally, some attention should be given to the pressure of operation since it can influence the performance of the other components in the Micro-Gas Analyzer (MGA).

3.1.1 Performance

Looking at Chapter 2, we can identify two equations that relate the key performance metrics, the resolution and the mass range, to the quadrupole dimensions. From Equation 2-10, we have

$$\Delta m = \frac{2V_z e h}{L^2 f^2} \tag{3-1}$$

where V_z is the axial ion energy, h is a constant depending on experimental and operating conditions, L is the length of the quadrupole, and f is the driving frequency. Throughout

the design process, the terms in the numerator can be assumed a constant. From Equation 2-6 and the fact that $\omega = 2\pi f$, we can derive

$$V_{max} = \pi^2 q \frac{m_{max}}{e} f^2 r_0^2 \tag{3-2}$$

where q is one of the Mathieu parameters, r_0 is the characteristic dimension of the quadrupole, m_{max} is the maximum mass range to be scanned, and V_{max} is the r.f. amplitude needed. Equation 3-1 states that the minimum peak-width will increase as the quadrupole gets smaller (decreased L), effectively reducing the resolution achievable. We can offset this decrease by having a proportionate increase in the drive frequency, but this will substantially increase the voltage needed to scan m_{max} as can be seen by Equation 3-2. If we are limited by the drive voltage and would like to scan the same mass range, we can decrease the radius of the device by the same factor the frequency was increased.

If we combine Equation 3-1 and 3-2 while eliminating the dependence on frequency, we obtain

$$R_{max} = \frac{m_{max}}{\Delta m} = \frac{(L/r_0)^2 V_{max}}{2\pi^2 V_z hq} = \frac{k^2 V_{max}}{2\pi^2 V_z hq} \tag{3-3}$$

where k is the aspect ratio of the quadrupole. This equation states that for a given maximum voltage, axial ion energy, and operating point (a, q), any quadrupole with the same aspect ratio will have the same maximum resolving power regardless of frequency. In an ideal world, we would be able to arbitrarily shrink a QMF without adverse affects on the performance as long as we kept the aspect ratio constant. This conclusion is far from reality since there are many factors that are not included in the equation. As r_0 decreases, the device will be more susceptible to misalignments and fringing-fields that degrade performance [54], [60]-[62]. A small device cross-section will make it difficult to couple ions into the QMF, and space-charge effects may come into play. The impact of the fringing-fields also has a dependence on frequency [60], [62], which is removed in Equation 3-3. These factors will affect the constant h since it is an empirical value that is partially used to reflect how well ions are coupled into the mass filter.

To guide the design of our chip-scale QMF, we returned to the first two equations of this chapter. A mass range of 400 amu with a peak-width of 1 amu was targeted since these performance metrics are useful for a wide range of applications. Assuming an ion

energy of 5 eV and operation in the first stability region, we chose $(a, q) = (0.23, 0.7)$ and a corresponding h value of 15. These values were utilized in conjunction with Equations 3-1 and 3-2 to form the plots of Figure 3-1. One plot gives the minimum peak-width as a function of frequency for various device lengths, while the other gives V_{max} for 400 amu as a function of frequency and various device radii. In consideration of the voltages used in other MEMS devices, a maximum operation r.f. amplitude of 150 Volts (300 V_{pp}) was imposed.
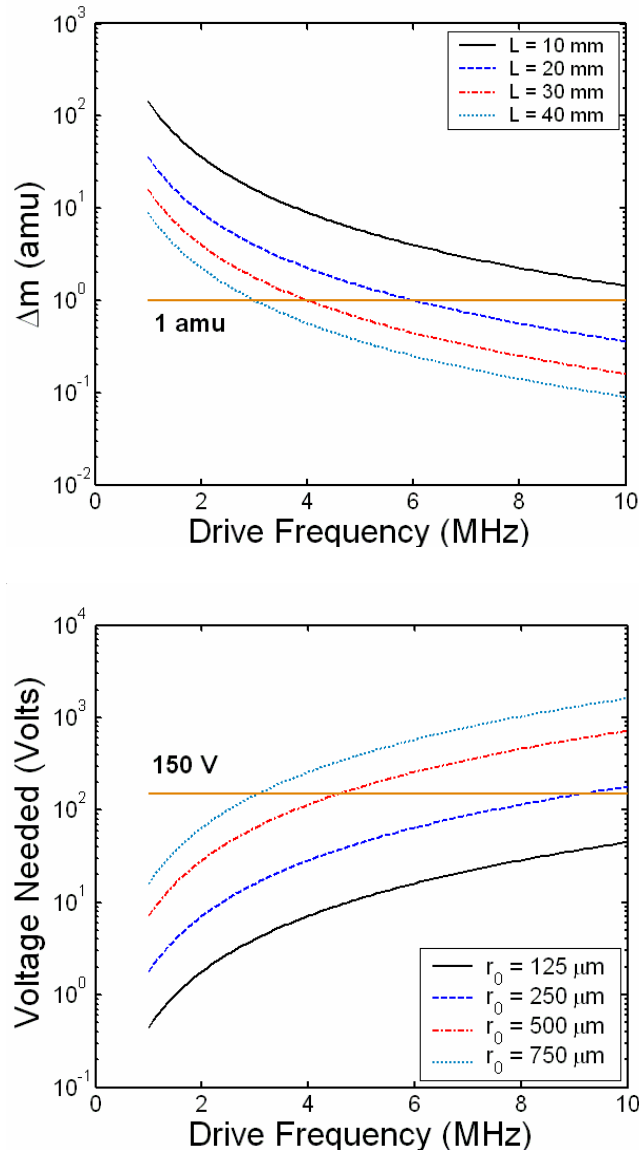
Figure 3-1: Design space for a chip-scale QMF

From Figure 3-1, we saw that if we chose a device length of 30 mm, we would need a drive frequency of at least 4 MHz to meet the resolution specification. By setting 4 MHz as the quadrupole drive frequency, we needed a device radius of no larger than 500 μm to meet the specified mass range and imposed voltage limit.

3.1.2 Capacitance

The device capacitance is a crucial factor in determining the frequency at which the QMF can be driven at. Typically, a QMF is driven in an LC tank configuration where the resonance frequency is given by $f = 1/[2\pi(LC)^{1/2}]$ and L is the inductance in the circuit. Since scaling down a quadrupole usually calls for an increase in drive frequency, we need to have a corresponding decrease in device capacitance or drive inductance. A good understanding of the capacitances will facilitate the design of drive electronics.

Boumsellek at al. argued that as a quadrupole decreases in size, the capacitance will increase [4] but a simple 2D model can be used to show otherwise. Our model assumes an ideal quadrupole potential established by hyperbolic electrodes that are truncated in the orthogonal directions at a distance $D + r_0$, where $D = 2 \cdot (\psi \cdot r_0)$. This choice is to reflect the geometry of a typical QMF with an aperture radius r_0 and an electrode r-to-r_0 ratio of ψ. A schematic of our model is shown in Figure 3-2 for clarification. From Gauss' law, the charge on the electrode surface is

$$Q = \varepsilon_0 \oint \vec{E} \cdot d\vec{A} \tag{3-3}$$

where ε_0 is the permittivity of free space, $d\vec{A}$ is the normal area differential, and $\vec{E}$ is the electric field. Taking the Gaussian loop as shown in Figure 3-2, the electric field along the hyperbolic surfaces is

$$\vec{E} = -\vec{\nabla}\phi = -\frac{\phi_0}{r_0^2}(x\hat{x} - y\hat{y})\bigg|_{x^2 - y^2 = r_o^2} \tag{3-4}$$

with field lines parallel to $d\vec{A}$, and is assumed to be zero on the truncated surfaces. From our model, the total capacitance of a quadrupole with length L can be approximated by

$$C_0 = \frac{4\varepsilon_0 L}{r_0^2} \int\limits_{x=r_0}^{x=(2\psi+1)r_0} \frac{2x^2 - r_0^2}{\sqrt{x^2 - r_0^2}} dx = \frac{4\varepsilon_0 L}{r_0^2}\left[x\sqrt{x^2 - r_0^2}\right]_{x=r_0}^{x=(2\psi+1)r_0}$$

$$C_0 = C^* L = [8(2\psi + 1)\sqrt{\psi^2 + \psi}]\varepsilon_0 L \tag{3-5}$$
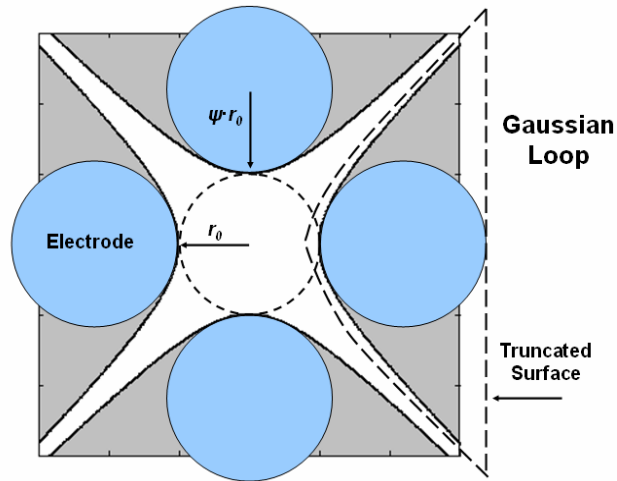
Figure 3-2: Model for capacitance calculation

Our model predicts that the device capacitance scales with length, so scaling-down a quadrupole should decrease capacitance. Equation 3-5 implies that the capacitance per unit length is constant and was verified using MAXWELL 2D from Ansoft. Simulations with energy error < 0.1% were utilized to calculate the capacitances of devices with $\psi =$ 1.148 and r_0 values ranging between 50 μm and 500 μm. MAXWELLL returned a capacitance of 2.1 pF/cm while Equation 3-5 gives 3.67 pF/cm. These values are overestimates because they neglect the 3D effects present in quadrupoles with finite length. To get a better estimate of the capacitance, quadrupoles with electrode diameters ranging from 500 μm to 1500 μm, and lengths between 25 mm and 100 mm were simulated with an energy error < 5% in MAXWELL 3D. The average capacitance per unit length was 1.75 pF/cm and was found to be nearly constant for quadrupoles with aspect ratios greater than 100. This value is very close to the 1.67 pF/cm measured for the out-of-plane MEMS quadrupole reported by Velásquez-García [47].

Aside from the device capacitance mentioned, parasitic capacitances also play an important role in the drive electronics. A quick circuit diagram can be used to determine the net capacitance as shown in Figure 3-3. The transformation is accomplished by assuming that the capacitance between adjacent electrodes (C_{quad}) is comprised of two capacitors in series with the value $2C_{quad}$. Additionally, the point between these two capacitors is tied to ground because the voltages applied to adjacent electrodes are anti-

symmetric. If we assume that each electrode is identical and the associated parasitic capacitance (C_{para}) is also identical, the total capacitance is given by $4C_{quad} + C_{para}$. The quantity $4C_{quad}$ should be approximately equal to the quadrupole capacitance given by Equation 3-5. From this analysis, we see that parasitics can potentially dominate the device capacitance for scaled-down devices (small L) so attention should be paid to minimize them.

$$C_{TOTAL} = 4C_{quad} + C_{para} = C^{*}L + C_{para}$$
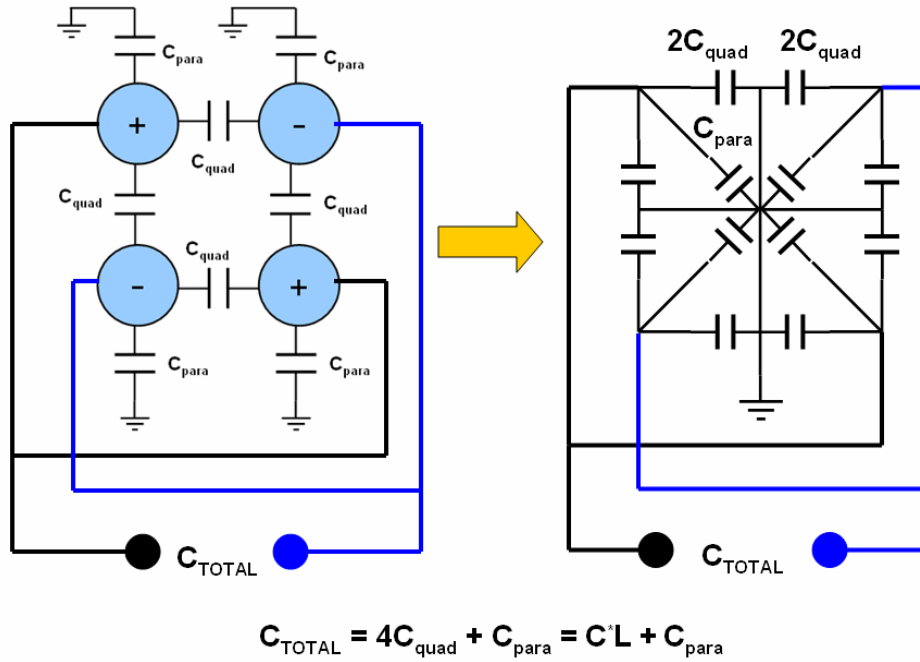
Figure 3-3: Device model for parasitic capacitances

Power consumption in the device can be estimated from the formula $CV^{2}f/2$ where V is given by Equation 3-2, and C is the total capacitance of the device.

$$P = \frac{1}{2}\left(C^{*} + \frac{C_{para}}{L}\right)\left[2\pi^{2}\frac{m}{e}qf^{2}r_{0}^{2}\right]^{2}Lf \tag{3-6}$$

From Equation 3-6, we see that if the quadrupole length and radius are scaled-down by the same factor that the frequency is increased, effectively maintaining the aspect ratio and performance metrics, the power consumed won't be significantly affected unless the C_{para}/L term dominates. At this point, power consumption will increase as the device length shrinks. Ultimately, the biggest drain on total system power will still be the vacuum pump.

3.1.3 Pressure

For proper QMF operation, the mean free path of the gas to be analyzed should be larger than the largest dimension of the quadrupole. The reason for this criterion is to ensure that an ion will traverse the length of the device without colliding with another ion or a neutral molecule. The mean free path for air at room temperature is given by

$$\lambda = \frac{k_B T}{\sqrt{2}\pi d^2 P} \sim \frac{50}{P}$$

(3-7)

where k_B is the Boltzmann constant, T is the temperature, d is the diameter of the gas molecules, P is the pressure in Torr and λ is the mean free path in microns.

Work on ionizers for the MGA demonstrated a maximum operational pressure around 1 mTorr [40], [41]. This pressure translates to a quadrupole that can't be longer than 50 mm for proper operation. If higher pressures can be achieved, the vacuum pump will have relaxed pumping requirements, and the detector can be less sensitive. Unfortunately, the quadrupole will need to be shorter, leading to increased drive frequencies and larger voltages if performance is to remain unchanged. Throughout the design process and device characterization, one should be aware of the potential for arcing between the QMF electrodes and plasma formation in the ionizer. This electrical breakdown is dictated by the Paschen curve (Figure 3-4) which plots the breakdown voltage as a function of the operational pressure and the spacing between electrodes.
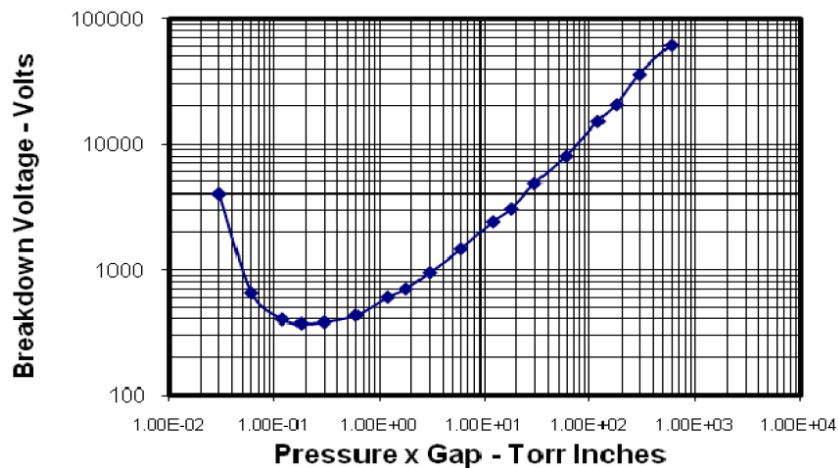
Figure 3-4: Paschen curve

3.2   Device Concept

A review of MEMS-based quadrupoles in Chapter 2 revealed several limiting factors in the reported device designs. Despite the performance achieved, these quadrupoles all suffered from electrode-to-housing misalignments that arose from the post-fabrication electrode assembly. Misalignments limit the maximum performance attainable in a QMF [1], [54], and the reported assembly methodologies placed a bottleneck on the ability to mass produce these devices. Additionally, portable mass spectrometers have applications in harsh environments where high temperatures and vibrations are a concern [82]-[84]. The reported MEMS-based quadrupoles will have limited lifetimes in such environments due to the manner in which the electrodes are attached to the housing.

Our device concept aimed to integrate the electrodes, ion optics, and housing into one monolithic block. The design eliminated the electrode-to-housing misalignments that limit maximum performance, and enabled truly chip-scale quadrupoles mass filters. From the design arguments in Section 3.1, we wanted a quadrupole with a large aspect ratio for good performance, and an adequately sized device cross-section to minimize the effects of fringing-fields. In order to meet these requirements with only microfabrication techniques, the quadrupole electrodes were made in-plane.

Most commercially available quadrupoles utilize cylindrical rods as an approximation to ideal hyperbolic electrodes due to manufacturing simplicity. Cylindrical rods have been used in the other MEMS-based QMFs [23], [27], [47] but this geometry is not readily feasible with in-plane microfabrication. To address this issue, we proposed utilizing rectangular electrode geometry since it can be easily realized with established microfabrication techniques [85]. In essence, we took the approximation used in industry one step further as portrayed in Figure 3-5. These approximations work because a quadrupole potential is a boundary value problem. An ion that is sufficiently far away from the quadrupole electrodes will see a potential field that is nearly identical in all three geometries shown in Figure 3-5. Researchers have proposed using other non-standard geometries [86]-[89], but their designs are not compatible with planar microfabrication.

Due to the unconventional geometry proposed in this thesis, extensive optimization and design analyses were conducted.

The ability to batch-fabricate our devices with wafer-scale processing enables mass production with high precision and repeatability, thereby reducing costs since each device will not require individual tuning. The proposed integration makes the device affordable and robust, enabling it to be readily used in harsh environments. More importantly, the design concept is extremely versatile and has the potential for advanced architectures that were previously unachievable.
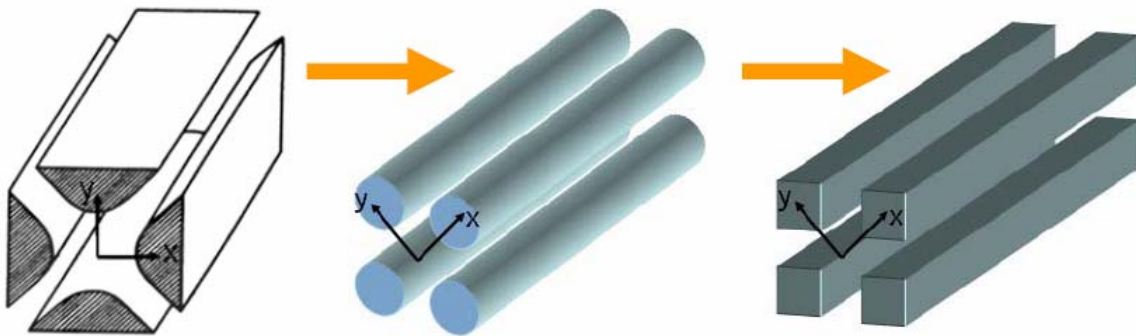
Figure 3-5: Technical progression of electrode geometries

3.3 Optimization

Since an unconventional geometry was proposed, a study was conducted to optimize the device design. Following the optimization work of Syms et al. [90], we conducted a similar analysis to determine the ideal dimensions for our geometry. Critical dimensions of our device were parameterized as shown in Figure 3-6, and the potential field solutions were solved using MAXWELL 2D. A quadrant of the field solutions were exported as a grid into a MATLAB script that performed a multipole expansion. The results of these expansions were then used to determine the optimized dimensions.
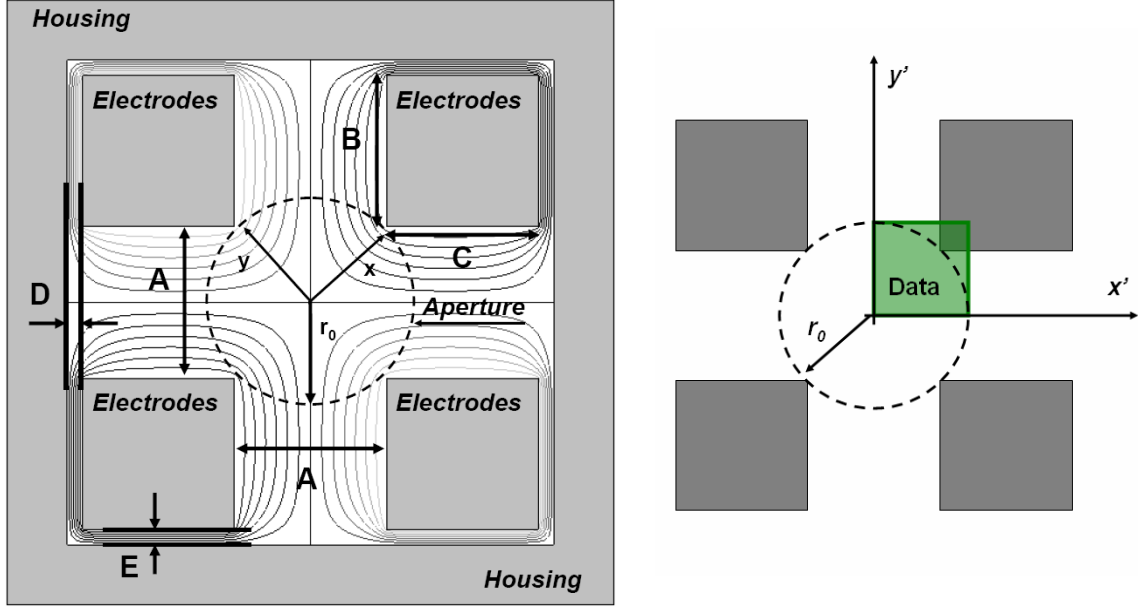
Figure 3-6: Geometries used for optimization

3.3.1 Multipole Expansion

For our device geometry, we can approximate the potential field within the circular aperture region as an infinite sum of even and odd functions. A general solution to Laplace's equation in cylindrical coordinates can be given by

$$\Phi(r,\theta) \approx \Phi'(r,\theta) = \sum_{j=1}^{\infty} C_j \left(\frac{r}{r_0}\right)^j \cos(j\theta) + \sum_{k=1}^{\infty} S_k \left(\frac{r}{r_0}\right)^k \sin(k\theta) \tag{3-8}$$

$$C_j = \frac{8(j+1)}{r_0^2 \pi} \int_{-\pi/4}^{\pi/4} \int_0^{r_0} \Phi'(r,\theta)\left(\frac{r}{r_0}\right)^j \cos(j\theta) r\,dr\,d\theta \tag{3-9}$$

$$S_k = \frac{8(k+1)}{r_0^2 \pi} \int_{-\pi/4}^{\pi/4} \int_0^{r_0} \Phi'(r,\theta)\left(\frac{r}{r_0}\right)^k \sin(k\theta) r\,dr\,d\theta \tag{3-10}$$

where r_0 is the radius of the aperture, θ is the angle measured from the x-axis, and C_j and S_k are weighing coefficients. Due to the anti-symmetry of the driving potential along the lines $y = x$ and $y = -x$, values for j can only be 2, 6, 10 … while values for k can only be 4, 8, 12…. The C_2 term corresponds to the ideal quadrupole field while the other terms correspond to non-ideal, higher-order field components. Optimization was conducted in a manner that minimized the magnitude of the higher-order terms with respect to C_2.

Since the first few terms of Equation 3-8 dominate the field solution, we focused our analysis on the coefficients C_2, S_4, C_6, S_8, and C_{10}.

For a given parameterized geometry, a quadrant of the MAXWELL 2D field solution was exported onto a Cartesian grid with spacing Δ. To perform the integrations of Equation 3-9 and 3-10 with the discretized potential field $\Phi'(x'_m, y'_n)$, the following approximations were used

$$C_j \approx \frac{8(j+1)}{r_0^2 \pi} \sum_m \sum_n \Phi'(x'_m, y'_n) \left(\frac{\sqrt{x'^2_m + y'^2_n}}{r_0} \right)^j \cos\left(j\left(\tan^{-1}\left(\frac{y'_n}{x'_m}\right) - \frac{\pi}{4}\right)\right)\Delta^2 \qquad (3\text{-}11)$$

$$S_k \approx \frac{8(k+1)}{r_0^2 \pi} \sum_m \sum_n \Phi'(x'_m, y'_n) \left(\frac{\sqrt{x'^2_m + y'^2_n}}{r_0} \right)^k \sin\left(k\left(\tan^{-1}\left(\frac{y'_n}{x'_m}\right) - \frac{\pi}{4}\right)\right)\Delta^2 \qquad (3\text{-}12)$$

where the primed coordinate system is the one shown in Figure 3-6. The calculations were conducted with a MATLAB script (Appendix C) that was very dependent on the grid size used. Useful information was extracted by keeping the grid size constant throughout the various simulations, and the coefficients for a given geometry were normalized to the calculated C_2.

3.3.2   Results

Initial simulations were conducted without the housing to determine the optimal dimensions for the electrodes and aperture. The results of these calculations are summarized in Figure 3-7. Dimension A is the characteristic size of the inscribed square within the circular aperture region, while B and C are the height and width of the electrodes respectively. We saw that setting B = C minimized the S_4 and S_8 terms. This makes physical sense since a square electrode induces four-fold symmetry, eliminating the odd terms of Equation 3-8. Analyzing the results revealed that setting B ≥ A generated a minimum for the C_6 and C_{10} terms. For the case of B/C = 1, having B larger than A did not provide any considerable decrease in the coefficients. From these results, we decided to utilize A = B = C for our device.
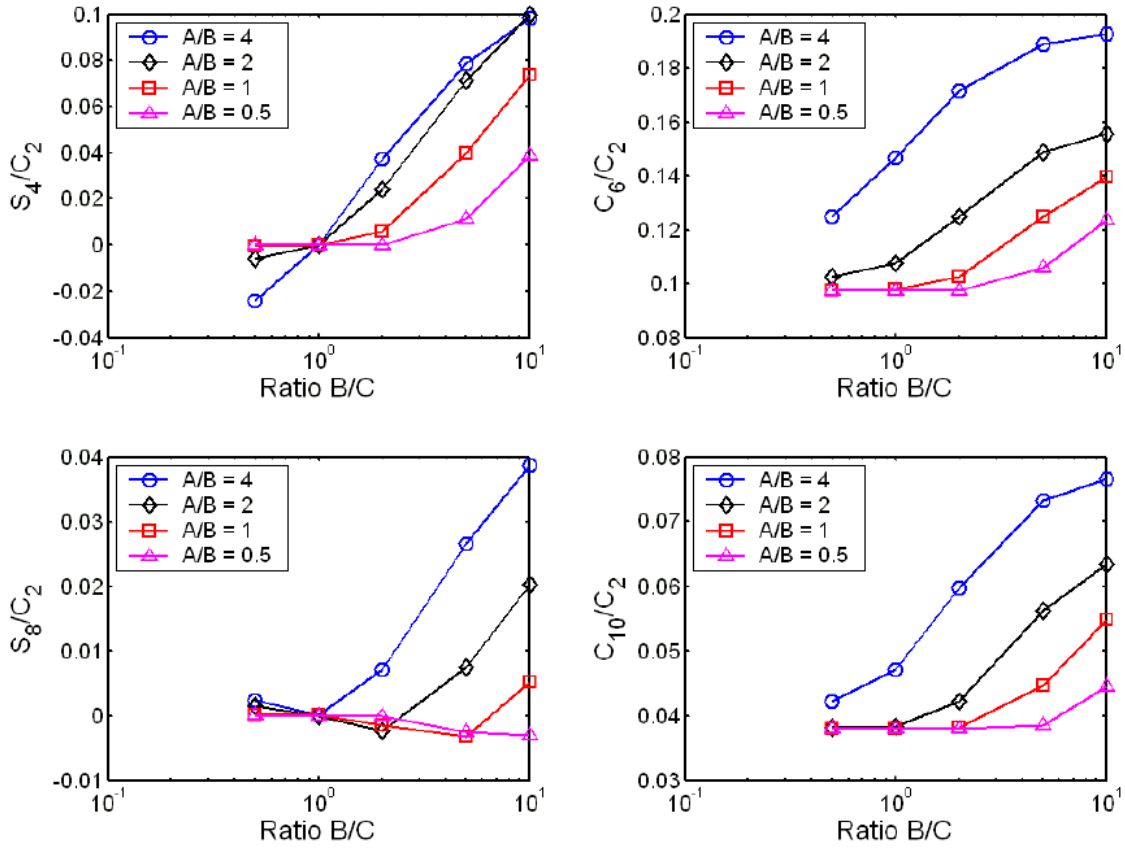
Figure 3-7: Optimization results for electrode dimensions

A device length of 30 mm was chosen to meet the operational pressure considerations introduced in Section 3.1.3. This dimension also happened to be the length of the quadrupoles reported by Taylor and Geear [23], [27], enabling us to make a direct comparison between their devices and ours. From the arguments in Section 3.1.1, we wanted to operate the device at 4 MHz, which forced the aperture to have a radius of 500 μm or less. To ensure that we had sufficient ion transmission during characterization of the proof-of-concept device, we chose dimension A to be 1 mm.

Additional simulations that included the quadrupole housing were conducted with A = B = C = 1 mm. Dimension D is the horizontal spacing between the electrodes and the housing while E is the vertical spacing. D is set by the device layout and has more flexibility in terms of possible values, whereas dimension E is limited by fabrication etch capabilities. The results of these simulations are summarized in Figure 3-8. We saw that setting D = E eliminated the odd terms, which should be the case since four-fold

symmetry was preserved. The even terms appeared to be minimized with larger values for D and E, but D = E = 100 μm was chosen for etch uniformity considerations. This choice results in non-optimal values for C_6/C_2 and C_{10}/C_2, but they are only ~1.5% greater than the case with the housing excluded. We believed that this increase would not substantially affect the device performance.
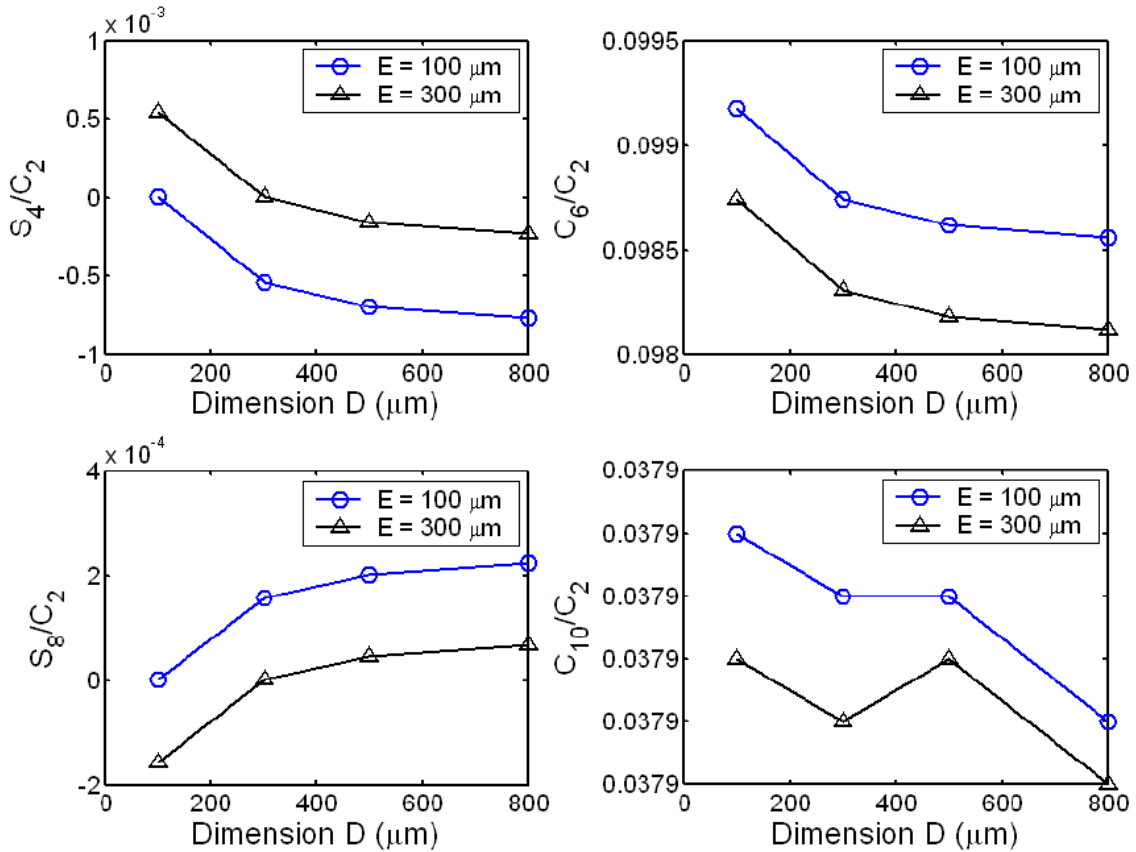
Figure 3-8: Optimization results including the housing

Our analysis showed that it is possible to reduce and eliminate the odd terms of Equation 3-8 by utilizing four-fold symmetry. Unfortunately, the even terms C_6 and C_{10} are non-zero in our geometry and present themselves as undesirable higher-order field components. These field components couple the motion between the x and y directions, resulting in non-linear resonances and degraded performance [54], [57]. Prior work showed that we could reduce the effects of these non-ideal terms by operating in the second stability region [47], [85], thereby providing a means to address the expected

performance loss. All the simulations were conducted for heavily-doped silicon and a pure metal using a drive frequency of 4 MHz. Both materials generated the same results, addressing concerns that the material choice would affect device behavior.

Additional simulations of our device design were conducted in collaboration with Thomas Hogan and Steve Taylor of the University of Liverpool [91]. Their software package was used to study the performance characteristics of our unconventional geometry and was able to perform a multipole expansion as well. Table 3-1 provides the coefficients for our device and an optimized cylindrical geometry obtained from their software. Values obtained from our calculations are also included for comparison. We see that the coefficients for the square electrodes are similar, giving confirmation that the methodology we used was sound. Comparing our device to the optimized cylindrical geometry highlights the significance of the non-negligible higher-order components.

	Circular Rods $r/r_0 = 1.128$	Square Electrodes (Liverpool)	Square Electrodes (MIT)
C_2	1.0016e0	0.7838e0	0.7691e0
C_6	1.200e-3	8.0909e-2	7.5569e-2
C_{10}	-2.4325e-3	3.2235e-2	2.9262e-2
C_{14}	-2.6928e-4	1.8101e-2	1.5755e-2

Table 3-1: Coefficients for different geometries and methods [91]

3.4   Integrated Optics

Ion lenses typically are used in mass spectrometers systems to help couple ions into the mass filter and out to the detector. Since the acceptance of a quadrupole is located at the central axis of the device, an increase in transmission can be achieved if the incoming ion stream is focused towards this point [61], [81], [92]. If we are able to integrate the ion optics with the device fabrication, there will be improved performance as well as cost savings.

Typical lens geometries used for ion optics are in the shape of circular or rectangular rings, but this was not feasible in our proposed design. To achieve the integration of ion optics, each lens was broken into four corresponding elements. The segmented lenses

have a similar cross-section to that of the QMF, allowing the electrodes and lens elements to be formed simultaneously. An Einzel lens configuration was simulated with Charged Particle Optics 3D (CPO-3D) to verify that this unconventional lens geometry is capable of focusing. First, the electrode geometry corresponding to the Einzel lens was defined along with part of the device housing that formed an inlet aperture. A series of singly charged ions of mass 40 were defined in such a way to represent a stream of ions with 5 eV of energy. CPO-3D has a feature to perform auto-focusing onto a specified focal plane by adjusting the voltages of various defined structures. The elements of Einzel lens 2 were varied while every other structure was grounded. The software found optimal focusing when the Einzel lens 2 elements were biased at -17 Volts. Figure 3-9 shows that an ion stream can be focused symmetrically onto a focal plane, unlike the astigmatic lenses reported for other MEMS-based quadrupoles [27], [81].
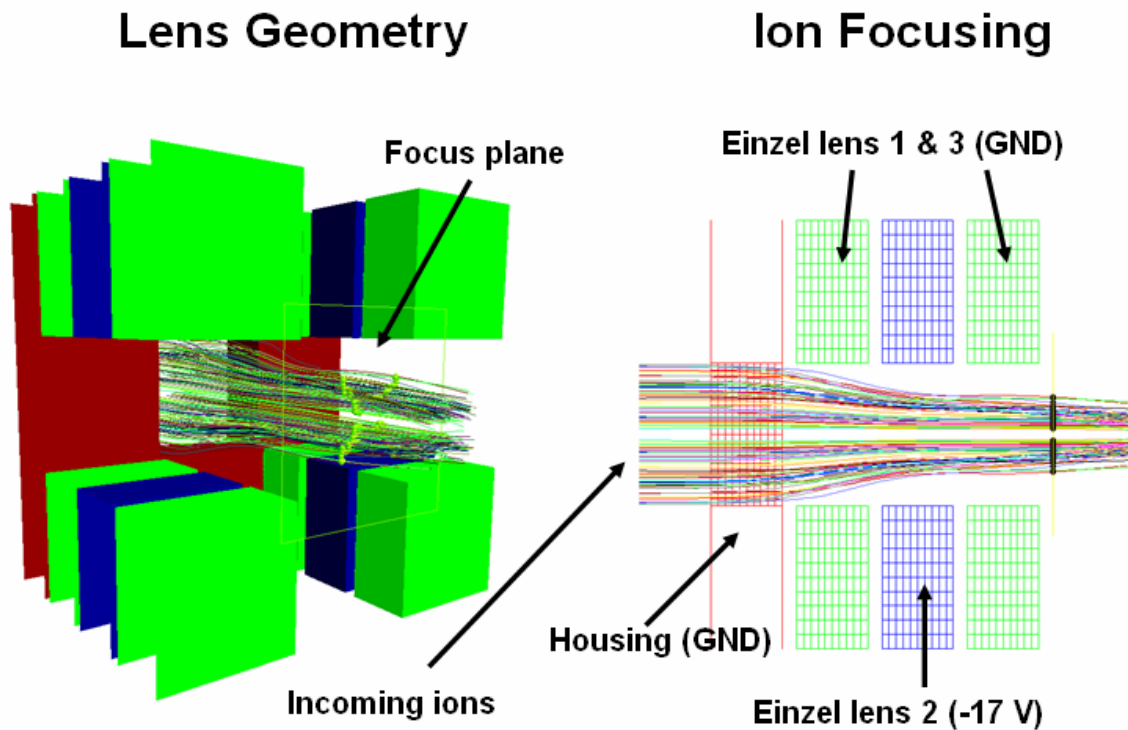
Figure 3-9: Einzel lens configuration of integrated optics

The concept used to define the integrated lenses can be extended to form more complex structures. For example, we know that transmission is dependent on the r.f.

53

phase in which an ion enters the quadrupole [1], [80]. If we utilize a lens configuration that serves as an ion trap and gate, we can time the release of ions into the device to improve performance. The current geometry can be easily extended to form a linear quadrupole ion trap [93]-[95]. Having an ion trap at the inlet will have the added benefit of performing analysis on limited samples. Additionally, the implementation of pre-filters would mitigate the effects of the fringing-fields inherent in all quadrupoles. There have been many reports of pre-filters improving transmission [96]-[98], as well as on the benefits of using post-filters [99].

More interesting configurations and architectures can also be implemented with the design concept proposed. Quadrupoles operated in tandem have been reported to demonstrate resolution better than what can be achieved by each quadrupole individually [100], [101]. Also, most modern mass spectrometer systems utilize different types of mass filters in series for improved performance. With a batch-fabricated quadrupole mass filter, we can imagine integrating a time-of-flight mass spectrometer [35] or an ion mobility spectrometer [102], [103] on the front end.

3.5   Positional Tolerance

To evaluate how potential misalignments in the electrode placement would affect our device performance, assistance from Thomas Hogan of the University of Liverpool was solicited. Using our basic cross-section and the intended device dimensions, mass spectra were simulated with various misalignments. These simulations were conducted after the fabrication of our devices to serve as a sanity check. There are two main misalignments that can occur during microfabrication – rotational misalignments during bonding and variations arising from different wafer thickness. For simplification, a horizontal shift was assumed for the rotational misalignments, while a vertical shift is assumed for variations in thicknesses. From the simulation results, we can clearly see that horizontal shifts have a minimal impact on device performance. On the other hand, vertical shifts have a greater impact but this issue can be addressed by purchasing wafers with very precise thicknesses. Most silicon wafers come with a tolerance of ±5 μm which is quite acceptable according to Figure 3-10.
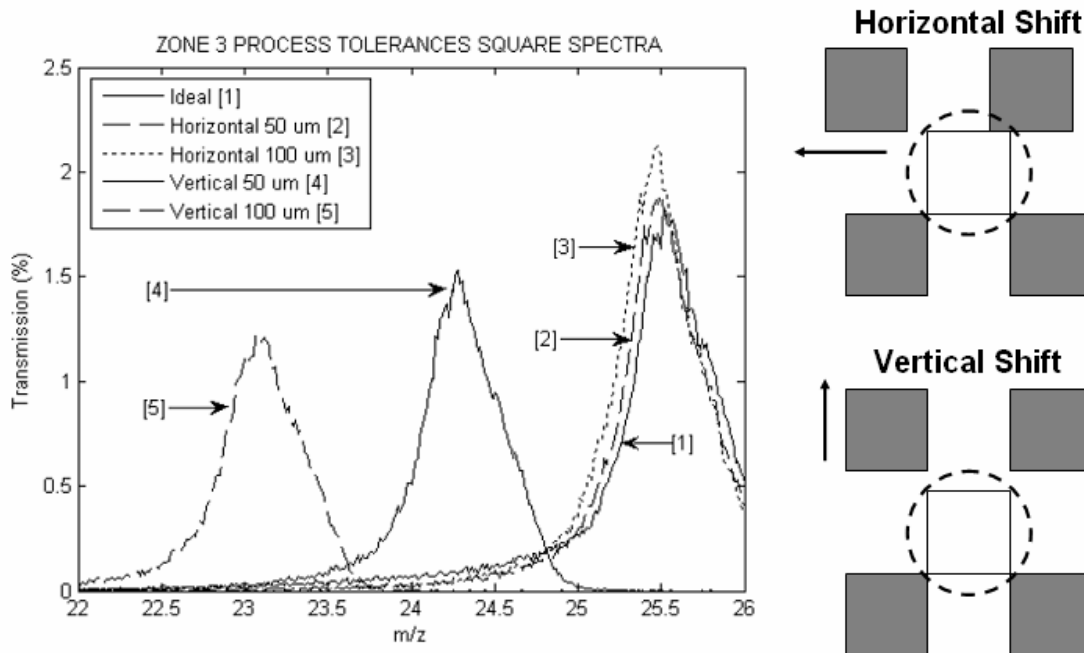
Figure 3-10: Misalignment effects [91]

3.6 Summary

In this chapter, we covered the many aspects of the design process. We began with scaling considerations to understand how the fundamental equations of operation affect the key performance metrics. Additional concerns with device capacitance, parasitics, and operational pressure were also addressed. The device concept was presented, which aimed to integrate the electrodes, optics, and housing into a single monolithic block. This integration was accomplished through the use of unconventional rectangular electrode geometry that required optimization. Furthermore, the details of ion optics integration were presented, promising improved performance and flexibility for future device evolutions. The effects of misalignments on the device performance were also evaluated through simulations. The results imply that the device design will be quite tolerant of positional misalignments, giving us confidence for microfabrication.

A summary of the design point, the device dimensions, and expected performance is provided in Table 3-2. One minor oversight in the device design was the fact that choosing dimension A = 1 mm actually gave a device radius of 0.707 mm instead of

0.500 mm. This oversight effectively reduced the maximum mass range that could be scanned with V_{max}. Instead of simply assuming $R_{max} = m_{max}/\Delta m$, we can also estimate the maximum resolution attainable by using the equation $R_{error} \sim 2r_0/\varepsilon$ presented in Chapter 2. This equation factors in the construction error ε, which was assumed to be 10 μm.

Device Dimensions		Operation Point		Expected Performance	
A = B = C	1 mm	f	4 MHz	m_{max}	250 amu
D = E	100 μm	V_{max}	150 V	Δm	1.00
L	30 mm	(a, q)	(0.23, 0.7)		
r_0	0.707 mm	h	15	R_{max}	250
ε	10 μm	V_z	5 Volt	R_{error}	140

Table 3-2: Summary of device design

Chapter

4

MuSE version 1.0

4.1   Overview

Stemming from the design work covered in Chapter 3, we created the device shown in Figure 4-1. Since the optimized geometry consisted of electrodes with square cross-section, we named the device the Micro-Square Electrode Quadrupole Mass Filter or MuSE-QMF for short. The device measured 4 mm x 15 mm x 33 mm and contained a QMF 30 mm in length, as well as associated inlet and outlet ion optics. Two versions of this device were fabricated simultaneously; one containing a simple inlet lens and the other with the more complex Einzel lens configuration.

The idea used to create the cross-section shown in Figure 3-6 was to have long, square electrodes that were suspended in space by anchor points that also served as electrical contact pads. Due to prior experience with using pogo-pins, contact vias were implemented into the design resulting in large anchor points.   The anchors of the electrode elements were attached to the housing structure, separated by a thick thermal oxide for electrical isolation.

A general schematic for ions trajectories through the MuSE-QMF is shown in Figure 4-2. Ions generated from an external ionizer get directed into the inlet aperture, where the integrated inlet optics focuses the ion beam towards the central axis of the quadrupole. Mass filtering is performed within the device, and the filtered ions are extracted and focused by the exit lens. The exiting ions are detected by an external detector to produce a mass spectrum.
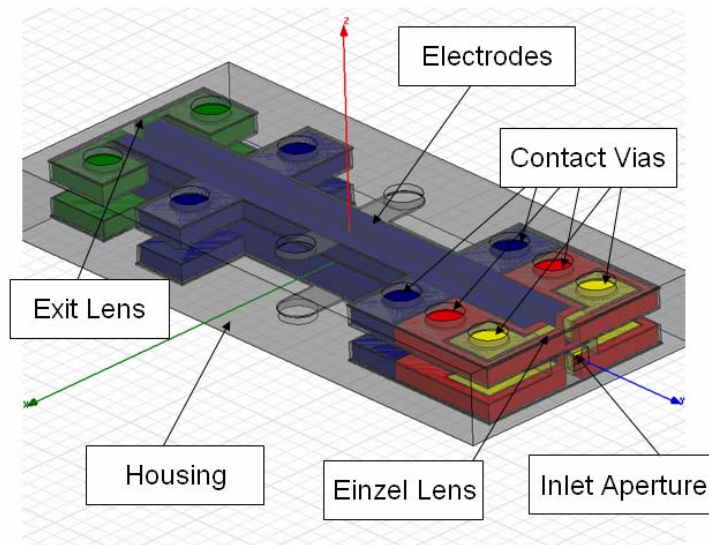
Figure 4-1: Schematic of the MuSE-QMF
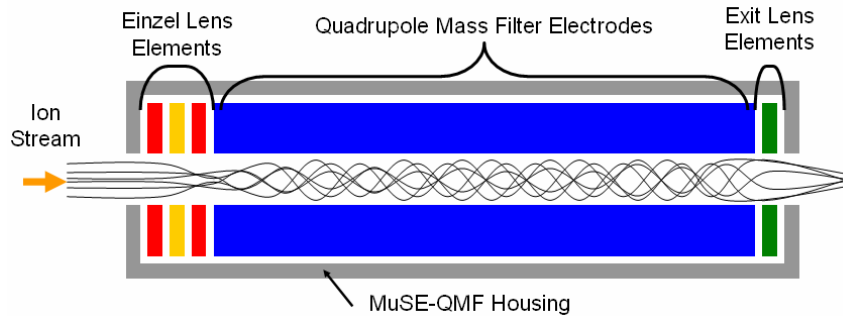
Figure 4-2: Cross-sectional schematic of the MuSE-QMF under operation

4.2   Device Fabrication

Fabrication of the MuSE-QMF was conducted at MIT's Microsystems Technology Laboratories. Five highly-doped silicon double-side polished (DSP) wafers were needed to complete the device. The wafers were doped with antimony to a resistance of 10-20 mΩ·cm to ensure that the electrodes and housing would behave as similar to a metal as possible. Two 500±5 μm wafers were used as the Cap Wafers, two 1000±10 μm wafers served as the Electrode Wafers, and another 1000±10 μm was utilized as the Aperture Wafer (Figure 4-3). All the wafers had 0.3 μm of thermal oxide initially grown by the vendor (Ultrasil Corp.) to serve as a protective layer throughout processing.
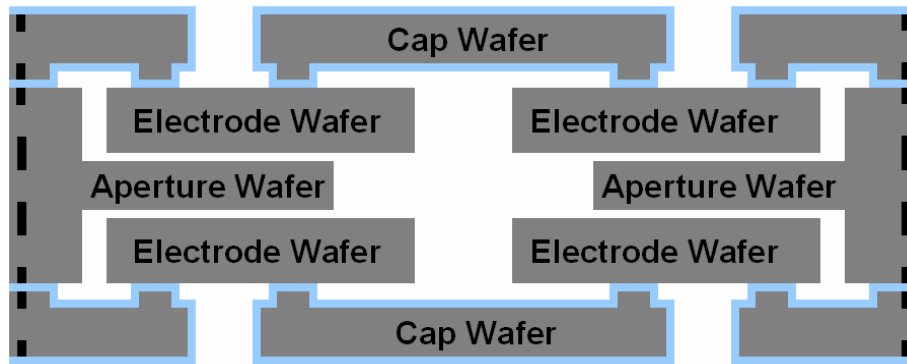
Figure 4-3: Device cross-sectional schematic

Since multiple wafer bond steps were needed to complete the device, it was important to put alignment marks on all the wafers. Thin resist was coated on both sides, and one side had the alignment marks transferred by contact photolithography. The protective oxide was removed through a buffered-oxide etch (BOE) and the alignment marks were defined with a 0.5 μm silicon reactive ion etch (RIE). The wafers were cleaned with piranha, and coated on both sides with thin resist again. The alignment marks were transferred onto the other side of the wafer through contact photolithography with backside alignment. The processing of these marks were the same as before, and all the wafers were cleaned with another piranha before subsequent fabrication steps.

Cap Wafers Processing

The cap wafers begin with spin coating of thick photoresist on both sides of the wafer. The cap trench that served as the vertical spacing between the electrodes and housing was exposed through contact photolithography on one side, while the other side was exposed with the contact vias mask. The protective oxide was removed with a BOE followed by a deep-reactive ion etch (DRIE) on both sides. The shallow trench was etched to a depth of 100 μm, the wafers were mounted onto quartz handle-wafers with the shallow trench down, and the contact vias underwent a through-wafer DRIE. At this point, the residual pieces of silicon in the contact vias fell out. The mounted wafers were dismounted in acetone, cleaned with piranha, followed by an oxygen plasma ash for 1 hour. The protective oxide was then fully removed with 49% hydrofluoric acid (HF), the

wafers were prepared with an RCA clean, and a 1 μm-thick thermal oxide was grown. The processing of the cap wafers is depicted in Figure 4-4.
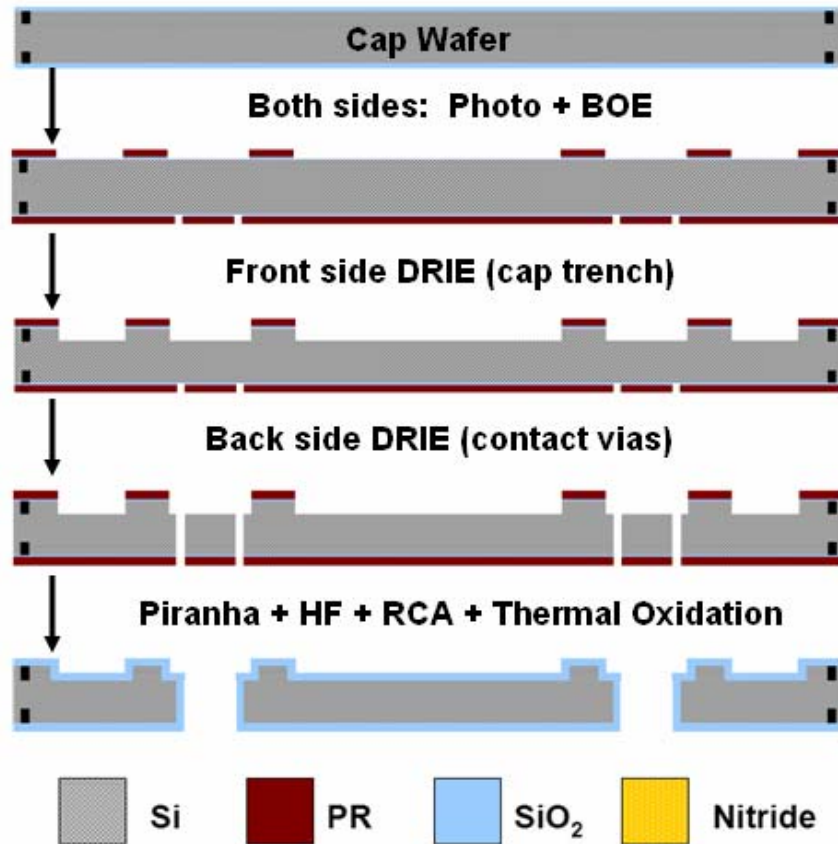
Figure 4-4: Cap wafer process flow

Electrode Wafers Processing

The electrode wafers began with 250 nm-layer of low-stress silicon nitride deposited through low-pressure chemical vapor deposition (LPCVD) to serve as a hard mask for the protective oxide. The wafers then underwent a RIE step to expose the underlying oxide on one side, which was subsequently removed by BOE as depicted in Figure 4-5. The electrode and completed cap wafers were RCA cleaned, aligned, and then fusion bonded. The bonding step occurred in a vacuum of 1 x 10^{-3} Torr, and with a compressive force of 2500 N for over 20 hours. The cap-electrode stacks were then annealed in nitrogen at 1000 °C for 1 hour to strengthen the bond. Thick photoresist was spun onto the cap-electrode stack, and the pattern for the electrode elements were transferred with contact

photolithography. The elements were initially defined with a RIE to remove the exposed nitride, and a short BOE was used to remove the protective oxide without substantially etching the thick thermal oxide on the cap wafers. The stacks were then mounted onto a quartz handle-wafer and underwent a 1000 μm-DRIE to form the electrode elements. The residual silicon block between the electrodes fell out after defining the electrodes. The stacks were dismounted in acetone, cleaned with piranha, followed by an oxygen plasma ash for 1 hour.
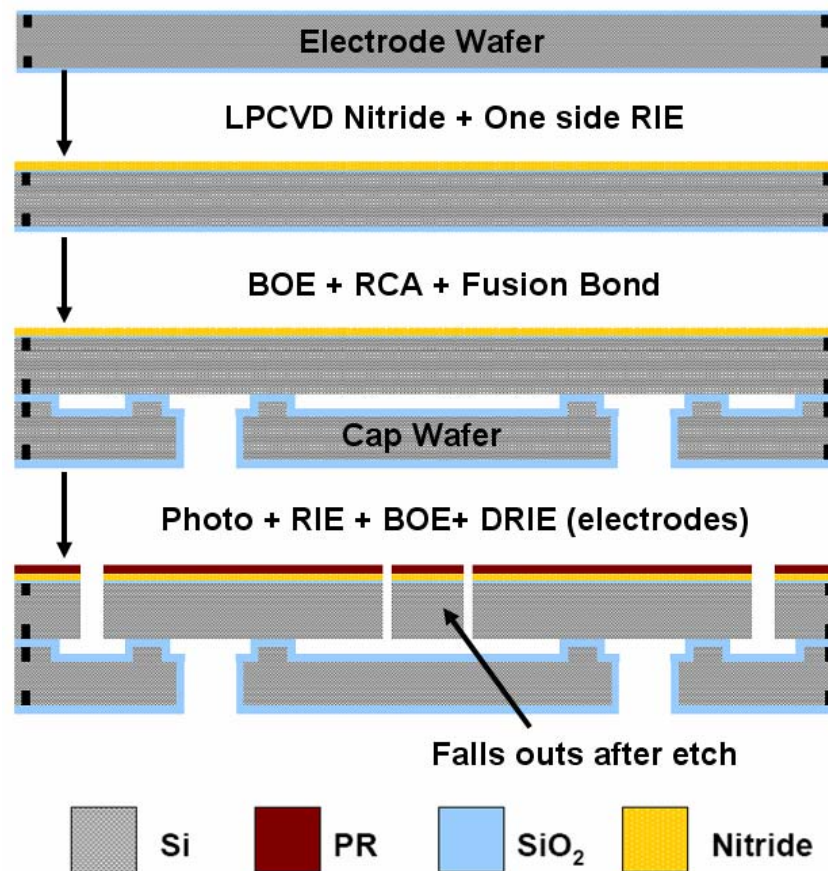
Figure 4-5: Electrode wafer process flow

Aperture Wafer Processing

The aperture wafer began with a 4 μm-thick layer of PECVD oxide deposited on both sides to serve as a hard mask for a subsequent nested etch. Thick resist was spun on both sides, and the pattern for the hard mask was transferred with contact photolithography. The PECVD oxide was then etched away with an RIE on both sides, and the photoresist

was cleaned with piranha. Thick resist was spun again on both sides, and the aperture etch is exposed. The wafer then underwent a 400 μm-DRIE on each side to partially define the aperture region. The resist was removed with piranha, and the entire wafer was etched with the PECVD oxide hard mask. A 100 μm-DRIE on both sides of the wafer formed the aperture trench and completed the aperture etch. At this point, the residual silicon block within the aperture region fell out. The wafer must be mounted to a quartz handle-wafer after patterning the first aperture trench. After all the etching was completed, the wafer was dismounted with acetone, cleaned with piranha, followed by an oxygen plasma ash. The process flow for the aperture wafer is outlined in Figure 4-6.
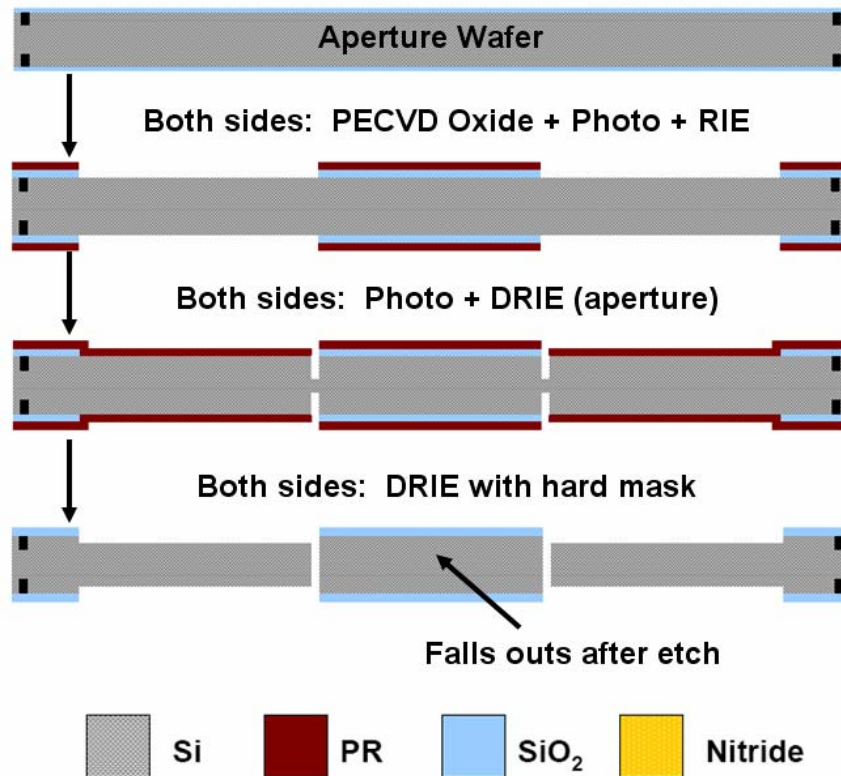
Figure 4-6: Aperture wafer process flow

Final Processing Steps

To complete the device, the cap-electrode stacks were placed in hot phosphoric acid (165 °C) for 1.5 hours to ensure that all the LPCVD nitride was removed. The cap-electrode stacks were then placed in a short BOE to remove the remaining protective

oxide that was underneath the nitride, while the aperture wafer had all the remaining PECVD oxide removed with concentrated HF. The two cap-electrode stacks and the aperture wafer were then RCA cleaned, aligned, and fusion bonded as depicted in Figure 4-7.
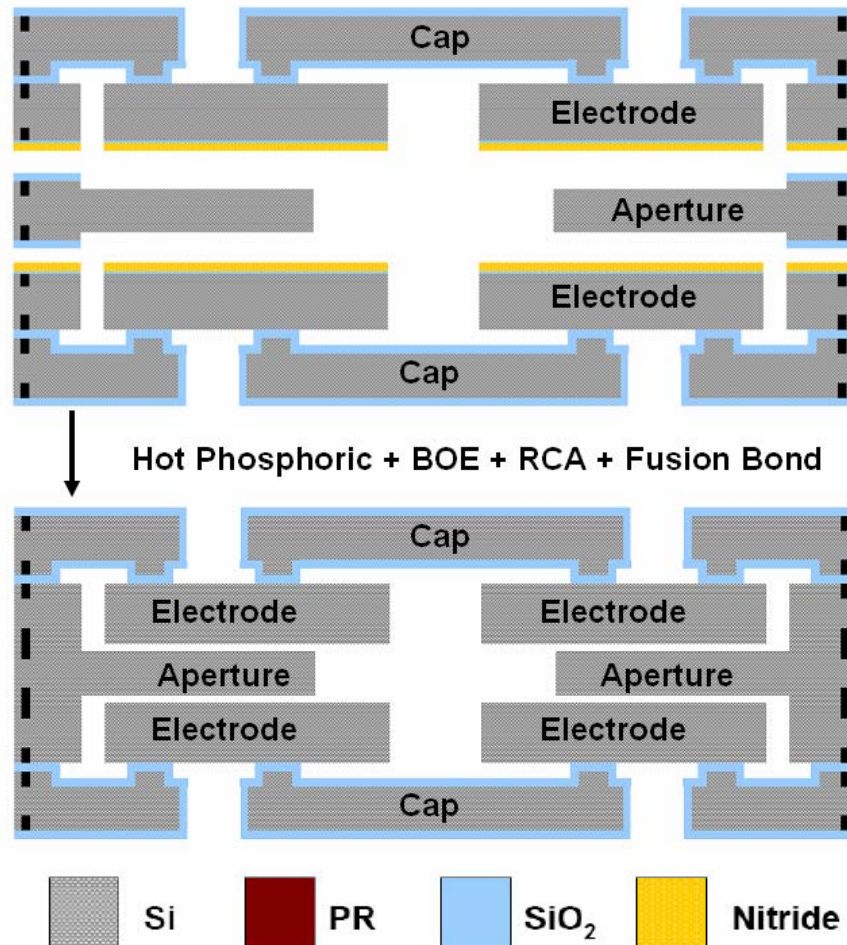
Figure 4-7: Final processing steps

After the post-bond anneal, the 5-wafer stack was cooled and die-sawed. The die-saw step opened the inlet and exit apertures of the device and separated the individual dies. Each 6" wafer contained fourteen devices, seven of which had the complex Einzel lens configuration and the other seven had a simple inlet lens. A completed device is shown in Figure 4-8 along with dotted lines to show where cross-sectional cuts were made to image the interior (Figure 4-9). The cut across the device shows the view looking into

the device from the exit aperture, while the cut along the length of the device shows the relative location and spacing of the electrode components. A more detailed process flow is given in Appendix A and the mask layouts used are provided in Appendix B.
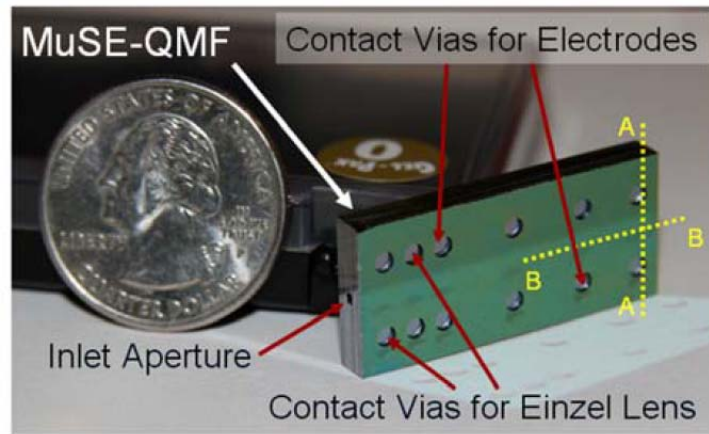
Figure 4-8: Completed MuSE-QMF with US quarter

Along line A of Figure 4-8   *Along line B of Figure 4-8*
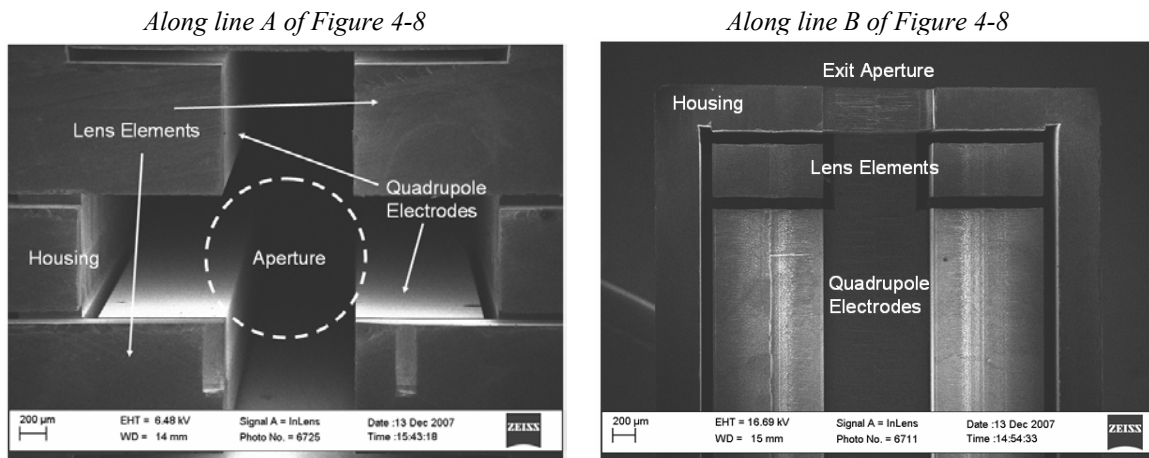
Figure 4-9: Cross-sectional SEMs of device

4.3   Fabrication Issues

While we were successful in fabrication the device with the process flow described in Section 4.2, there were two key issues that were encountered. Both issues concern the processing of the cap-electrode stacks, a crucial part of the MuSE-QMF fabrication. The first issue involved the 1000 µm-DRIE used to pattern the electrode components. We

noticed that black silicon formed after an etch-depth of approximately 800 μm. This made it extremely difficult to continue etching, almost rendering the wafer stacks useless. The second problem was noticed after the successful etching of a cap-electrode stack. We found that some of the patterned electrode components fell off the cap wafer after the DRIE, and even more so after a piranha clean. This was a significant problem since it was indicative of poor bonding between the cap and electrode wafers.

4.3.1 Deep Etching

Etching was initially conducted with JBETCH, a well established recipe used at MIT developed for the Micro-Engine Project. The etch recipe is quite robust and can readily create features with an aspect ratio of 10:1. Our mask layouts have etch-patterns no narrower than 100 μm in consideration of the wafer thicknesses used and the recipe capabilities. Despite this precaution, we found that etching the electrode components would slow and eventually stop at depths greater than 800 μm, most likely attributed to the formation of black silicon. A series of isotropic etches with SF_6 followed by deep etching with JBETCH finished the electrode patterning but was unsuccessful at fully removing the black silicon as shown in Figure 4-10. The blurred areas are due to the thickness of the electrode elements. This problem necessitated the development of a new etch recipe for future work.
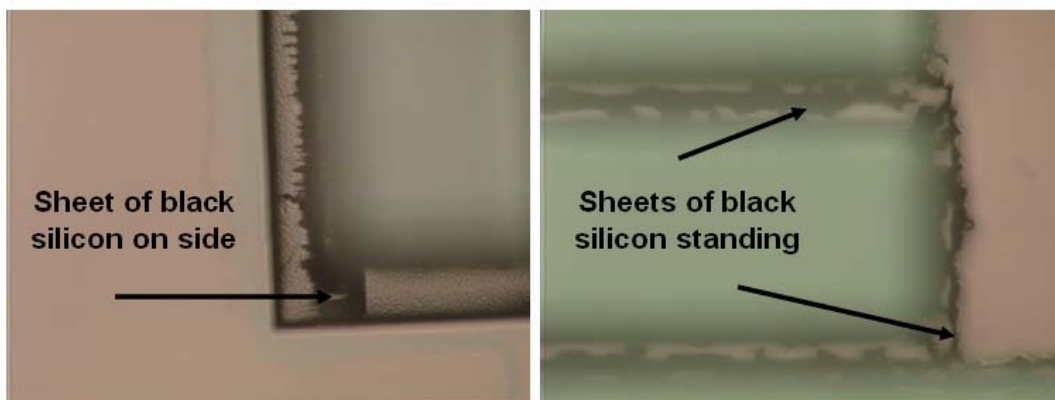
Figure 4-10: Remaining black silicon after electrode wafer DRIE

We speculated that the main reason for the problem encountered was that the etchant species was unable to reach the bottom of the trench at large depths. This would result in

the passivation cycle dominating the DRIE, leading to micro-masking and the formation of black silicon [104]. We started with the recipe for JBETCH and modified it to fulfill our etching needs. The first modification was an increase in the etch platen power along with a decrease in pressure but this led to the etch trench blowing out. An increase in pressure resolved the blowout but it created an uneven sidewall. These etch non-idealities are displayed in Figure 4-11. Adjusting the gas flow rates, etch time, and passivation time eventually resolved the sidewall issue. Table 4-1 outlines the recipe JBETCH and the new recipe developed named KERRY.
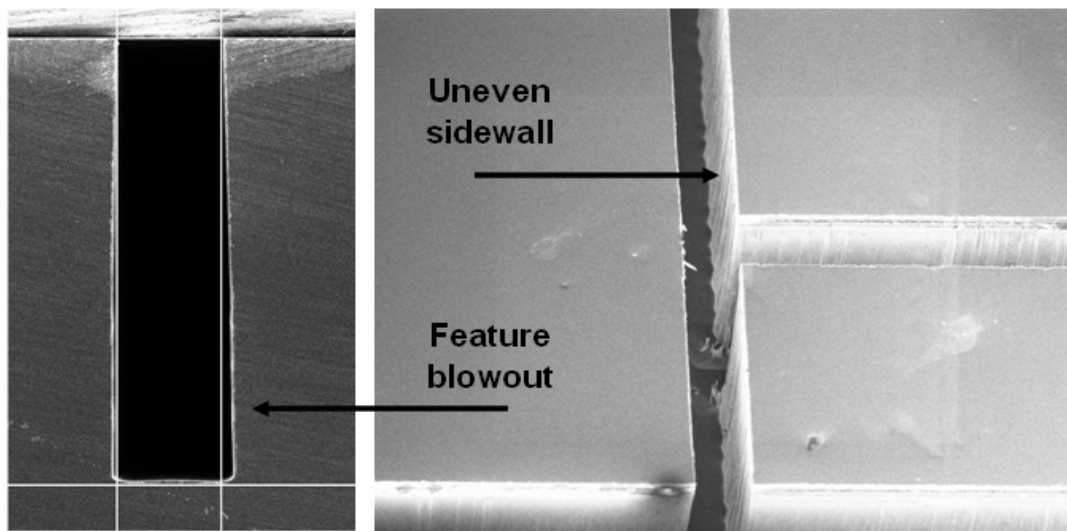
Figure 4-11: Etch non-idealities during recipe development

Parameters	JBETCH	KERRY
Etch Time (Overrun)	13 (0.0) seconds	13 (0.0) seconds
Passivation Time (Overrun)	11 (0.0) seconds	11 (0.5) seconds
Pressure	28 mTorr	33 mTorr
Etch Power (platen)	15 W	18 W
Passivation power (platen)	6 W	6 W
Etch Power (coil)	800 W	800 W
Passivation power (coil)	600 W	600 W
C_4F_8 flow rate	50 sccm	55 sccm
SF_6 flow rate	105 sccm	110 sccm

Table 4-1: Comparison between JBETCH and the etch recipe developed

4.3.2 Bonding

The bonding issue was only apparent after we were able to etch 1000 μm into the electrode wafer of the cap-electrode stack. Critical electrode components that were supposed to be bonded essentially fell off as shown in Figure 4-12. From discussions with Professor Martin Schmidt of MIT, this poor bond quality is most likely attributed to the oxidation of the patterned cap wafers. Thermal oxidation occurs faster along the edges of patterned features, effectively forming an uneven bonding surface [105]. It is also possible that the heavy doping was not uniform across the wafer. Areas that were more highly doped would oxidize quicker than the areas that were not, leading to unevenness. In Figure 4-13, a dummy bond between a quartz wafer and an oxidized cap wafer showed discoloration on areas where the electrode elements should be anchored. The discoloration is indicative of poor contact, confirming that the processing of the cap wafer was the main culprit for the weak bond strength. Despite this problem, we were able to fabricate several devices with all the electrode components intact.
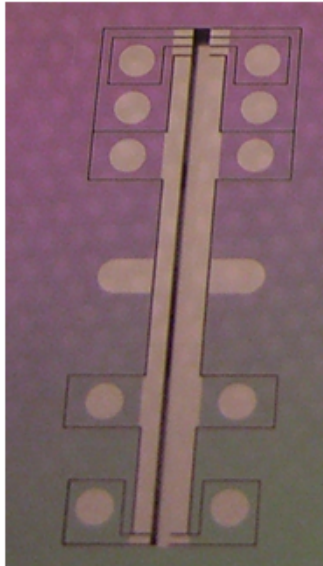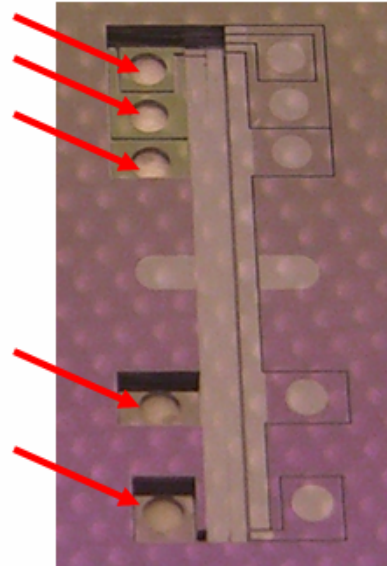
Figure 4-12: Comparison between dies with good bonding and poor bonding
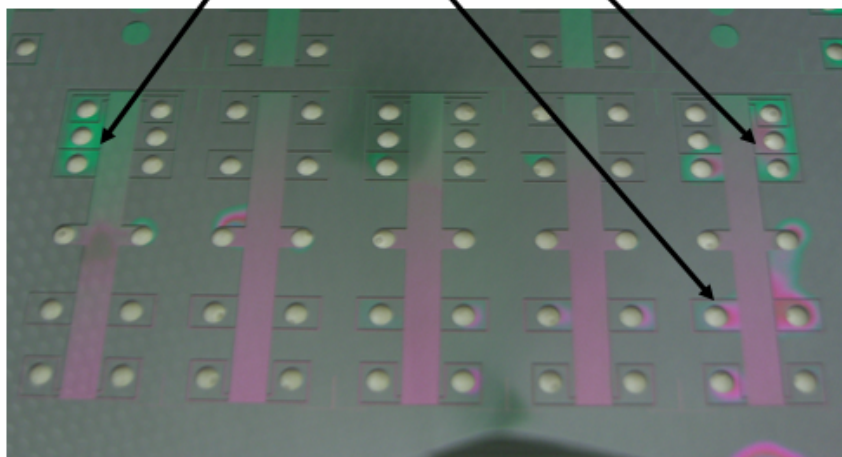
Figure 4-13: Dummy bond showing areas of poor contact

4.4   Characterization

The testing and characterization of the MuSE version 1.0 was conducted at Ardara Technologies in Ardara, PA. At the time fabrication was completed, we did not have a functional in-house testing facility so we solicited the assistance of Dr. Randall Pedder to benchmark our device. Dr. Pedder is very knowledgeable of mass spectrometers and has helped us in the past with the testing of the μ-Gripper quadrupoles [47]. In the first round of devices, only six dies had all the electrode components intact. Before the chip was placed into the testing jig, each electrode element was checked for electrical isolation with a multimeter. A finite resistance was indicative of shorting between electrode components, or between the measured electrode and the housing. This check revealed that only three devices had all four quadrupole electrodes electrically isolated, but none of these devices had all the lens elements isolated as well.

4.4.1   Experimentation

The testing jig into which the device was placed was made of peek and had pogo-pins to make electrical contact to the electrode components. Brass screws with thin sheets of Grafoil® were also incorporated to make electrical contact with the MuSE-QMF housing.

The testing jig was then placed within a cylindrical housing made of aluminum that was compatible with the flange mount system available at Ardara Technologies. A more detailed description of the testing jig and the flange mount concept is covered in Chapter 5 of this thesis.

The experimental setup comprised of the flange mount, a vacuum chamber that accepted the flange mount, an r.f. power supply, and a Merlin® data acquisition and control system. The flange mount contained a Slim-Line® ionizer from Ardara Technologies, the device, and a conversion dynode multiplier used as the detector. The vacuum chamber could be pumped down to a base pressure of 1×10^{-7} Torr through a turbo, and had a valve to introduce air, argon, or perfluorotributylamine (FC-43) as analytes. Several self-resonating r.f. power supplies were used to drive the device at 3.8 MHz, 2.95 MHz, and 1.98 MHz. The frequencies were set by the inductance of the coil used in the r.f. power supplies and the capacitance of the device. The Merlin® system supplied the d.c. voltages, scaled the r.f. voltages, controlled the ionizer, detector, and ion optics, as well as collected the spectra at a maximum sampling rate of 12.5 kS/s. Since the d.c. voltages supplied by the Merlin® system was substantially larger than what was needed for our application, it was scaled down through a voltage divider with various resistors. The diminished d.c. and r.f. voltages were combined through a bias-tee network consisting of 30 MΩ resistors and 47 pF blocking capacitors, and was ultimately connected to the device through the flange mount.

To prevent electrical breakdown, a 100 V_{pp} limit was imposed throughout testing. For a given operating frequency and operating region (first or second stability), a quick calculation with the voltage limit set the maximum mass range scanned. Once the mass range was known, the r.f. and d.c. voltages were scaled through the Merlin® system and resistive divider circuit respectively. The chosen analyte was introduced into the chamber, and we waited until a pressure of 5×10^{-5} Torr was reached before the ionizer was turned on. Initially, the device was operated in r.f.-only mode, and the ionization energy, emission current, and optic voltages were adjusted until maximum transmission was achieved. The r.f.-only mode turned the quadrupole into an ion guide, allowing all the ions to pass. Since some of the integrated lens elements were shorted, they were grounded throughout the maximization and subsequent testing. The device was then

switched to mass-filtering mode, and minor adjustments were made in the r.f. and d.c. voltages to improve the mass spectrum. After correction, the data was averaged to minimize noise and the spectrum was recorded for post processing and analysis.

4.4.2   Results

The first test conducted was at 3.8 MHz since we designed the device to operate at 4 MHz in the first stability region. Air was used as the analyte and we were able to get sufficient signal with an ion energy of 5 eV. This result indicates that out integrated housing did an adequate job at shielding the incoming ions from the fringing-fields that arose from the finite length of the quadrupole. The mass spectrum is shown in Figure 4-14 with a peak-width of 1.16 amu at mass 28, corresponding to a resolution of ~24. The peaks for nitrogen and oxygen are clearly visible and they show an accurate relative abundance to that of air. This first spectrum demonstrated that mass filtering with square electrodes is possible and with good peak-shape.
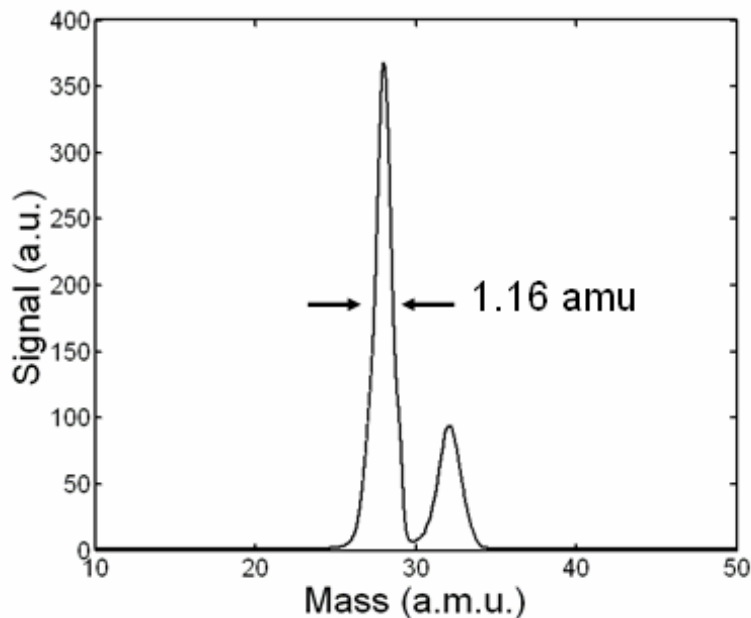
Figure 4-14: Mass spectrum of air at 3.8 MHz in the first stability region

The next set of experiments was conducted at 2.95 MHz with argon as the analyte and an ion energy of 4.5 eV. We wanted to generate a resolution versus transmission curve to

benchmark the ultimate resolution of the device. Argon was used to ensure that there would be no interference from other ion species at low resolutions. Starting with an operating point that produced a fairly good spectrum, the d.c. voltage was increased to give spectra of higher resolution, and decreased to give spectra of lower resolution. The relative transmission and resolution of these various spectra were calculated and plotted in Figure 4-15. We can use this plot to determine the resolution at which the device transmission falls below 1%, giving an indication of the ultimate resolution achievable. From these experiments, we found an ultimate resolution of ~17 which was less than what was achieved at 3.8 MHz. This clearly indicates that the ultimate resolution is dependent on the frequency of operation, and that we were not operating at a point where performance was dictated by misalignments within the device. A side experiment using a Faraday cup instead of the conversion dynode multiplier showed that our device was capable of fairly high transmission at moderate resolution.
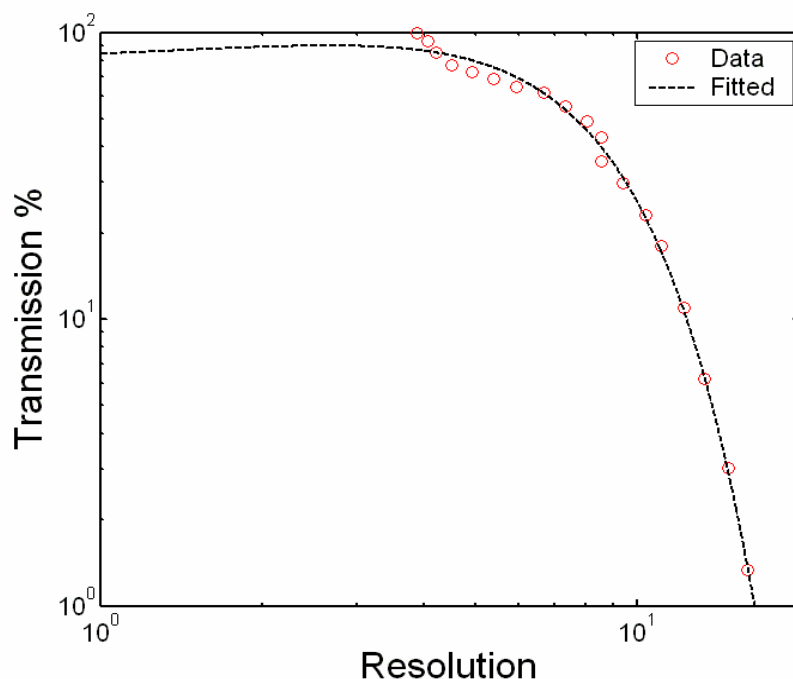
Figure 4-15: Resolution versus transmission curve using argon at 2.95 MHz

To explore the maximum mass range achievable, the device was driven at 1.98 MHz and FC-43 was used as the analyte. Due to the heavier fragments associated with this

calibration compound, an ion energy of 15.8 eV was needed to produce decent mass spectra. At low ion energies, heavier ions spend more time in the fringing-fields, resulting in poorer peak-shapes and decreased transmission [61], [62], [77]. Figure 4-16 shows a mass range of 250 amu with prominent peaks at mass 69, 131, and 219, which is expected for FC-43. We were able to obtain a peak-width of 7.6 amu at mass 69, corresponding to a resolution of ~9. Additionally, the relative peak intensities observed demonstrated good agreement with the NIST library spectrum for FC-43. It is important to note the uneven peak-shapes stemming from precursors on the low-mass tail of the detected peaks. These non-idealities are most likely attributed to the higher-order field components that are inherent in the square geometry. Comparing the peak-shapes with that in Figure 4-14, we see that the higher frequency data is more symmetric. Operating at higher frequencies decrease the quadrupole acceptance [58], minimizing the effects of undesirable field components since transmitted ions are located near the central axis. This result makes the case for integrated ion optics that channel the incoming ion stream towards the central axis of the quadrupole.
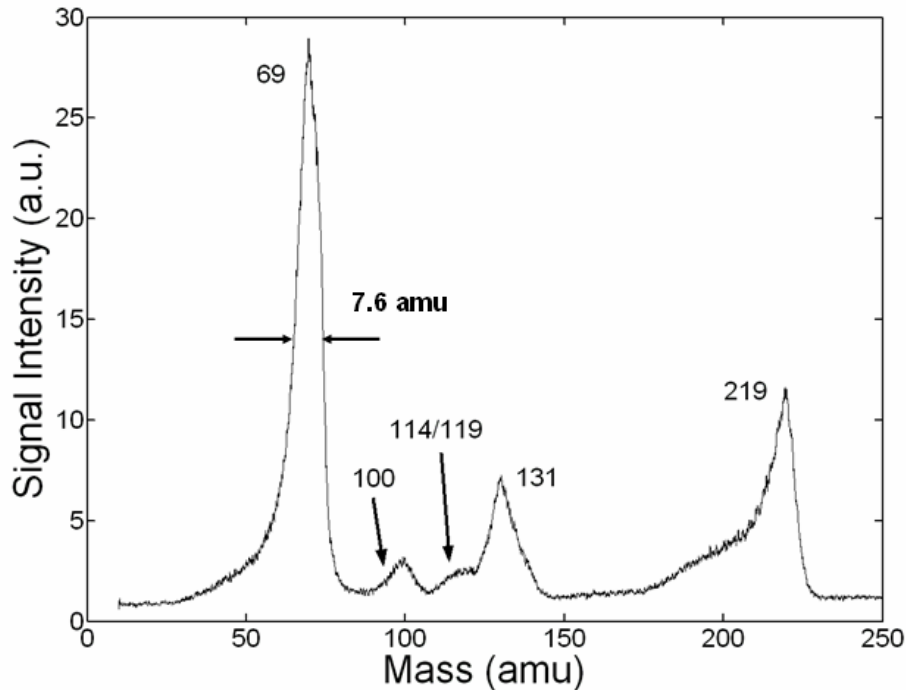
Figure 4-16: Mass spectrum of FC-43 at 1.98 MHz in the first stability region

To determine the minimum peak-width attainable, the device was driven at 1.98 MHz in the second stability region. Air was used as the analyte due to the closely spaced peaks of nitrogen and oxygen. An ion energy of 18.0 eV was required since fringing-fields are much more defocusing when operating in the second stability region [77]. The larger ion energy ensured that there was sufficient transmission to be detected by the conversion dynode multiplier. From Figure 4-17, we can see that the peak-shapes are substantially improved over that of Figure 4-16. We see clear peaks at mass 28, 32, 40, and 44 but the signal-to-noise is also significantly smaller than that of Figure 4-14. These results support claims that operation in a higher stability region leads to improved device performance but at the expense of transmission [47], [78]. A peak-width of 0.7 amu was achieved at mass 28, corresponding to a resolution of ~ 40, while another experiment with argon demonstrated a resolution of ~35. The spectrum shown in Figure 4-18 used an ion energy of 24.0 eV and shows similar peak-shape to those in Figure 4-17. This comparison gives a good indication that the MuSE-QMF has repeatable performance for different analytes.
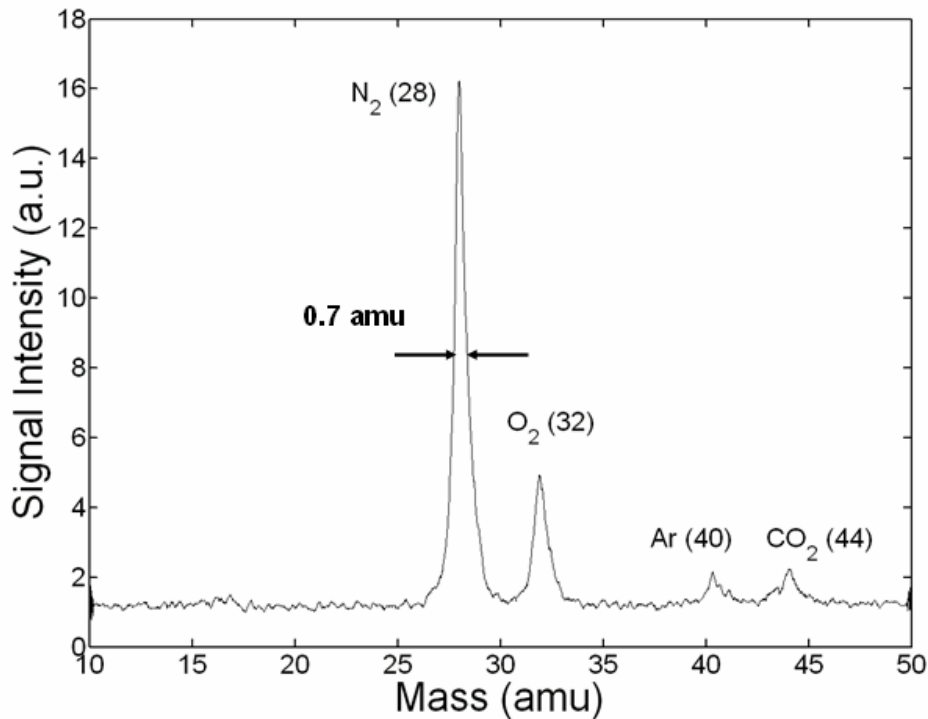
Figure 4-17: Mass spectrum of air at 1.98 MHz in the second stability region
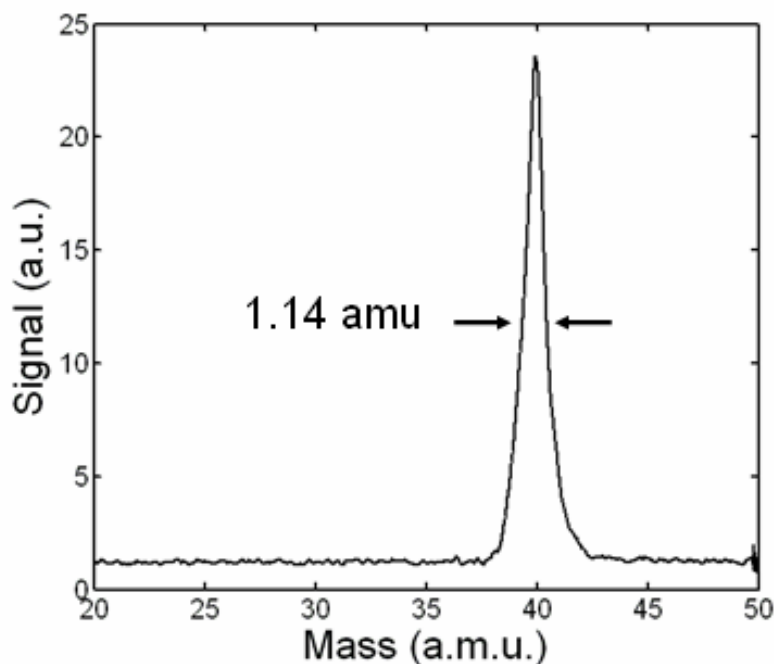
Figure 4-18: Mass spectrum of argon at 1.98 MHz in the second stability region

4.5   Discussion

During initial evaluation of the MuSE-QMF, two of the three remaining devices failed after being placed into the flange mount. The pogo-pins of the testing jig exerted too much force on the contact pads, dislodging the electrode elements from the anchor points. We decreased the force of the pogo-pins and were fortunate to obtain all the data shown in Section 4.4 with the remaining device. This last device had the Einzel lens configuration, but several of the lens elements were shorted rendering the optics useless. The poor bond strength can be attributed to the processing issues mentioned in Section 4.3.2, and potentially the frequent exposure of the cap-electrode stacks to BOE before the device was completed. Addressing these fabrication problems will increase the bond strength between the cap wafer and electrode components, thereby raising device yield and reliability.

The data reported in this chapter was obtained without functional integrated ion optics. Shorting between the lens elements required all the lenses to be grounded during characterization. The shorting issue was most likely the result of black silicon fragments

that remained after the electrode wafer DRIE with JBETCH. The new etch recipe developed should address this problem in future devices. Since poor control of the inlet and exit conditions leads to degraded peak-shapes and transmission [77], [78], we would expect improvements in these areas with a device that has functional ion optics.

Attempts at driving the device with a voltage greater than 100 V_{pp} resulted in electrical breakdown of the insulating oxide. We noticed current leakage on one pair of electrodes when the device was driven above 100 V_{pp}. The voltage would scan but the device could not sustain the applied voltage, indicating some sort of oxide break down. This voltage corresponded to a field-strength of 5 x 10^5 V/cm across the oxide, much smaller than the reported breakdown limit of 10^7 V/cm. There could have been local thinning of the oxide from the frequent exposures to BOE during processing, or die-saw particles that enabled tunneling when the voltages became large enough. Improved processing and a thicker oxide would address these issues, allowing us to extend our mass range.

Despite these shortcomings, this device was able to demonstrate proof-of-concept mass filtering with square electrode geometry. We scanned a mass range of 50 amu and obtained a peak-width of 1.16 amu when the device was driven at 3.8 MHz (Figure 4-14). If we take this result and use Equation 2-10, we would expect a peak-width of 1.05 amu at a drive frequency of 4 MHz, which is very close to what was aimed for in Chapter 3. The mass range scanned was less than the desired value due to the voltage limitations, but 50 amu is in-line with what we would expect from a three-fold decrease in V_{max}. Staying within the confines of the voltage limitation, a mass range of 250 amu was achieved with FC-43 by dropping the drive frequency. If we take Equation 2-10 and the peak-width achieved in Figure 4-14, we would expect a peak-width of 13.5 amu with the operating conditions of Figure 4-16. Instead, a peak-width of 7.6 amu was demonstrated which corresponds to a higher resolution. This discrepancy can be due to changes in the value for h associated with improved ion coupling that arise from the different operating conditions.

Operation in the second stability region with a drive frequency of 1.98 MHz demonstrated a peak-width of 0.7 amu at mass 28. This result corresponds to a resolution of 40 which is comparable to the first MEMS-based quadrupole [23]. Utilizing Equation

2-10 once again, this data represents a 12.4 improvement in peak-width over that of Figure 4-16. This enhancement is in-line with the 7 to 20 fold improvement that we would expect from using the second stability region. The maximum resolution reported in this chapter is far below the value of 140 estimated in Chapter 3. To fully evaluate the limits of this technology, we need to operate at higher frequencies which correspond to larger voltages. The voltage limitation of the MuSE-QMF was due to fabrication issues that were addressed in the work of Chapter 6.

4.6   Summary

In this chapter, we introduced a chip-scale quadrupole mass filter that was named the MuSE-QMF. The fabrication steps were outlined and several issues encountered during processing were addressed. Issues with bonding resulted in low yield, and problems with deep etching required the formulation of a new etch recipe. Characterization of the device was conducted at Ardara Technologies, and operational proof-of-concept was demonstrated. Areas of improvement were identified and a plan of attack was formulated. Overall, the MuSE-QMF showed good performance with a mass range of 250 amu when operated at 1.98 MHz. A minimum peak-width of 0.7 amu at mass 28 was also achieved in the second stability region, corresponding to a resolution of 40.

Chapter

5

QMF Characterization System

5.1 Overview

The construction of an in-house testing facility was a significant component of this thesis. A substantial portion of our setup was modeled after the experimental facility available at Ardara Technologies (Ardara, PA). This was to ensure that we would have the capability to test at both locations if the need arose. Dr. Randall Pedder played a vital role in obtaining the data presented in Chapter 4, so we wanted to keep the option open for potential future collaborations.

After characterization of the MuSE version 1.0, several concerns motivated the need for an in-house testing facility. First and foremost, it was costly and challenging to coordinate a testing trip to an external vendor. Ardara Technologies needed one to two months of advance notice before we were able to utilize their facilities for a time span of one week. With a MEMS project where the microfabrication timeline and device yield was uncertain, this arrangement would have substantially slowed the iteration process. Secondly, having the ability to perform rapid assessments of the device and the flexibility to conduct experiments without time constraints is extremely beneficial.

More importantly, the equipment available at Ardara was not well suited for the testing of MEMS devices. The r.f. and d.c. supplies were much more powerful than needed, which required us to find creative ways to scale-down the voltages. Also, the detector available at Ardara was not as sensitive as we would have liked. The small dimension of our device led to reduced transmission, and the conversion dynode used had

poor signal-to-noise characteristics. Finally, the control software was overly complex and not very user friendly. It was designed to drive standard quadrupoles that have been thoroughly tuned with the system, not proof-of-concept devices. There was also limited flexibility in adjusting driving parameters and the software did not save data effectively. A mass spectrum was stored as a single list of voltages with no explicit correlation to the mass range scanned, leading to confusion and errors during analysis.

5.2   Components

A block diagram of the testing facility is shown in Figure 5-1. The entire system is organized into three main categories – the vacuum chamber and flange mount, the drive circuit and electronics, and the control software and data acquisition. The vacuum chamber is where the device is situated along with the ionizer and the detector. The electronics control and power the various components of the setup and supply the combined r.f. and d.c. voltages required for mass filtering. The control software scans the r.f. and d.c. voltages to produce a mass spectrum and records the signal from the detector. The various pieces of hardware that are used in the test facility are shown and labeled in Figure 5-2.
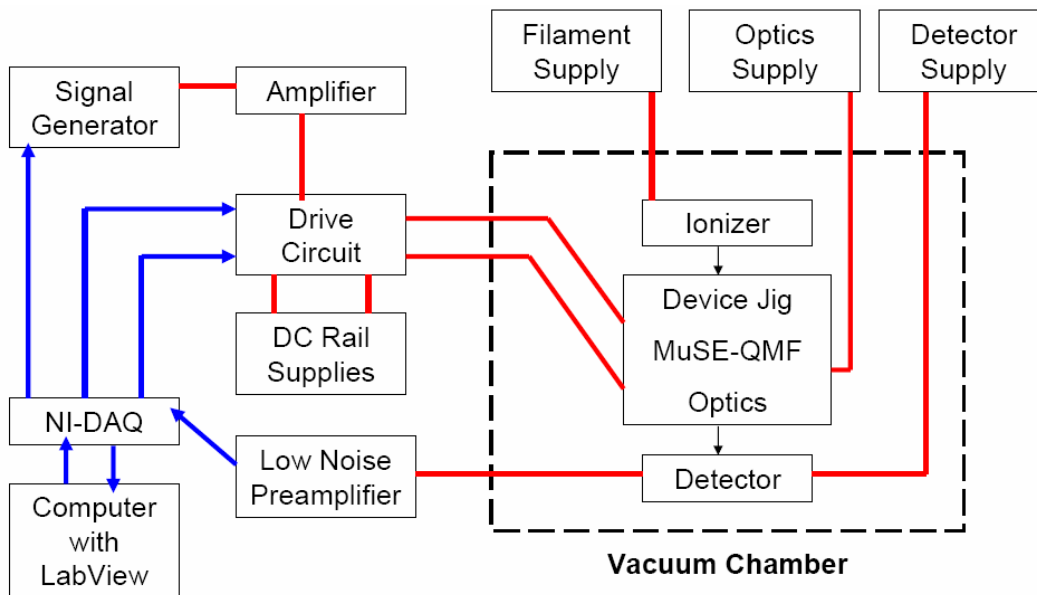
Figure 5-1: Block diagram of in-house testing facility

78
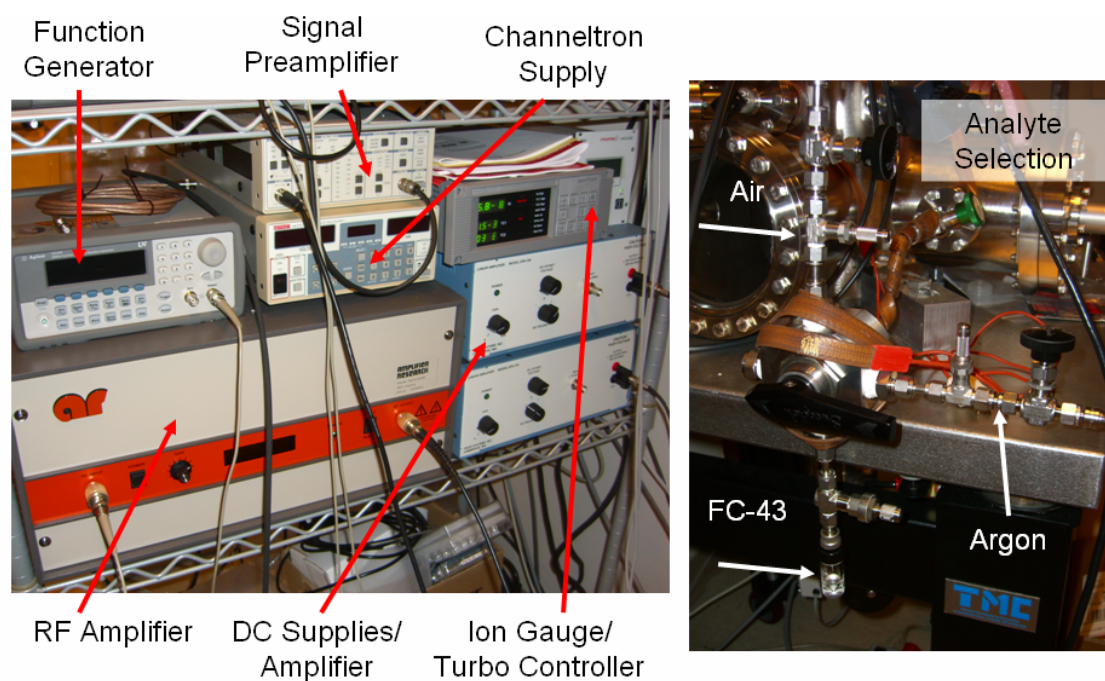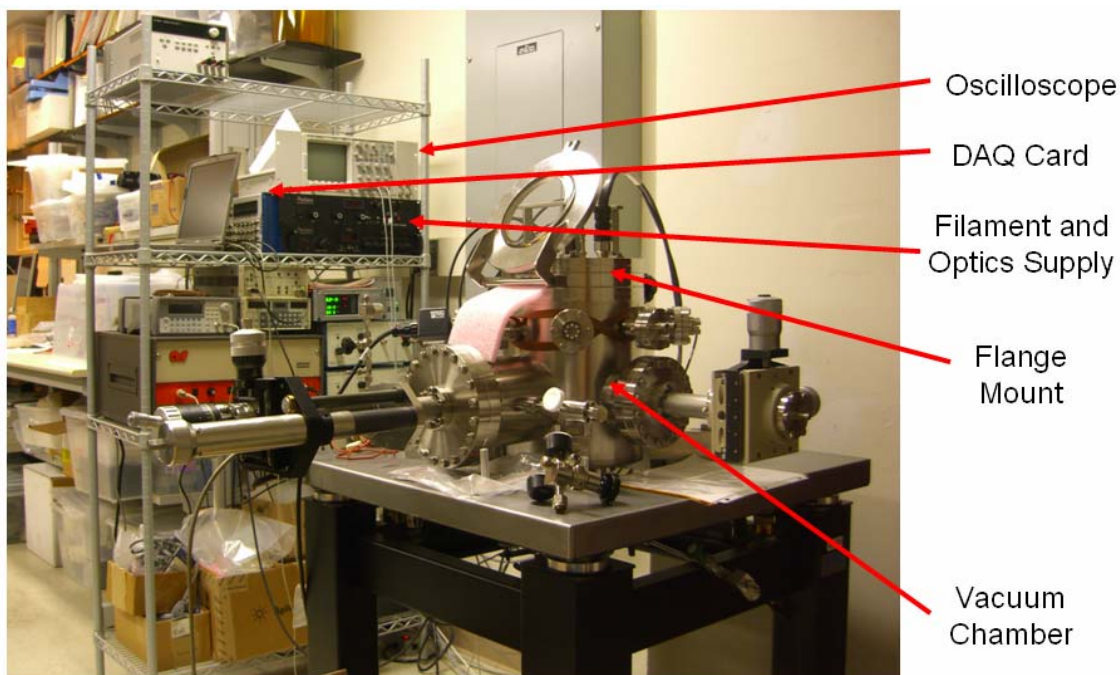
Figure 5-2: Photographs of the in-house testing facility

5.2.1   Vacuum Chamber and Flange Mount

The vacuum chamber used in our testing facility was designed and assembled by Dr. Luis Velásquez-García of MIT.   The custom chamber was manufactured from MDC

Vacuum Products and contains twelve flange ports of various sizes. An assortment of electrical connectors, thermocouples, and manipulators occupy most of the flanges but they were not used in our device characterization. A Varian CC2 SenTorr unit with a vacuum gauge and a 525 cold cathode gauge are connected to the chamber to monitor the pressure. The chamber is pumped by a Pfeiffer turbo molecular pump (TMU-071-P) that is backed by a Pfeiffer diaphragm pump (MVP-025-02). A Swagelok five-way valve (SS-45ZF8-ND-093) is used to introduce various analytes into the chamber. By switching the valve port, we can choose between nothing, air, argon, and the standard mass spectrometer calibration compound, perfluorotributlyamine (FC-43). Metering valves (SS-SS4) connected to each line are set to maintain a pressure of ~3 x 10^{-5} Torr when the analytes are introduced. There is also a gate valve that separates the chamber from the turbo, and a vent valve that is connected to the chamber underside.

A vital component of the testing hardware is the custom flange mount which was modeled after the experimental setup at Ardara Technologies. The flange mount is a basic 10" stainless steel flange that was machined to include five BNC connectors, four MHV connectors, a 10-pin electrical feed-through, and handles to facilitate transport. The flange mount is designed to hold and align the Slim-Line® ionizer (Ardara Technologies), the device, the Channeltron® electron multiplier (Burle Industries, CEM 4502), as well as stainless steel ion lenses as depicted in Figure 5-3. A picture of the assembled flange mount is shown in Figure 5-4 for reference. The multiplier and device housings are made from aluminum, and the electrically isolated components are separated by aluminum oxide spacers. Circular recesses on the housing caps and lenses are utilized to seat the spacers, and to align the various components. The 10-pin connector interfaces with the filament and optics supply (Ardara Technologies) which controls the ionizer and lens voltages. The wiring scheme for the 10-pin connector is summarized in Table 5-1. When the multiplier housing is attached to the vacuum flange, the Channeltron® input contact is attached to an MHV connector for the supply voltage, the output contact is attached to a BNC connector for the detected signal, and the anode contact is attached to ground. The quadrupole connects to the drive signals through the device housing and a pair of MHV connectors on the flange. Detailed drawings of the ionizer, detector, and machined components are provided in Appendix E.
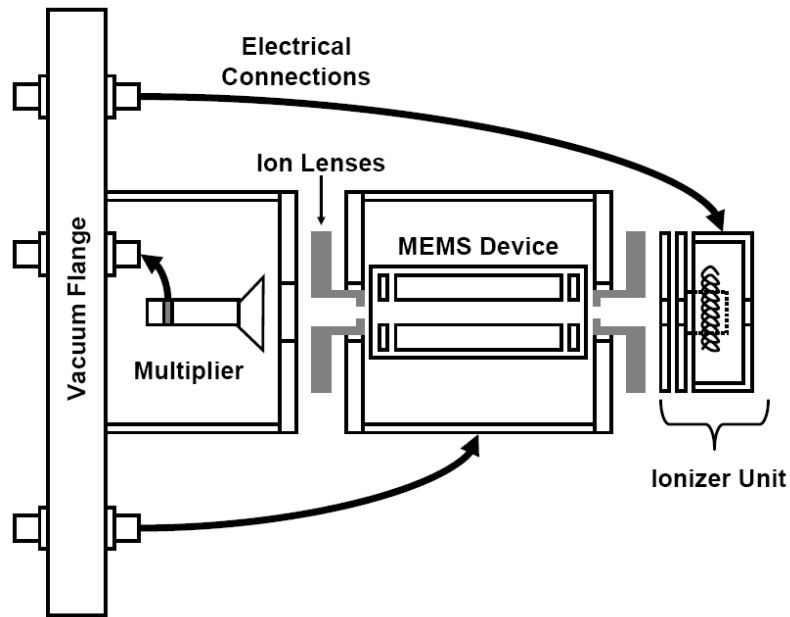
Figure 5-3: Flange mount schematic
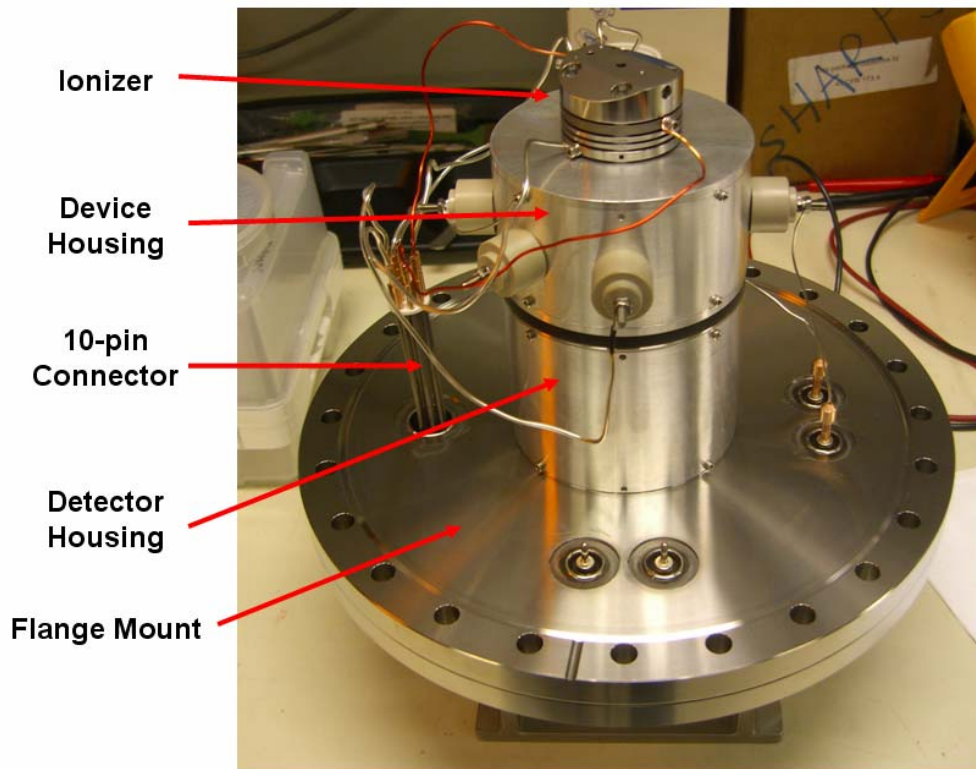
Figure 5-4: Assembled flange mount

PIN	Control Name
A	Optics 3
B	Optics 2
C	Filament (+)
D	Filament (-)
E	Ion region
F	Optics 5
G	Optics 1
H	Optics 4
I	Optics 6
J	Not Used
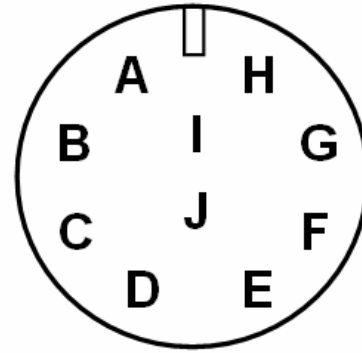
Table 5-1: 10-pin connection scheme

The chip-scale quadrupole is placed into the same testing jig as the one mentioned in Chapter 4. The jig is comprised of two machined blocks of peek that hold and align the device when fully assembled (Figure 5-5). The peek blocks contain small through-holes that accept the housings for the pogo-pins (Everett Charles Technology, HPA-0L), and custom-made spring-loaded plungers. These plungers are positioned to utilize the unused contact vias of the device to hold and align the MuSE-QMF within the package. Slots are also included to accommodate the insertion of small Grafoil® sheets. These sheets can be compressed with brass screws through the sides of the testing jig to make electrical contact with the MuSE-QMF housing. Wires are soldered onto the pogo-pin housings for electrical connection to the aluminum device housing.
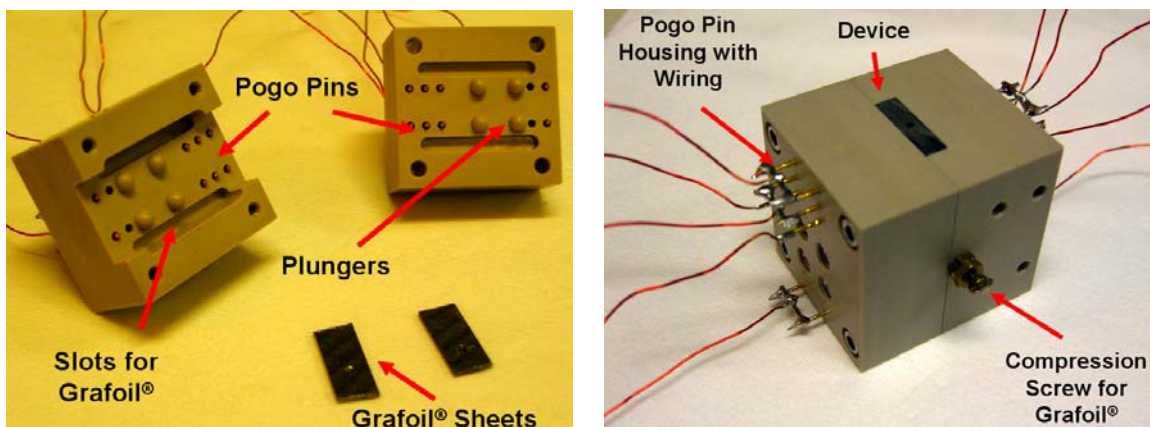
Figure 5-5: The peek testing jig
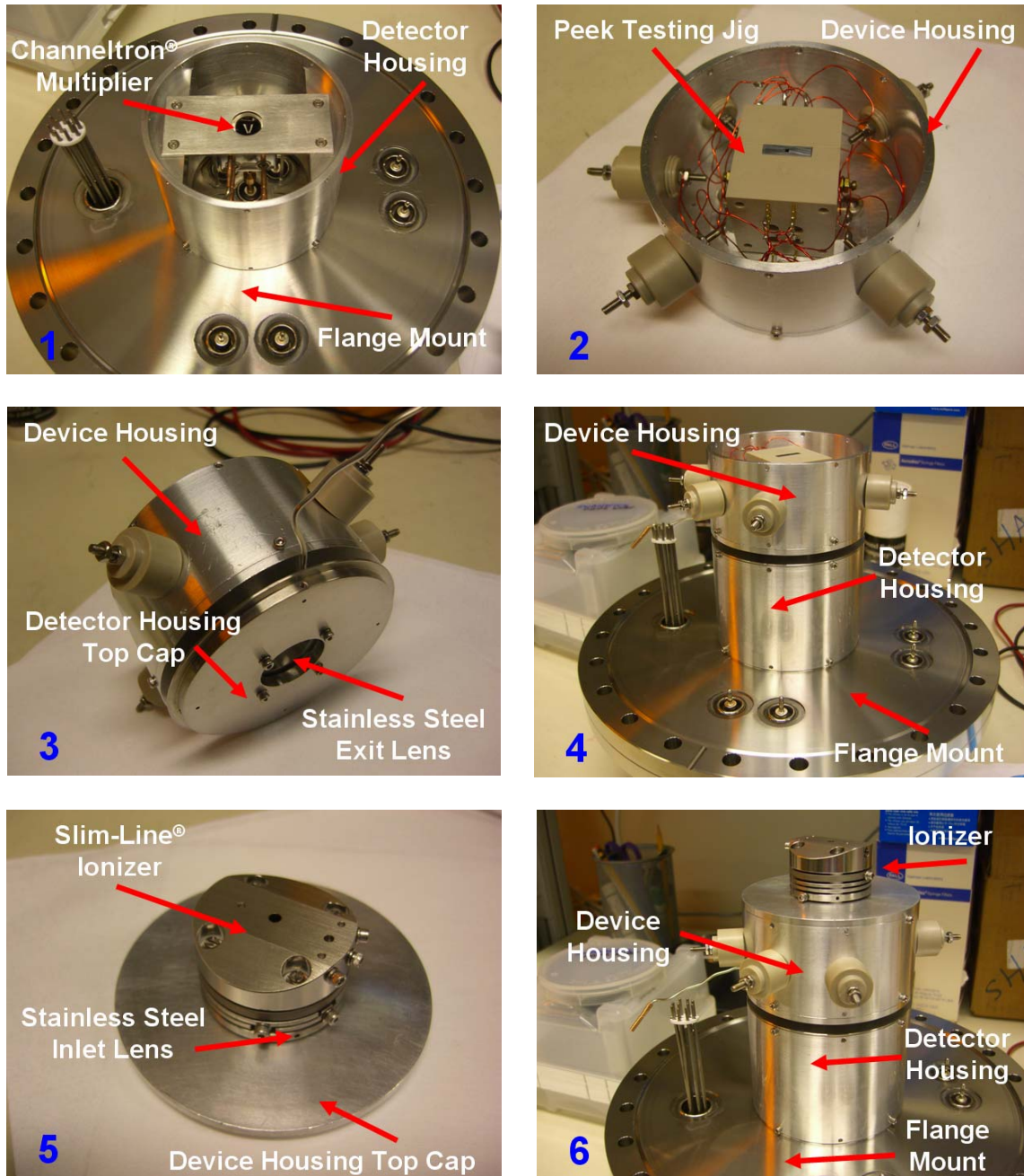
Figure 5-6: Assembly of flange mount

Figure 5-6 details the assembly process of the flange mount. (1) Initially, the detector housing was attached to the vacuum flange and the Channeltron[®] multiplier was wired up. (2) Next, the device was placed into the peek blocks, the assembled testing jig was screwed onto the device housing, and the electrical connections were made. (3) The detector housing top cap and exit lens were then screwed onto the device housing, and (4)

the assembled structure was attached to the multiplier housing. (5) Lastly, the ionizer and inlet lens were screwed to the device housing top cap, and (6) the entire structure was attached on top of the device housing. After the assembly, the ionizer, optics, and device housing were wired to the electrical connections on the flange mount. Nickel wires in Tygon tubing were used for the voltage connections, and magnet wire with a polyamide coating was used for the filament connections. The entire mount was moved as a single unit and placed onto the vacuum chamber. Typically, the chamber can reach a base pressure of 1 x 10^{-8} Torr within a few hours but the pump time increased to a day when the flange mount was attached. The extra time was a result of the numerous components attached and from trapped air within the Tygon tubes that serve as electrical insulation for the nickel wires.

5.2.2 Drive Circuit and Electronics

The core of the drive electronics can be summarized by Figure 5-7. This design was realized through discussions with Dr. Randall Pedder, and focuses around using a center-tapped air-core transformer to combine the r.f. and d.c. signals. The r.f. drive component originates from a function generator (Agilent 33220 A) that sets the frequency and initial amplitude. This amplitude can be modulated from an external control signal ranging from -5 V to 5 V, corresponding to minimum to full-scale. The modulated signal then enters a wide-band amplifier (Amplifier Research 150A100B) where it is amplified by a variable gain. Next, the amplified voltage enters the central loop of the center-tapped air-core transformer connected to the drive circuit shown in Figure 5-8. The transformer was hand-made using a polycarbonate tube with magnet wire, and designed to have a specific inductance. The amplified signal splits into two components that are 180° out-of-phase and is stepped-up once again due to the windings in the transformer. Trimmer capacitors (Voltronics AM25HV) are included to balance the r.f. amplitudes, compensating for variations that may arise from the transformer or other circuit components.
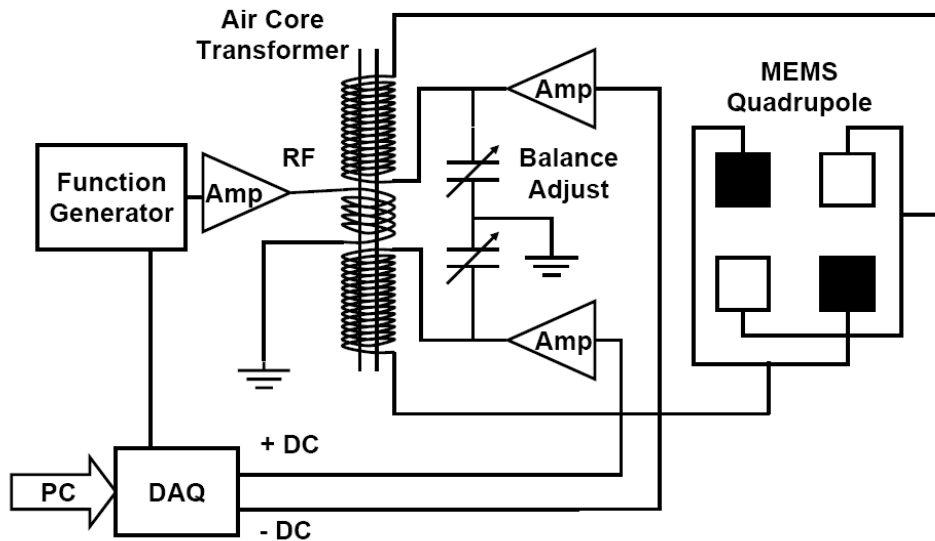
Figure 5-7: Schematic of drive electronics
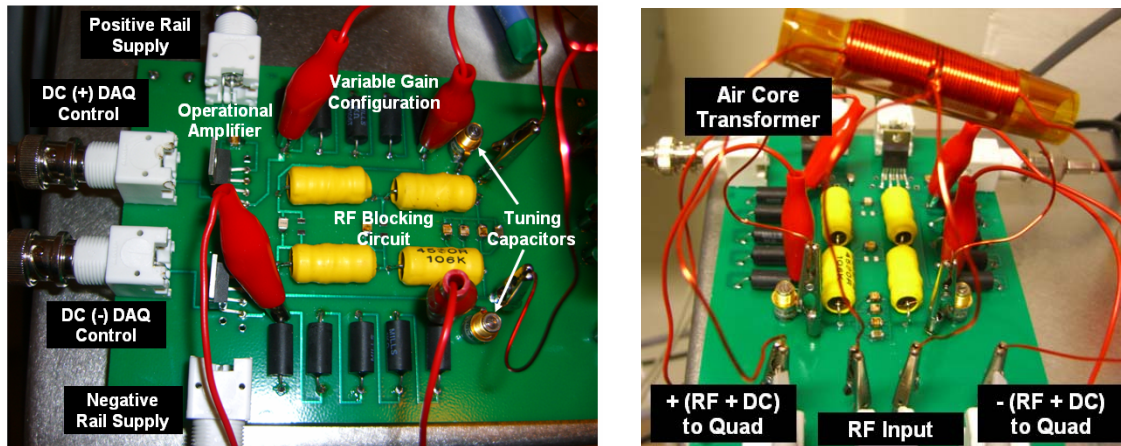
Figure 5-8: Drive circuit

The d.c. drive components stem from two analog outputs of a computer controlled DAQ card (National Instruments USB-6259) that can produce voltages in the range of ±10 V. These outputs are amplified individually with d.c. amplifiers that have a specified gain. In our most recent circuit, the d.c. amplifiers are operational amplifiers (Apex PA 240CX) set in a non-inverting amplifier configuration. High-precision resistors (Mills ¼ W 0.05% tolerance) are used to set the gain. Two 250 Ω and three 1000 Ω resistors are arranged in a way to provide a gain of either 1, 2, 6, 10, or 14 depending on how a wire is connected (Figure 5-8). The op-amps can output ±175 V and have rail voltages supplied

by the d.c. offsets of two linear amplifiers (Piezo Systems EPA-104-115). The d.c. signals are added to the r.f. components at the center tap of the transformer.

A detailed Spice model of the drive electronics is shown in Figure 5-9. The actual circuit includes a two-stage L-C filter that was used to protect the operational amplifiers from the large r.f. voltages associated with driving the quadrupoles. This model was used to help determine the values of the passive components, and to show tuning capacitors were effective in balancing the circuit. 10 mH inductors from Delevan were used in conjunction with NGO-type ceramic capacitors (American Technical Ceramics) to form the L-C filters. The combined signals were connected to the flange mount through 3' RG-59 cables to minimize the parasitic load capacitance of the cables (75 Ω, 15 pf/ft). An oscilloscope (Agilent 54624A) was used to monitor the voltages with 10076A probes (66.7 MΩ // 3pF) at the point where the RG-59 cables were attached. The probes were left affixed to the circuit since they presented a capacitive load that affects the resonance of the circuit. The drive electronics operate the most efficiently when the r.f. frequency utilized is tuned to the natural frequency of the circuit. This natural frequency is mainly determined by the transformer inductance and the load capacitances.
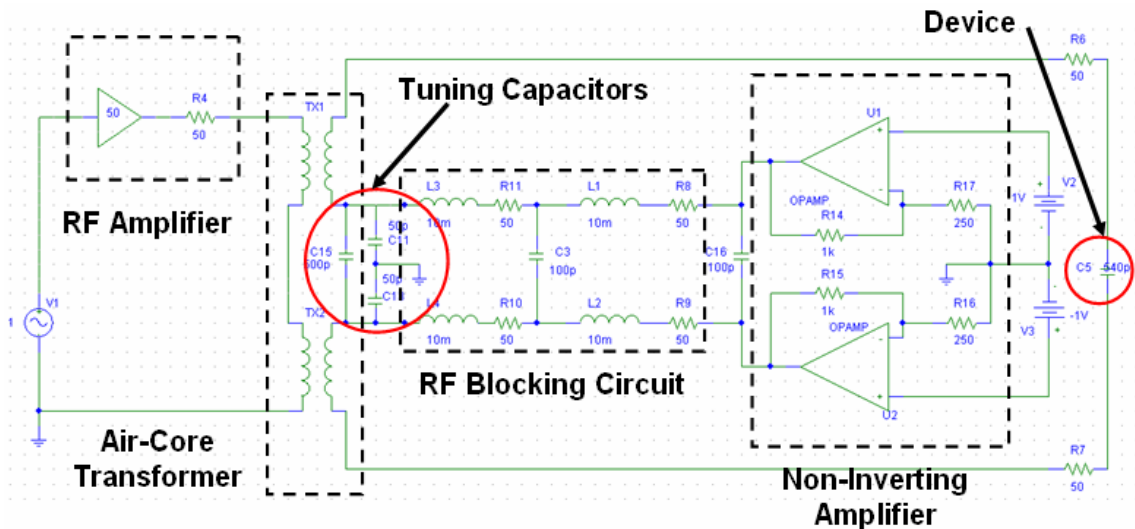
Figure 5-9: Spice model of drive circuit

The Slim-Line® ionizer and ion lenses were controlled with a filament power supply and optics supply. The filament supply has three terminals and three controls which are

summarized in Table 5-2. The BIAS voltage controls the energy of the ionizing electrons, the SINK voltage determines the initial ion energy, and the emission current is the current across BIAS which is regulated by a feedback circuit. The optics supply is comprised of six independently controlled d.c. voltages that can vary from -400 V to 400 V. Voltage control can be conducted manually with a resolution of 1 V. The three terminals from the filament supply and the six terminals from the optics supply are combined into a 10-pin connector that is detailed in Table 5-1.
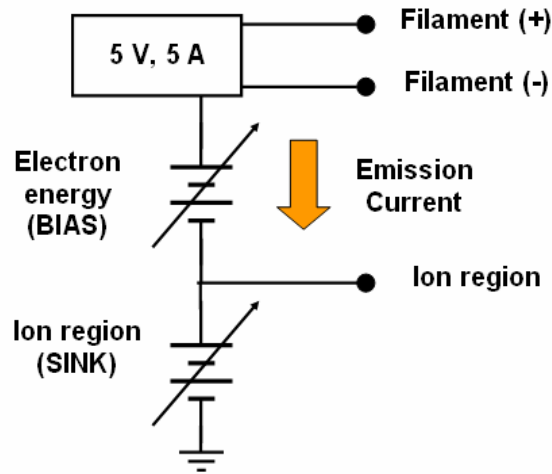
Control	Electron Energy	Ion Region	Emission Current
Range	-15 V to -150 V	-100 V to 100 V	0.12 mA to 5.0 mA

Table 5-2: Summary of filament supply

5.2.3 Control Software and Data Acquisition

The control software used in our testing facility was written in LabVIEW 8.5. The program is comprised of two main modules named GenValues.vi and Scan Control.vi. The Scan Line Generation module (GenValue.vi) is used to generate the various control voltages to be scanned, while the Data Acquisition and Scan Line Control module (Scan Control.vi) is used to communicate with the DAQ card. Scan Control.vi outputs the control voltages of GenValue.vi, and collects the detected signal. A screenshot of the software is shown in Figure 5-10 while more explicit details of the module programming are provided in Appendix D.
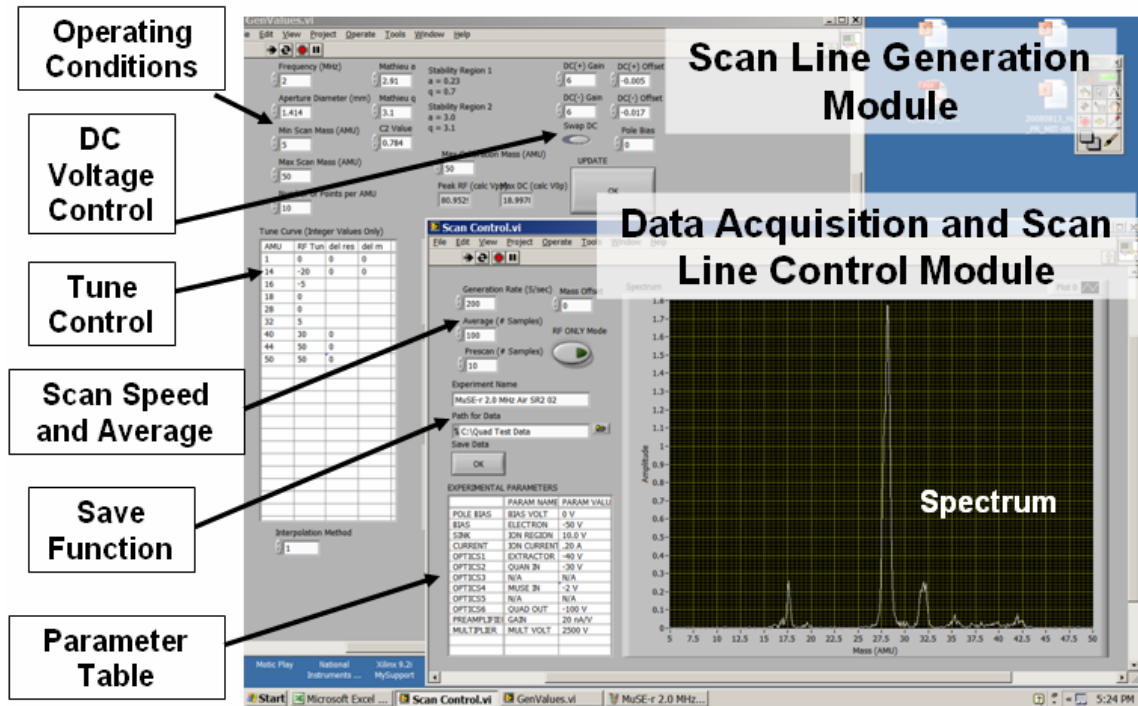
Figure 5-10: Screenshot of testing software

Scan Line Generation Module

GenValues.vi calculates the control voltages from the various parameters that are specified through the virtual instrument. The operating point (a, q), the device diameter, the drive frequency, the maximum mass to be scanned (calibration mass), and the spectral resolution (points per amu) are used to generate a list of r.f. and d.c. voltages which corresponds to the desired mass data points. The start and end scan masses are used in conjunction with the calibration mass and d.c. gain values (specified by the drive circuit) to scale and truncate the control voltages accordingly. The update button is depressed to perform new calculations, reflecting any changes made to the parameters. Extra features such as the d.c. offsets, pole bias, "swap d.c." button, and tune table were added to make adjustments to the control voltages. The function of these features and how they are used to improve device performance will be covered in Section 5.3. There is also a C_2 compensation factor that was included that divides all the generated voltages by the number specified. This addition was a result of lessons learned during the testing of our chip-scale quadrupoles and is discussed in Chapter 6.

Scan Line Generation Module

Scan Control.vi takes the control voltages generated from the first module and outputs it to the DAQ card. Three analog outputs (AO) and one analog input (AI) are used for communication. The AI is used to collect the signal from the detector, two of the AO are used to set the d.c. voltages, and the last AO is used to modulate the r.f. amplitude. The scan rate and the number of times each point is averaged are specified as parameters in this module. Additionally, a prescan is specified to eliminate the signal spiking that occurs when data is collected the moment a scan starts. Finally, a button that toggles the module into "r.f. only" mode is included to facilitate with troubleshooting and is utilized in the system operation discussed in Section 5.3.

The experiment name, file path, and parameter table are features added for post-processing and analysis. The experiment name is used to identify the data sets, the file path chooses the location to save the data, and the parameter table is used to keep track of experimental parameters that are manually controlled. Clicking the "Save" button generates three files with the extensions *_spec.txt, *_scan.txt, and *_param.txt, where * is the experiment name. The first file contains the mass spectrum, the second file contains a list of the control voltages, and the last file contains the values inputted into the parameter table.

Data Acquisition Hardware

In addition to the software, a Channeltron® electron multiplier is used to amplify the signal of the transmitted ions. The gain of the multiplier is set with a high voltage power supply (Keithely 248) where 2500 V corresponds to a gain of ~5 x 10^7. The multiplier current is detected with a low-noise preamplifier (Stanford Research Systems SR570), and is converted to a voltage with a gain specified on the equipment. The final voltage from the preamplifier is measured by the AI of the DAQ card with a maximum sampling rate of 1.25 MS/s. This corresponds to a scan from 0-650 amu with 10 data points per amu and 100 averages per point in approximately 2 second. The test system at Ardara Technologies only had a sampling rate of 12.5 kS/s which means our system is capable of operating 100 times faster. Despite the added speed, it was determined that a slower scan rate produced cleaner mass spectra.

5.3   System Operation and Calibration

During construction of the in-house testing facility, a macroscale quadrupole that is compatible with the system flange mount was designed and machined. This "knockoff" quadrupole was based on a concept that was introduced to us by Dr. Randall Pedder, and was utilized in the initial benchmarking our system. The "knockoff" was made from machined stainless steel rods that were aligned and held in place by two peek spacers. These components formed a quadrupole with an aperture diameter of 3 mm and measured 90 mm in length. The motivation behind using this device was to have a conventional quadrupole that would allow us to properly evaluate and calibrate our testing system. Several system improvements discussed in Section 5.4 were implemented as a result of testing with the "knockoff". The macroscale quadrupole and a mass spectrum for FC-43 obtained with the device are shown in Figure 5-11. We see that our test system is capable of producing high-resolution spectra with good linearity and decent relative abundance. The shift in the peak for mass 219 was due to non-linearity of the r.f. amplifier at large voltages (~ 750 V_{pp} at 250 amu).
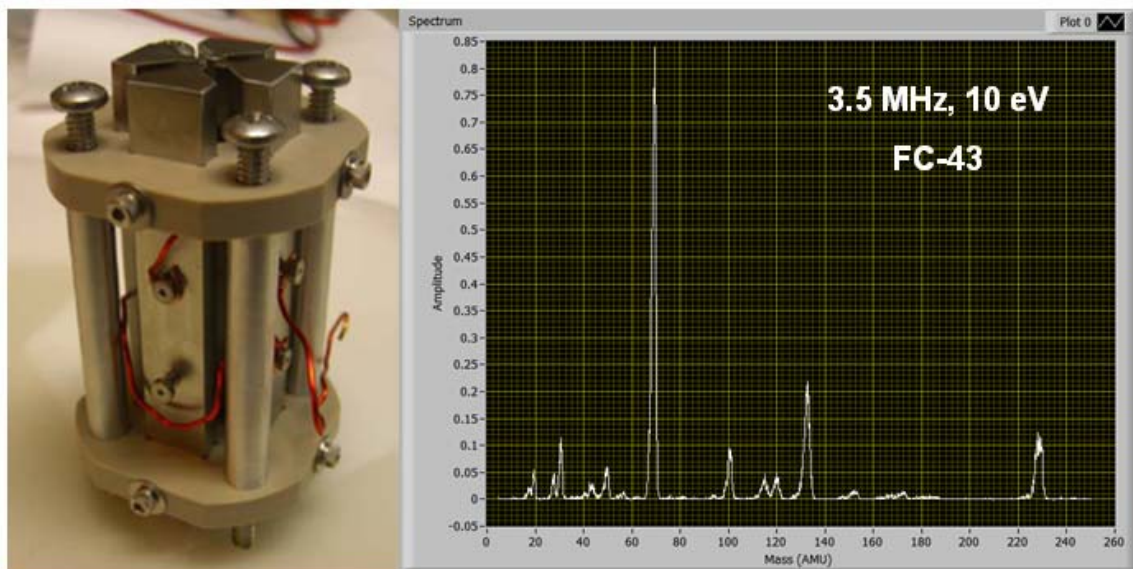
Figure 5-11: System calibration with macroscale quadrupole

After most of the system improvements were made, the μ-Gripper quadrupoles designed by Velásquez-García [47] were also tested. This was the next logical step for benchmarking our system since we wanted to evaluate our system capability for characterizing MEMS devices. We were able to demonstrate operation of a quadrupole with electrodes 1.0 mm in diameter and 37 mm long within the first and second stability regions. As a note, testing of this device at the external vendor was unable to produce data when operated in the second stability region. Additionally, we were able to demonstrate operation up to 9 MHz, significantly higher than what was previously achieved. These results clearly indicate that our system is able to surpass the capabilities available at Ardara Technologies. Our next step was to re-test the MuSE version 1.0 discussed in Chapter 4 but the device was no longer functional. We then proceeded to test new devices that are presented in Chapter 6.

Characterization of the "knockoff" quadrupole, the μ-Gripper quadrupoles, and our devices followed the same procedure. We first loaded the device into the flange mount as described in Section 5.2.1, checked for shorts, and made the necessary electrical connections. The flange mount was placed onto the vacuum chamber and the system was pumped down to a base pressure of $\sim 1 \times 10^{-7}$ Torr. The analyte was introduced and we waited until the pressure stabilized at $\sim 3 \times 10^{-5}$ Torr before proceeding. Next, we chose the operating frequency and made the necessary adjustments to the drive circuit to obtain resonance. The r.f. amplitude was calibrated to the maximum mass range to be scanned through adjustments in the r.f. amplifier gain and the control software. The appropriate d.c. gain was selected and the d.c. offsets were adjusted to ensure a proper zero.

Once the drive signals were taken care of, the filament supply was turned on to generate ions. The multiplier power supply and current preamplifier were turned on to begin signal detection. Initially, the control software was set to "r.f. only" mode to ensure that there were no physical obstructions to the ion transmission. Next, the various lens voltages were adjusted to maximize the transmitted signal before switching-off the "r.f. only" mode to produce a mass spectrum. Minor adjustments were made to the hardware and software to calibrate the system, essentially lining-up the detected mass peaks to where they should be. Additional adjustments were made to the system to improve the peak-shapes, abundance sensitivity, and resolution before the data was saved.

Once the desired data was acquired, all the electronics were turned off. The analyte line was sealed-off and the system was allowed to cool. After several minutes, the pump was turned-off and the system was vented. Detailed instructions of the system operation and methods for improving the mass spectrum are outlined in Appendix F.

5.4   Issues and Improvements

The test system presented in this chapter had gone through several iterations to reach the state of its current capabilities. Most of the improvements involved changes to the drive circuit or to the testing software. While using the "knockoff" quadrupole to conduct initial experiments, we found utility in having the ability to make adjustments to the scan line. This allowed for improved resolution at high masses, and was implemented as the tune table. Eventually, this capability was expanded to tuning at different masses and a save feature was also included.

Operating the "knockoff" in the second stability region highlighted the importance of stable drive voltages. Initially, the d.c. amplification was conducted through linear amplifiers (Piezo Systems EPA-104-115) but the detected spectrum was not very stable. The gain was adjusted through a potentiometer and was quite susceptible to noise and fluctuations. To address this issue, we decided to use operational amplifiers with high-precision resistors to create non-inverting amplifiers. This required a redesign of the drive circuit to include the L-C filters and variable gains as discussed in Section 5.2.2. The linear amplifiers were subsequently used as the rail voltages for the operation amplifiers since they had the ability to provide a ± 200 V d.c. offset.

Several issues encountered during testing of our chip-scale quadrupoles were a result of the large device capacitance. One problem with the capacitance value was that the drive circuit resonance frequency was typically smaller than the desired operating frequency. This required the construction of a smaller air-core transformer with a lower inductance to achieve the desired frequency. As a result, the impedance of the LC-tank formed by the device and transformer was small. In order to produce the desired operating voltages, the small impedance drawed a lot of power from the r.f. amplifier, leading to non-linear behavior in the equipment. Compensation for this non-linearity was

attempted by expanding the tune table to include an r.f. tune component, but a better solution is to redesign the device to have a much smaller capacitance. Overall, improved drive electronics along with improved fabrication will lead to better device performance [106].

In the future, there are several improvements that we can make that will improve the capabilities of the system. We can

- implement computer control over all the electronics to achieve full automation
- add feedback and direct measurements for all the electrically driven components to minimize noise and maintain linearity
- have the air-core transformers manufactured to achieve more symmetric drive signals
- redesign the testing jig to simplify the wiring and enhance alignment to the aluminum device housing
- remove the trace air leak in the argon line to improve characterization
- replace the Tygon tubing to improve pump-down time
- install a conversion dynode with the detector to minimize mass discrimination
- modify the software to conduct averaging over multiple scans to get cleaner spectra

5.5 Summary

In this chapter, we motivated and detailed the construction of an in-house testing facility. An extensive description of the system hardware, the drive electronics, and the control software was provided to facilitate an understanding of the entire system. Additionally, the experimental procedure was outlined so that someone unfamiliar with quadrupole testing can utilize the facility to generate mass spectrum. Issues encountered during experimentation and subsequent improvements were addressed. Ultimately, we established a testing facility that rivals the system available at the external vendor. Our in-house system was used for the subsequent characterizations presented in this thesis.

Chapter

6

MuSE version 1.5

6.1   Overview

In Chapter 4, we demonstrated proof-of-concept mass filtering with the MuSE-QMF. Unfortunately, several issues were encountered that limited fabrication yield, device reliability, and device performance. Taking the lessons learned from MuSE version 1.0, we made several changes to the device. With the intent of demonstrating improvements over the old version, MuSE version 1.5 utilized the same dimensions and mask set as its predecessor. The key differences between the two versions are in the process flows and device cross-sections as illustrated in Figure 6-1.
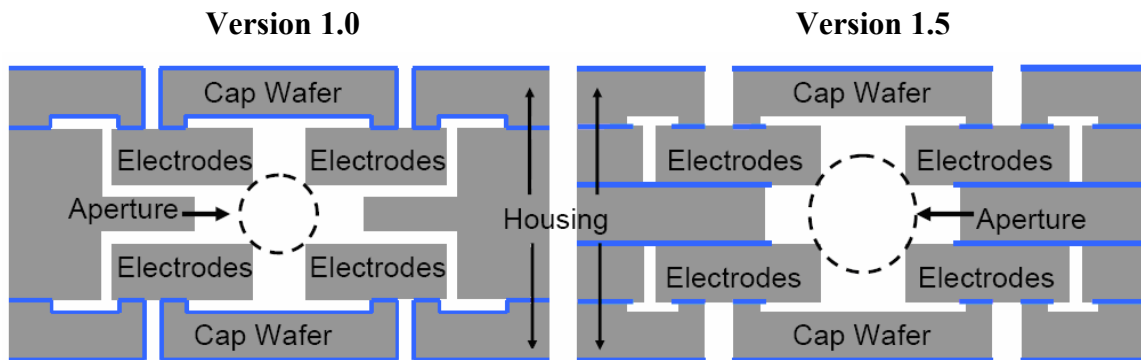
Figure 6-1: Differences between the two MuSE versions

One of the most significant issues encountered previously was the poor bond quality between the electrode and cap wafers. Modifying the process flow so that all wafer

processing occurred after the insulating oxide growth addressed the problem. Another issue was the device reliability since the contact force exerted by the pogo-pins during testing was sufficient to dislodge the electrode components from the cap wafer. This problem might have been alleviated with the changes in the cap wafer but an extra precaution was added. The electrode anchor points were sandwiched between the cap and aperture wafers for improved rigidity. An oxide layer was introduced between the layers to maintain electrical isolation of the components. This modification increased parasitic capacitances, so the insulating oxide was made as thick as possible to compensate. The increased oxide thickness had the added benefit of raising the electrical breakdown voltage of the devices. The modified processing called for oxide-to-oxide fusion bonding which needed evaluation for viability. Other researchers have reported successful bonding [107]-[109], addressing the concerns we had with the new process.

6.2   New Process Flow

All fabrication steps in this version were conducted at MIT's Microsystems Technology Laboratories. Once again, the device was comprised of five double-side polished silicon wafers that were heavily doped with antimony. The wafers had a sheet resistance of 10-20 mΩ·cm, and the thicknesses used were the same as those in version 1.0. The wafers were purchased from Ultrasil Corp., but now they had 0.5 μm of thermal oxide instead of 0.3 μm.

Initially, alignment marks were placed on both sides of the wafers in the same manner as prescribed in Chapter 4. It was important to make sure the first set of alignment marks were centered so subsequent bonding steps would produce wafer-stacks with minimal offset between layers. After the alignment marks were defined, the wafers were cleaned with piranha and an oxygen plasma ash. Next, the protective oxide was stripped with 49% HF followed by an RCA clean. A 2.5 μm wet-oxidation was conducted at 1050 ˚C and 250 nm of LPCVD low-stress silicon nitride was deposited right afterwards. Since we planned on performing an oxide-to-oxide fusion bond, this nitride layer was crucial for preserving the quality of the oxide surface throughout subsequent processing.

Cap/Aperture Wafers Processing

The cap wafers and aperture wafer were processed in a very similar manner. Thick photoresist was spun on both sides, followed by double-sided contact photolithography. The nitride and thick oxide on each side were etched away using a two-step RIE. The cap wafers underwent a 100 μm-DRIE on one side to define the cap trench, and a 400 μm-DRIE etch on the other to produce the contact vias (Figure 6-2). At this point, the residual silicon blocks in the contact vias fell out. The aperture wafer had the same pattern exposed on both sides, followed by a two-step RIE on each side. Subsequently, a 500 μm-DRIE etch was performed on both sides to ensure symmetry (Figure 6-3). At the end of the second etch, the silicon block in the aperture region fell out. These wafers were all mounted onto quartz handle wafers after the front-side DRIE was completed. After the back-sides were etched, the wafers were dismounted in acetone, cleaned with piranha, and ashed for 1 hour.
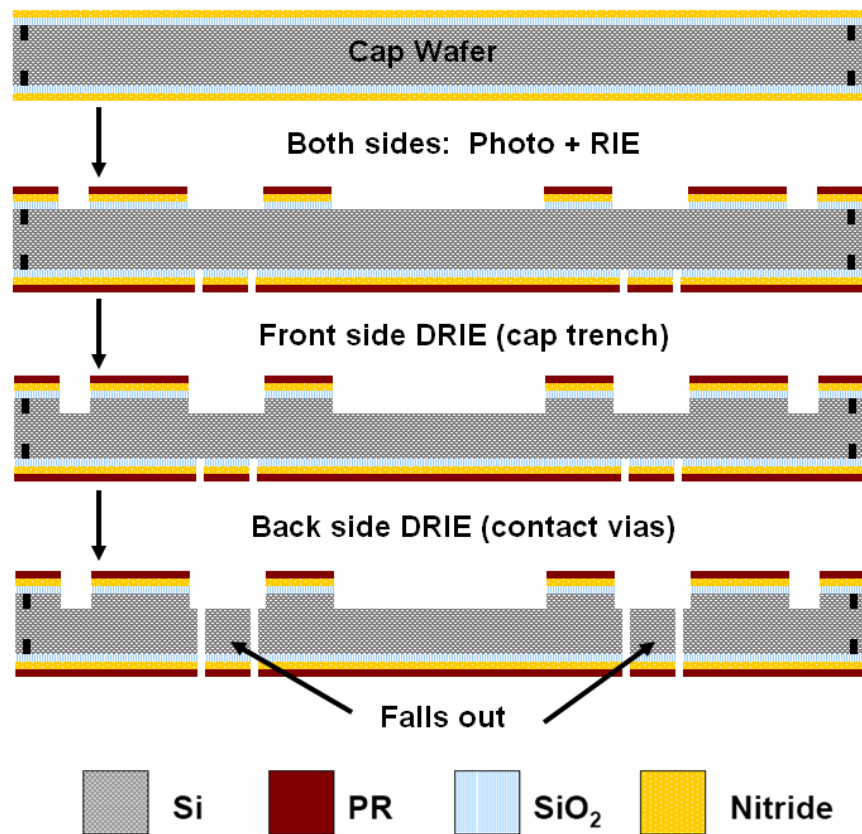
Figure 6-2: New process flow for cap wafer
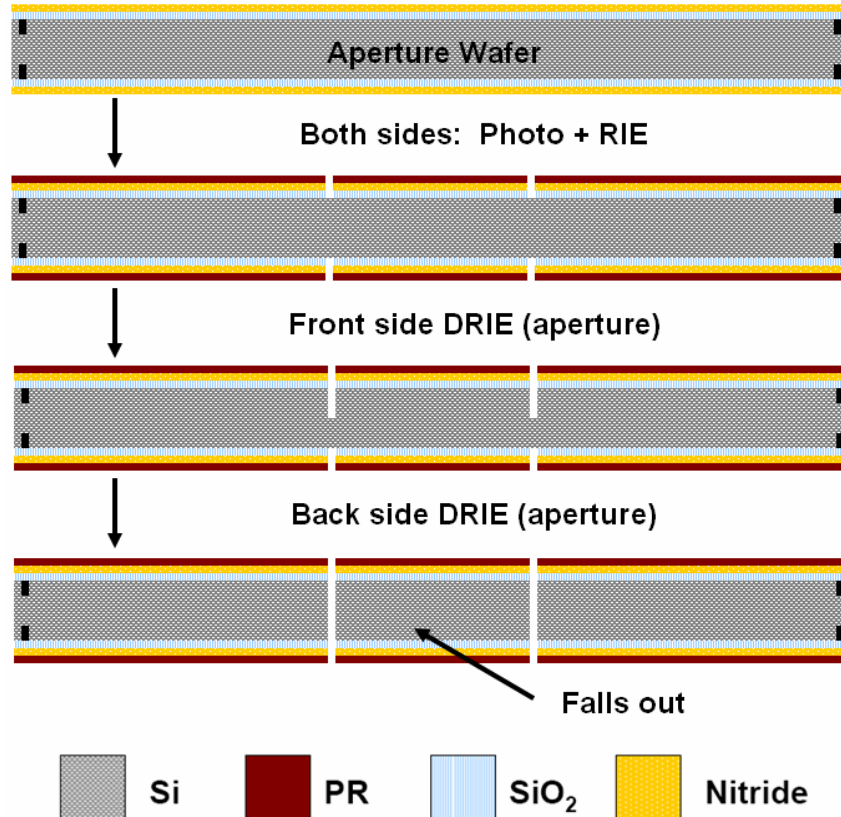
Figure 6-3: New process flow for aperture wafer

Electrode Wafers Processing

The electrode wafers started with thick resist being spun on both sides followed by double-sided contact photolithography of the same pattern. The nitride and thick oxide was etched away using a two-step RIE on both sides, and was followed by a resist-strip and wafer-clean with piranha. The electrode wafers then had 1.4 μm of PECVD low-stress nitride deposited on one side to serve as a timed-etch mask. At this time, the completed cap wafers and electrode wafers were placed in phosphoric acid at 165 ˚C for 1.5 hours. This removed all the LPCVD nitride on the cap wafers and left 150 nm of LPCVD nitride on one side of the electrode wafers. The wafers were RCA cleaned, and aligned as shown in Figure 6-4. The two wafer pairs were then bonded by being pressed with 2500 N for 20+ hours in a vacuum of 1 mTorr. The cap-electrode stack was then annealed in nitrogen for 1 hour at 1000 ˚C to strengthen the bond. The stacks were coated with thick resist on the side with nitride, and the pattern for the electrodes and lens elements were transferred. Another two-step RIE was used to remove the underlying

nitride and thermal oxide before etching the electrode components. The wafer stacks
were mounted, etched with a 1000 μm-DRIE, dismounted, cleaned, then ashed.
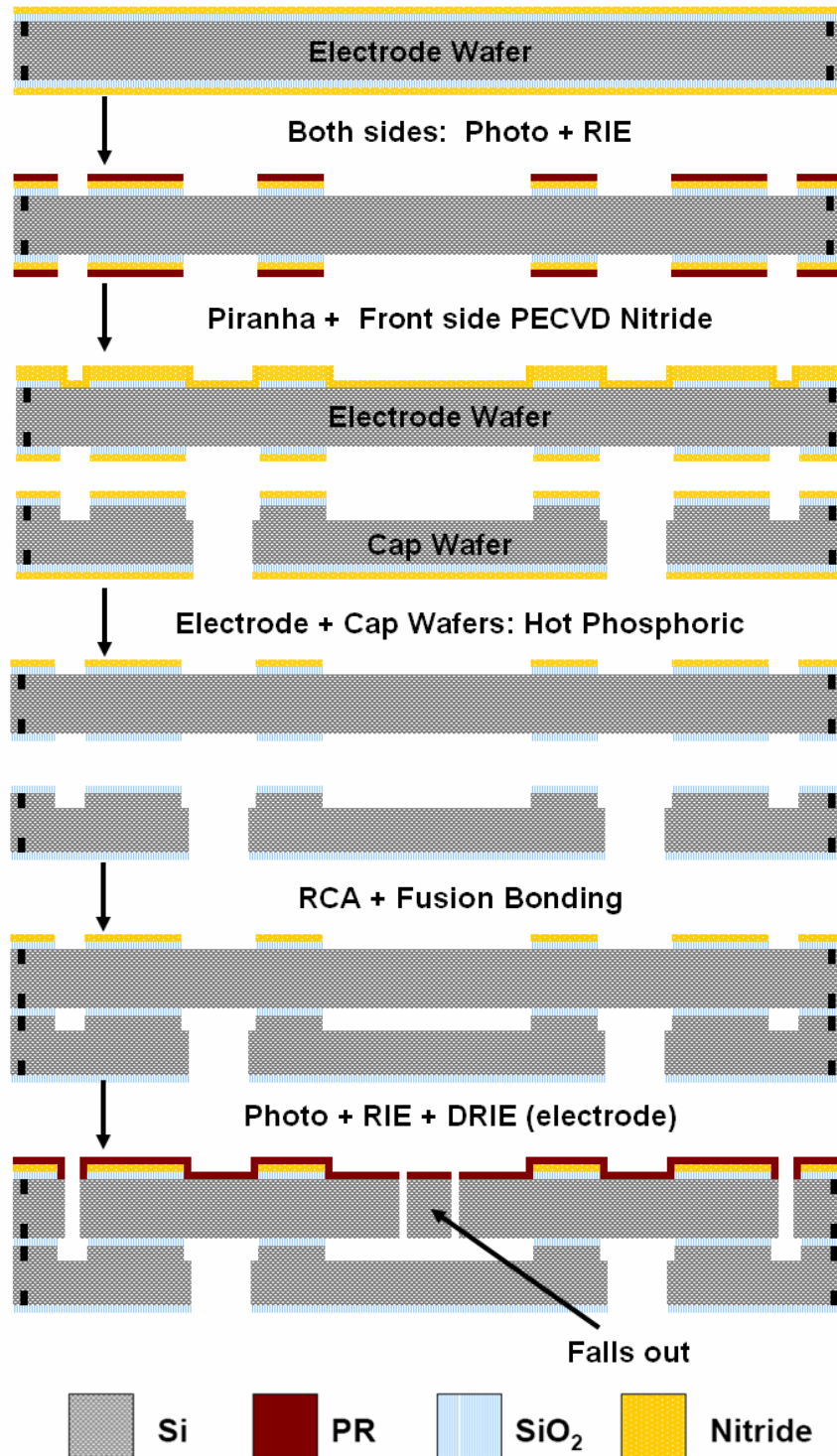
Figure 6-4: New process flow for electrode wafer

Final Processing Steps

The two cap-electrode stacks and the aperture wafer were all placed in hot phosphoric acid at 165 ˚C for 1.5 hours to remove all the remaining nitride from the bonding surfaces. The stacks and aperture wafer were RCA cleaned, aligned with the aperture wafer sandwiched between the two stacks, and bonded as shown in Figure 6-5. To perform the final bond, one cap-electrode stack was initially bonded to the aperture wafer in atmosphere using silicon direct bonding. The 3-wafer stack was pressed for 10 minutes with 1100 N before it was aligned to the other cap-electrode stack for fusion bonding.
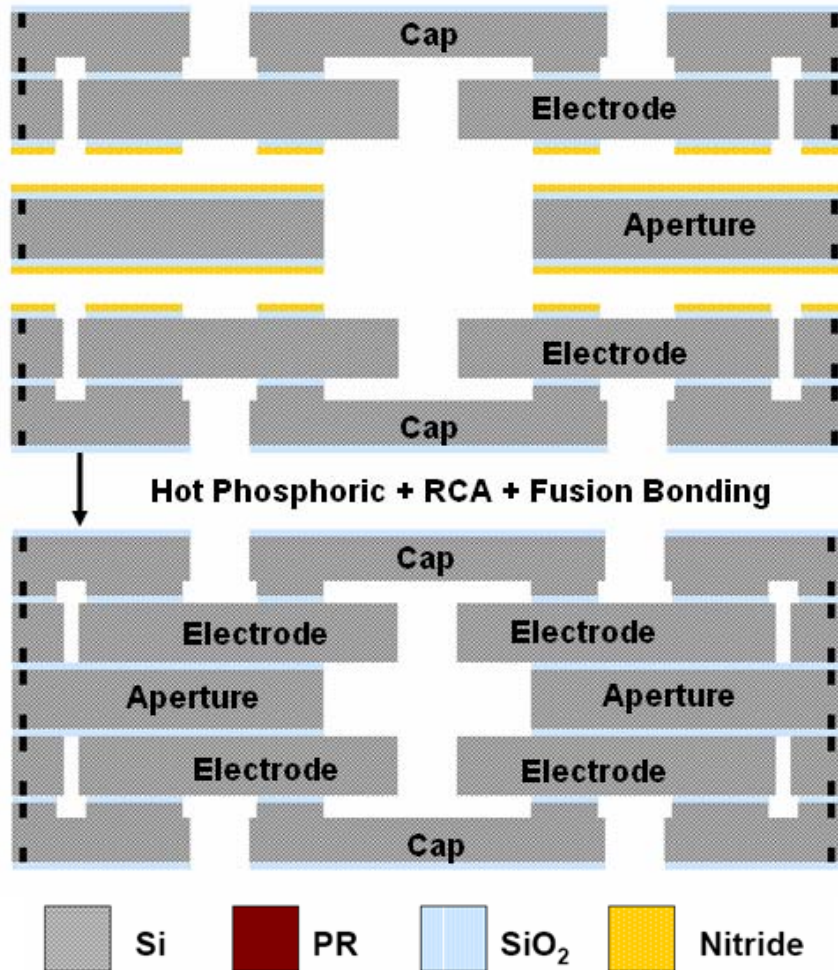
Figure 6-5: Final processing of version 1.5

The accuracy of each alignment step was measured with an Electronic Visions TBM8 and quantified to be within ±2.5 μm. A total of nine alignment steps were needed during fabrication of the wafer stack – the five front-to-backside alignments used to place alignment marks and the four bond alignments between each of the five wafers. The bond alignment had a similar accuracy to that of the front-to-backside alignment, and was assumed to be within ±2.5 μm as well. The combination of experimental error for sums can be expressed as

$$\Delta_{total} = \left[\sum_i \Delta_i^2 \right]^{1/2} \qquad\qquad (6\text{-}1)$$

where Δ_i is the misalignment of the ith step. Since there were nine alignment steps used, each with an accuracy of ±2.5 μm, Equation 6-1 gives a total misalignment of ±7.5 μm.

The 5-wafer stack was then die-sawed to complete the devices by simultaneously opening the inlet and outlet apertures while separating individual dies. This step required a good deal of care since large particles formed during die-sawing led to shorting issues between the electrodes, lens elements, and housing. Die-saw tape was used on both sides to cover the contact vias, and the cut devices were kept in DI water until testing. The tape was used to minimize particles entering the device and the DI water soak was used to prevent particles from settling. An ultrasonic clean with solvents before testing helped alleviate some of the shorting issues encountered. A detailed outline of this new process flow is included in Appendix A.

6.2.1   Improvements

One of the major improvements with the new process flow was the bond quality between the cap and electrode wafers. The improvement in bond quality is evident from Figure 6-6. The new process led to 100% yield in terms of electrode components remaining intact after the electrodes were defined. The old process suffered from poor bonding at random die locations that varied between wafer-stack to wafer-stack. This problem led to significantly low device yields since two cap-electrode stacks were needed to complete the device. With the improved processing, it was possible to have 100% fabrication yield.
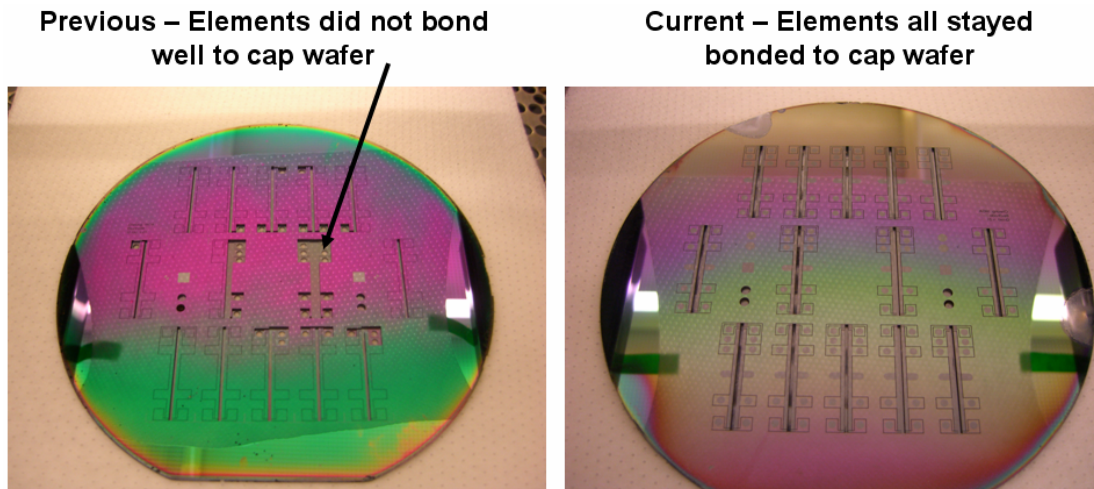
Figure 6-6: Improvement in bond quality with new process flow

Another benefit of the new process flow was the relative simplicity. All the wafers begin with the same processing steps – alignment marks, thick oxidation, LPCVD nitride, photolithography, and a two-step RIE to pattern the nitride and oxide. This greatly reduced the time needed to fabricate the devices, which can lead to lowered costs. The wafers were essentially streamlined until a much later stage in the processing when compared to the old process flow. Additionally, the oxide-to-oxide bonding utilized produced a thick, high-quality insulating layer. This oxide lowered parasitic capacitances and raised the breakdown voltage, which ultimately improved device performance.

6.2.2 Issues

Despite the improvements mentioned, we still encountered shorting issues between the electrode components during testing. We believe that this was due to particles from die-sawing, or potentially silicon stringers that remained after the electrode patterning. Stringers are material that remains after a processing step due to the directionality of the process. To address the potential issue of die-saw particles, the devices were put through an RCA clean followed by a 2 minute soak in 50:1 dilute HF before testing. This clean did not significantly improve the shorting issue, indicating that the stringers were the main reason for the shorting observed.

The etch recipe developed in Chapter 4 sufficiently addressed the formation of black-silicon but it produced the etch profile shown in Figure 6-7. The center of the trench

etched slightly slower than the edges so it was likely that pieces of silicon remained after the DRIE step. These silicon stringers could have been shadowed by the other electrode structures, preventing their removal during an over-etch step. Cross-sectional SEMs taken along the length of the device are shown in Figure 6-8. We can clearly see large pieces of silicon wedged between the electrode components, and also between the lens element and the housing. The characteristic width of the debris was on the order of 100 μm, which is the dimension of the etch-trenches. These images serve as a good indicator of stringer formation since the die-saw process should not generate particles of this size.
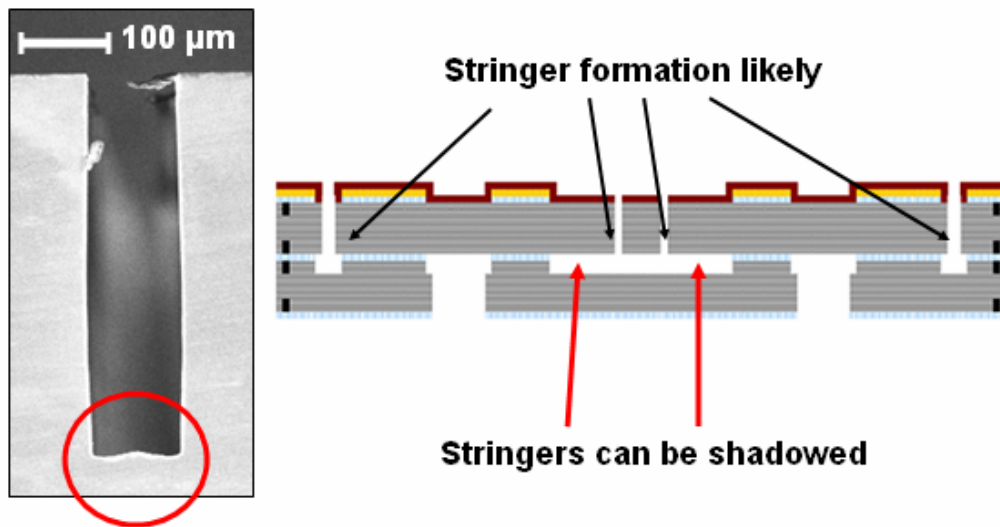
Figure 6-7: Stringer formation on cap-electrode stack

Figure 6-8: SEMs showing shorting from stringers

An ultrasonic clean with solvents was utilized in attempts to dislodge these particles. After processing for 10 minutes in acetone, 10 minutes in IPA, then 10 minutes in DI water, testing showed a decrease in the number of shorted components. Even though this clean was successful in producing devices we could characterize, there was a high likelihood of damage. In some of the devices, the ultrasound produced cracks near the anchor points which led to breakage of the electrodes as shown in Figure 6-9.
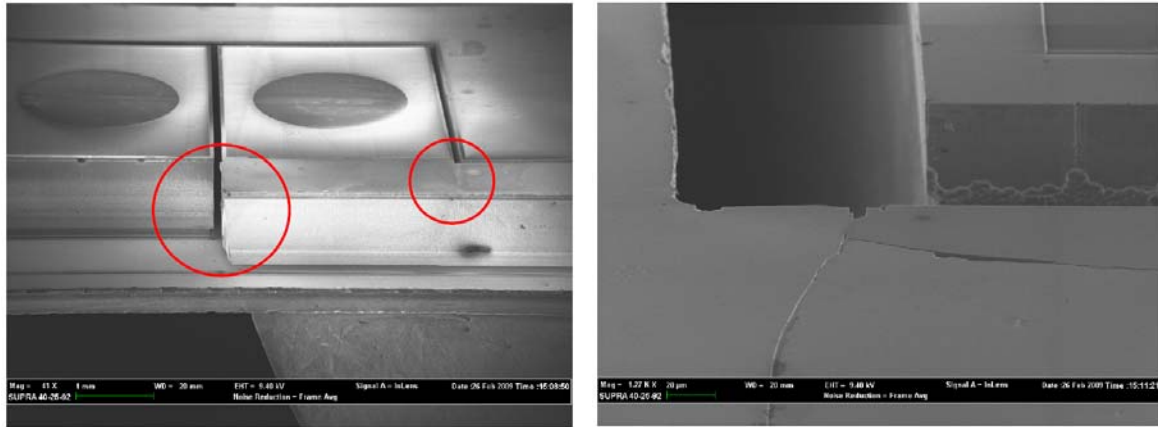
Figure 6-9: Electrode damage after ultrasonic cleaning

6.3   Characterization

Characterization of the new MuSE-QMF was conducted entirely with the in-house testing facility described in Chapter 5. We aimed to repeat the experiments conducted at Ardara to verify the capabilities of our system, and to expand upon those experiments to obtain a better understanding of our device. Conversations with John Syka of Thermo Fisher helped identify key experiments needed to benchmark our device. Performance metrics are typically given for entire systems, so assistance was needed to determine metrics specific to the mass filter. The work presented in this section focused on the following tasks:

- Demonstrating the effects of integrated ion optics
- Understanding how ion energy affects the peak-shapes and spectra
- Studying peak-shapes and mass spectra for various analytes
- Obtaining resolution versus Transmission curves

Different drive frequencies and stability regions were utilized throughout the testing to explore the capabilities of the MuSE-QMF.

From our batch of fourteen devices, two were severely damaged from a broken blade during die-sawing. The remaining devices were kept in DI water until they were tested. Several devices were lost to damage during the ultrasonic clean utilized to alleviate the shorting issue, but we were able to identify a few dies that had functional inlet optics. All the data reported in this chapter were from one of those devices.

6.3.1 Experimentation

Due to the large parasitic capacitance inherent in the current MuSE-QMF, we were only able to drive the device at a maximum frequency of 4.0 MHz. The larger coil used in the experiments resonated around 2 MHz, while the smaller coil resonated around 4 MHz. Frequencies of 3.0 MHz and 3.5 MHz were obtained by adding capacitors in parallel with the smaller coil.

During initial evaluation at 2.0 MHz, we found that the r.f. and d.c. amplitudes had to be increased by a factor of ~1.27 to align the detected masses with what was known for the analytes used. This compensation factor is attributed to the magnitude of the C_2 term listed in Table 3-1 for the square electrode geometry. It appears that we needed to scale up the voltages to bring the effective C_2 to unity for proper operation. Curiously, when the device was operated at higher drive frequencies, the compensation factor needed for the r.f. approached ~1.0 while the d.c. factor remained at ~1.27. The implications of this observation will be expanded in Section 6.4.

Figure 6-10 gives a detailed schematic of how the ionizer, MuSE-QMF, and ion optics were situated in our in-house testing facility. Ions were generated in the ion region, and extracted with the extractor lens. The ion beam was then focused with the inlet lens, followed by additional focusing with the MuSE inlet lens. Filtered ions were pulled out of the device with the exit lens, and sent to the detector. By adjusting the voltages on the extractor, inlet lens, and MuSE inlet lens, we were changing the inlet conditions which had a direct impact on peak-shape and transmission. Ion energy also had a significant impact on the transmission and peak-shape, and was adjusted by the changing the voltage difference between the ion region and the quadrupole centerline potential. The pole bias

is a d.c. offset that is added to the quadrupole drive signals, thus giving control of the centerline potential. Adjustments to the exit lens voltage had little impact on the detected signal, and the MuSE exit lens was kept grounded due to shorting issues.
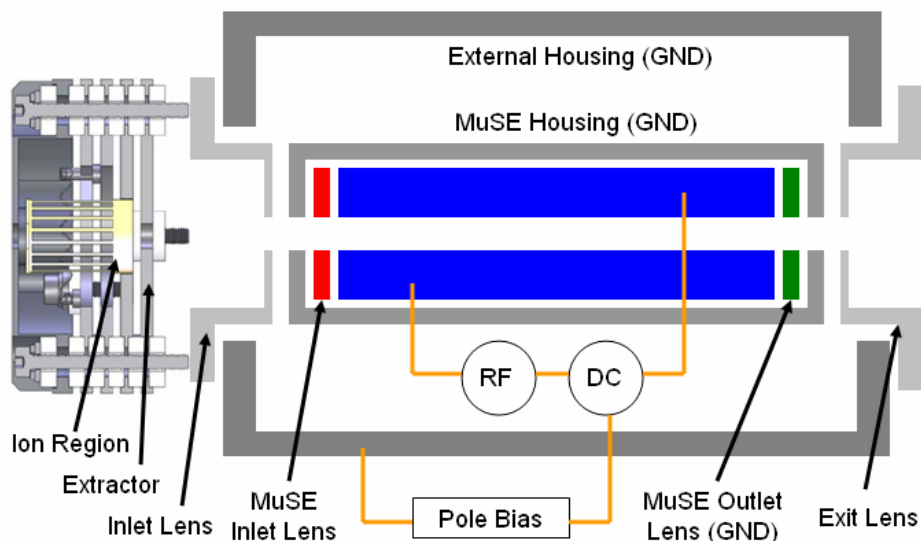
Figure 6-10: Detailed schematic of ionizer and device

After a device was loaded into the vacuum chamber and was ready to be tested, the operational frequency was chosen and the drive circuit was tuned accordingly. The correct coil was selected, load capacitances were added if needed, and the r.f. amplitudes were balanced by adjusting the tuning capacitors. The experimental procedure used in obtaining data is discussed thoroughly in Chapter 5.

6.3.2 Results

The first set of experiments conducted was to evaluate the functionality of the integrated ion optics. Argon was selected as the analyte and several drive frequencies were used. Initially, a mass spectrum was obtained with the MuSE inlet lens grounded. After optimizing the ion energy, the voltages of the extractor lens and inlet lens were adjusted to maximize transmission through the device. At this point, the integrated inlet lens elements had their voltages varied to determine how the optics affected the spectra. From Figure 6-11, we can clearly see an enhanced transmission when the MuSE inlet

voltage was -3 Volts. The same effect was demonstrated during operation in the second stability region as shown in Figure 6-12. These results validate that the unconventional ion lens geometry can be used to improve device performance.
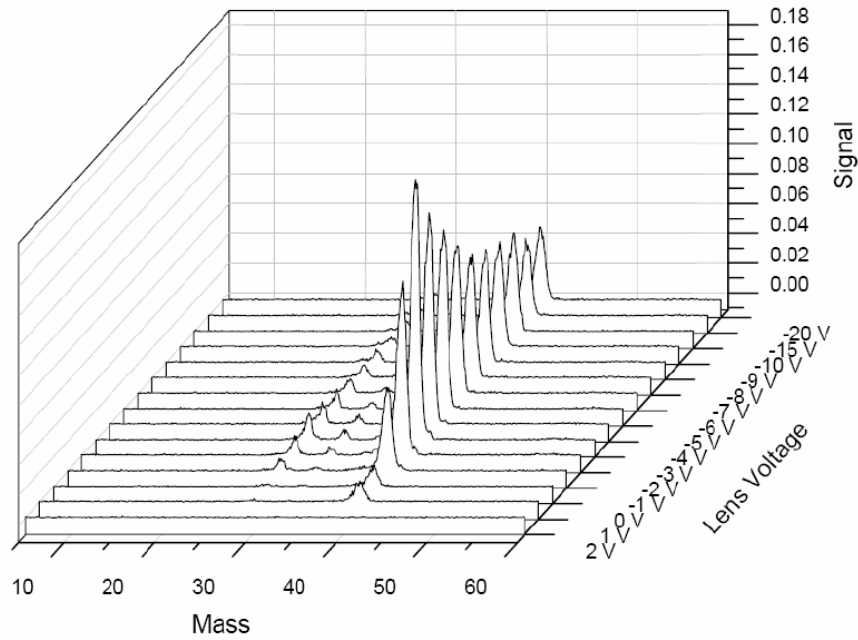
Figure 6-11: Lens data at 3.5 MHz in the first stability region, 3.0 eV
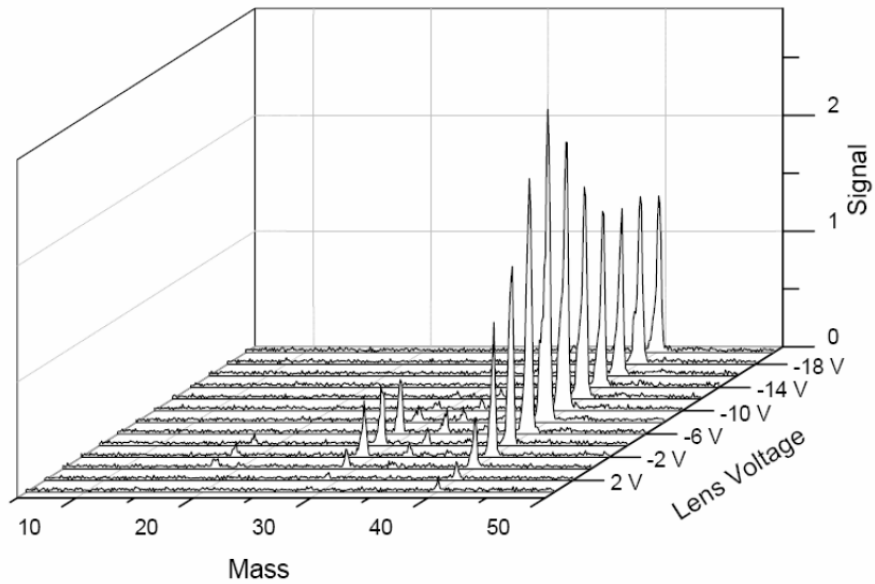
Figure 6-12: Lens data at 2.0 MHz in the second stability region, 5.0 eV

To evaluate the effect of ion energy on the peak-shapes, argon was used as the analyte once again. Since the ion energy is defined by the potential difference between the ion region and the pole bias, we had two ways of changing the ion energy. One method was to adjust the ion region voltage but this would change the way the ions interacted with the extractor and inlet lenses. Adjusting ion energy in this manner would combine many effects and was not preferred. The other method was to change the pole bias, which was controlled by the software and was generally zero. After obtaining an initial spectrum and minimizing the ion region potential, the lenses were tuned to maximize transmission. At this point, the pole bias was varied and the resulting spectra recorded. We found that transmission increased as the pole bias became large and negative (Figure 6-13). The same effect was also noticed for operation in the second stability region. This result makes sense since larger ion energy translates to higher axial velocities, and faster ions spend less time in the device. Less time implies less filtering, so we would expect more ions to make it through the device and to the detector. However, it is important to note that the resolution did not decrease substantially when the transmission was increased in this manner. These results show that we have a way to increase transmission without degrading resolution, giving us another lever for performance optimization.
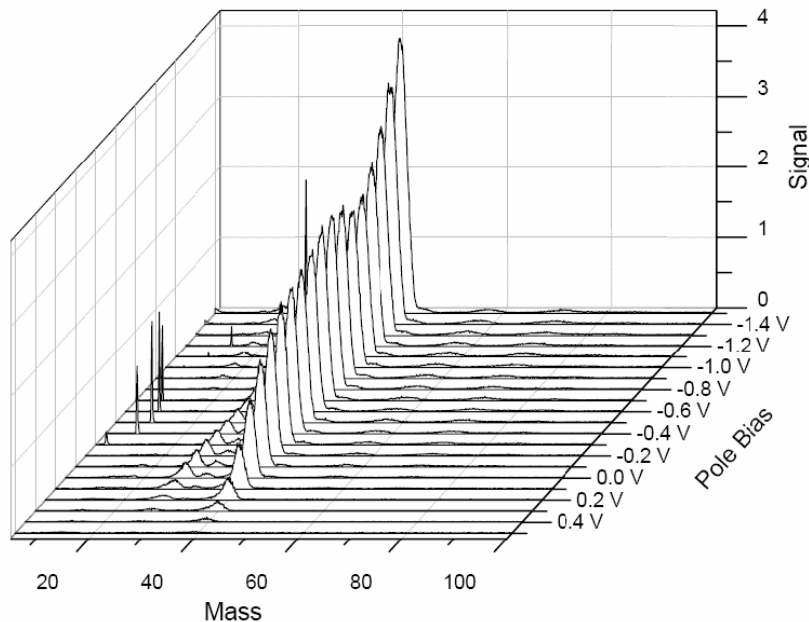
Figure 6-13: Pole bias data at 2.0 MHz in the first stability region, 3.0 eV

Once we established the capabilities of the ion optics and the ion energy control, we proceeded to conduct experiments to benchmark the capabilities of the device. Air was selected as the analyte, and mass spectra were collected at several frequencies. For each frequency, the ion energy was minimized and the optics tuned. Figure 6-14 shows a compilation of these results. The first thing to note is the improvement in peak-shape and resolution with operation at higher frequencies in the first stability region (SR1). As the drive frequency increased, the abundance sensitivity improved as can be seen by the "cleaner" spectra and more distinct peaks. Secondly, we see that operation in the second stability region demonstrated a much higher resolution at 2 MHz despite the increased ion energy. This result validates improved device performance with operation in higher stability regions.
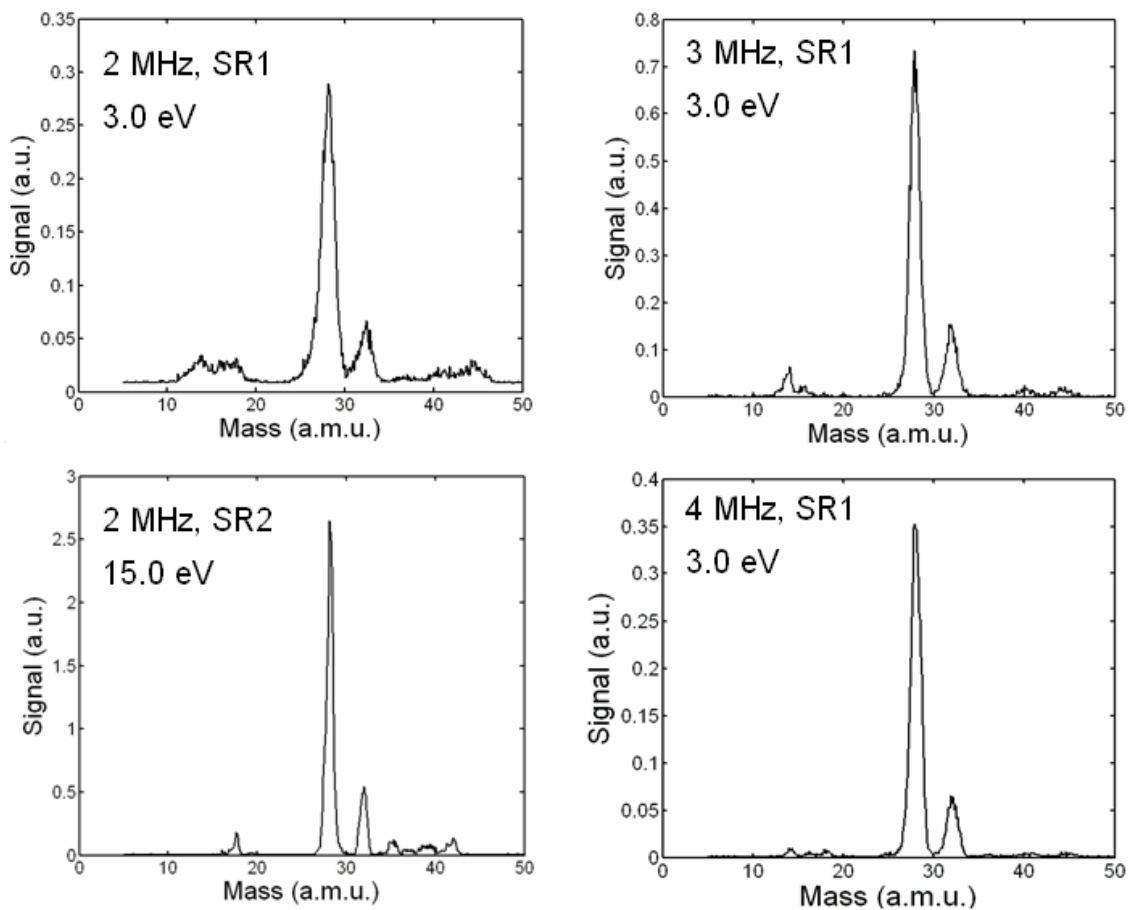
Figure 6-14: Mass spectra for air at various operating conditions

All the spectra of Figure 6-14 show prominent peaks at mass 28 and mass 32 which corresponds to nitrogen and oxygen respectively. We can also see some peaks located between 10 and 20 amu, which is representative of monatomic nitrogen (14), monatomic oxygen (16), and water (18). Additionally, the peaks around 40 amu correspond to argon (40) and carbon dioxide (44). These results demonstrated that the device was able to identify the key constituents of air. Looking at the relative abundance of the two main peaks, we see that the nitrogen to oxygen ratio is approximately 5:1 for all the data. This result gives us confidence in the device due to the consistency. Air is comprised of ~78% nitrogen and ~21% oxygen so we would have expected a ratio of about 4:1. This small discrepancy can arise from the ionization method and is not indicative of any device limitations.

If we compare the data in Figure 6-14 to the data presented in Chapter 4, we see similar performance metrics. We previously demonstrated a peak-width of ~1.2 amu at mass 28 when the device was driven at 3.8 MHz in the first stability region, and a peak-width of ~0.7 amu at mass 28 when driven at 1.98 MHz in the second stability region. Using our in-house testing facility, we achieved a peak-width of ~1.3 amu at mass 28 with 4.0 MHz in the first stability region, and a peak-width of 0.7 amu at mass 28 when the device was driven at 2.0 MHz in the second stability region. Despite the similar peak-widths obtained, our test facility demonstrated an improvement over the external vendor due to the better detector signal-to-noise. This allowed for the less abundant peaks absent in the mass spectra of Chapter 4 to be detected. Some skewing of the mass peaks was observed in Figure 6-14, but this was due to linearity issues with our drive electronics.

To probe the ultimate performance of the device, we generated resolution versus transmission plots (RT curves) at various frequencies using argon as the analyte. After the ion energies were minimized and the optics tuned, the operating point (a, q) was varied through the control software. Keeping q fixed, choosing larger values for a increased the resolution while selecting smaller values for a increased the transmission. The results of these experiments are shown in Figure 6-15. We extracted a maximum resolution of ~21 at 2.0 MHz, ~30 at 3.0 MHz, ~36 at 3.5 MHz, and ~42 at 4.0 MHz

assuming a minimum transmission of 1%. It would appear that the ultimate resolution of our device has a near-linear dependence on driving frequency. This performance deviates from the square dependence of Equation 2-6, and might be explained by the phenomena discussed by Dawson [1] and mentioned by Titov [110]. They state that there is a maximum number of r.f. cycles in which an ion can spend within a quadrupole field before non-idealities begins to add up. The non-idealities will cause dispersion resulting in resolution degradation and deviation from the square dependence.
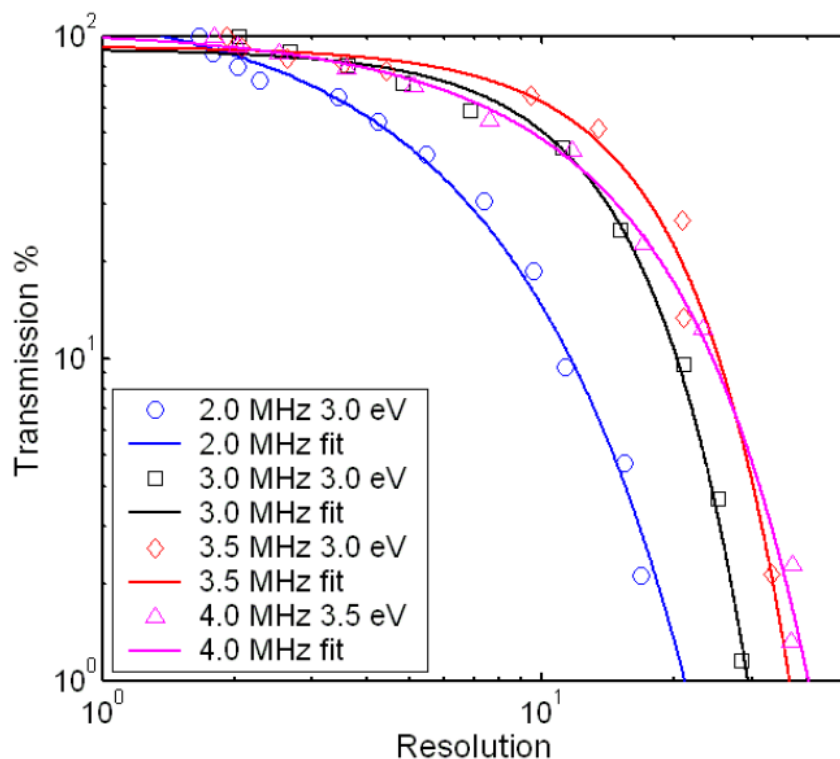
Figure 6-15: Resolution versus transmission curves at various conditions

To evaluate the maximum mass range achievable without damaging the MuSE-QMF, we utilized the low frequency coil. Higher frequencies demanded much larger voltages to scan a particular mass range, and the associated decrease in device impedance made it difficult to deliver power effectively with our drive circuit. The device was driven at 1.8 MHz, the resonance frequency of the circuit, to provide the largest voltage range possible. Figure 6-16 shows a mass range of 650 amu with FC-43 as the analyte. This corresponds to a V_{pp} of over 200 Volts, doubling what was previously achieved.
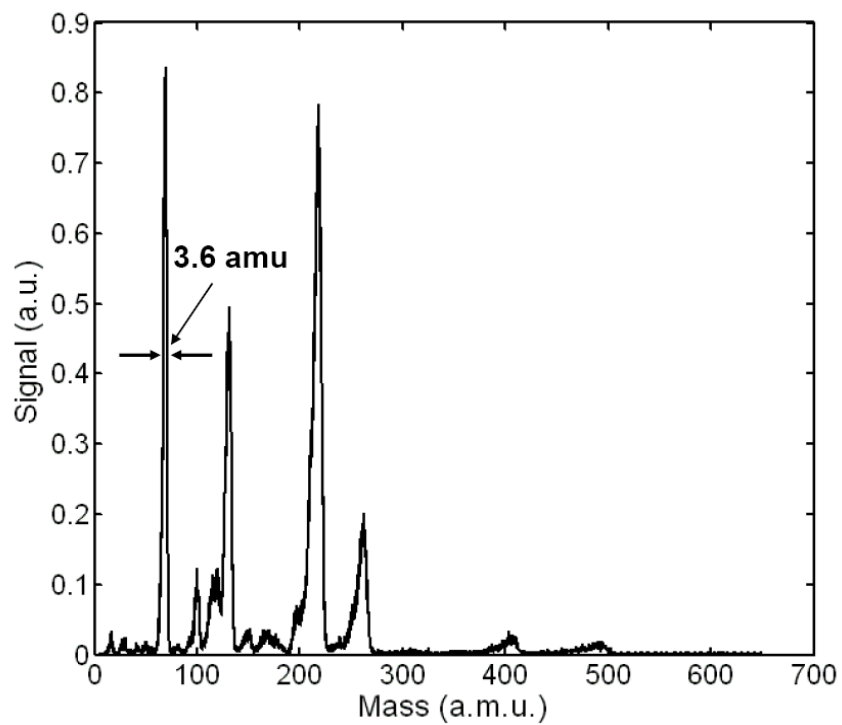
Figure 6-16: Mass spectrum of FC-43 at 1.8 MHz in the first stability region, 3.5 eV
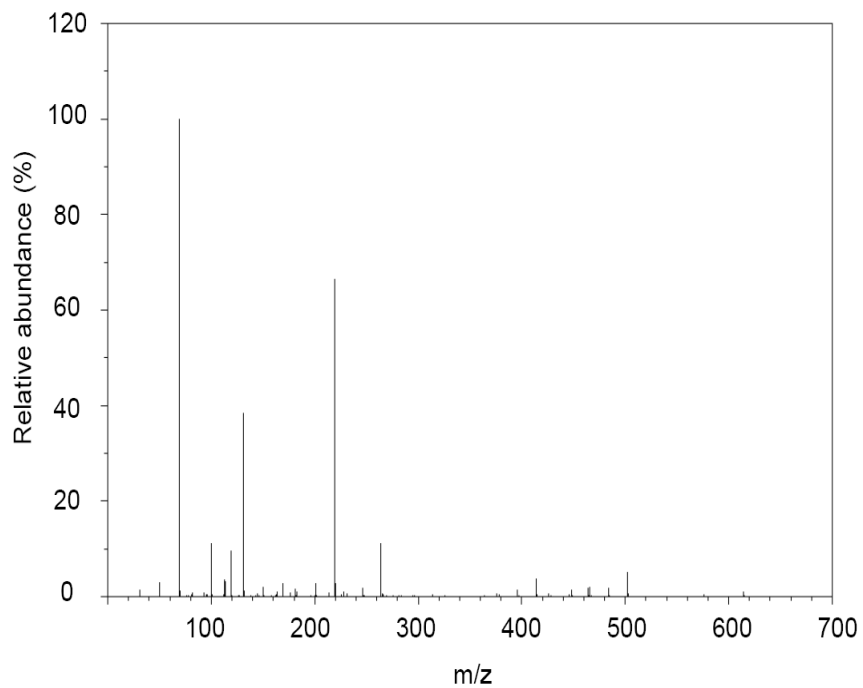
Figure 6-17: NIST library spectrum for FC-43

After optimizing the transmission through the device, a peak-width of 3.6 amu was achieved at mass 69, and a peak-width of 6.5 amu was achieved at mass 131, both corresponding to a resolution of ~ 20. For the same spectrum, a peak-width of 7.8 amu at mass 219 was recorded, while a peak-width of 9.8 amu was achieved at mass 264, both corresponding to a resolution of ~ 28. This result shows that the device was operated in a constant resolution mode attributed to the linear scan line used. The change in resolution at the higher masses was most likely due to the non-linearity of the r.f. amplifier at large voltages. An increase in the a/q ratio of the operating point will correspond to a higher resolution, while a decrease will result in a lower resolution. Overall, the device showed good correlation to the NIST library spectrum of FC-43 (Figure 6-17) included for reference.

In order to explore the limitations of our device, several experiments were conducted with argon that pushed resolution. From the results of Figure 6-14, we saw that the highest resolution was achieved with operation at 4.0 MHz in the first stability region, and at 2.0 MHz in the second stability region. While testing with these two conditions, ion energies were minimized and the lens voltages were adjusted to improve resolution. The operating point (a, q) was also varied in attempt to locate the corners of the stability regions.

The 4.0 MHz data demonstrated a peak-width of 1.0 amu at mass 40, and a peak-width of 0.7 amu at mass 28 (Figure 6-18). Both values correspond to a resolution of ~40, verifying operation in the constant resolution mode. Due to the high resolution scan, we could clearly see the effects of the higher-order field components [61], [77]. These non-idealities manifest as precursor peaks that are apparent on the low-mass side of the argon and nitrogen peaks. Operation at 2.0 MHz in the second stability region (Figure 6-19) showed a peak-width of 0.5 amu at mass 40, which corresponds to a resolution of ~80. We were also able to demonstrate a resolution of ~93 with a peak-width of 0.3 amu at mass 28. In comparison to Figure 6-18, Figure 6-19 shows no evidence of precursor peaks. Additionally, the relative abundance of each spectrum is consistent. These results make a strong case for establishing operation in the second stability region as a viable method for mitigating the effects of higher-order field components.
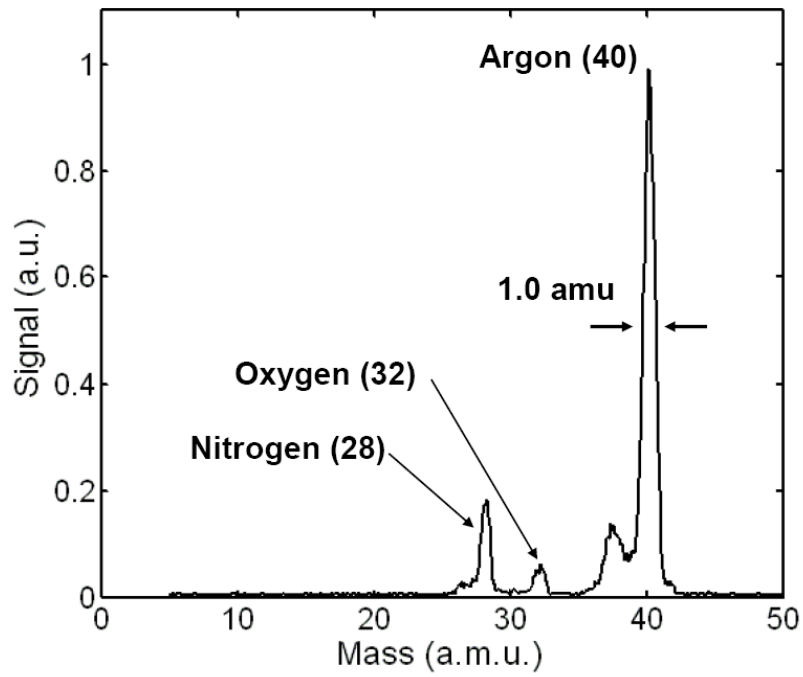
Figure 6-18: Argon mass spectrum at 4.0 MHz in the first stability region, 3.0 eV
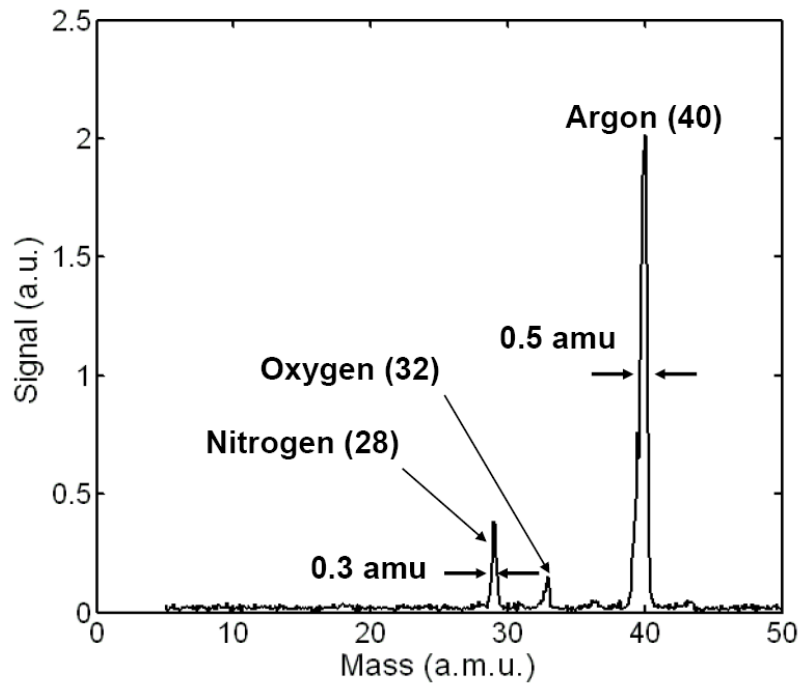
Figure 6-19: Argon mass spectrum at 2.0 MHz in the second stability region, 5.0 eV

6.4   Discussion

The new process flow introduced in this chapter led to noticeable improvements in terms of fabrication yield, robustness, and cost. Despite these enhancements, the shorting issue encountered previously still persisted. We identified stringer formation as the main culprit, but this problem can be resolved with an improved etch recipe or minor changes to the processing. The ultrasonic clean used to alleviate the shorting problem revealed an inherent flaw in our design at concave corners. The stress concentration at these sharp corners can be eliminated if we introduce adequately sized fillets in the mask layout. These engineering issues can be solved with the future work discussed in Chapter 8.

Characterization of the MuSE-QMF with our in-house testing facility helped identify the problems associated with large device capacitance. From the capacitance calculations covered in Chapter 3, we estimated a parasitic capacitance of approximately 300 pF. Simulations with MAXWELL 2D returned a capacitance value of 4.55 pf/cm for our device cross-section, indicating that parasitics are dominant. At the time the MuSE-QMF was designed, we had a poor understanding of how quadrupoles are driven. Sufficient attention was not given to the device capacitance, but a new design covered in Chapter 8 can easily reduce the parasitic capacitance by a factor of 10. A lower device capacitance will permit operation at much higher frequencies with our electronics and help to extend the mass range achievable at those frequencies.

Issues with drive voltage linearity and stability were limiting factors in determining the ultimate performance achievable [54], [57]. During characterization, non-linear behavior resulting from the large device capacitance was noticed. Modifications to the testing facility was attempted to address this issue with moderate success. Eventually, a drive circuit with feedback that can set the r.f. and d.c. ratio precisely should be used as recommended in Chapter 5. Additionally, it should be possible to get a better sense of the maximum resolution of the quadrupoles by driving the devices in the constant peak-width mode [53]. We can achieve smaller peak-widths at larger masses under this mode of operation.

The frequency dependent nature of the compensation factor mentioned in Section 6.3.1 was something that needed to be understood. We speculated that this strange

behavior was attributed to either issues with the drive electronics, parasitics within the device and/or testing jig, or possibly new ion dynamics for the square geometry. No issues were encountered with testing of the "knock-off" quadrupole or the μ-Grippers, so issues with the drive electronics were ruled out. To evaluate the possibility of new ion dynamics, Thomas Hogan from the University of Liverpool helped conduct simulations of our device at different frequencies. His results revealed that there were no shifts in the detected mass for the various frequencies, ruling out new ion dynamics. This analysis leaves parasitics in the device or in the testing jig as the most likely culprit. It is quite possible that there was some impedance that was lowered at the higher frequencies, permitting a smaller r.f. voltage to produce the desired results.

The MuSE version 1.5 demonstrated performance that was equal to or better than other MEMS-based quadrupoles. The minimum peak-width achieved (0.3 amu) and the maximum mass range attained (650 amu) was on par with the work by Velásquez-García [47], and exceeded that of Taylor [23] and Geear [27]. Additionally, the maximum resolution demonstrated (~ 90) was similar to the values reported by Velásquez-García and Geear. Using the estimated fabrication misalignment of 7.5 μm, we can expect a maximum resolution on the order of 190. This value is far from what was demonstrated, but operation at higher frequencies can reveal how accurate this estimate is.

The peak-widths obtained for air at 4.0 MHz in the first stability region, and 2.0 MHz in the second stability region was in-line with the results from version 1.0. We would have expected narrower peak-widths from the decreased ion energies used to test version 1.5, but this discrepancy could be due to several reasons. Misalignments in the ion optics could have limited the transmission and resolution, and the low ion energies itself could have negatively impacted the peak-shapes [59]. Additionally, the spectra were collected without extensive calibration and tuning. If more time was spent on the calibration and tuning of the mass spectrum, it could be possible to demonstrate higher resolutions.

If we compare Figure 6-16 with the spectrum for FC-43 presented in Chapter 4, we see that we demonstrated more than double the mass range and half the peak-width at mass 69. Interestingly enough, if we take the results in Chapter 4 and use Equation 2-10, we calculate a peak-width of 2.0 amu with the operating conditions of Figure 6-16. In actuality, a peak-width of 3.6 amu was achieved, corresponding to a lower performance

116

than expected. Some insight can be found from the pole-bias experiment (Figure 6-13). We found that increasing the ion energy improved transmission without much change to the resolution. This seems counterintuitive since we know an increase in transmission should lead to a decrease in resolution. This insight combined with our experimental data seems to indicate that we were not operating at the optimal ion energy [59].

The precursor peaks apparent in Figure 6-18 is an indicator of the disadvantage of using the square electrode geometry. The existence of these peaks will limit the device performance, especially during high-resolution scans. Fortunately, the second stability region offers a good solution to this problem. Compared to Figure 6-18, the data in Figure 6-19 demonstrated twice the resolution at half the frequency. If we also consider the r.f. voltage used to scan 50 amu in the first stability region at 4.0 MHz, and that which was used in the second stability region at 2.0 MHz, we find that they were nearly the same. By operating the MuSE-QMF in the second stability region, we could improve peak-shape and resolution without any major penalty. The only real difference is the larger d.c. voltages needed, but this could be a blessing in disguise. If the MuSE-QMF continues to scale-down, smaller d.c. voltages will be needed making the drive signals very susceptible to noise in the electronics. Utilizing larger voltages would help maintain drive signal stability in this situation.

From the data presented in this chapter, we speculate that there might be some new ion dynamics associated with our device. The results of the RT curves (Figure 6-15) and the operating point used throughout the experiments are indicators of new dynamics. The near-linear dependence of the ultimate resolution with drive frequency can be partially explained by the arguments presented by Dawson [1] and Titov [110], but it can also be a fundamental trend of the new geometry. Generating new RT curves for frequencies less than 2.0 MHz and higher than 4.0 MHz can provide some insight into this phenomenon. Most of the spectra in this chapter used an operating point near $(a, q) = (0.28, 0.7)$ instead of the conventional $(a, q) = (0.23, 0.7)$, which corresponds to the corner of the first stability region. This fact indicates there is a new stability diagram associated with our device, calling for new studies on ion behavior in non-standard, non-ideal geometries. These two observations motivated the work covered in Chapter 7.

6.5   Summary

In this chapter, we presented the process flow and characterization of the new MuSE-QMF. Improvements in the fabrication were highlighted, and persisting issues were addressed. Future modifications to the fabrication and a new device design will rectify many of the issues encountered. One of the key lessons learned from experimentation was the need for a smaller device capacitance. We also benchmarked the in-house testing facility, demonstrated device improvements, and identified several interesting phenomena with MuSE version 1.5. Additionally, enhanced performance with an unconventional lens configuration was demonstrated and many future directions were motivated. Ultimately, we achieved a mass range of 650 amu with operation at 1.8 MHz in the first stability region, and a minimum peak-width of 0.3 amu at mass 28 when driven at 2.0 MHz in the second stability region. This corresponds to a resolution of ~93 and demonstrates performance equal to or better than the other MEMS-based quadrupoles covered in Chapter 2.

Chapter

7

New Ion Dynamics

7.1 Overview

During experimental characterization of the MuSE-QMF, we observed several interesting results that alluded to some new ion dynamics. One main observation was that the operating point corresponding to the tip of the first stability region differed from what we would expect for a conventional quadrupole mass filter. Another interesting result was that the ultimate resolution of the device seemed to follow a near-linear dependence on the drive frequency. The work presented in this chapter was conducted to explore and understand these observations. Insights into the ion dynamics for our device can be extended to other non-ideal geometries.

7.2 Modified Stability Regions

The conventional Mathieu stability diagram maps the stable and unstable solutions for an ideal quadrupole with infinite length. Changes to the Mathieu equation through the introduction of higher-order non-ideal field components will alter the solutions to a degree. Therefore, we would expect some modifications to the stability regions as a direct result of using the square electrode geometry. Since we are establishing the use of a new geometry, it is beneficial to accurately identify the corners of the stability regions for optimal operation. The new stability boundaries can be determined through detailed simulations with the modified geometry [26] but a more practical method is through

experimental mapping. We present a mapping technique that was used to determine the boundaries of the first and second stability regions for our device.

7.2.1   Mapping Technique

To understand the mapping technique, the first thing to remember is that every ion mass has a set of r.f. and d.c. voltages that will produce stable ion trajectories for a given drive frequency and quadrupole dimension. These sets of voltages correspond to the Mathieu parameters (a, q) that result in stable solutions and can be used to map the boundaries of the stability regions. When an operating point (a, q) is chosen, we are effectively choosing the slope of the scan-line used to produce a mass spectrum. Figure 7-1 shows the "stability triangles" associated with mass 32 (oxygen) and mass 40 (argon) for the first stability region. The operating point (a, q) is set near the tip of the triangles for typical operation, and the corresponding scan-line is shown in green. The peak-width of the generated spectrum will be proportional to the overlap of the scan-line and the "stability triangle" so scanning near the tip will produce higher-resolution spectra.
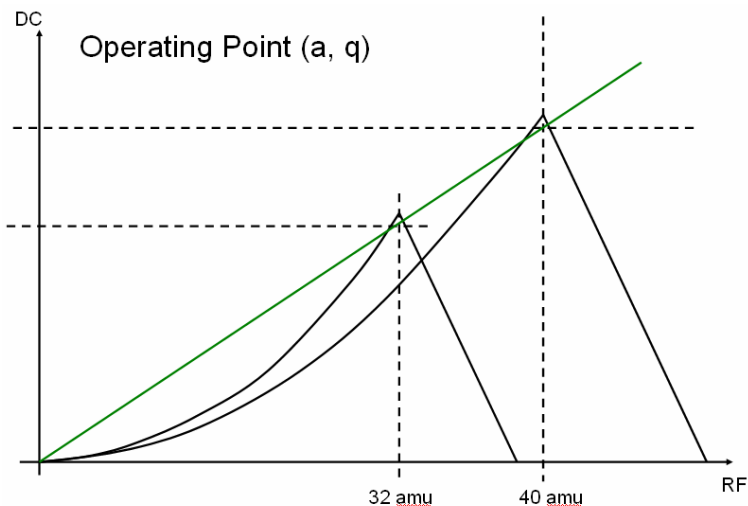
Figure 7-1: Typical scan-line

To perform the mapping, we utilized argon as the analyte since we wanted a single peak in the generated spectrum. Unfortunately, there was a trace leakage of air into the system which led to slight complications during the mapping. After the mass spectrum for argon was properly tuned as described in Chapter 5, we utilized the control software

and manual control of the r.f. gain to locate the stability boundaries. The value for the Mathieu parameter a was kept constant in the testing software, and the r.f. gain was adjusted to increase or decrease the value of the Mathieu parameter q. This adjustment was achieved by changing the amplitude of the function generator signal used in the test system. When the r.f. voltage was increased, the mass peak shifted left due to the tuning of the system and the reverse happened with a decrease in the voltage. The "mass 40" displayed on the collected spectrum corresponds to the actual r.f. voltage applied. While adjusting q, when the transmitted signal at "mass 40" went to zero, we knew we had moved to the edge of the stability boundary. Once these locations were found, the voltages corresponding to "mass 40" were recorded to calculate the respective q values.

In Figure 7-2, we depict the scan-lines (blue) that corresponded to the low-mass edge (left) and high-mass edge (right) of the first stability region when a large value for a was utilized. The green scan-line corresponds to the tuned operating point where "mass 40" is aligned to the center of the detected peak. The high-mass edge was fairly simple to locate due to the larger transmission associated with the scan-line of lower resolution. Conversely, the low-mass edge was a bit more difficult to pinpoint accurately due to the low transmission associated with the higher resolution scan-line.
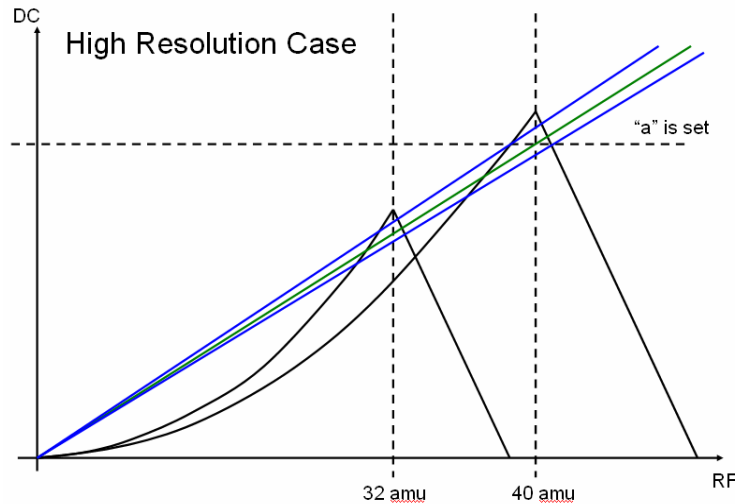
Figure 7-2: High resolution mapping

Another issue with mapping of the low-mass edge occurred because of the trace leakage of air in our test system. At lower values for a, we encountered overlap with the

peaks from oxygen and nitrogen (mass 32 and 28 respectively). Figure 7-3 illustrates the issue in more detail. Determining the high-mass edge was relatively simple, but the low-mass edge now had a signal from the trace oxygen. When locating the value of q where the signal dropped off, we had to change the scan-line to that indicated in red. This change gave an erroneous value for the r.f. voltage associated with the low-mass edge of argon. We encountered this issue again when the signal overlapped with the signal from the trace nitrogen.
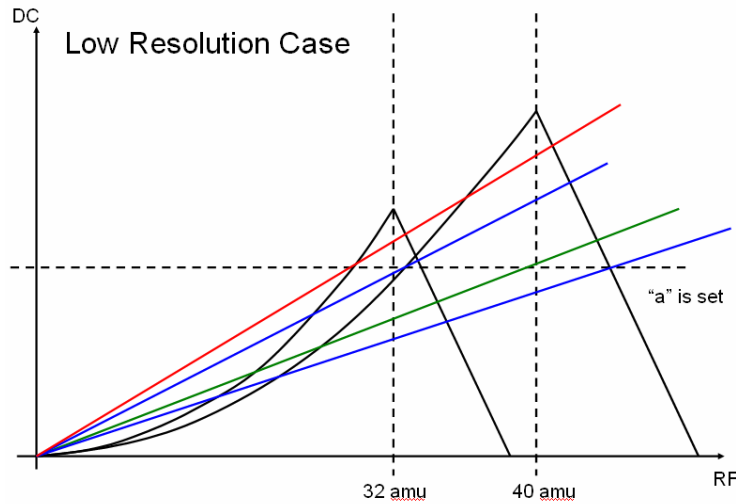
Figure 7-3: Low resolution mapping

7.2.2 First Stability Region

Despite the issues with locating the low-mass edge, we were still able to obtain a general sense of the boundaries for the first stability region. Figure 7-4 shows the results of the mapping technique for operation at 2.0 MHz. We can clearly see the two bumps that correspond to the trace air in the test system. The curvature associated with the low-mass edge of the "stability triangles" is also quite apparent. The important point to note is that the tip of this stability region is centered around $(a, q) = (0.28, 0.7)$, noticeably different from the conventional value of $(a, q) = (0.23, 0.7)$. Another interesting feature of Figure 7-4 is the blunting at the tip of the stability region. The implication of this feature is that we have reached a point where the resolution can't be significantly improved by moving the scan-line closer to the tip. This widening could be a result of

the finite length of the quadrupole or possibly an indicator of poor drive electronic stability. Since the Mathieu stability diagram corresponds to solutions in a quadrupole with infinite length, a quadrupole with finite length will be unable to produce the sharp corners of the stability regions. The maximum resolution that can be achieved is also limited by how accurately the Mathieu parameters can be controlled, which is directly related to drive electronic stability. Another potential reason can be from the square electrode geometry used. Schulte et al. reported that non-linear resonance arising from higher-order field components leads to a widening of the stability tip [71].
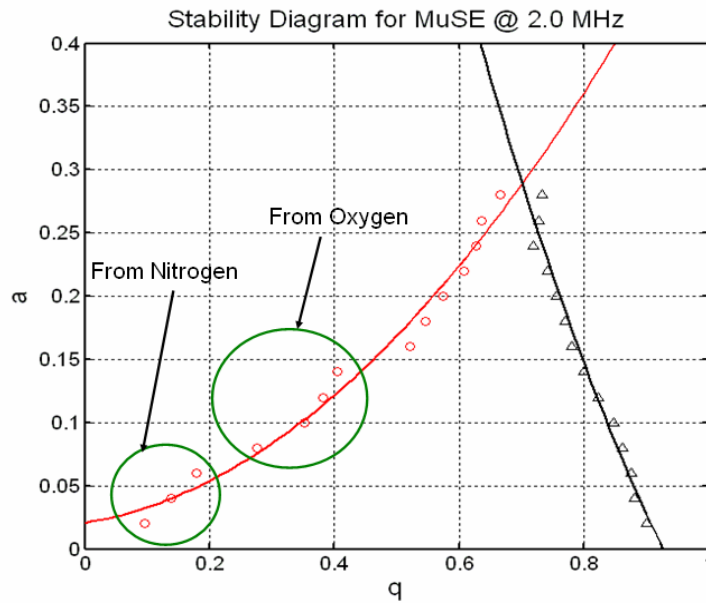
Figure 7-4: First stability region, 2.0 MHz

Mapping of the first stability region was also conducted at 4.0 MHz to provide some additional insight into the ion dynamics of our device. The values for q were calculated factoring in the change to the compensation factor at higher frequencies as mentioned in Chapter 6. If the tip-widening observed was a result of the finite length of the quadrupole, then an increased drive frequency should reduce the widening. Figure 7-5 presents the results of this mapping, and we can see that it is essentially identical to Figure 7-4. We still witnessed the two bumps on the low-mass edge arising from the trace leakage of air, as well as the tip-widening. We might conclude that the finite length of the quadrupole has no effect on the widening observed, but there is another possibility to consider. It is

possible that there are competing phenomena that dictates the width of the stability tip. We would expect a narrowing from operation at higher frequencies due to the effective lengthening of the quadrupole, but as the ions spends more time within the device, non-linear resonances add up that can lead to widening. Ultimately, the tip-width could still be dictated by drive electronic stability.
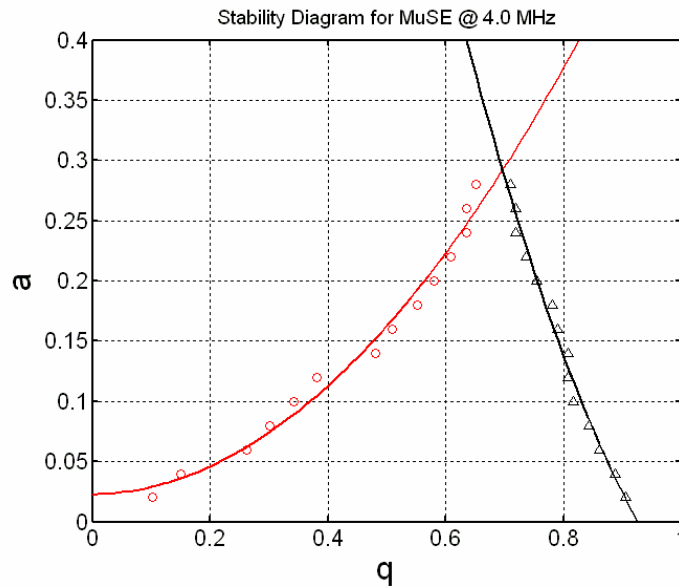
Figure 7-5: First stability region, 4.0 MHz

7.2.3 Second Stability Region

The second stability region at 2.0 MHz was mapped in a similar fashion as described for the first stability region. Issues with low transmission during location of the low-mass edge persisted in this stability region but the problem with the trace leakage of air was removed. Due to the location of the second stability region, there was little chance for the "stability quadrangles" of argon and oxygen to overlap. Figure 7-6 shows the results of this mapping and we can see that the corners are located in slightly different locations than that of the standard Mathieu stability diagram. In the typical Mathieu stability diagram, the bottom edge is located at approximately $(a, q) = (\sim 2.52, 2.77\text{-}2.82)$, while the top edge is located at approximately $(a, q) = (\sim 3.16, 3.2\text{-}3.25)$. Another interesting feature to note is that for a given value of a, the average width of the stability region is similar to the widths seen at the stability tips of Figure 7-4 and 7-5. This can be

124

an indication that the drive electronics are a limiting factor in the performance of the devices. Figure 7-7 plots the first and second stability region with best-fit lines to produce an equivalent Mathieu stability diagram.
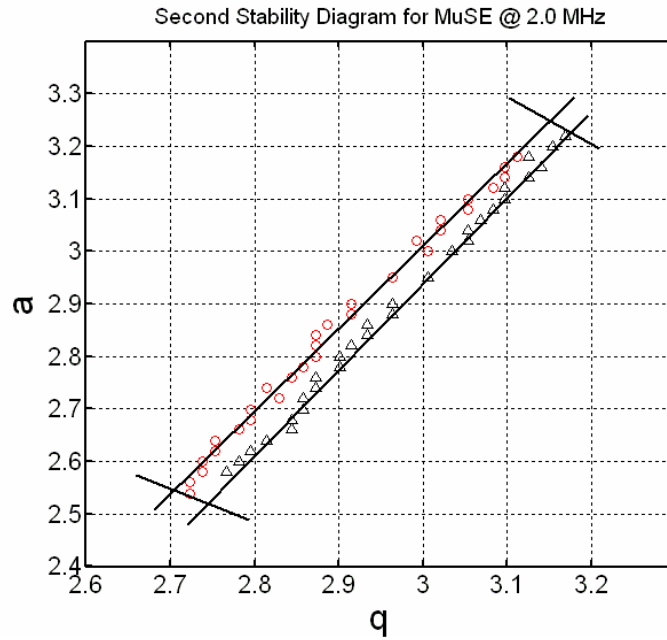
Figure 7-6: Second stability region, 2.0 MHz
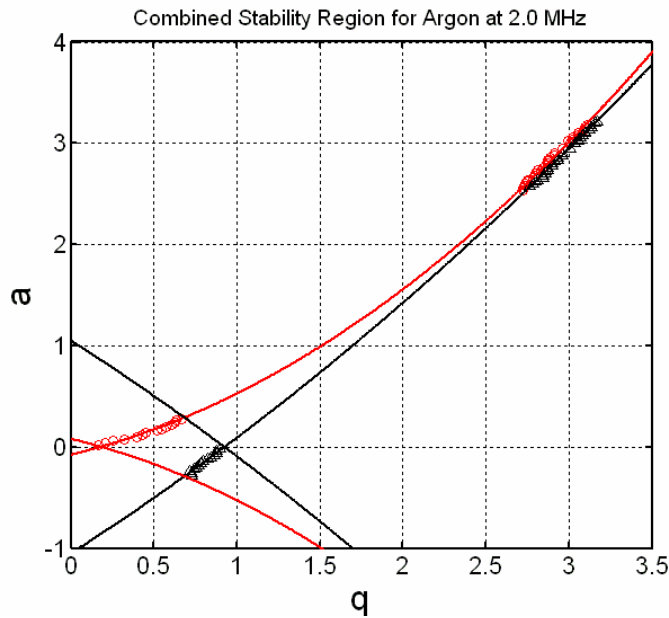
Figure 7-7: Best fit Mathieu stability diagram

7.3   Modified Performance

In attempts to understand the deviation of resolution from the square dependence on frequency, generation of resolution versus transmission (RT) curves were extended to lower frequencies. If the near-linear trend observed was a direct result of excessive non-idealities, then lower frequencies should hopefully show a return to the conventional square dependence. Data was obtained at 1.5 MHz but we found that the peak-shapes were extremely poor and it was difficult to calculate the resolution accurately. The test system was unable to control the low voltages reliably for 1.5 MHz so testing at lower frequencies was not conducted. Figure 7-8 shows the transmission versus resolution curve at 1.5 MHz with a maximum resolution of ~9. This value appears to deviate from the linear dependence established by Figure 6-15 but if we factor in the difference in ion energy, a resolution of ~16.5 is expected. This value is in-line with the linear dependence observed; hinting that this trend may be a result of the geometry used. Unfortunately, more data points will be needed before any final conclusions can be made.
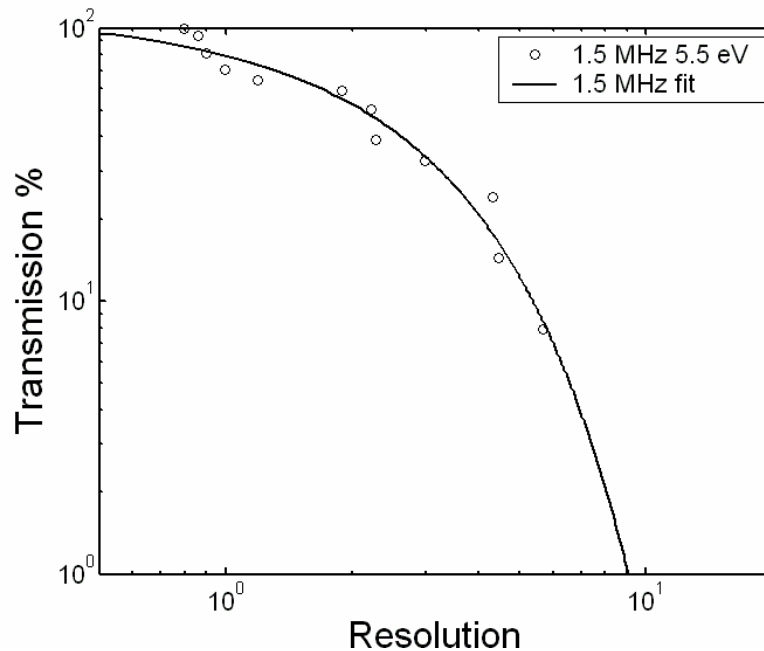
Figure 7-8: Resolution versus transmission curve at 1.5 MHz

To put the performance of the MuSE-QMF in perspective with other MEMS-based quadrupoles in the literature, Table 7-1 was generated. Reported devices have varying dimensions, different operating points and drive frequencies, as well as different analytes. An apple-to-apples comparison was difficult to produce due to these variations. If we look at Equation 2-8, we see that the resolution of the devices should depend on n, the number of r.f. cycles an ion spends in the device. Table 7-1 summarizes the various MEMS-based quadrupoles with (1) the dimensions and operating conditions, (2) the mass range demonstrated M_{max}, (3) the corresponding r.f. peak-to-peak voltage needed to span the mass range V_{pp}, (4) the ion energy E_z, (5) the mass of the ion that was measured m, (6) the calculated number of r.f. cycles n, (7) the maximum measured resolution R, and (8) the predicted maximum resolution R_{pred}. The tabulated values for R correspond to the maximum resolution obtained with a full mass scan. There were reports of higher values where drive electronics were tuned to minimize the peak-width of a single peak. These values were excluded to maintain a better comparison between the different technologies. R_{pred} is calculated using the tabulated values for n assuming $h = 10$ for operation in the first stability region, and $h = 0.7$ for operation in the second stability region.

Device and Operating Condition	M_{max}	V_{pp}	E_z	m	n	R	R_{pred}
Geear 6 MHz, SR1 (0.5 mm x 30 mm)	400	~130	10.0	69	34.055	86.25	116.95
Taylor 6 MHz, SR1 (0.5 mm x 30 mm)	50	~16	10.0	40	25.929	30.77	67.80
Velasquez-Garcia 1.44 MHz, SR1 (1.58 mm x 90 mm)	650	~121	13.6	69	21.025	36.32	44.23
Velasquez-Garcia 2.0 MHz, SR1 (1.58 mm x 90 mm)	50	~18	13.6	28	18.602	28.00	34.57
Velasquez-Garcia 4.0 MHz, SR1 (1.58 mm x 90 mm)	50	~40	13.0	28	38.053	40.00	147.37
Velasquez-Garcia 2.0 MHz, **SR2** (1.58 mm x 90 mm)	50	~77	60.0	28	8.856	70.00	112.00

Velasquez-Garcia 4.0 MHz, SR1 (1.00 mm x 37 mm)	250	~143	40.0	69	14.000	17.25	19.60
Cheung 1.5 MHz, SR1 (1.414 mm x 30 mm)	50	~10	5.5	40	8.741	8.89	7.63
Cheung 1.8 MHz, SR1 (1.414 mm x 30 mm)	650	~192	3.5	69	17.269	19.17	29.87
Cheung 2.0 MHz, SR1 (1.414 mm x 30 mm)	50	~18	3.0	28	13.202	18.66	17.39
Cheung 3.0 MHz, SR1 (1.414 mm x 30 mm)	50	~37	3.0	28	19.803	21.54	39.44
Cheung 4.0 MHz, SR1 (1.414 mm x 30 mm)	50	~58	3.0	40	31.559	40.00	100.00
Cheung 1.5 MHz, **SR2** (1.414 mm x 30 mm)	50	~44	8.0	28	6.064	20.00	52.83
Cheung 2.0 MHz, **SR2** (1.414 mm x 30 mm)	50	~78	5.0	40	12.223	80.00	210.53
Cheung @ Ardara 3.8 MHz, SR1 (1.414 mm x 30 mm)	50	n/a	5.0	28	19.430	23.93	37.84
Cheung @ Ardara 2.95 MHz, SR1 (1.414 mm x 30 mm)	50	n/a	4.5	40	19.004	16.67	36.04
Cheung @ Ardara 1.98 MHz, SR1 (1.414 mm x 30 mm)	250	n/a	15.8	69	8.940	9.08	8.00
Cheung @ Ardara 1.98 MHz, **SR2** (1.414 mm x 30 mm)	50	n/a	18.0	28	5.336	40.00	40.58
1Cheung @ Ardara 1.98 MHz, **SR2** (1.414 mm x 30 mm)	50	n/a	24.0	40	5.523	35.09	43.48

Table 7-1: Summary of MEMS-based QMFs [23], [27], [47]

Figure 7-9 was generated to obtain a better sense of the relative performance of the reported devices. From Equation 2-8, namely $R = n^2/h$, we see that if we plot the

resolution as a function of n^2, h can be utilized as a performance figure of merit. If h is small, we have a high-performance device since less r.f. cycles are needed for a certain resolution. Conversely, large values for h will correspond to low performance devices. If we plot Equation 2-8 on a log-log plot, high-performance devices will fall on the top-left corner while low performance devices will fall on the bottom-right corner. The solid lines in Figure 7-9 correspond to the range of h values reported in the literature for the first stability region and the dashed lines correspond to the range of values reported for the second stability region [1]. From the data, we see that the MEMS-based quadrupoles all fall near the range of reported h values in the literature.
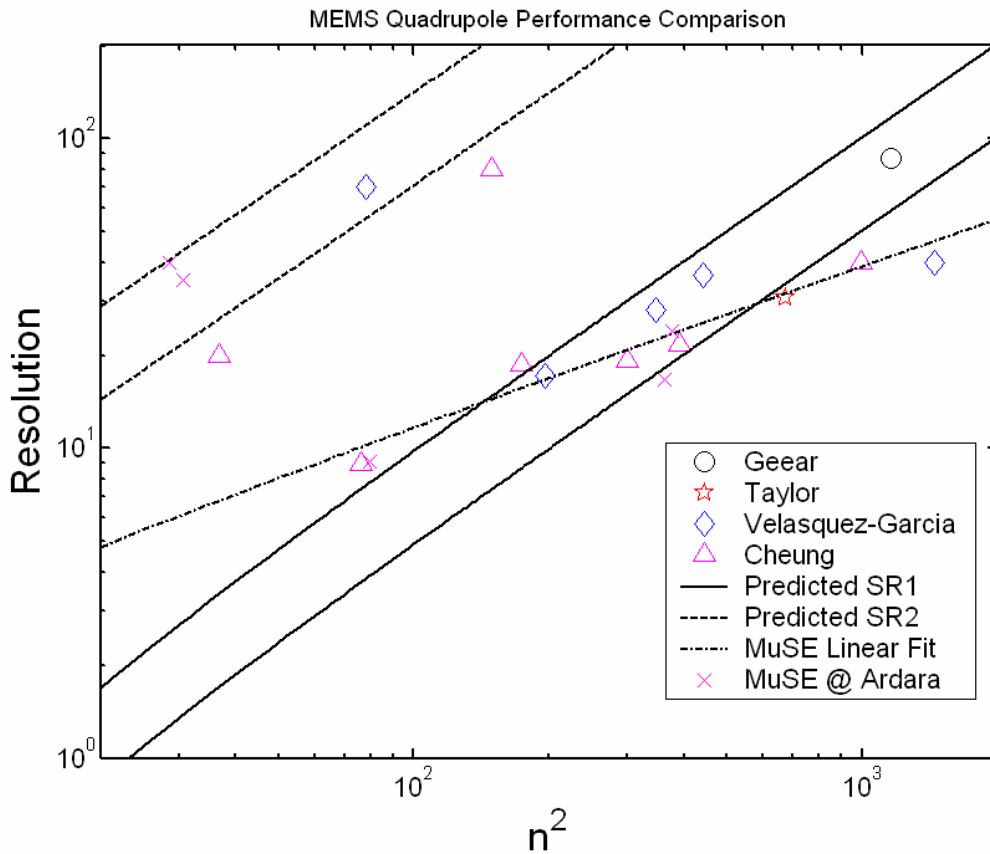
Figure 7-9: Performance comparisons of MEMS-based QMFs [23], [27], [47]

Looking at the MuSE-QMF data in the first stability region, we see that a best-fit line reveals a linear dependence with n. This result is consistent with what was observed in the RT curves of Figure 6-15, making the case for modified performance with the square

129

electrode geometry. An implication of this observation is that our devices will not be able to match the performance of other MEMS-based quadrupoles at higher frequencies, corresponding to larger values of n. In Chapter 6, we demonstrated that it is more beneficial for the MuSE-QMF to operate in the second stability region. Fortunately, the second stability region appears to maintain the squared dependence on frequency but more data points will be needed to see if the trend continues. Overall, the MuSE-QMF demonstrated the best performance to date if we utilize the value for h as a figure of merit. Additionally, the device was able to demonstrate similar maximum resolution as some of the other reported quadrupoles.

7.4   Summary

In this chapter, we presented some experimental work that was conducted to explore the possibility of new ion dynamics of the MuSE-QMF. We utilized a mapping technique to identify the boundaries of the stability regions of interest and located points that correspond to high-resolution operation. These points are located in areas that are slightly different from what was expected using the standard Mathieu stability diagram. Additionally, there was evidence of modified performance which limits the utility of the MuSE-QMF at higher frequencies. Fortunately, operation in the second stability region still appeared promising. Detailed studies with simulations and investigation with a machined square electrode QMF can provide more insights into the modified performance. Overall, the devices have demonstrated performance equal to or better than other MEMS-based quadrupoles but with the added benefit of being entirely batch-fabricated.

Chapter

8

Conclusions and Future Work

8.1   Conclusions

In this thesis, we presented the design, fabrication, and characterization of a chip-scale quadrupole mass filter for a Micro-Gas Analyzer. The post-fabrication assembly required of other MEMS-based quadrupoles served as a bottleneck to mass production and introduced electrode-to-housing misalignments.   To address these issues, the integration of the quadrupole electrodes, the ion optics, and the device housing was proposed. This integration was achieved through the use of an unconventional square electrode geometry which called for optimization and analysis.

A first generation of the conceived devices showed proof-of-concept mass filtering with square electrode geometry. Lessons learned throughout the processing and testing of the first generation devices led to an improved process flow utilized in the second generation. The new process flow increased processing yield substantially and the total process time required was decreased. Additionally, the simplicity of the new fabrication steps has the potential to establish this technology as a low-cost method to produce micro-square electrode quadrupole mass filters (MuSE-QMFs).

Testing the second generation of devices demonstrated the functionality of integrated ion optics with non-standard geometry, as well as showing improved performance over the first generation. Experimental data suggested some new ion dynamics associated with the square electrode geometry and limitations of the design were also identified. Overall, the MuSE-QMF performed equal to or better than the other MEMS-based

quadrupoles but with the benefit of being entirely batch fabricated. Furthermore, the device concept is very flexible and can be extended to much more complex architectures that are not readily achievable with the other reported technologies.

This thesis establishes the MuSE-QMF as a high-performance and cost-effective technology for mass filtering. The flexibility associated with the design concept can lead to device evolutions which can significantly impact the field of portable mass spectrometry. Eventually, the reported devices will pave the way for ubiquitous gas sensors that are fast, reliable, and affordable. Potential applications for versatile chemical sensor demand further investigation of the MuSE-QMF.

8.2   Future Work

Despite the promising results presented in this thesis, there are many avenues for improvement that can be pursued as future work. One of the main issues that were encountered was the large parasitic capacitance associated with the design. A new version of the device that utilizes a different mask set can readily decrease this unwanted capacitance. Other than the device design, there can be many improvements made to the drive electronics. We were not able to fully gauge the ultimate performance of the MuSE-QMF due to stability and linearity limitations in the electronics. Additional work with more in-depth simulations can also provide deeper insights into the ion dynamics associated with the square electrode geometry. Finally, we would like to integrate the ionizers and the detectors of the Micro-Gas Analyzer project with the quadrupole to see how the components work together.

8.2.1   MuSE version 2.0 and beyond

A new version of the MuSE-QMF has been proposed that has two significant changes made to the design. The first change is reducing the wafer thicknesses of the electrode and aperture wafers so that the effective aperture diameter will be 1.000 mm instead of 1.414 mm. The other modification is to change the mask layouts to reduce the parasitic capacitances in the device. In this new design, the electrode-to-housing spacing will be increased from 100 μm to 250 μm and the electrode contact pads will be made a factor of

10 smaller. This modification will effectively decrease the parasitic capacitance of the device by a factor of 10. Additional features added to device are the inclusion of pre-filters for enhanced transmission, and the placement of the Einzel lens farther away from the quadrupole. The extra distance will improve the focusing abilities of the Einzel lens. The processing of MuSE version 2.0 is identical to what has been outlined in Chapter 6 so minimal process development will be needed. Figure 8-1 shows the ELECTRODE mask layer to highlight the changes in the new version, but a more thorough mask set is included in Appendix B.
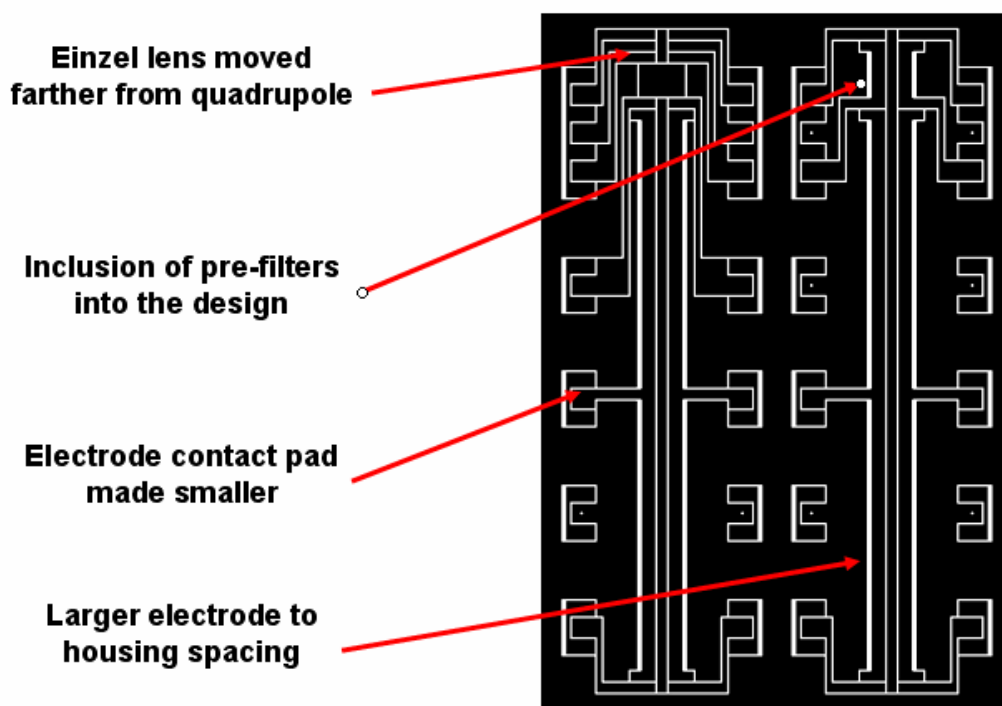
Figure 8-1: Electrode mask for MuSE version 2.0

For future versions of the MuSE, we can conceive of implementing rectilinear ion traps [93]-[95] on the front end of the device or quadrupoles in tandem [100]. The rectilinear ion trap will be useful for the analysis of limited species. Quadrupoles have certain r.f. phases where the transmission is maximized [1], [78]. If we can trap and release the analyte at the appropriate r.f. phase, more of the analyte will make it to the detector thus decreasing the amount of analyte needed to produce a spectrum. For quadrupoles in tandem, Du and Douglas reported an increase in resolution by a factor of

10 by utilizing the reported configuration [101]. They suggested tandem operation as a method to achieve high-resolution spectra with low-precision quadrupoles. The performance depended on the proximity and alignment of the devices, but these criteria are readily met with the MuSE-QMF technology.

If the device continues to scale-down, we may need to utilize silicon-on-insulator (SOI) wafers. From the optimization work conducted in this thesis, we know that having the electrodes larger than the aperture will not be detrimental to performance. The limiting factor in scaling-down will be the fragility of the aperture wafer during processing. To address this issue, we can imagine using two double-side polished SOI wafers to form the electrodes and the aperture. The device layer of the SOI wafers can be bonded together after it has been patterned to define the aperture, and the handle wafers can then be patterned to form the electrodes. This new processing should be explored for devices with an aperture diameter smaller than 500 μm.

More exotic improvements to the device design can involve bonding with sub-micron precision [111] and silicon rounding with hydrogen [112]. We can imagine rounding the edges of our square electrodes with hydrogen to enhance device performance. Implementing these two improvements will require substantially more complex fabrication steps that might not be desired.

8.2.2 Electronics

For the drive electronics, we can implement most or all of the suggestions made in Chapter 5 regarding the test setup. The improvement in the hardware will address the linearity and stability issues encountered throughout testing. This will enable proper evaluation of the ultimate capabilities of the MuSE-QMF and possibly address the tip-widening mentioned in Chapter 7.

Other enhancements that can be made with electronics are through the control and optimization of the drive signals. Sheretov reported opportunities for improved performance through optimization of the applied r.f. signal [113]. On a different note, Konenkov et al. reported that the addition of an auxiliary field to a quadrupole can produce stability islands as shown in Figure 8-2. Scan-lines through these stability

islands have demonstrated improved resolution [114], [115]. We can imagine utilizing these methods to enhance the performance of the MuSE-QMF.
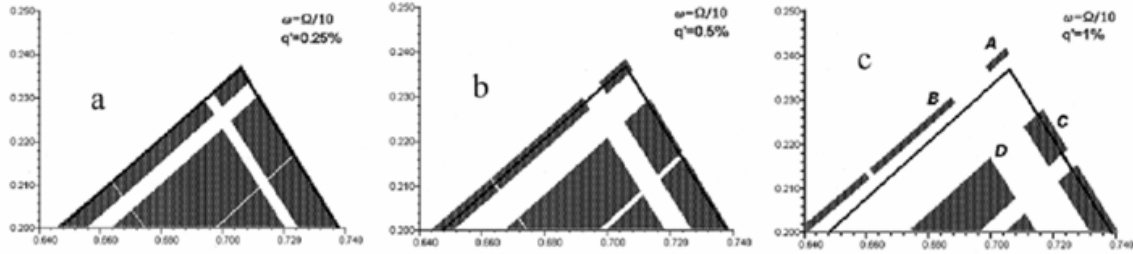
Figure 8-2: Stability islands with auxiliary drive signals [114]

8.2.3   Improved Studies

With the improvements in the drive electronics and a new device with less parasitic capacitance, we can perform more accurate experimental studies on the capabilities of the MuSE-QMF. Simulations should be conducted alongside these experiments for a more complete understanding of the device. We can continue collaboration with Steve Taylor and Tom Hogan at the University of Liverpool to develop a model of the ion dynamics for square electrode geometries. Eventually, we would like to have an understanding of the physics of operation to guide future designs. There are a wealth of simulation techniques and tools used for quadrupole mass filters [116], [117] that can be explored. Ding et al. have also reported improvements in performance through the deliberate introduction of octopole fields [118]. Numerical or analytical studies conducted on how rectangular electrode geometries (which introduces octopole terms) affect device performance will be an interesting avenue to pursue.

8.2.4   Integration

Since the ultimate goal of the work presented in this thesis is to achieve a portable mass spectrometer, integration with other microfabricated components developed in the Micro-Gas Analyzer project will be a logical step. Other than demonstrating how the various components work together, we will also be able to operate at a higher pressure. The current test setup is limited to ~10^{-5} Torr due to lifetime concerns of the ionizer. If

we can utilize the microfabricated field ionizers, we can operate up to the milliTorr regime. This capability will allow us to obtain information on how the quadrupole performance changes as a function of pressure.

8.3   Contributions

The main contributions of this thesis are as follows:

(1) We designed, fabricated, and characterized a chip-scale quadrupole mass filter that was achieved entirely through wafer-scale processing. A high-yield process flow was developed that can potentially produce these devices at relatively low costs.

(2) We reported for the first time, a functional quadrupole mass filter with square electrodes that have performance equal to or better than other MEMS-based quadrupoles. The devices demonstrated a mass range of 650 amu at 1.8 MHz, a peak-width of 1.0 at mass 40 in the first stability region at 4.0 MHz, and a peak-width of 0.5 at mass 40 in the second stability region at 2.0 MHz.

(3) We demonstrated functional integrated ion optics with unconventional geometry. The design concept can be extended to more advanced architectures such as pre-filters, post-filters, rectilinear ion traps, tandem quadrupoles, and many other configurations that can lead to enhanced performance.

(4) We identified some new ion dynamics associated with the square electrode geometry, motivating further investigation of quadrupoles with non-ideal electrodes. Operation in the second stability region was also shown to be advantageous for the reported geometry.

Appendix

A

Process Flows

The following list is the process flow for MuSE-QMF version 1.0. All fabrication steps were conducted at MIT's Microsystems Technology Laboratories so the tool names and protocols listed correspond to those specified at the facilities.

Starting material (150 mm diameter wafers with 0.3 μm of thermal oxide):

Wafer name (Quantity)	Thickness	Polish	Dopant	Resistivity
ELECTRODE (2)	1000 ± 10 μm	DSP	Sb	5-20 mΩ·cm
CAP (2)	500 ± 5 μm	DSP	Sb	5-20 mΩ·cm
APERTURE (1)	1000 ± 10 μm	DSP	Sb	5-20 mΩ·cm

Place Alignment Marks (ELECTRODE, CAP, APERTURE wafers)

HMDS		HMDS Oven	TRL
Spin thin Resist (2000 rpm)		Coater	TRL
prebake (10 min)		Prebake Oven	TRL
Spin thin Resist (2000 rpm)	on back-side	Coater	TRL
prebake (30 min)		Prebake Oven	TRL
Expose - ALIGNMENT (MASK0)		EV1	TRL
Develop		Photowet	TRL
Postbake (30 min)		Postbake	TRL
BOE Pattern (~0.07 microns/min)	5 min	BOE	ICL
Etch Alignment (60 sec)	Black-Si	LAM 490	ICL
Piranha Wafer Clean		Acid Hood	TRL
HMDS		HMDS Oven	TRL
Spin thin Resist (2000 rpm)		Coater	TRL
prebake (10 min)		Prebake Oven	TRL
Spin thin Resist (2000 rpm)	on patterned side	Coater	TRL
prebake (30 min)		Prebake Oven	TRL

Expose - ALIGNMENT (MASK0)	back-side align	EV1	TRL
Develop		Photowet	TRL
Postbake (30 min)		Postbake	TRL
BOE Pattern (~0.07 microns/min)	5 min	BOE	ICL
Etch Alignment (60 sec)	Black-Si	LAM 490	ICL
Piranha Wafer Clean		Acid Hood	TRL
Asher	60 min	Asher	TRL

Define Cap Trenches and Contact Vias (CAP wafers)

HMDS		HMDS Oven	TRL
Spin thick Resist (1500 rpm)		Coater	TRL
prebake (20 min)		Prebake Oven	TRL
Spin thick Resist (1500 rpm)	on back-side	Coater	TRL
prebake (60 min)		Prebake Oven	TRL
Expose – CAP TRENCH (MASK1)		EV1	TRL
Expose – CONTACT VIAS (MASK2)	on back-side		
Simultaneous Develop		Photowet	TRL
Postbake (30 min)		Postbake	TRL
BOE Pattern (~0.07 microns/min)	5 min	Acidhood2	TRL
Etch MASK1 (100 μm)	JBETCH	STS3	TRL
Target Mount on Quartz		Coater	TRL
Etch MASK2 (Through-wafer)	JBETCH	STS3	TRL
Acetone Dismount		Photowet	TRL
Piranha Wafer Clean		Acid Hood	TRL
Asher	60 min	Asher	TRL

Grow Insulating Oxide (CAP wafers)

HF Strip Protective Oxide		Acidhood2	TRL
RCA Clean		RCA	TRL
Grow thermal oxide (1 μm)		Tube A2	TRL

Form a Protective Nitride Layer on One Side (ELECTRODE wafers)

Piranha		Acidhood2	TRL
RCA Clean		RCA	TRL
VTR Nitride (250 nm)		VTR	ICL
Etch One Side of Nitride (3.5 min)	Nitride-on-Ox	LAM 490	ICL
Piranha		Acidhood2	TRL
Asher	60 min	Asher	TRL

Define Electrodes (CAP, ELECTRODE wafers)

Strip exposed protective oxide on ELECTRODE wafers with BOE	5 min	Acidhood2	TRL
RCA Clean (ELECTRODE and CAP wafers)	no HF dip	RCA	TRL
Align CAP wafer to ELECTRODE wafer		Aligner	TRL
Fusion Bond Silicon to Oxide, overnight	2500 N	Bonder	TRL
Anneal Bond	1000 C	Tube B3	TRL
HMDS		HMDS Oven	TRL
Spin thick Resist (1500 rpm)	on nitride side	Coater	TRL
Expose - ELECTRODES (MASK3)		EV1	TRL
Develop		Photowet	TRL
Postbake (30 min)		Postbake	TRL
Etch MASK3 (nitride)	SF6	STS3	TRL
Remove underlying oxide (BOE)	5 min	Acidhood2	TRL
Target Mount on Quartz		Coater	TRL
Etch MASK3 (Through-wafer)	JBETCH	STS3	TRL
Acetone Dismount		Photowet	TRL
Piranha Wafer Clean		Acid Hood	TRL
Asher	60 min	Asher	TRL

Define Aperture (APERTURE wafers)

RCA Clean		RCA	TRL
Deposit Oxide Hard Mask	4 μm, both-sides	DCVD	ICL
HMDS		HMDS Oven	TRL
Spin thick Resist (1500 rpm)		Coater	TRL
prebake (20 min)		Prebake Oven	TRL
Spin thick Resist (1500 rpm)	on back-side	Coater	TRL
prebake (60 min)		Prebake Oven	TRL
Expose – APERTURE TRENCH (MASK4)		EV1	TRL
Expose – APERTURE TRENCH (MASK4)	on back-side		
Simultaneous Develop		Photowet	TRL
Postbake (30 min)		Postbake	TRL
Etch MASK4 (Pattern Oxide)	both sides	AME5000	ICL
Piranha Clean		Acid Hood	TRL

HMDS		HMDS Oven	TRL
Spin thick Resist (1500 rpm)		Coater	TRL
prebake (20 min)		Prebake Oven	TRL
Spin thick Resist (1500 rpm)	on back-side	Coater	TRL
prebake (60 min)		Prebake Oven	TRL
Expose - APERTURE (MASK5)		EV1	TRL
Expose - APERTURE (MASK5)	on back-side		
Simultaneous Develop		Photowet	TRL
Postbake (30 min)		Postbake	TRL
Etch MASK5 (400 μm)	JBETCH, both-sides	STS3	TRL
Piranha Wafer Clean		Acid Hood	TRL
Asher	60 min	Asher	TRL
Etch wafer with hard mask (100 μm)	JBETCH	STS3	TRL
Target Mount on Quartz	etched-side down	Coater	TRL
Etch wafer with hard mask (100 μm)	JBETCH	STS3	TRL
Acetone Dismount		Photowet	TRL
Piranha Wafer Clean		Acid Hood	TRL
Asher	60 min	Asher	TRL

Bond Final Device (APERTURE, CAP+ELECTRODE wafers)

Remove nitride on CAP+ELECTRODE wafers	hot phosphoric	Nitride	ICL
Remove protective oxide on CAP+ELECTRODE stacks with BOE	5 min	Acidhood2	TRL
Remove all oxide on APERTURE wafer	HF	Acidhood2	TRL
RCA Clean all wafers	no HF Dip	RCA	TRL
Align APERTURE to ELECTRODE+CAP		Aligner	TRL
Align ELECTRODE+CAP to STACK		Aligner	TRL
Silicon Fusion Bond overnight	2500 N	Bonder	TRL
Anneal Bond	1000 C	Tube B3	TRL
Die Saw	mode G	Diesaw	ICL

The following list is the process flow for MuSE-QMF version 1.5. All fabrication steps were conducted at MIT's Microsystems Technology Laboratories so the tool names and protocols listed correspond to those specified at the facilities.

Starting material (150 mm diameter wafers with 0.5 μm of thermal oxide):

Wafer name (Quantity)	Thickness	Polish	Dopant	Resistivity
ELECTRODE (2)	1000 ± 10 μm	DSP	Sb	5-20 mΩ·cm
CAP (2)	500 ± 5 μm	DSP	Sb	5-20 mΩ·cm
APERTURE (1)	1000 ± 10 μm	DSP	Sb	5-20 mΩ·cm

Place Alignment Marks (ELECTRODE, CAP, APERTURE wafers)

HMDS		HMDS Oven	TRL
Spin thin Resist (2000 rpm)		Coater	TRL
prebake (10 min)		Prebake Oven	TRL
Spin thin Resist (2000 rpm)	on back-side	Coater	TRL
prebake (30 min)		Prebake Oven	TRL
Expose - ALIGNMENT (MASK0)		EV1	TRL
Develop		Photowet	TRL
Postbake (30 min)		Postbake	TRL
BOE Pattern (~0.07 microns/min)	7 min	BOE	ICL
Etch Alignment (60 sec)	Black-Si	LAM490	ICL
Piranha Wafer Clean		Acid Hood	TRL
Asher	60 min	Asher	TRL
HMDS		HMDS Oven	TRL
Spin thin Resist (2000 rpm)		Coater	TRL
prebake (10 min)		Prebake Oven	TRL
Spin thin Resist (2000 rpm)	on patterned side	Coater	TRL
prebake (30 min)		Prebake Oven	TRL
Expose – ALIGNMENT (MASK0)		EV1	TRL
Develop		Photowet	TRL
Postbake (30 min)		Postbake	TRL
BOE Pattern (~0.07 microns/min)	7 min	BOE	ICL
Etch Alignment (60 sec)	Black-Si	LAM490	ICL
Piranha Wafer Clean		Acid Hood	TRL
Asher	60 min	Asher	TRL

Grow Oxide and Protective Nitride (ELECTRODE, CAP, APERTURE wafers)

Strip Protective Oxide	HF	TRL
RCA Clean	RCA	TRL
Grow thick insulating oxide (2.5 μm)	Tube A2	TRL
Deposit Low-Stress Nitride (250 nm)	VTR	ICL

Define Cap Trench and Contact Vias (CAP wafers)

HMDS		HMDS Oven	TRL
Spin thick Resist (1500 rpm)		Coater	TRL
prebake (20 min)		Prebake Oven	TRL
Spin thick Resist (1500 rpm)	on back-side	Coater	TRL
prebake (60 min)		Prebake Oven	TRL
Expose – CAP TRENCH (MASK1)		EV1	TRL
Expose – CONTACT VIAS (MASK2)	on back-side	EV1	TRL
Simultaneous Develop		Photowet	TRL
Postbake (30 min)		Postbake	TRL
Etch nitride on both-sides (3.5 min each)	Nitride-on-Ox	LAM490	ICL
Etch thick thermal oxide	both-sides	AME5000	ICL
Etch MASK1 (100 μm)	KERRY	STS3	TRL
Target Mount on Quartz		Coater	TRL
Etch MASK2 (Through-wafer)	KERRY	STS3	TRL
Acetone Dismount		Photowet	TRL
Piranha Wafer Clean		Acid Hood	TRL
Asher	60 min	Asher	TRL

Prepare Electrode Wafers (ELECTRODE wafers)

HMDS		HMDS Oven	TRL
Spin thick Resist (1500 rpm)		Coater	TRL
prebake (20 min)		Prebake Oven	TRL
Spin thick Resist (1500 rpm)	on back-side	Coater	TRL
prebake (60 min)		Prebake Oven	TRL
Expose – OXIDE ETCH (MASK1)		EV1	TRL
Expose – OXIDE ETCH (MASK1)	on back-side	EV1	TRL
Simultaneous Develop		Photowet	TRL
Postbake (30 min)		Postbake	TRL
Etch nitride on both-sides (3.5 min each)	Nitride-on-Ox	LAM490	ICL
Etch thick thermal oxide	both-sides	AME5000	ICL
Piranha Wafer Clean		Acid Hood	TRL
Asher	60 min	Asher	TRL
		Pre-metal	
Piranha and HF dip		Piranha	ICL
Deposit silicon rich nitride on top-side	1.4 μm	DCVD	ICL

Produce ELECTRODE+CAP Stack (CAP, ELECTRODE wafers)

Timed strip of nitride on CAP and ELECTRODE	300 nm removal	HotPhos	ICL
Prep wafers for bonding		RCA	TRL
Align wafers		EV620	TRL
Bond wafers overnight	2500 N	EV501	TRL
Anneal wafers (60 min)	1000 C	Tube B3	TRL
HMDS		HMDS Oven	TRL
Spin thick Resist (1500 rpm)		Coater	TRL
prebake (60 min)		Prebake Oven	TRL
Expose - ELECTRODES (MASK3)	on nitride side	EV1	TRL
Develop		Photowet	TRL
Postbake (30 min)		Postbake	TRL
Etch nitride (3.5 min)	Nitride-on-Ox	LAM490	ICL
Etch thick thermal oxide		AME5000	ICL
Target Mount on Quartz		Coater	TRL
Etch MASK3 (through-wafer)	KERRY	STS3	TRL
Acetone Dismount		Photowet	TRL
Piranha Wafer Clean		Acid Hood	TRL
Asher	60 min	Asher	TRL

Define Aperture (APERTURE wafers)

HMDS		HMDS Oven	TRL
Spin thick Resist (1500 rpm)		Coater	TRL
prebake (20 min)		Prebake Oven	TRL
Spin thick Resist (1500 rpm)	on back-side	Coater	TRL
prebake (60 min)		Prebake Oven	TRL
Expose - APERTURE (MASK4)		EV1	TRL
Expose - APRETURE (MASK4)	on back-side	EV1	TRL
Simultaneous Develop		Photowet	TRL
Postbake (30 min)		Postbake	TRL
Etch nitride on both-sides (3.5 min each)	Nitride-on-Ox	LAM490	ICL
Etch thick thermal oxide	both-sides	AME5000	ICL
Etch MASK4 (500 μm)	KERRY	STS3	TRL
Target Mount on Quartz		Coater	TRL
Etch MASK4 (500 μm) (backside)	KERRY	STS3	TRL
Acetone Dismount		Photowet	TRL
Piranha Wafer Clean		Acid Hood	TRL
Asher	60 min	Asher	TRL

Bond Final Device (APERTURE, CAP+ELECTRODE wafers)

Remove nitride on CAP+ELECTRODE wafers	extended time	HotPhos	ICL
Remove nitride on APERTURE wafer	extended time	HotPhos	ICL
RCA Clean	no HF Dip	RCA	TRL
Align APERTURE to ELECTRODE+CAP		EV620	TRL
Align ELECTRODE+CAP to STACK		EV620	TRL
Silicon Direct Bond	2500 N	EV501	TRL
Anneal Bond	1000 C	Tube B3	TRL
Die Saw	mode G	Diesaw	ICL

Appendix
B

Mask Layouts
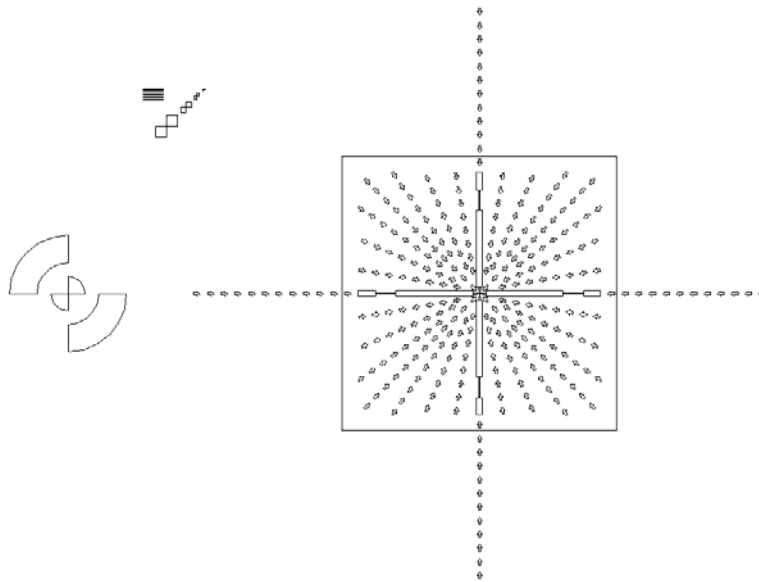
Figure B-1: Initial alignment marks (detailed)
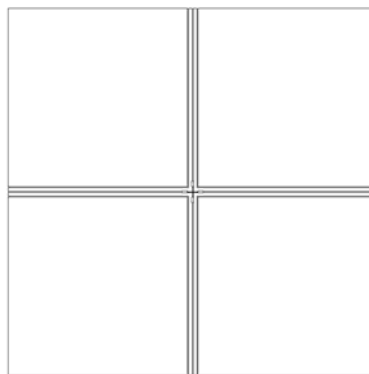
Figure B-2: Alignment marks on subsequent masks (detailed)

Cheung MGA
Alignment
Quad v.01
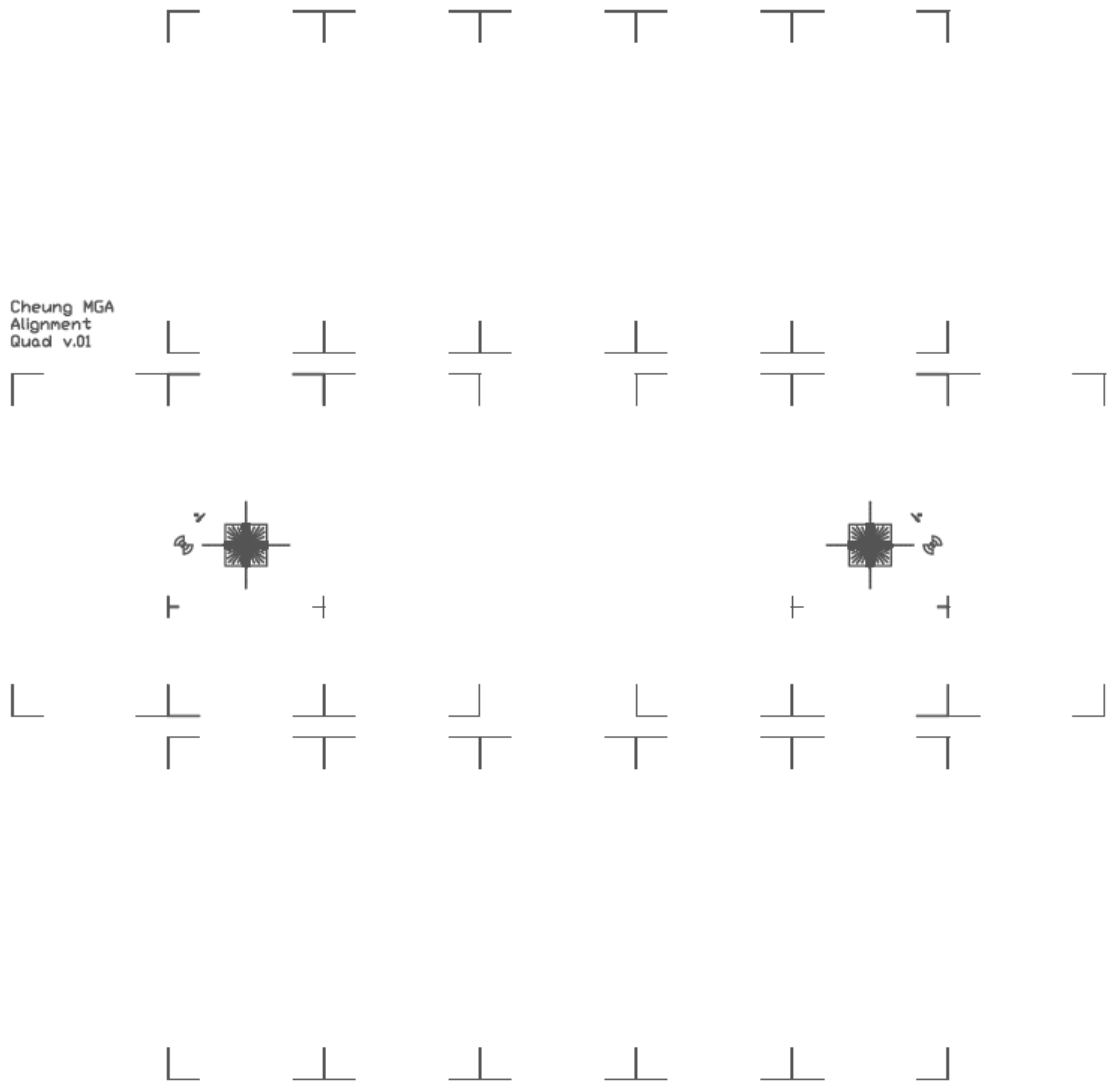
Figure B-3: ALIGNMENT mask for MuSE v. 1.0 and 1.5

Cheung MGA
Cap Trench
Quad v.01
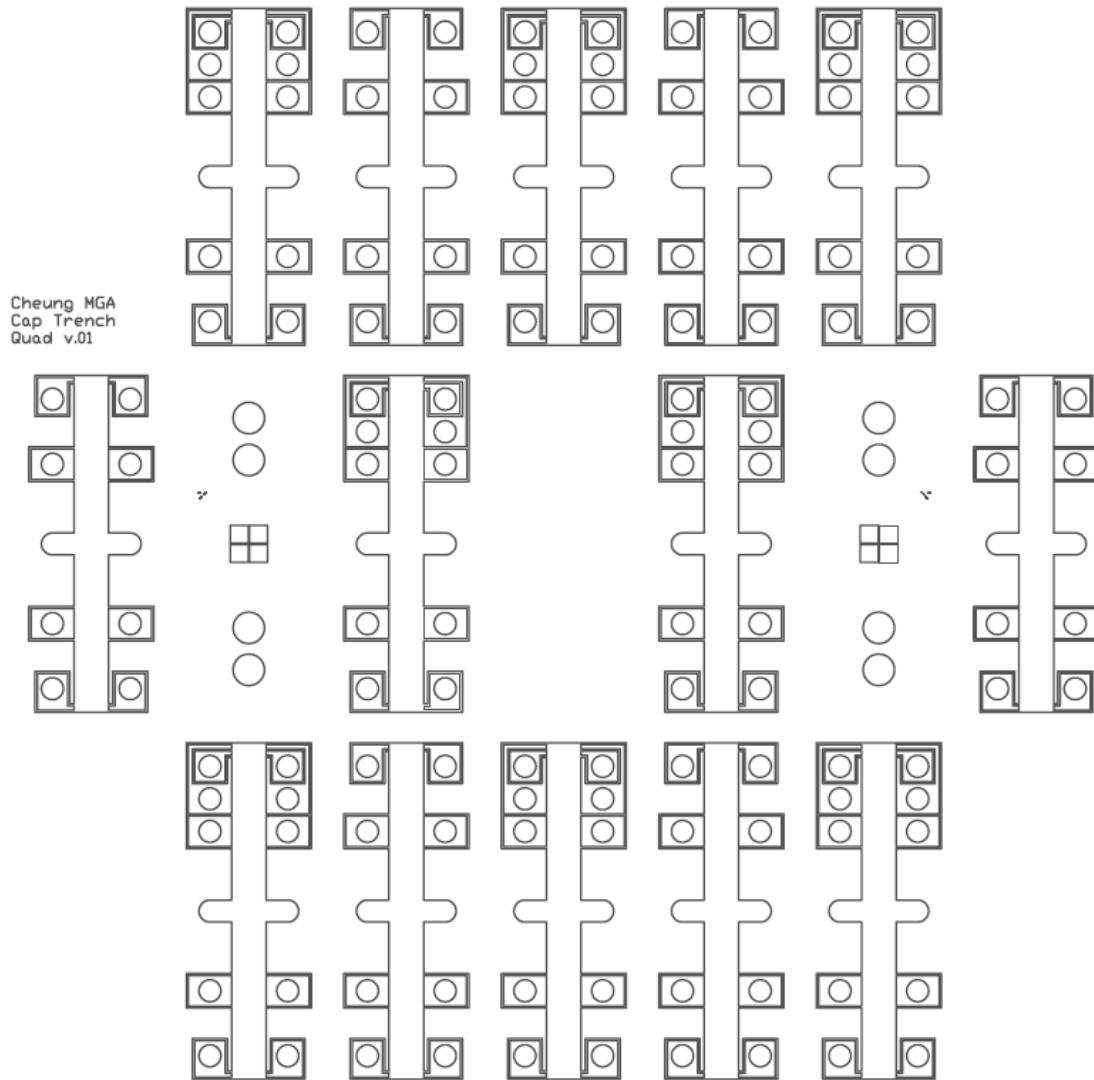
Figure B-4: CAP TRENCH & OXIDE ETCH mask for MuSE v. 1.0 and 1.5

Cheung MGA
Through Vias
Quad v.01
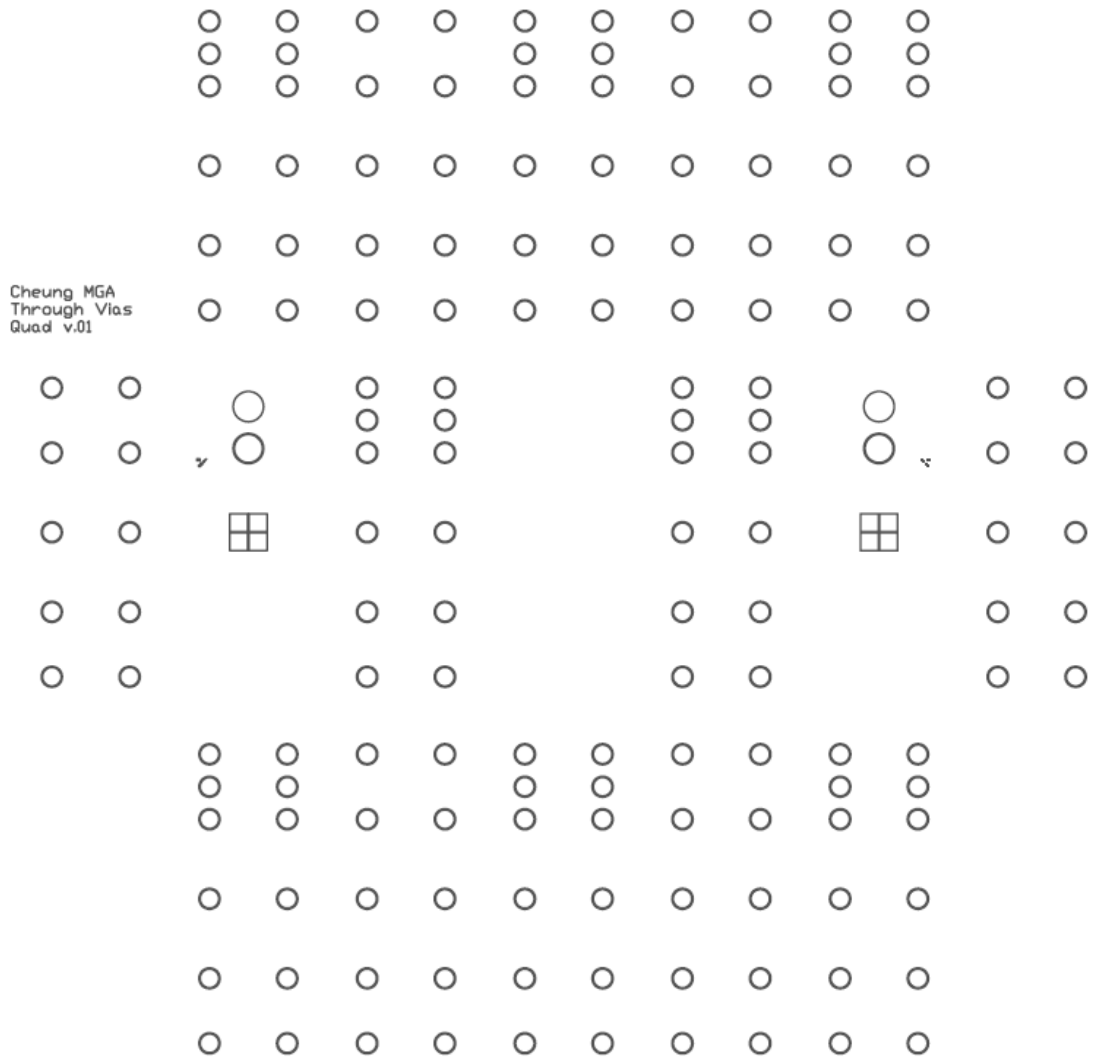
Figure B-5: CONTACT VIAS mask for MuSE v. 1.0 and 1.5
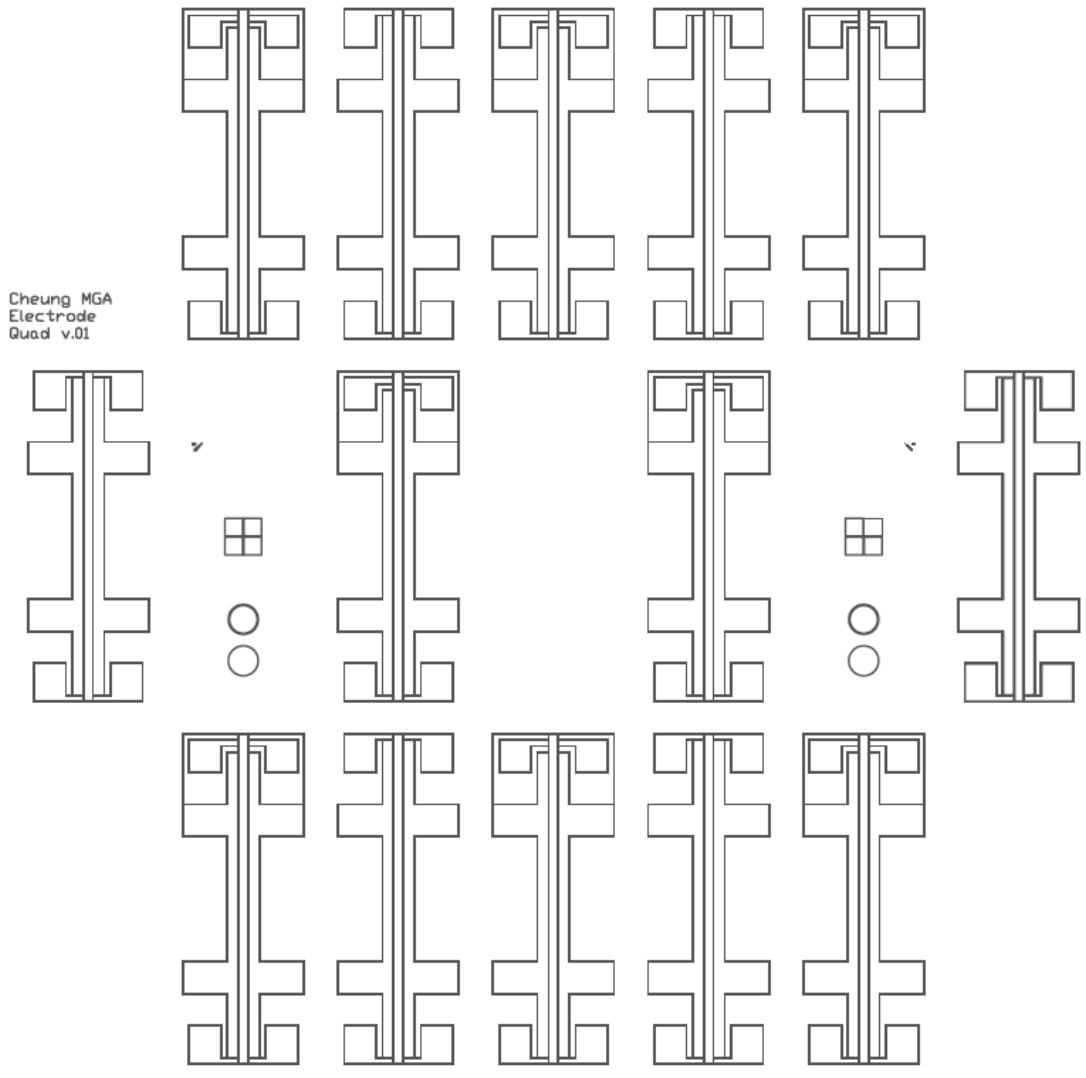
Figure B-6: ELECTRODE mask for MuSE v. 1.0 and 1.5

Cheung MGA
Spacer Trench
Quad v.01
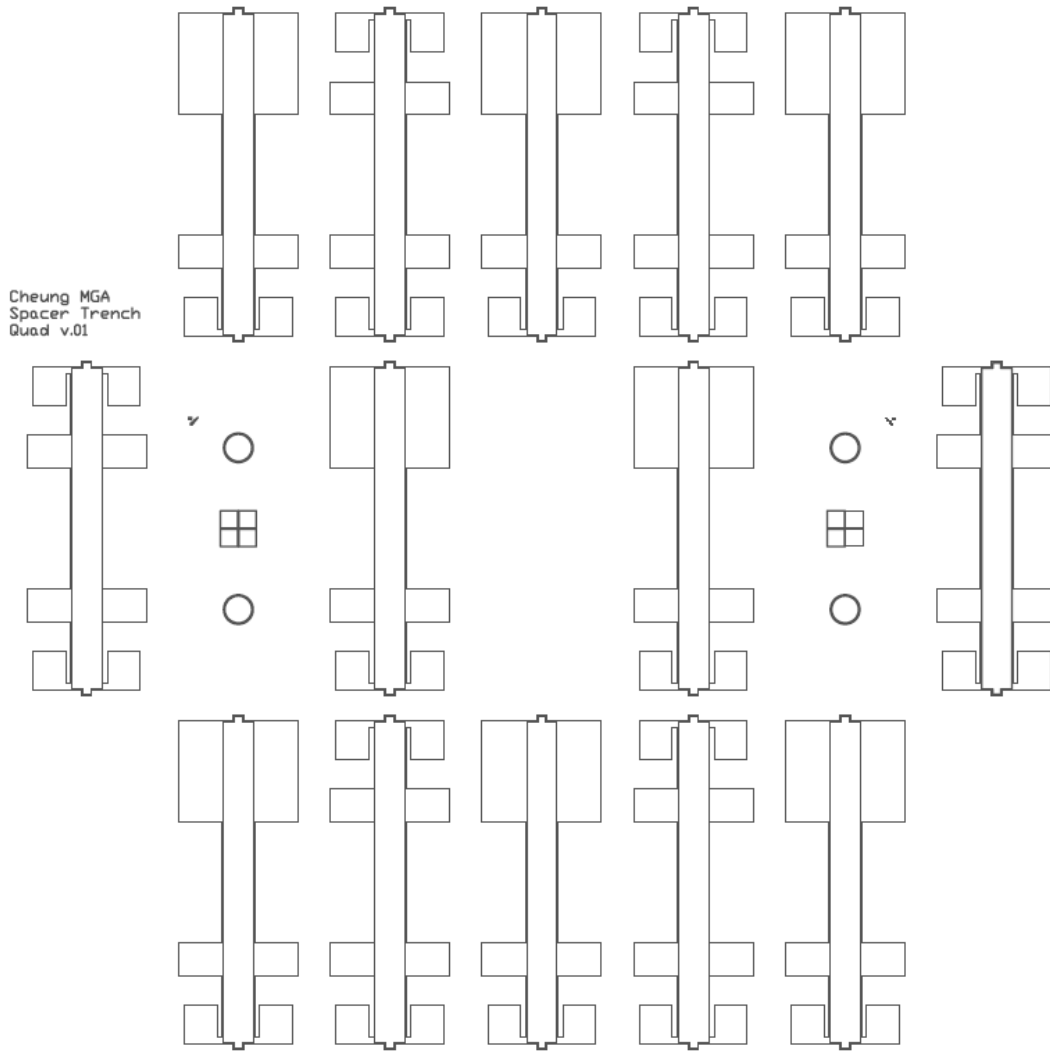
Figure B-7: APERTURE TRENCH mask for MuSE v. 1.0

Cheung MGA
Aperture
Quad v.01
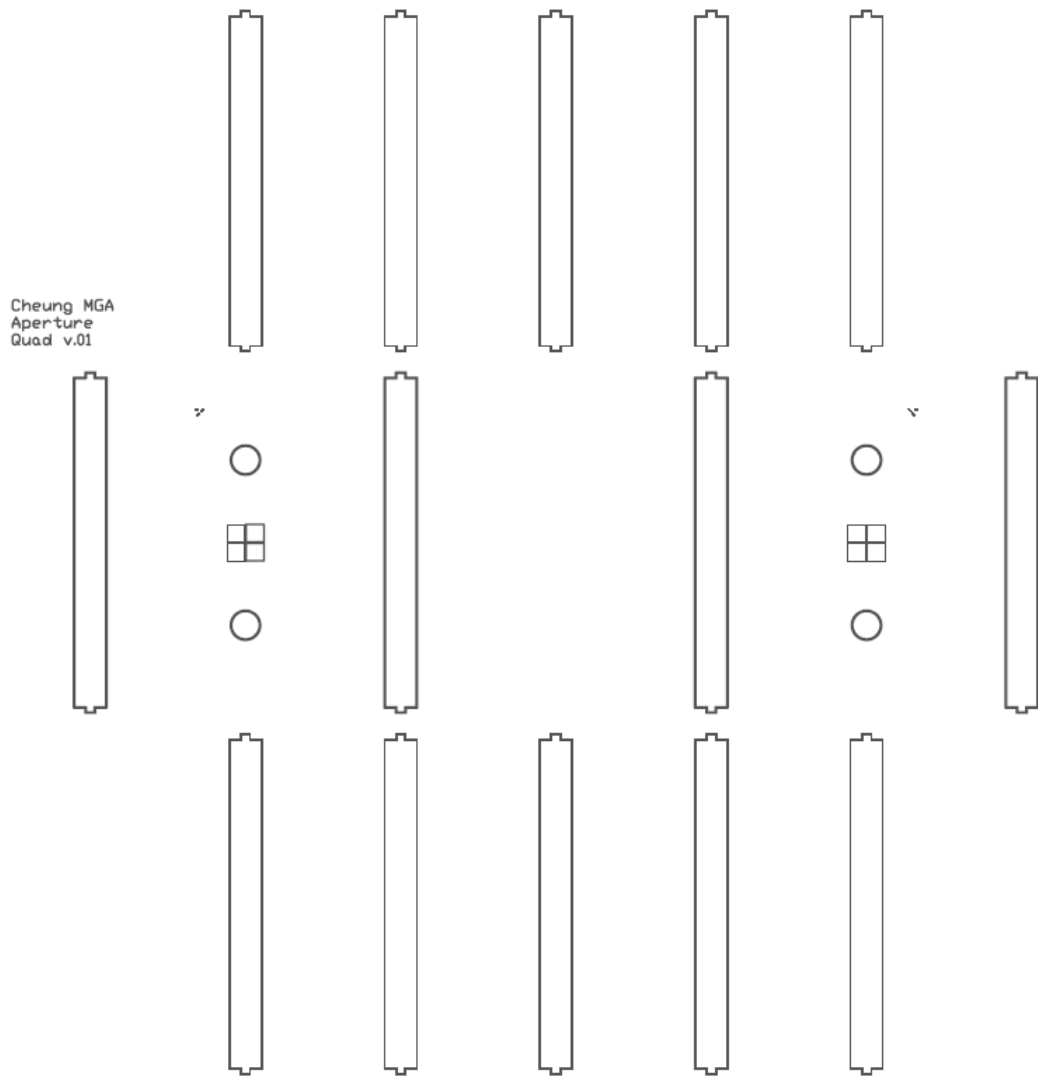
Figure B-8: APERTURE mask for MuSE v. 1.0 and 1.5
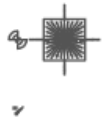
MuSE v.2.0
Alignment
K. Cheung
2009
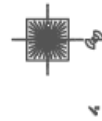
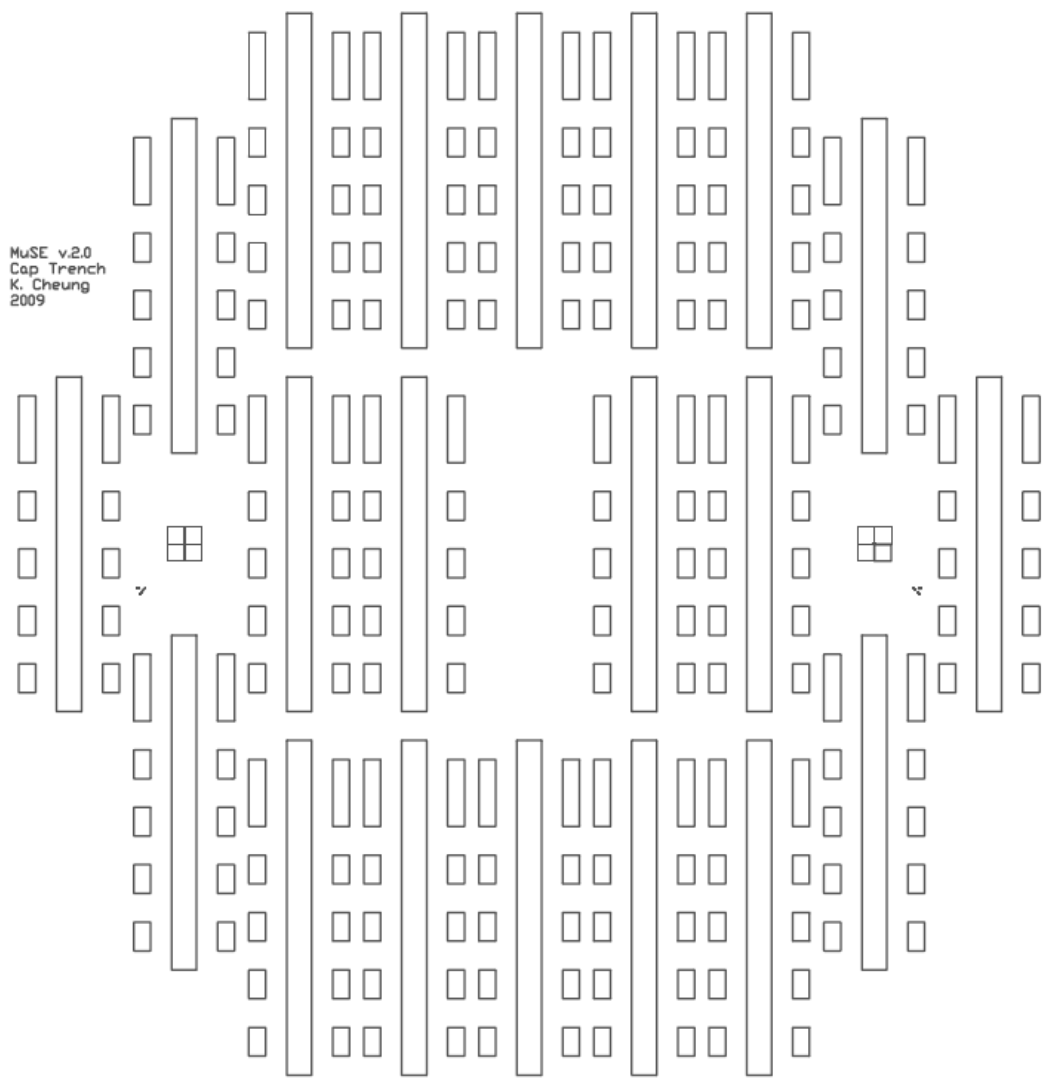**Figure B-9: ALIGNMENT mask for MuSE v. 2.0**

Figure B-10: CAP TRENCH mask for MuSE v. 2.0
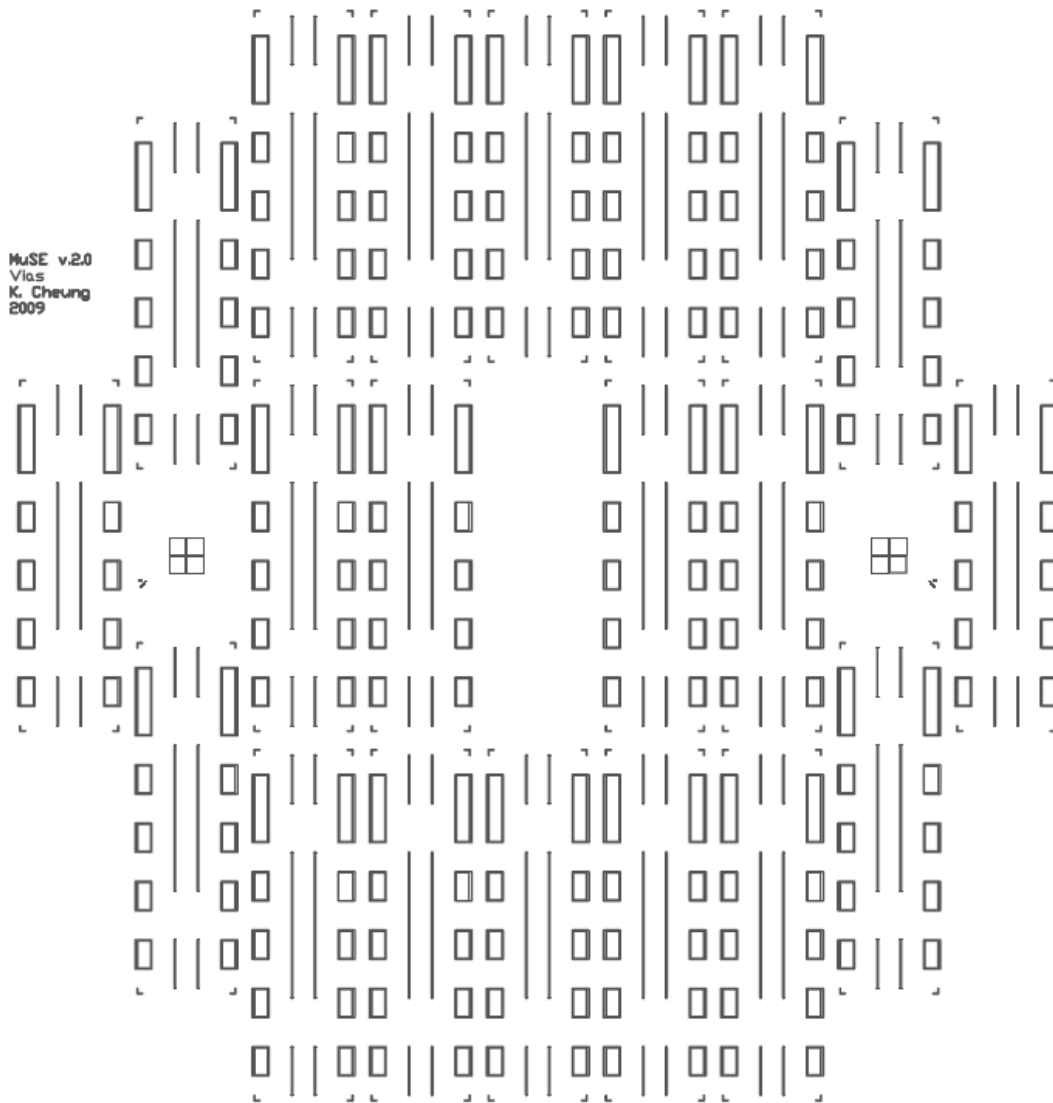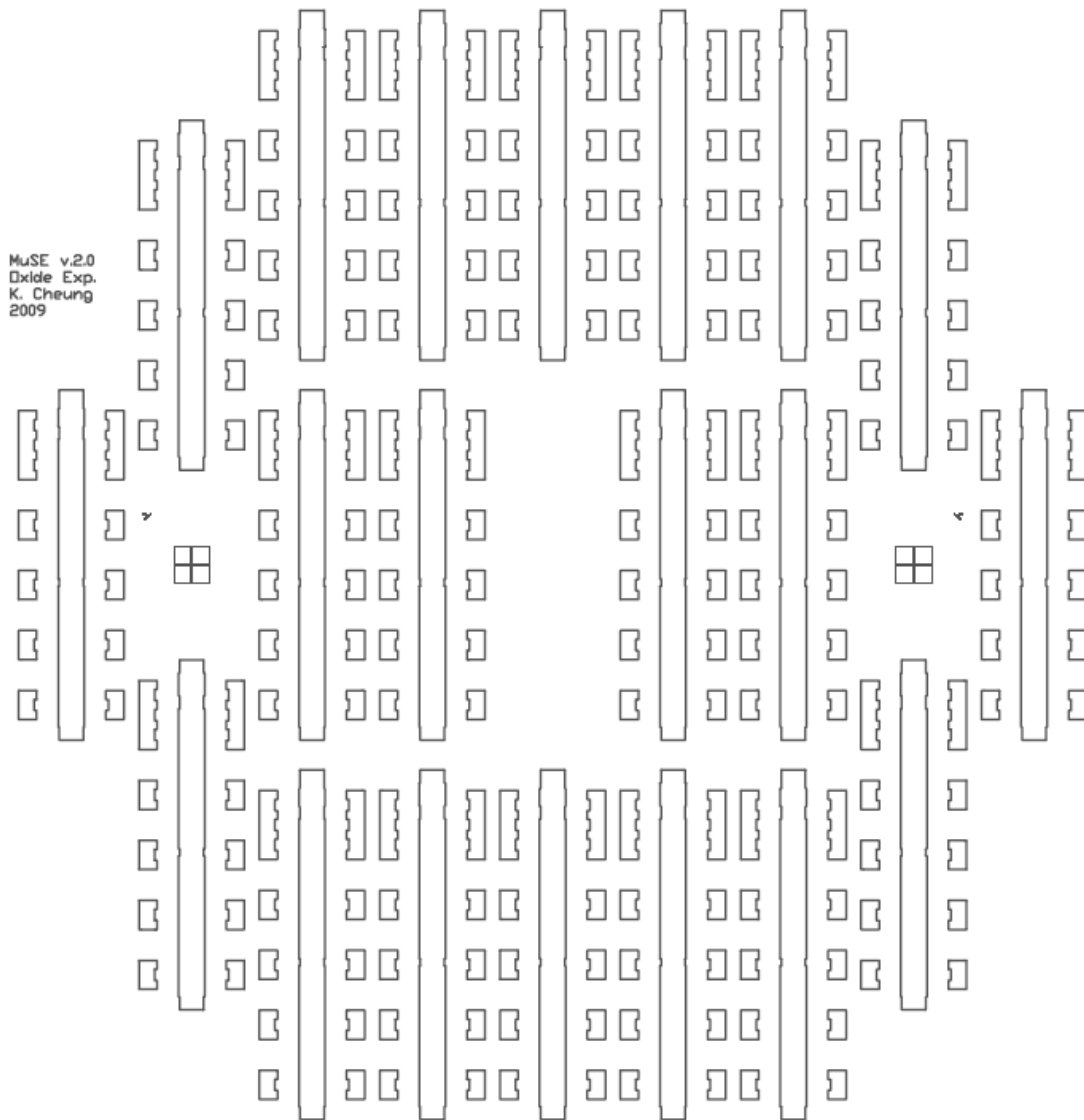
Figure B-11: CONTACT VIAS mask for MuSE v. 2.0

MuSE v.2.0
Oxide Exp.
K. Cheung
2009

Figure B-12: OXIDE ETCH mask for MuSE v. 2.0
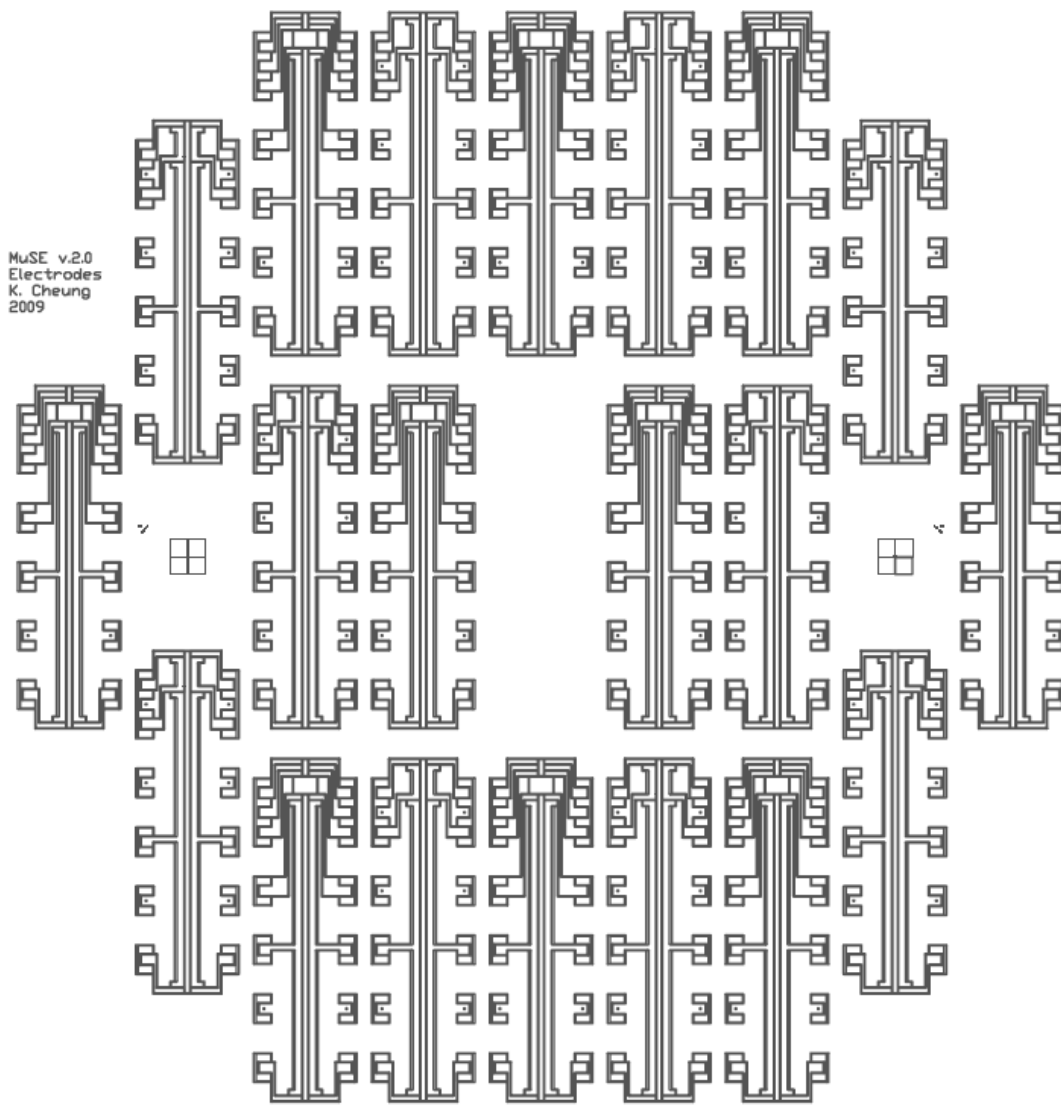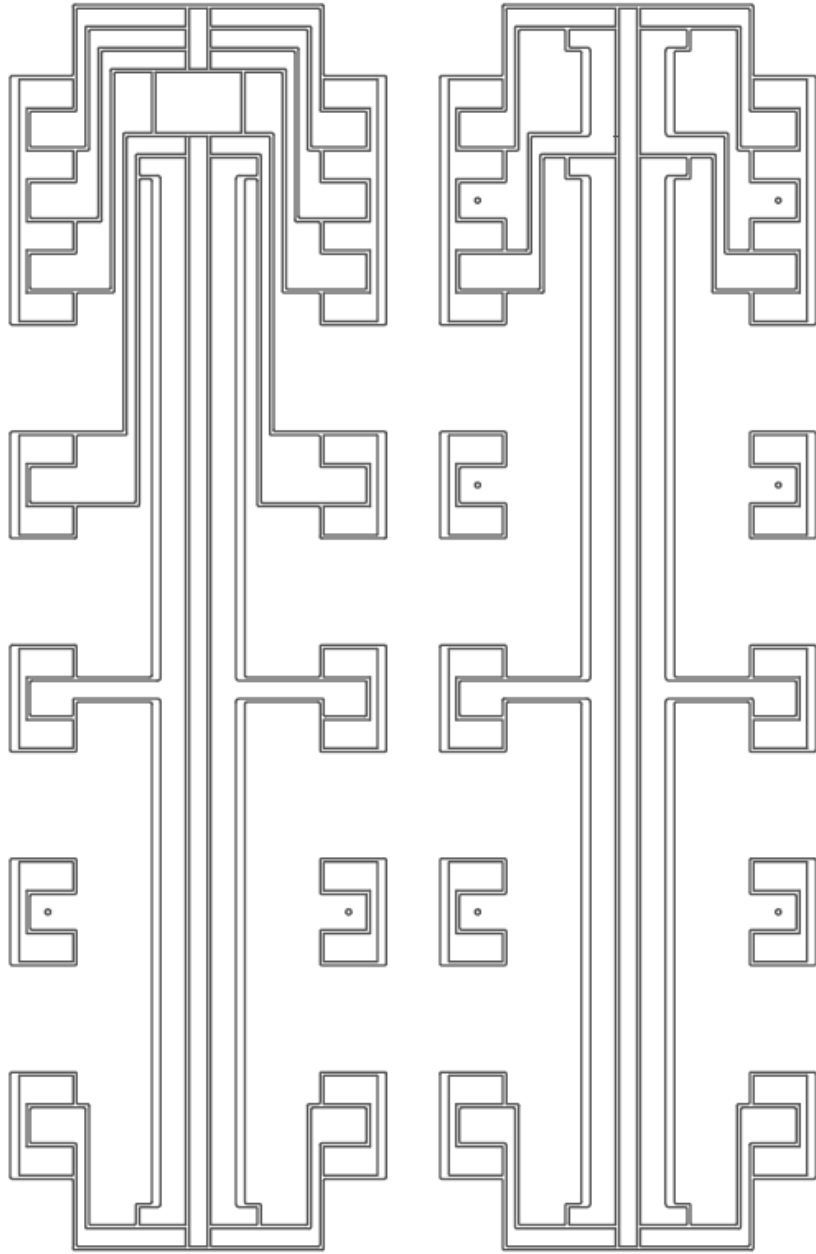
Figure B-13: ELECTRODE mask for MuSE v. 2.0

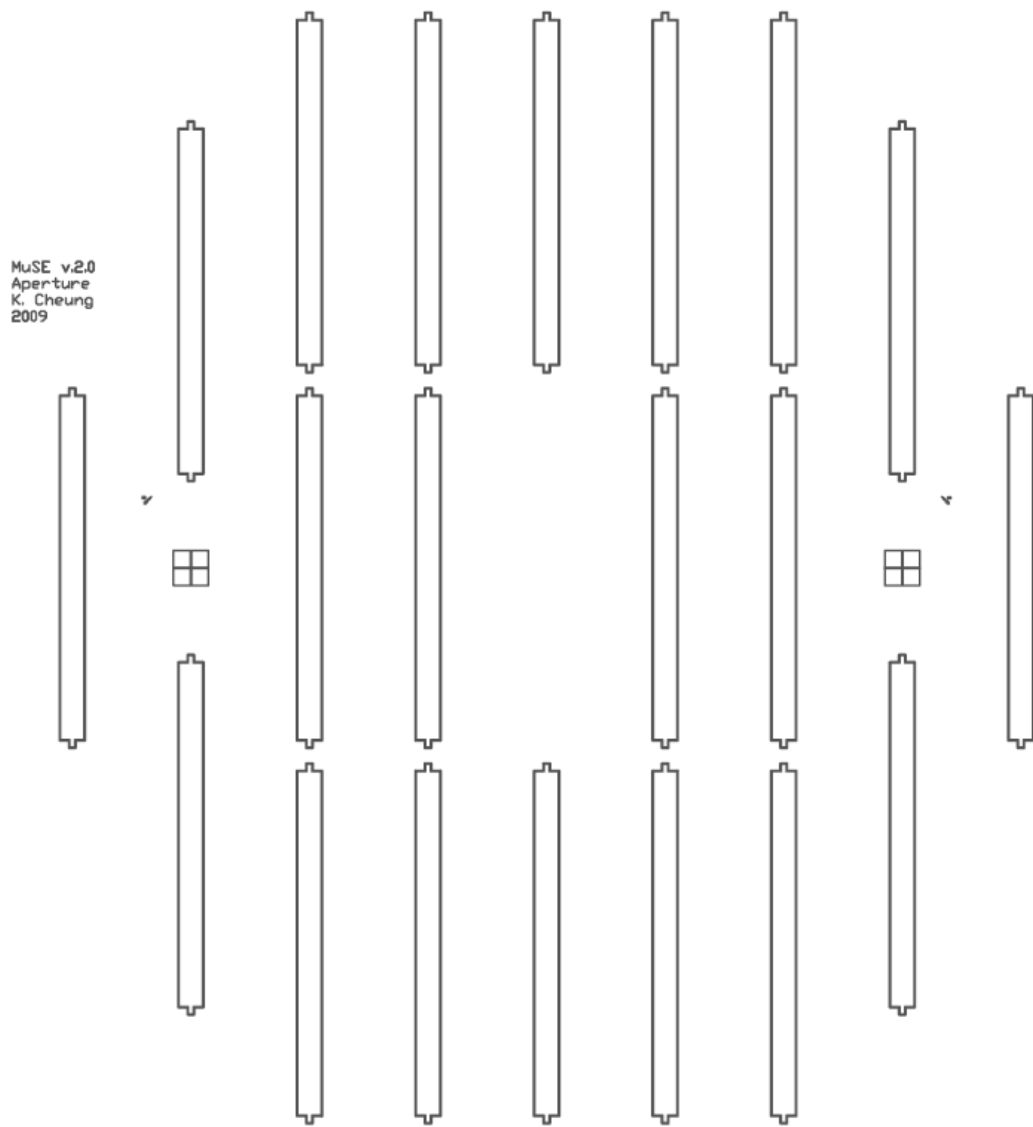**Figure B-14: ELECTRODE mask for MuSE v. 2.0 (detailed)**

Figure B-15: APERTURE mask for MuSE v. 2.0

Appendix

C

MATLAB Scripts

This appendix provides the MATLAB scripts used to perform the multipole expansion discussed in Chapter 3. The potential field solutions from MAXWELL 2D are saved as a *.reg file and need to be converted to a *.txt file before processing with this code.

expansion.m
```
% Program to solve the coefficients for the field expansion

% load data
% need to open *.reg in Wordpad and save as *.txt with MSDOS format
clear all;
[x,y,z,V] = textread('devb_0100_sym_r.txt','%f%f%f%f');
r0 = 500;
C = [];
S = [];

for i = 1:6
   n = 2*(2*(i-1)+1);
   C(i) = cmsolve(x,y,V,r0,n);
end;

for i = 1:6
   m = 4*i;
   S(i) = snsolve(x,y,V,r0,m);
end;

normC = C./C(1)
normS = S./C(1)
```

cmsolve.m
```
% solves the expansion coefficient Cm
function cm = cmsolve(x,y,V,r0,m)

del = y(2)-y(1);
sum = 0;
for i = 1:length(x)
   r = sqrt(x(i)^2+y(i)^2);
   if r <= r0
      if x(i) == 0
         theta = pi/4;
      else
         theta = atan(y(i)/x(i))-pi/4;
      end;
      sum = sum + V(i)*(r/r0)^m*cos(m*theta)*del^2;
   end;
end;

sum = sum/((r0^2*pi)/(8*(m+1)));

cm = sum;
```


snsolve.m
```
% solves the expansion coefficient Sn
function sn = snsolve(x,y,V,r0,n)

del = y(2)-y(1);
sum = 0;
for i = 1:length(x)
   r = sqrt(x(i)^2+y(i)^2);
   if r <= r0
      if x(i) == 0
         theta = pi/4;
      else
         theta = atan(y(i)/x(i))-pi/4;
      end;
      sum = sum + V(i)*(r/r0)^n*sin(n*theta)*del^2;
   end;
end;

sum = sum/((r0^2*pi)/(8*(n+1)));

sn = sum;
```

Appendix
D

LabVIEW Programming

This appendix contains several screen shots of the LABVIEW program used for the control software in the characterization system described in Chapter 5. Other than the two main modules included, there were two auxiliary virtual instruments that were also used. Global Control Arrays.vi was used to store the voltages calculated by GenValue.vi. so they could be accessed by Scan Control.vi throughout scanning. Quad Math.vi was a simple sub-module of GenValue.vi used to calculate the corresponding r.f. and d.c. voltages for a specified operating condition.
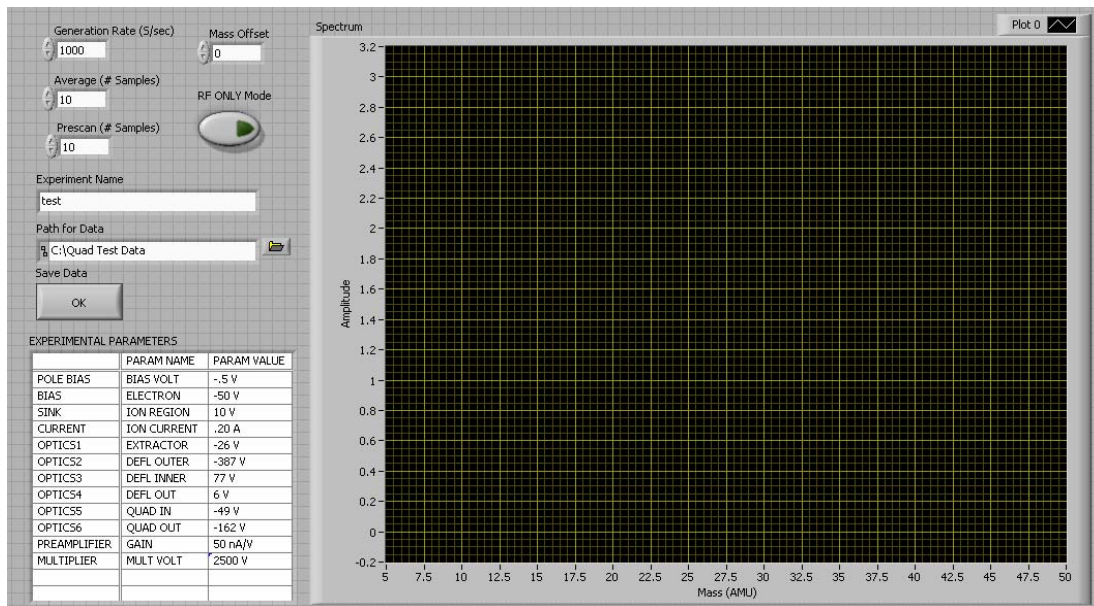
Figure D-1: Front panel of Scan Control.vi
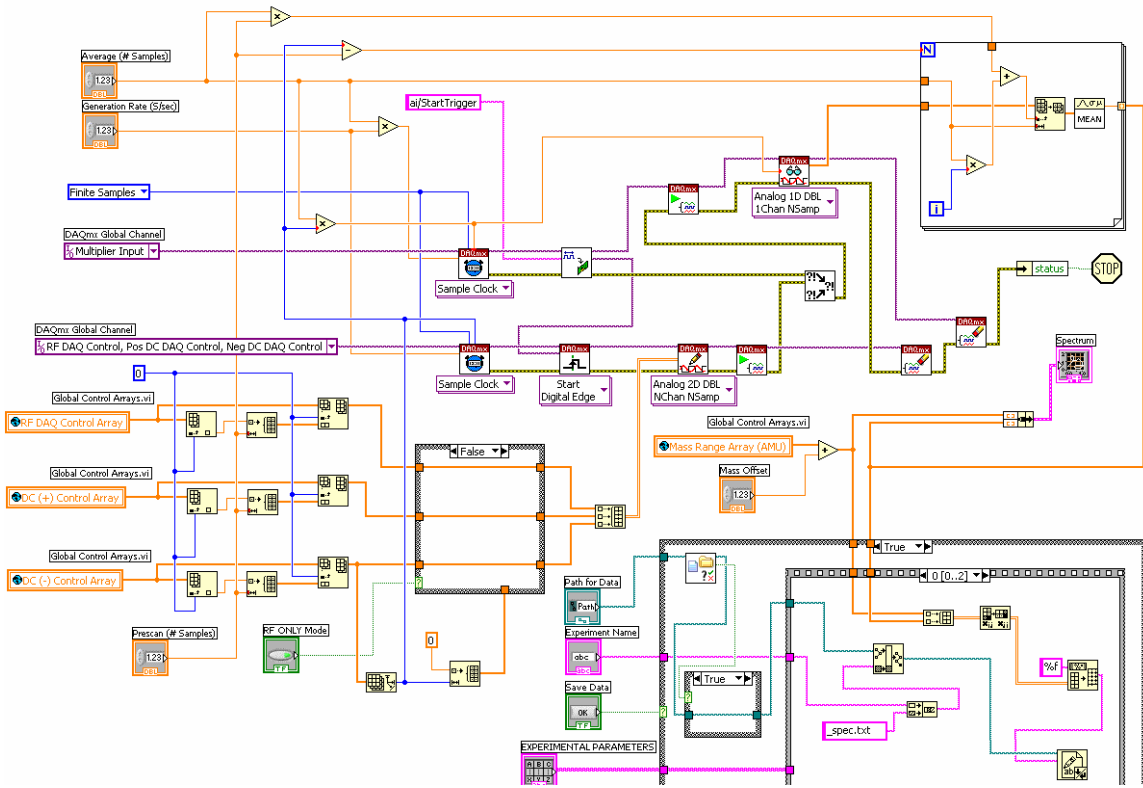
Figure D-2: Block diagram 1 of 4 for Scan Control.vi
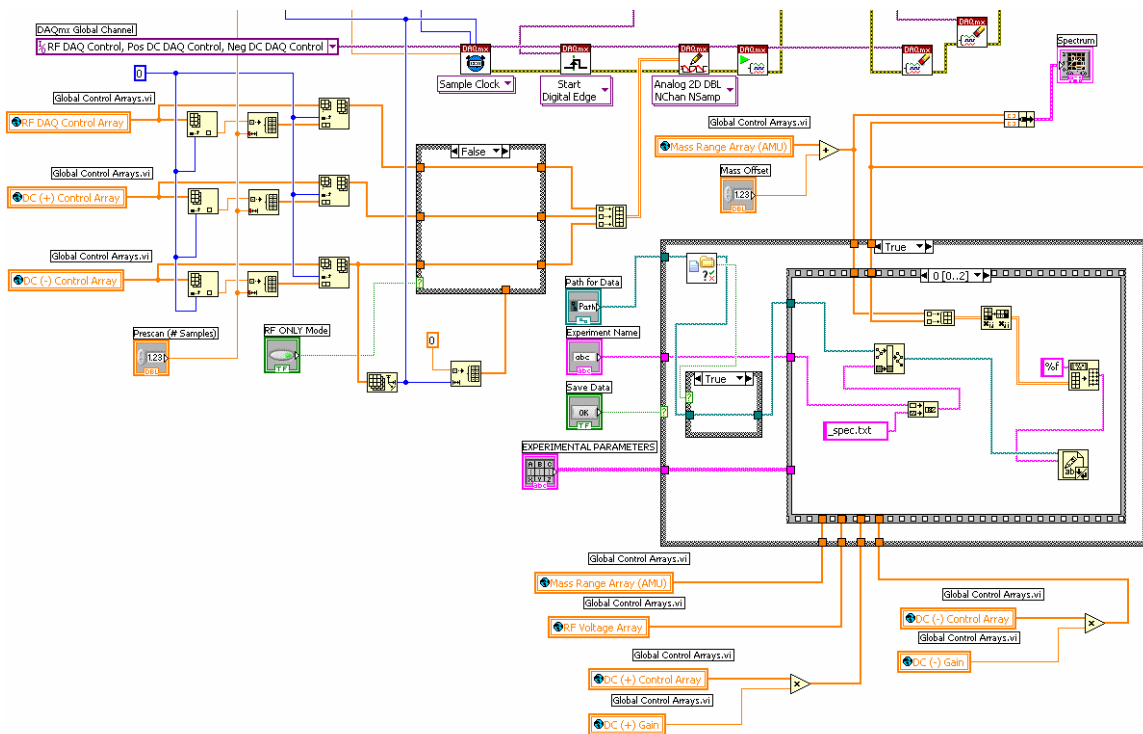
Figure D-3: Block diagram 2 of 4 for Scan Control.vi
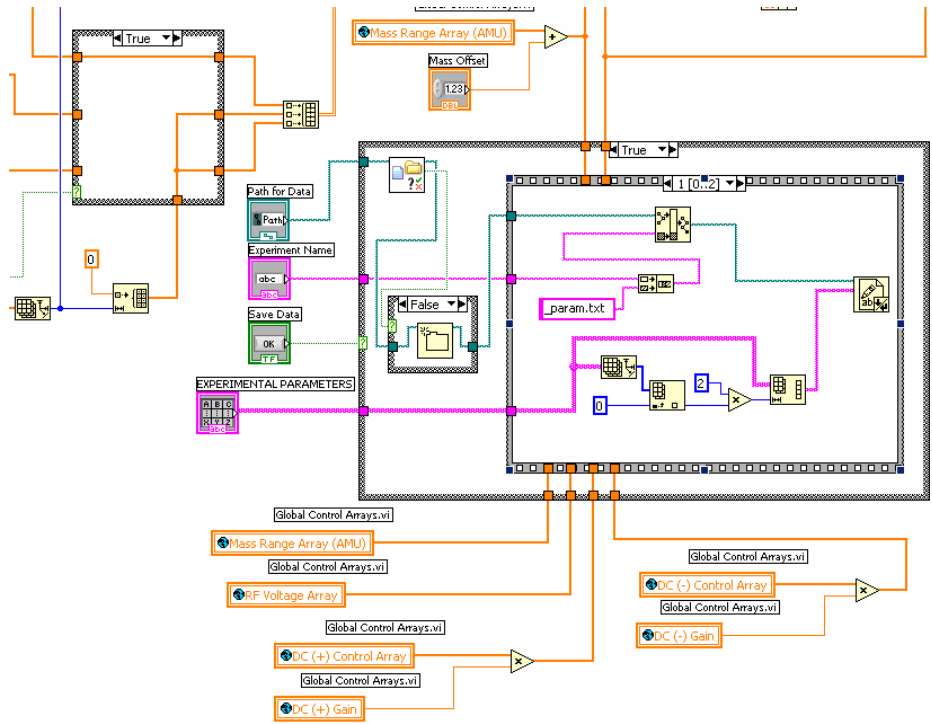
Figure D-4: Block diagram 3 of 4 for Scan Control.vi
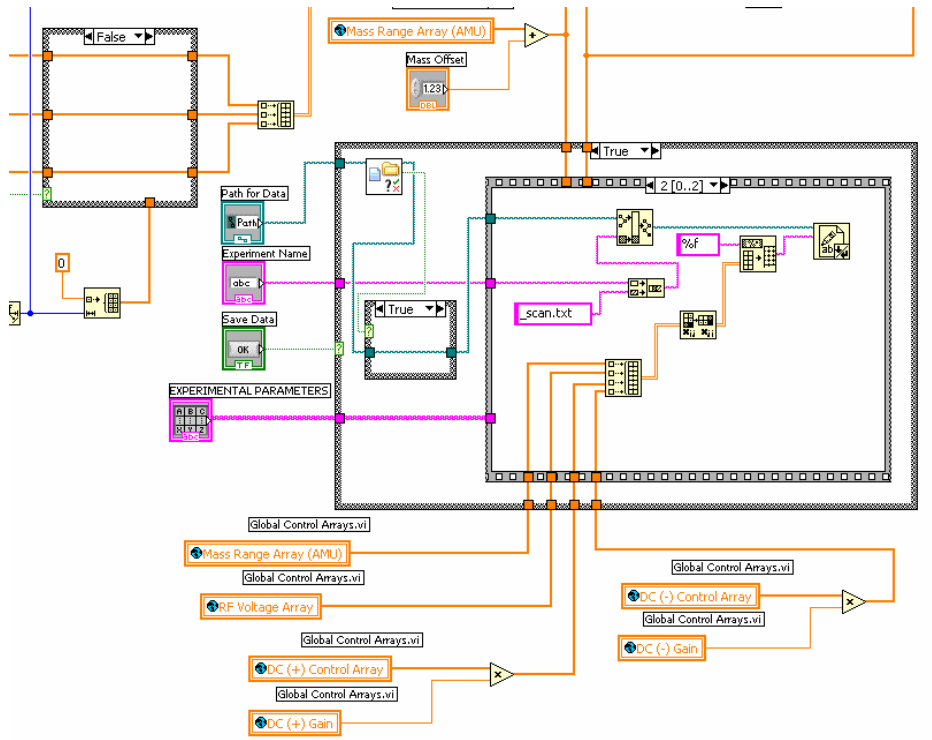
Figure D-5: Block diagram 4 of 4 for Scan Control.vi

163

Figure D-6: Front panel of GenValue.vi
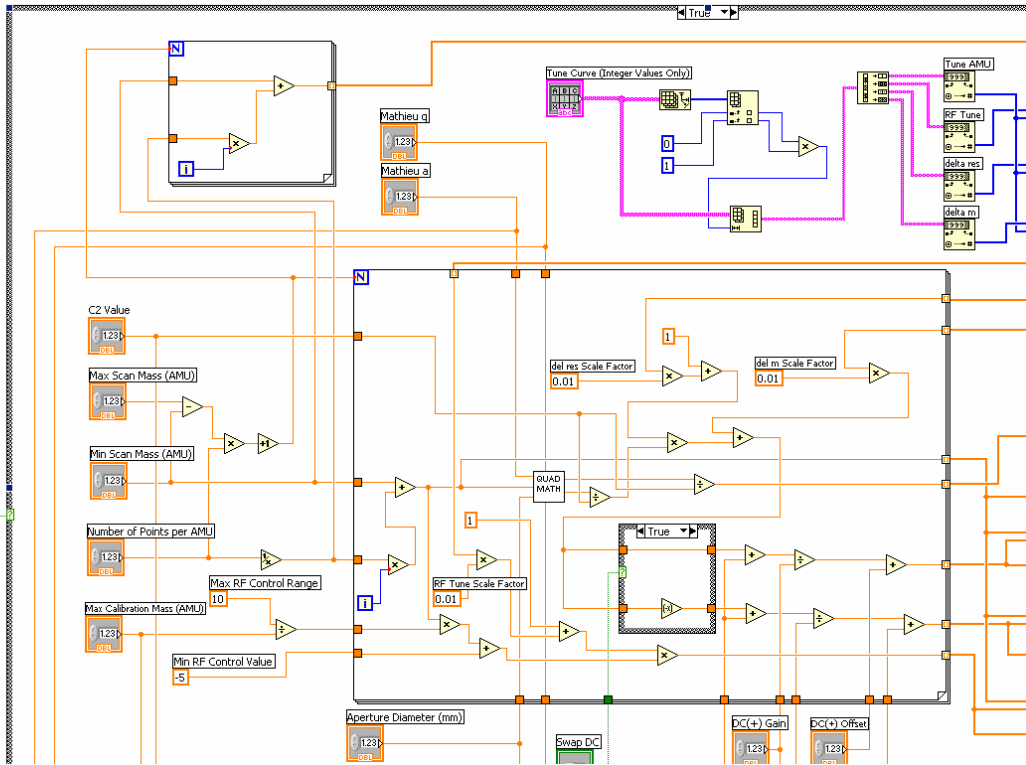
Figure D-7: Block diagram 1 of 4 for GenValue.vi
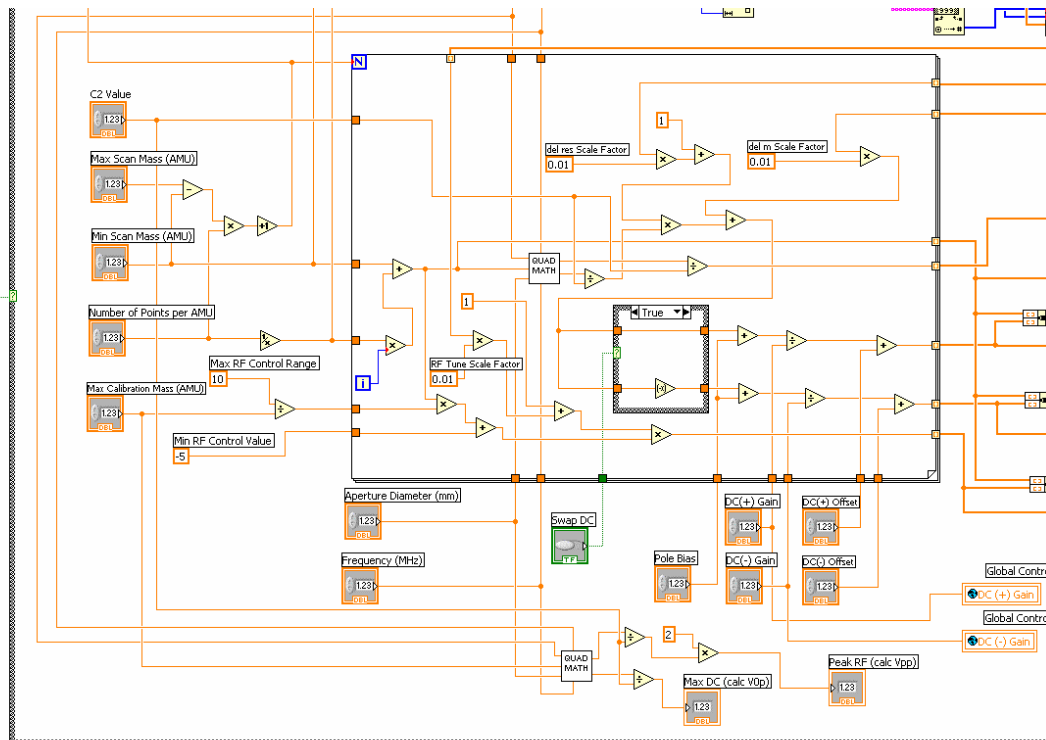
Figure D-8: Block diagram 2 of 4 for GenValue.vi
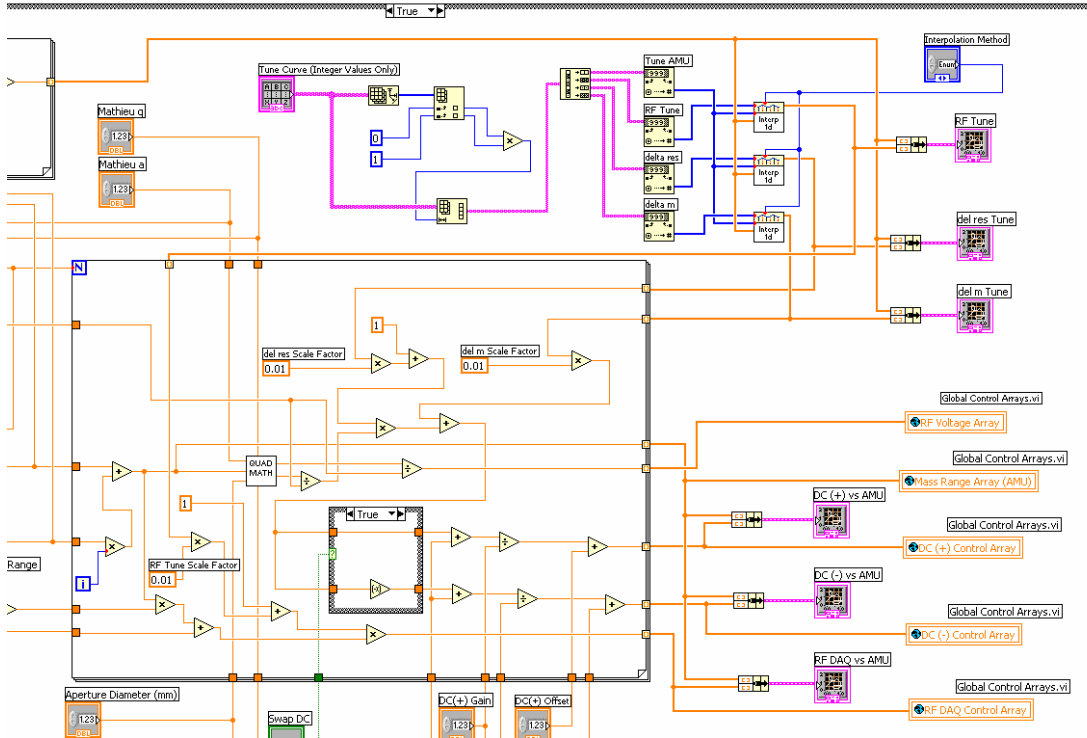
Figure D-9: Block diagram 3 of 4 for GenValue.vi
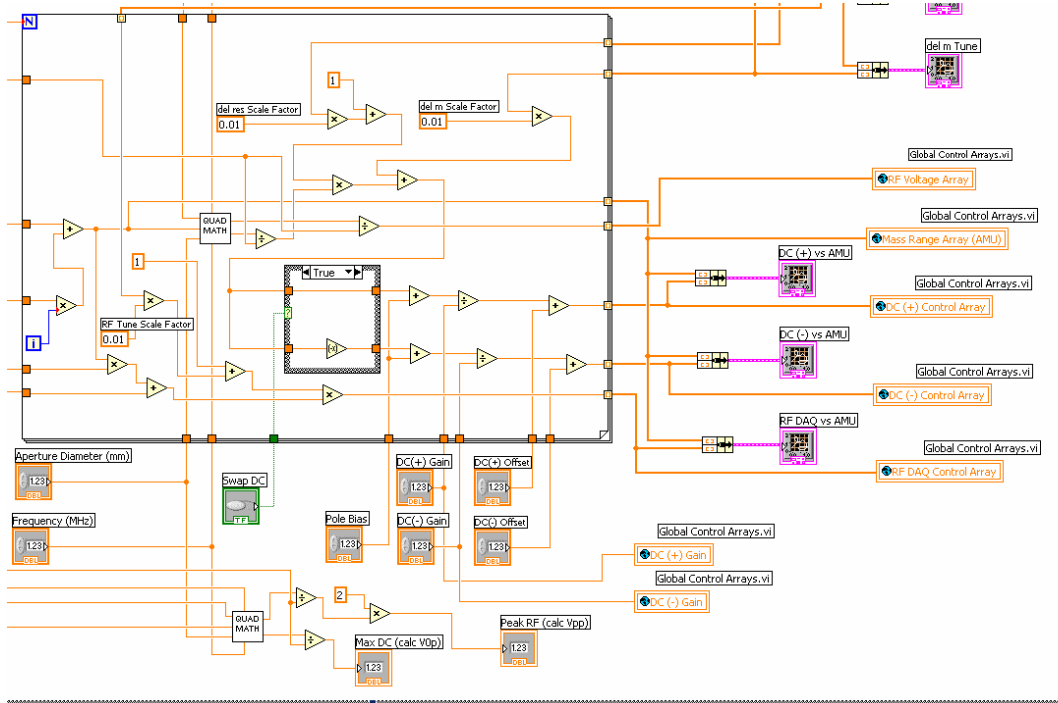
Figure D-10: Block diagram 4 of 4 for GenValue.vi

Appendix
E

Technical Drawings
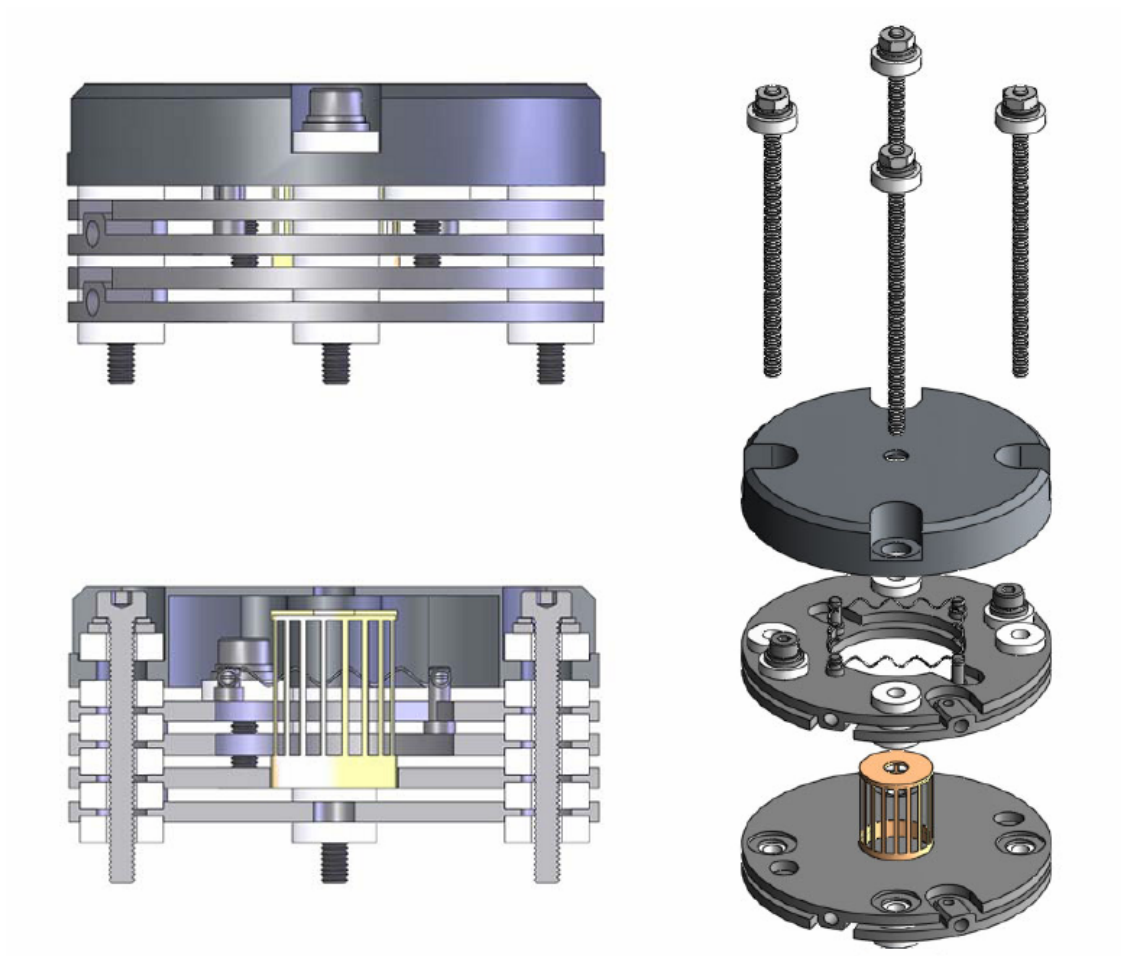
Figure E-1: Schematic of Slim-Line® ionizer
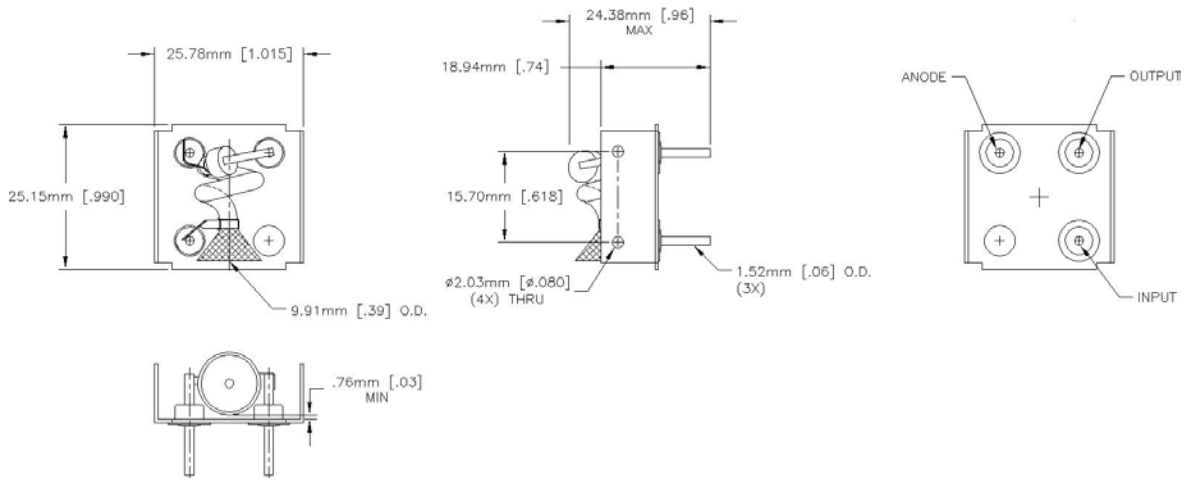
Figure E-2: Drawing of Channeltron® electron multiplier
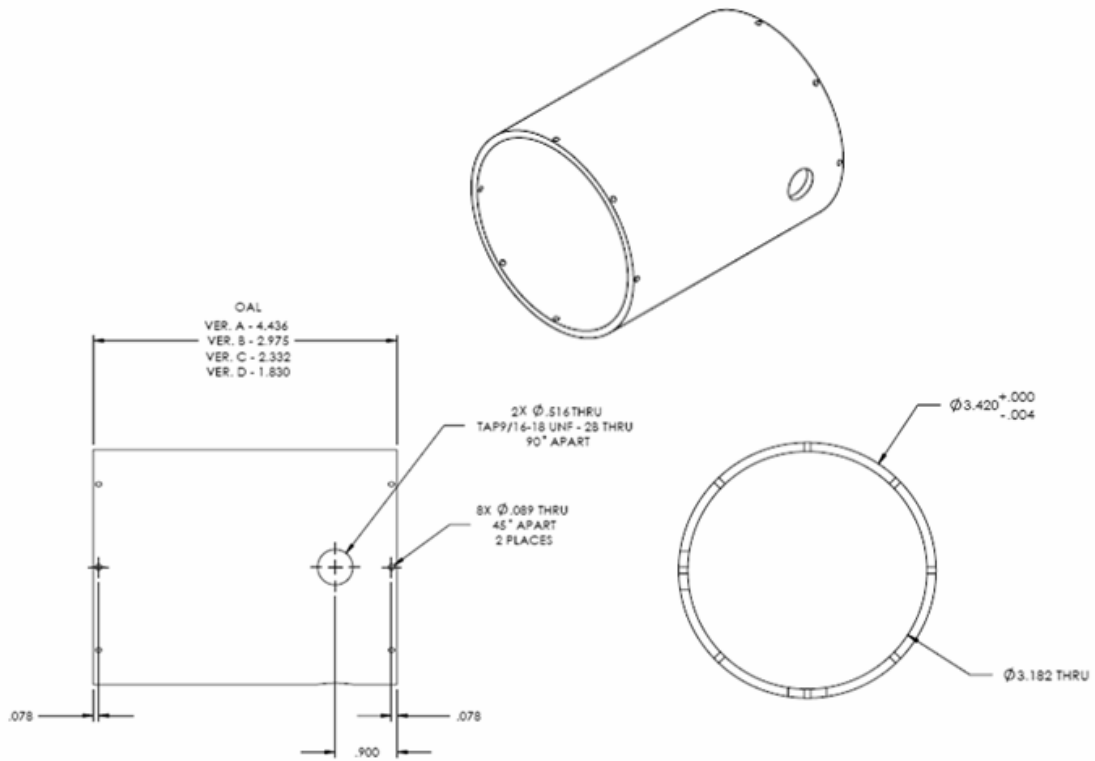
Figure E-3: General dimensions for the aluminum device housing

4X Ø.063 ∇ .28
TAP M2 X 0.4 ∇ .20
90° APART

.130

⬦ .001 – B –

MAX R.008

4X Ø.052 THRU TO M2
90° APART ON Ø2.750 B.C.

45.00°

4X R.063
⌴ .0200

Ø2.710

1.916

⌴ .0200

1.916

4 threaded holes 8-
32, 90 deg. apart
on circle 2.120"
Diameter

∥ .001 B

.140

3.178±.001

3.420

– A –

.078

Ø1.2500

45.00°

4X Ø.063 THRU
TAP M2 X 0.4 THRU
⌴ Ø.2515 ∇ .0200
90° APART

⊕ Ø .001 A

Ø.960 THRU

Ø2.128

4X Ø.089 THRU
TAP 4-40 UNC - 2B THRU
90° APART
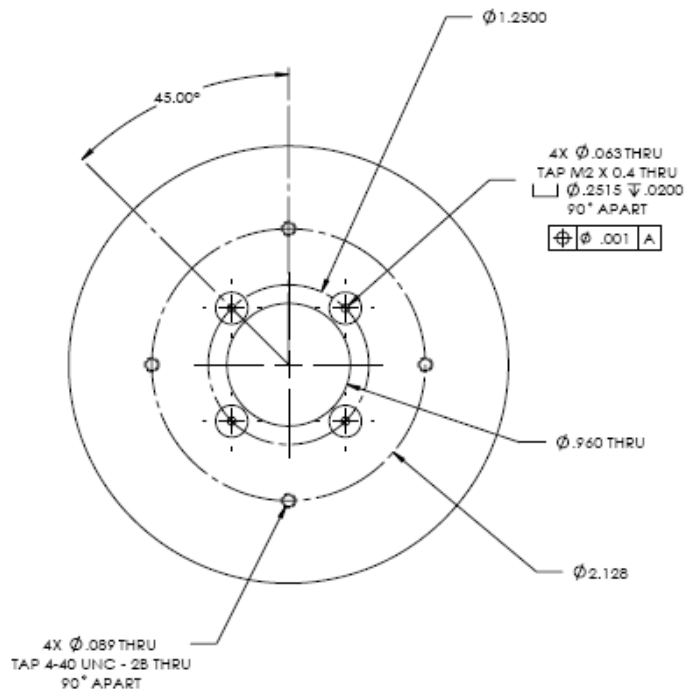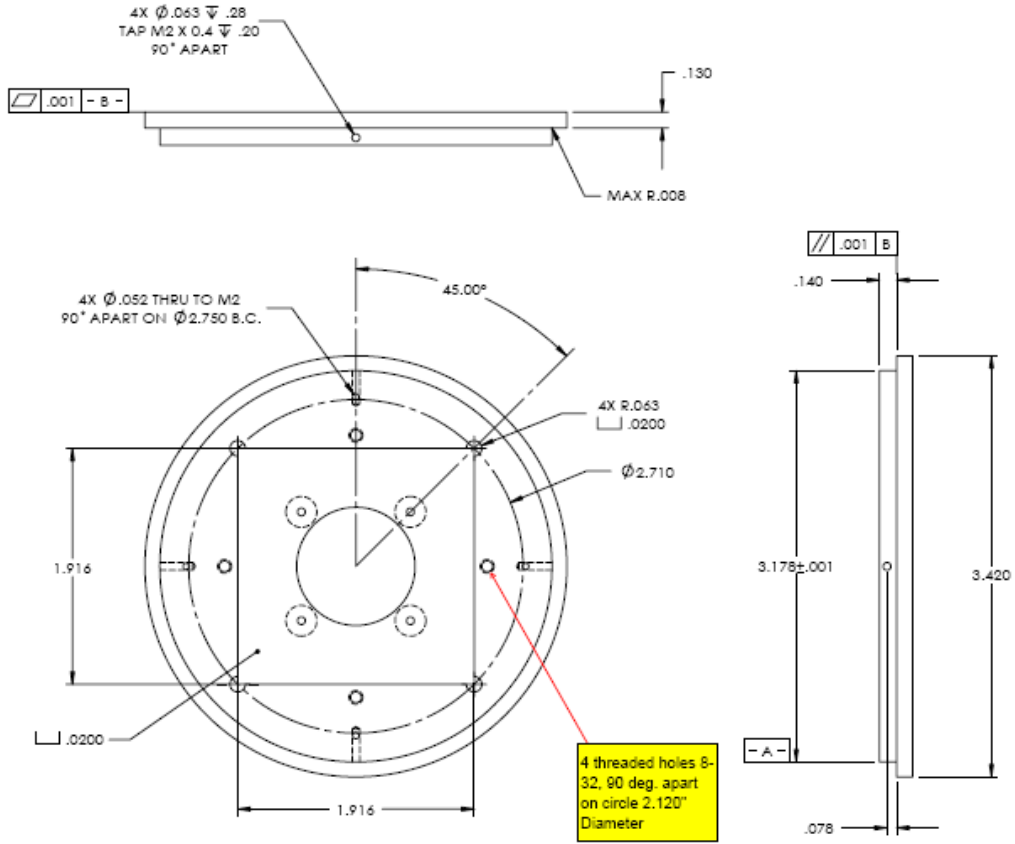
Figure E-4: General dimensions for the device housing bottom cap
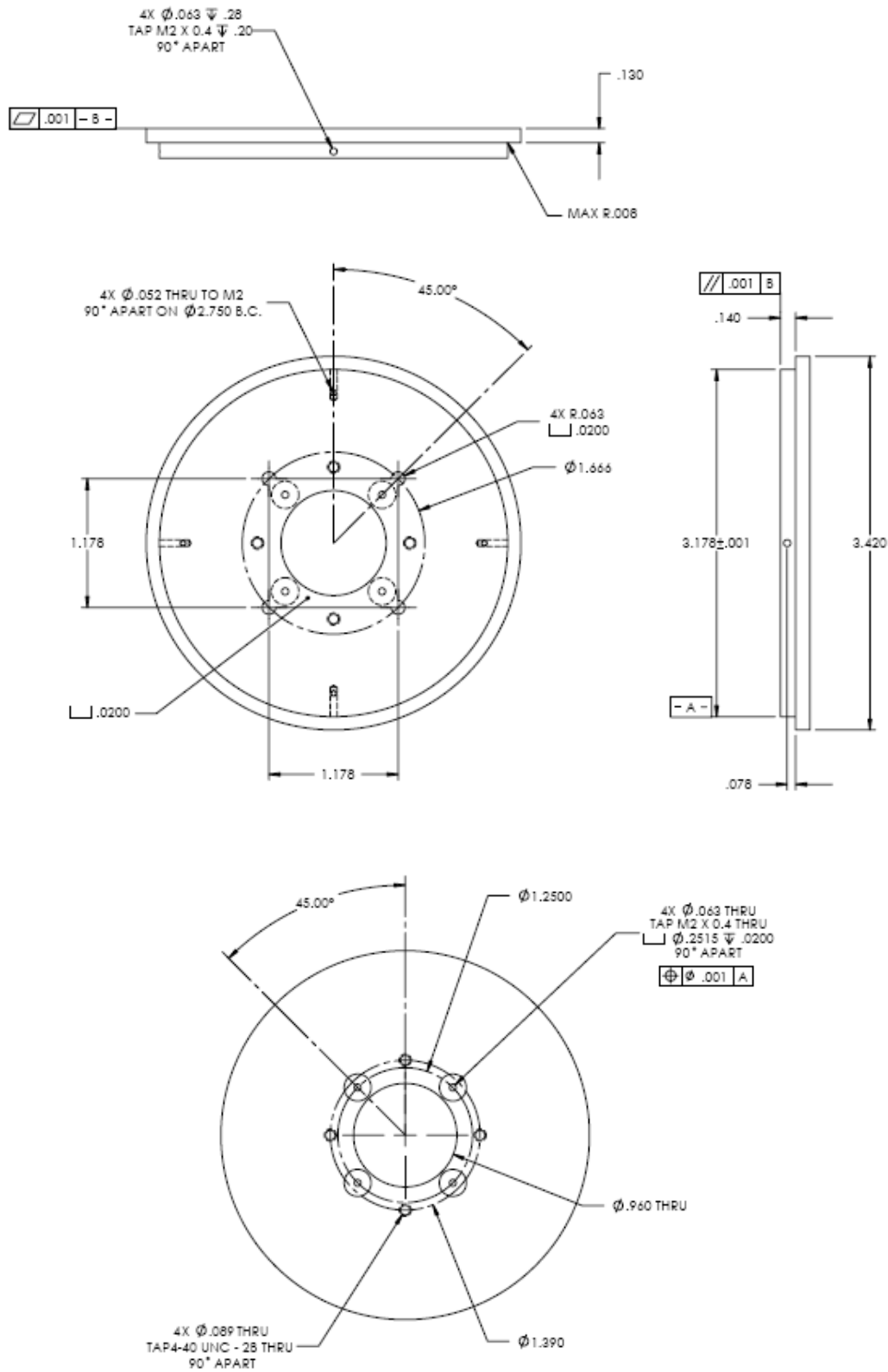
Figure E-5: General dimensions for the device housing top cap
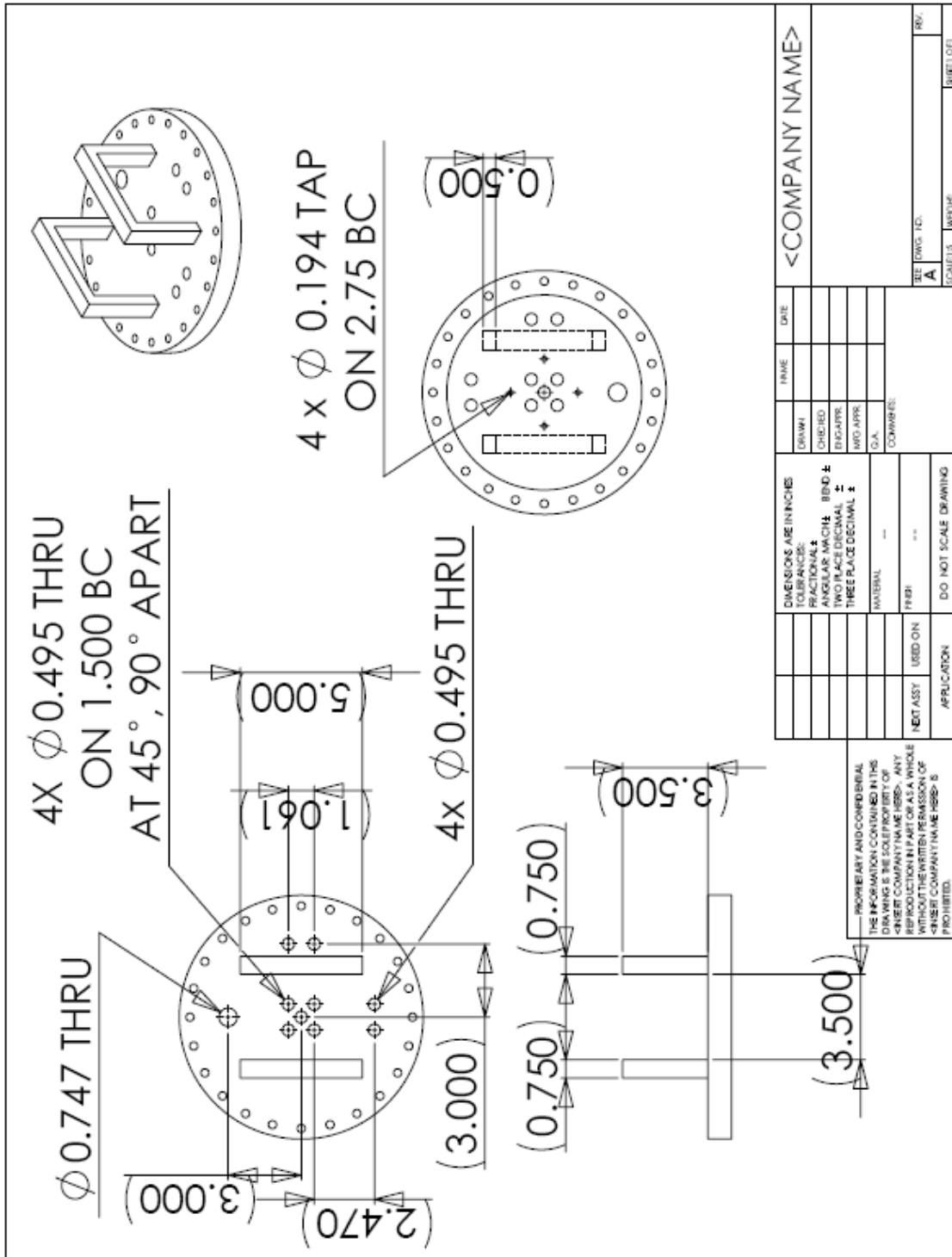
Figure E-6: Drawing for the flange mount
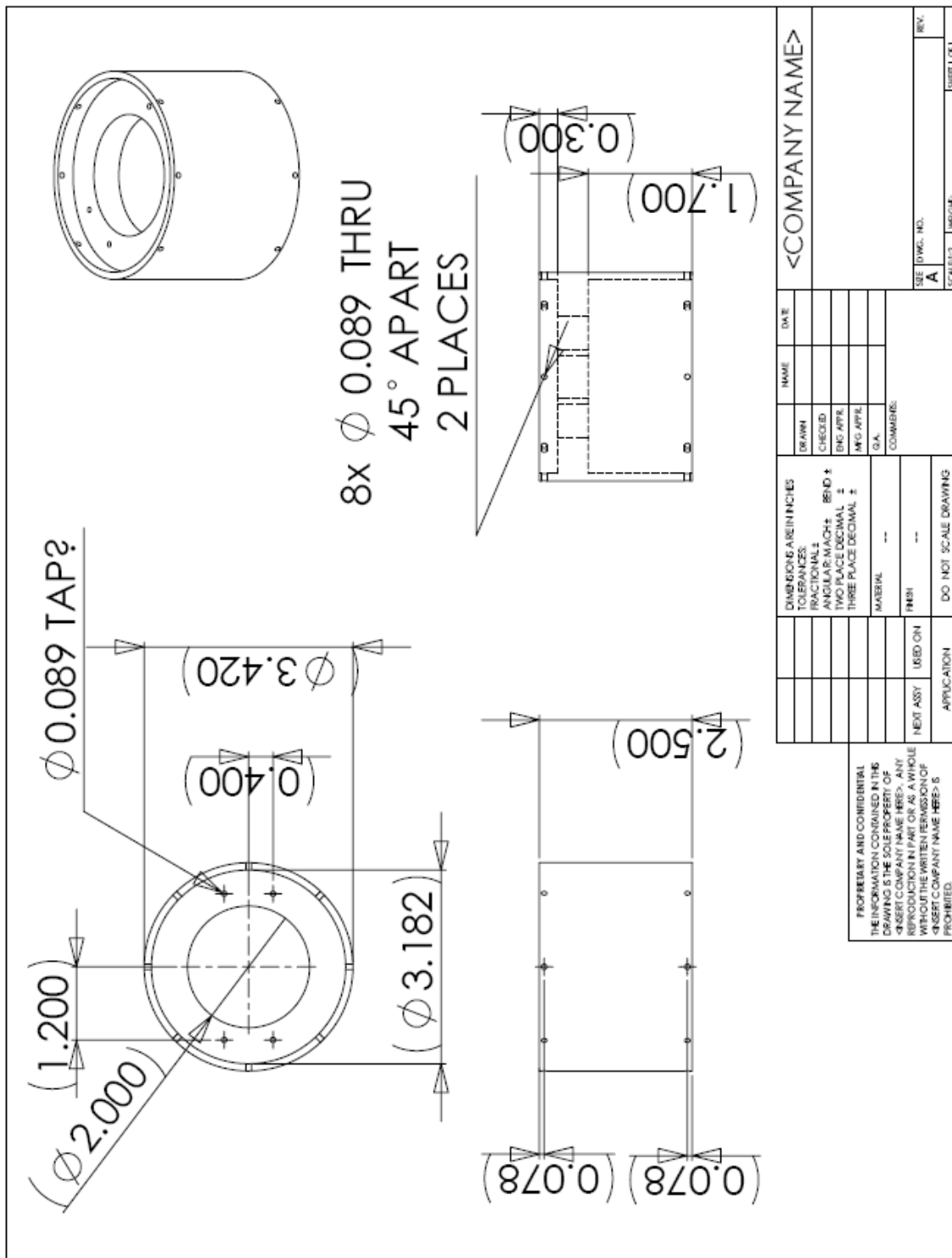
Figure E-7: Drawing for the detector housing
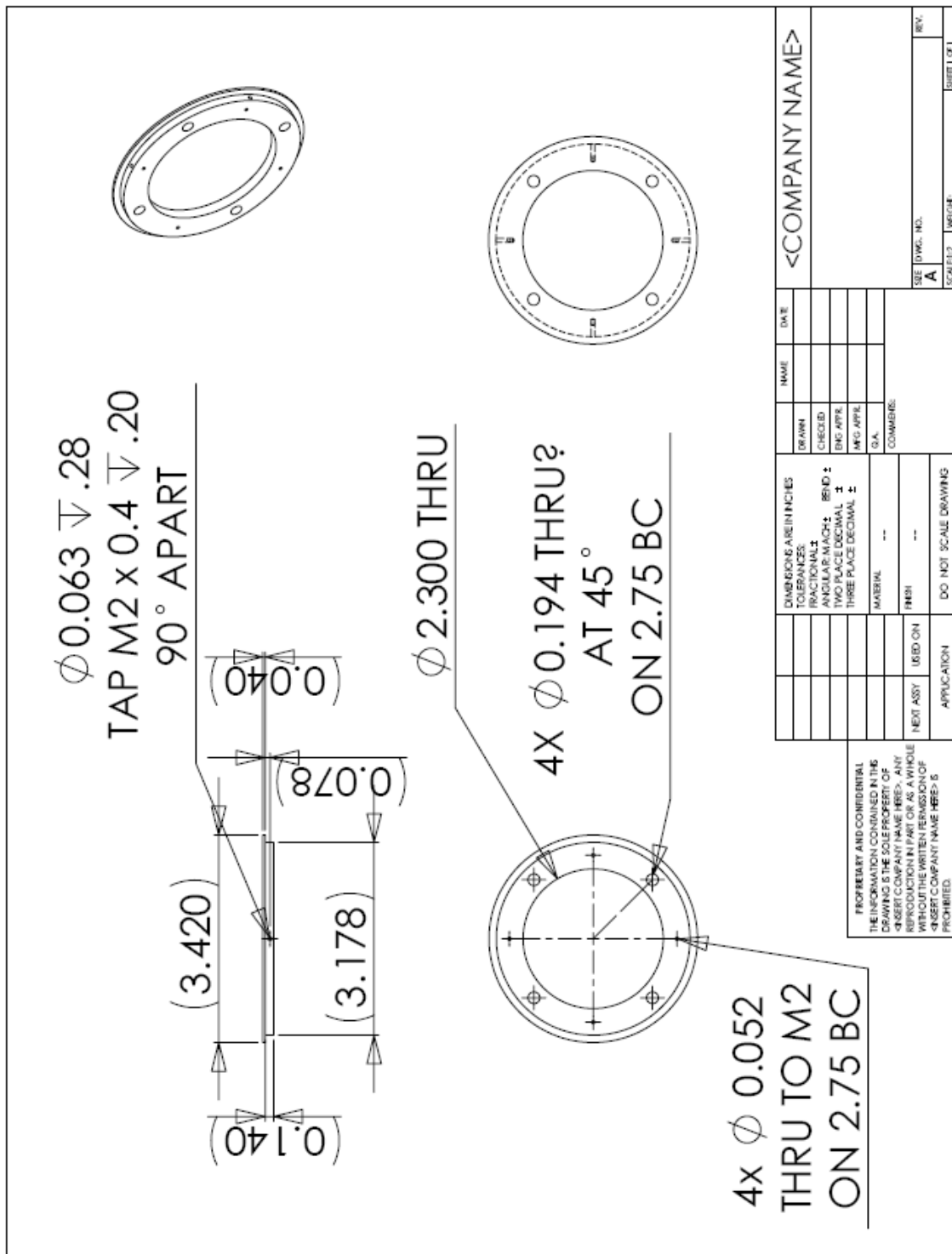
Figure E-8: Drawing for the detector housing base plate
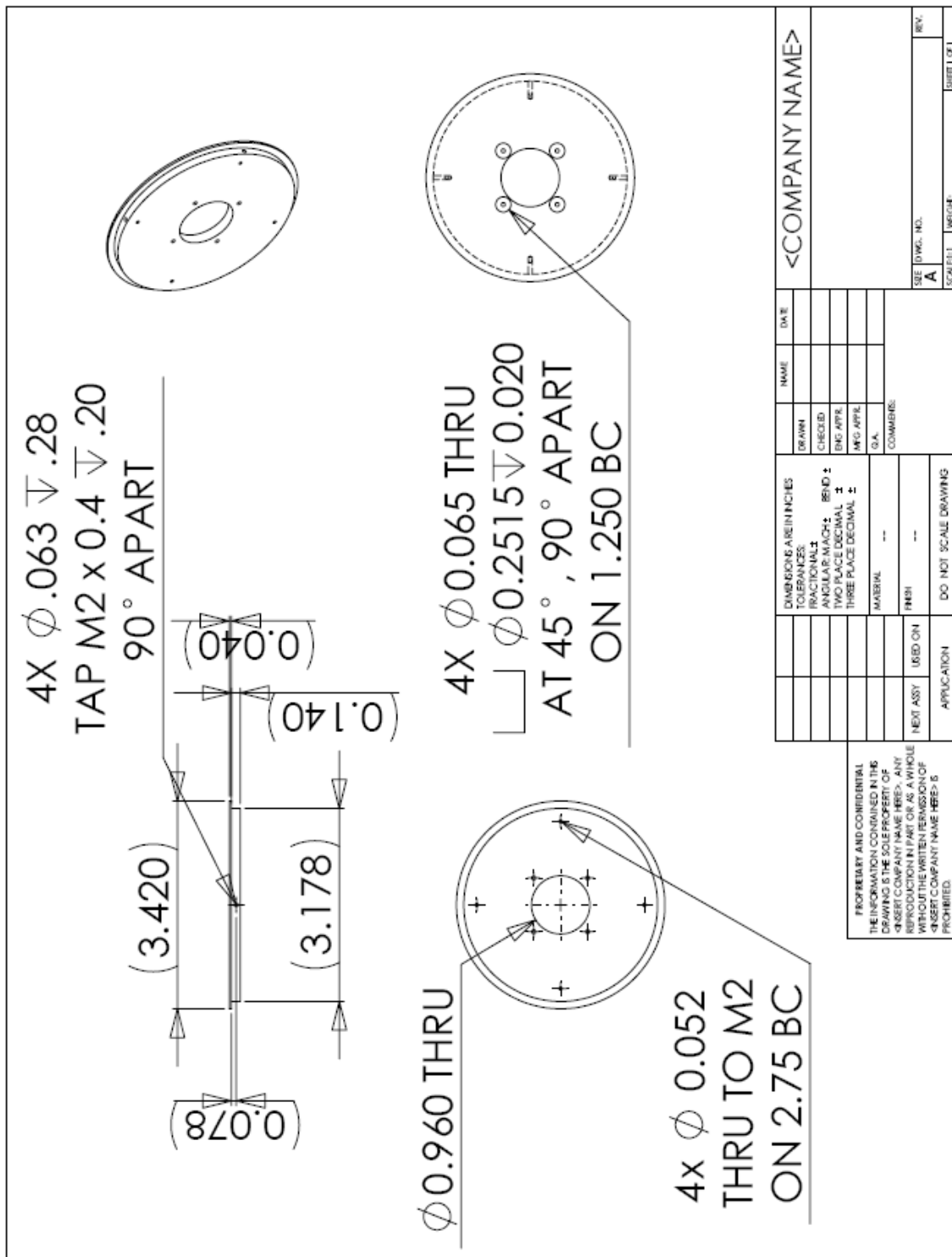
Figure E-9: Drawing for the detector housing top cap
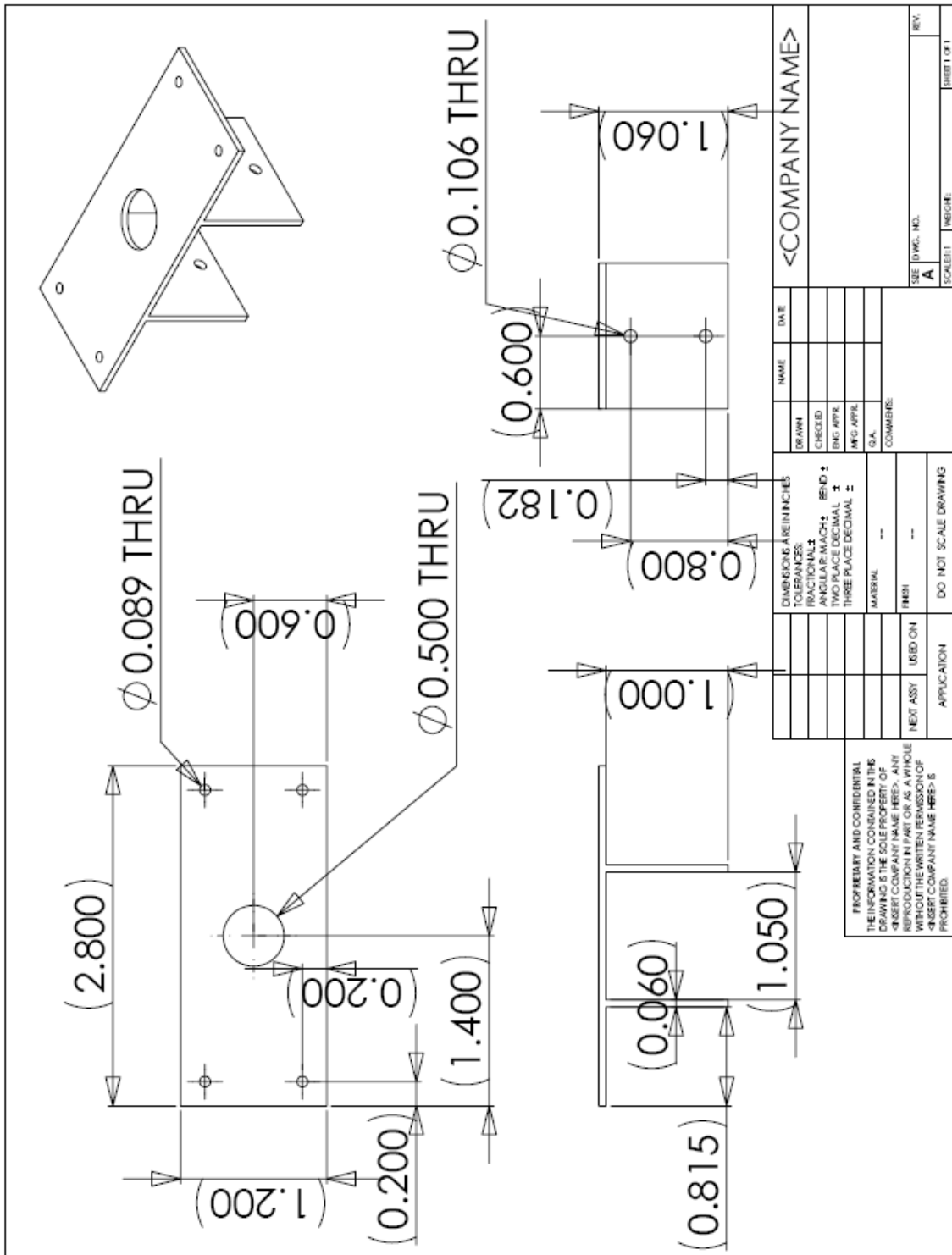
Figure E-10: Drawing for the multiplier bracket mount

Appendix

F

Test System Operating Instructions

This appendix contains the detailed operation instructions for the characterization system outlined in Chapter 5. These instructions begin with the assumption that the chamber is vented and all the electronics are off, and end with returning the system to the original state.

Load the device

Assemble the device into the testing jig, device housing, and flange mount as described in Section 5.2.1. Throughout the assembly, use a multimeter to ensure that there is no shorting between electrically isolated components. Make all the associated electrical connections and take note of how the ion optics is wired to the 10-pin connector.

Prepare the chamber

Carefully transport the flange mount to the vacuum chamber and place it on the 10" flange. Be sure to align the flange correctly and to clean the o-ring beforehand. Open the gate valve, and start the diaphragm pump until a pressure below 10 Torr is reached. At this point, start the turbo and turn on the ion gauge after the chamber pressure reads less than 1 mTorr. Once a base pressure of $\sim 1 \times 10^{-7}$ Torr is reached, you can select an analyte to introduce. To protect the ion gauge from damage, open and close the analyte line valve repeatedly to maintain the pressure below 1×10^{-4} Torr. Make the electrical connections to the flange mount as you wait for the analyte to stabilize to $\sim 3 \times 10^{-5}$ Torr.

Set the frequency

Choose the coil to be used and attach it to the drive circuit. Turn on the oscilloscope and make sure the probes are connected to the circuit at the location described in Section 5.2.2. Connect the function generator to the amplifier, and the amplifier to the circuit. Turn on the function generator and set the voltage amplitude to 100 mV$_{pp}$. Turn down the gain of the r.f. amplifier and engage the unit. Enable the output of the function generator and adjust the frequency until the resonance frequency is located. This frequency is identified when the r.f. amplitude detected by the oscilloscope is a maximum. Add load capacitors as needed to shift the resonance frequency near the desired operating frequency, and adjust the trimmer capacitors to balance the signals at the selected frequency. Disengage the function generator when this step is completed.

Calibrate the r.f.

Turn on the DAQ card, start the PC, and run the LabVIEW virtual instrument GenValues.vi. Enter the device aperture diameter, the selected operating frequency, the operating point (a, q), and the desired maximum mass to scan (calibration mass). Make sure that the start and end scan masses (mass scan range) are consistent with the calibration mass. The module will display the r.f. peak-to-peak voltage required to scan the maximum mass. Re-engage the function generator and adjust the r.f. amplifier gain (course adjust) and the function generator amplitude (fine adjust) until the calculated voltage is reached. Be sure to keep the function generator amplitude to less than 1.0 V$_{pp}$ since the broadband amplifier has a limit on the input power. If the circuit is unable to deliver the required voltage with the specified limitations, a different operating point, calibration mass, or frequency needs to be used. Disengage the function generator once the r.f. has been properly calibrated.

Scale the d.c.

Using the d.c. amplitude calculated for the calibration mass, move the alligator clips on the drive circuit to select an adequate d.c. gain. Turn on the linear amplifiers (op-amp rail voltages), zero the d.c. offsets and pole bias controls on the software, and input the correct value for the d.c. gains. Run the LabVIEW virtual instrument Scan Control.vi,

and set the start and end masses on GenValues.vi to 0 and 0.1 respectively. Adjust the d.c. offsets so that the value detected on the oscilloscope is as close to zero as possible. Reset the mass scan range to the desired start and end masses and update GenValues.vi.

Generate ions

Turn on the filament and optics supplies, the multiplier power supply, and the preamplifier. On the filament supply, set the ion region to 10.0, the electron energy to -50.0, and the emission current to 0.20 before switching on the current. On the optics supply, zero most of the voltages but make the one connected to the exit lens large and negative. Set the multiplier supply voltage to -2500 V and engage the unit. Set the function generator to external modulation, and engage the unit once again. Next, select the "r.f. only" mode on Scan Control.vi, and adjust the extractor lens voltage and inlet lens voltages until a signal is detected. Occasionally, the ion energy may need to be increased to improve transmission. The gain of the preamplifier should be adjusted accordingly to prevent saturating the output. Additionally, make sure that the multiplier signal registers as a positive voltage to avoid confusion. A simple selection of the INVERT command on the preamplifier will correct this issue.

Obtain a mass spectrum

Once there is clear evidence that ions are transmitting through the device, turn off the "r.f. only" mode and a mass spectrum should appear. Inspect the spectrum and check to see if the mass peaks line up where they should. If the r.f. calibration was done properly, the peaks should be close to the correct masses. If not, adjustments to the r.f. can be made by changing the gain of the amplifier or the initial amplitude of the function generator. Once the masses are lined up, there are many "levers" that can be adjusted to improve the device performance. There are no specific instructions on how to accomplish this, but it is something learned through actual experimentation.

Improve the mass spectrum

One major improvement comes from decreased ion energy. This can be done by reducing the ion region potential or increasing the pole bias. The pole bias is essentially

178

the centerline potential of the quadrupole and can be set by the software. Decreased ion energy will increase resolution but the transmission will drop, the relative abundances may change, and the peak-shapes can worsen. There is a more drastic effect from adjusting the ion region since the ion dynamics with the optics will change as well. Adjustments made on the extractor and lenses can be used to increase transmission and improve peak-shape but resolution may degrade. Changing the operating point, namely increasing *a* specified in the software, will increase resolution leading to decreased transmission and potentially degraded peak-shape. The transmission, peak-shape, and resolution are interrelated and depend on many different factors. This fact necessitates the adjustments of several of these "levers" simultaneously to achieve overall improvements. The preamplifier gain can be changed to higher sensitivities to compensate for decreased transmissions but should be no smaller than 20 nA/V. Another interesting option is to toggle the "swap d.c." button which essentially switches the d.c. drive voltages on the quadrupole. Typically, one set of electrodes is better suited for a particular axis due to alignment considerations. Proper selection of the electrodes will lead to improved peak-shape and resolution. Finally, the tune table can be used to correct abundance sensitivities and is needed to operate in constant peak-width mode as described in Chapter 2. GenValue.vi takes the specified masses and the associated adjustments, and modifies the control voltages accordingly.

Experimentation

Once the mass spectrum appears satisfactory, specify a file path for saving, and name the experiment with a self explanatory name. Update the parameter table with the correct information before pushing the save button. Take a screen-shot and save it with the experimental information for reference. The software saves over old data if the experiment name is the same so give unique names to each spectrum recorded. To choose a different analyte, start with turning-off the filament and optics supply, and disengaging the function generator and multiplier power supply. This step is important for preventing damage to the device and test system. Close the analyte line valve and choose another analyte. Open and close the line valve to regulate the chamber pressure as mentioned previously. Turn on the electronics that were disengaged and resume

testing. Changing the frequency will require shutting down the system and repeating the procedure starting at point "Set the frequency".

Shutdown and venting

To shutdown the system, disengage the filament and optics supply first, followed by halting the software. Next, turn-off the multiplier supply voltage, the preamplifier, the r.f. amplifier, and the function generator in no particular order.   Turn-off the rail supplies used for the circuit, and close the analyte line valve.   Once all the electronics are powered-down and the program stopped, close the chamber gate value. Turn-off the vacuum gauge and start the ramp-down of the turbo. Wait approximately 10 minutes for the rotation rate to drop from 1500 Hz to 0 Hz. At this point, turn-off the diaphragm pump, and open the air vent valve. Close the valve when the flange mount can be removed from the vacuum chamber.

References

[1]   P. H. Dawson, *Quadrupole Mass Spectrometry and its Applications*. New York: American Institute of Physics, 1995.

[2]   American Society for Mass Spectrometry :: Education, "What is Mass Spectrometry?," December 2001, http://www.asms.org/whatisms/p8.html.

[3]   E. R. Badman, and R. G. Cooks, "Special Feature: Perspective, Miniature mass analyzers," *Journal of Mass Spectrometry*, vol. 35, pp. 659-671, 2000.

[4]   S. Boumsellek, and R. J. Ferran, "Trade-offs in Miniature Quadrupole Designs," *Journal of the American Society for Mass Spectrometry*, vol. 12, pp. 633-640, 2001.

[5]   D. Smith, and P. R. Cromey, "An inexpensive, bakeable quadrupole mass spectrometer," *Journal of Scientific Instruments (Journal of Physics E)*, ser. 2, vol. 1, pp. 523-527, 1968.

[6]   R. J. Ferran, and S. Boumsellek, "High-pressure effects in miniature arrays of quadrupole analyzers for residual gas analysis from 10^{-9} to 10^{-2} Torr," *Journal of Vacuum Science and Technology A*, vol. 14, no. 3, pp. 1258-1265, 1996.

[7]   S. Boumsellek, and R. J. Ferran, "Miniature Quadrupole Arrays for Residual and Process Gas Analysis," *Journal of the IEST*, pp. 27-31, January 1999.

[8]   O. J. Orient, A. Chutjian, and V. Garkanian, "Miniature, high-resolution, quadrupole mass-spectrometer array," *Review of Scientific Instruments*, vol. 68, no. 3, pp. 1393-1397, 1997.

[9]   D. H. Holkeboer, T. L. Karandy, F. C. Currier, L. C. Frees, and R. E. Ellefson, "Miniature quadrupole residual gas analyzer for process monitoring at milliTorr pressures," *Journal of Vacuum Science and Technology A*, vol. 16, no. 3, pp. 1157-1162, 1998.

[10]   J. Wang, X. Zhang, F. Mao, M. Xiao, Y. Cui, D. den Engelson, and W. Lei, "Study of a micro chamber quadrupole mass spectrometer," *Journal of Vacuum Science and Technology A*, vol. 26, no. 2, pp. 239-243, 2008.

[11]   P. M. Holland, A. Chutjian, M. R. Darrach, and O. J. Orient, "Miniaturized GC/MS instrumentation for *in situ* measurements: micro gas chromatography coupled with miniature quadrupole array and Paul ion trap mass spectrometers," in *Proceedings of SPIE*, 2003, vol. 4878, pp. 1-7.

[12]   O. Kornienko, P. T. A. Reilly, W. B. Whitten, and J. M. Ramsey, "Micro Ion Trap Mass Spectrometry," *Rapid Communications in Mass Spectrometry*, vol. 13, pp. 50-53, 1999.

[13]   J. A. Diaz, C. F. Giese, and W. R. Gentry, "Sub-Miniature ExB Sector-Field Mass Spectrometer," *Journal of the American Society for Mass Spectrometry*, vol. 12, pp. 619-632, 2001.

[14]   Y. Song, G. Wu, Q. Song, R. G. Cooks, Z. Ouyang, and W. R. Plass, "Novel Linear Ion Trap Mass Analyzer Composed of Four Planar Electrodes," *Journal of the American Society for Mass Spectrometry*, vol. 17, pp. 631-639, 2006.

[15]   C. Janfelt, N. Talaty, C. C. Mulligan, A. Keil, Z. Ouyang, and R. G. Cooks, "Mass spectra of proteins and other biomolecules recorded using a handheld

instrument," *International Journal of Mass Spectrometry*, vol. 278, pp. 166-169, 2008.

[16]   R. R. A. Syms, "Advances in microfabricated mass spectrometers," *Analytical and Bioanalytical Chemistry*, vol. 393, pp. 427-429, 2009.

[17]   H. Peddanenikalva, K. Potluri, S. Bhansali, R. T. Short, and D. Fries, "64.4: A Microfabrication Strategy for Cylindrical Ion Trap Mass Spectrometer Arrays," in *Proceedings of IEEE Sensors*, 2002, vol. 1, p. 651-655.

[18]   S. Pau, S. S. Pai, Y. L. Low, J. Moxom, P. T. A. Reilly, W. B. Whitten, and J. M. Ramsey, "Microfabricated Quadrupole Ion Trap for Mass Spectrometer Applications," *Physical Review Letters*, vol. 96, no. 120801, pp. 1-4, 2006.

[19]   M. G. Blain, L. S. Riter, D. Cruz, D. E. Austin, G. Wu, W. R. Plass, and R. G. Cooks, "Towards the hand-help mass spectrometer: design considerations, simulation, and fabrication of micrometer-scaled cylindrical ion traps," *International Journal of Mass Spectrometery*, vol. 236, pp. 91-104, 2004.

[20]   N. Sillon, and R. Baptist, "Micromachined mass spectrometer," *Sensors and Actuators B*, vol. 83, pp. 129-137, 2002.

[21]   H. J. Yoon, J. H. Kim, E. S. Choi, S. S. Yang, and K. W. Jung, "Fabrication of a novel micro time-of-flight mass spectrometer," *Sensors and Actuators A*, vol. 97-98, pp. 441-447, 2002.

[22]   J. J. Tunstall, S. Taylor, R. R. A. Syms, T. Tate, and M. M. Ahmad, "Silicon micromachined mass filter for a low power, low cost quadrupole mass spectrometer," in *Proceedings of MEMS*, 1998, pp. 438-442.

[23]   S. Taylor, R. F. Tindall, and R. R. A. Syms, "Silicon based quadrupole mass spectrometry using microelectromechanical systems," *Journal of Vacuum Science and Technology B*, vol. 19, no. 2, pp. 557-562, 2001.

[24]   S. Taylor, J. R. Gibson, and B. Srigengan, "Miniature mass spectrometry: implications for monitoring of gas discharges," *Sensor Review*, vol. 23, no. 2, pp. 150-154, 2003.

[25]   D. Wiberg, N. V. Myung, B. Eyre, K. Shcheglov, O. Orient, E. Moore, and P. Munz, "LIGA Fabricated Two-Dimensional Quadrupole Array and Scroll Pump for Miniature Gas Chromatography/Mass Spectrometer," in *Proceedings of SPIE*, 2003, vol. 4878, pp. 8-13.

[26]   S. H. Deshmukh, L. B. King, and C. R. Monroe, "A microscale quadrupole mass spectrometer for ion species analysis," in *Proceedings of the 40th AIAA*, 2004, pp. 1-9.

[27]   M. Geear, R. R. A. Syms, S. Wright, and A. S. Holmes, "Monolithic MEMS Quadrupole Mass Spectrometers by Deep Silicon Etching," *Journal of Microelectromechanical Systems*, vol. 14, no. 5, pp. 1156-1166, 2005.

[28]   P. Siebert, G. Petzold, A. Hellenbart, J. Müller, "Surface microstructure/miniature mass spectrometer: processing and applications," *Applied Physics A*, vol. 67, pp. 155-160, 1998.

[29]   D. E. Austin, Y. Peng, B. J. Hansen, I. W. Miller, A. L. Rockwood, A. R. Hawkins, and S. E. Tolley, "Novel Ion Traps Using Planar Resistive Electrodes: Implications for Miniaturized Mass Analyzers," *Journal of the American Society for Mass Spectrometry*, vol. 19, pp. 1435-1441, 2008.

[30] H. J. Yoon, S. H. Song, N. T. Hong, k. W. Jung, S. Lee, and S. S. Yang, "Fabrication of two types of micro ion sources for a micro time-of-flight mass spectrometer," *Journal of Micromechanics and Microengineering*, vol. 17, pp. 1542-1548, 2007.

[31] H. J. Yoon, J. H. Kim, T. G. Park. S. S. Yang, and K. W. Jung, "The test of hot electron emission for the micro mass spectrometer," in *Proceedings of SPIE*, 2001, vol. 4408, pp.360-367.

[32] A. Desai, Y-C. Tai, M. T. Davis, T. D. Lee, "A MEMS Electrospray Nozzle for Mass Spectrometry," in *Proceedings of Transducers*, 1997, pp. 927-930.

[33] B. G. Jamieson, B. A. Lynch, D. N. Harpold, H. B. Niemann, M. D. Shappirio, and P. R. Mahaffy, "Microfabricated silicon leak for sampling planetary atmospheres with a mass spectrometer," *Review of Scientific Instruments*, vol. 78, no. 065109, pp. 1-8, 2007.

[34] P. Siebert, G. Petzold, and J. Müller, "Processing of complex microsystems: A Micro Mass Spectrometer," in *Proceedings of SPIE*, 1999, vol. 3680, pp. 562-571.

[35] E. Wapelhorst, J-P. Hauschild, J. Müller, "Complex MEMS: a fully integrated TOF micro mass spectrometer," *Sensors and Actuators A*, vol. 138, pp. 22-27, 2007.

[36] J-P. Hauschild, E. Wapelhorst, J. Müller, "Mass spectra measured by a fully integrated MEMS mass spectrometer," *International Journal of Mass Spectrometry*, vol. 264, pp. 53-60, 2007.

[37] T. T. King, S. A. Getty, P. A. Roman, F. A. Herrero, H. H. Jones, D. M. Kahle, B. Lynch, G. Suarez, W. B. Brinckerhoff, and P. R. Mahaffy, "Simulation of a Miniature, Low-Power Time-of-Flight Mass Spectrometer for *In Situ* Analysis of Planetary Atmospheres," in *Proceedings of SPIE*, 2008, vol. 6959, no. 69590E, pp. 1-15.

[38] P. A. Roman, W. B. Brinckerhoff, S. A. Getty, F. A. Herrero, R. Hu, H. H. Jones, D. Kahle, T. T. King, and P. Mahaffy, "A Miniature MEMS and NEMS enabled Time-of-Flight Mass Spectrometer for Investigations in Planetary Science," in *Proceedings of SPIE*, 2008, vol. 6959, no. 69590G, pp. 1-13.

[39] R. Bogue, "MEMS sensors: past, present and future," *Review of Sensors*, vol. 27, no. 1, pp. 7-13, 2007.

[40] L.-Y. Chen, L. F. Velásquez-García, X. Wang, K. Teo, and A. I. Akinwande, "A Micro Ionizer for Portable Mass Spectrometers using Double-gated Isolated Vertically Aligned Carbon Nanofiber Arrays," in *Proceedings of IEDM*, 2007, pp. 843-846.

[41] L.-Y. Chen, "Double-gated Isolated Vertically Aligned Carbon Nanofiber Field Emission and Field Ionization Arrays," Doctoral Thesis, Massachusetts Institute of Technology, Cambridge, 2007.

[42] L. F. Velásquez-García, and A. I. Akinwande, "A PECVD CNT-Based Open Architecture Field Ionizer for Portable Mass Spectrometry," in *Technical Digest of MEMS*, 2008, pp. 742-745.

[43] L. F. Velásquez-García, B. Gassend, and A. I. Akinwande, "CNT-Based Gas Ionizers with Integrated MEMS Gate for Portable Mass Spectrometry," to be presented at *Transducers*, Denver, CO, June 2009.

[44]   Y. Zhu, J. Lee, A. Seshia, "System-level simulation of a micromachined electrometer using a time-domain variable capacitor circuit model," *Journal of Micromechanics and Microengineering*, vol. 17, pp. 1059-1065, 2007.

[45]   Y. Zhu, J. Lee, A. Seshia, "MEMS electrometer system simulation using a time-domain variable capacitor model," in *Proceedings of Transducers*, 2007, pp. 1685-1688.

[46]   J. E.-Y. Lee, B. Bahreyni, Y. Zhu, and A. A. Seshia, "Ultrasensitive mass balance based on a bulk acoustic mode single-crystal silicon resonantor," *Applied Physics Letters*, vol. 91, no. 234103, pp. 1-3, 2007.

[47]   L. F. Velásquez-García, K. Cheung, A. I. Akinwande, "An Application of 3-D MEMS Packaging: Out-of-Plane Quadrupole Mass Filters," *Journal of Microelectromechanical Systems*, vol. 17, no. 6, pp. 1430-1438, 2008.

[48]   R. Syms, "Miniaturized Mass Spectrometers," presented at *PITTCON*, New Orleans, LA, March 2008.

[49]   D. R. Denison, "Operating Parameters of a Quadrupole in a Grounded Cylindrical Housing," *Journal of Vacuum Science and Technology*, vol. 8, no. 1, pp. 266-269, 1971.

[50]   A. J. Reuben, G. B. Smith, P. Moses, A. V. Vagov, M. D. Woods, D. B. Gordon, and R. W. Munn, "Ion trajectories in exactly determined quadrupole fields," *International Journal of Mass Spectrometry and Ion Processes*, vol. 154, pp. 43-59, 1996.

[51]   D. J. Douglas, and N. V. Konenkov, "Influence of the 6th and 10th spatial harmonics on the peak shape of a quadrupole mass filter with round rods," *Rapid Communications in Mass Spectrometry*, vol. 16, pp. 1425-1431, 2002.

[52]   T. J. Hogan, and S. Taylor, "Performance Simulation of a Quadrupole Mass Filter Operating in the First and Third Stability Zones," *IEEE Transactions on Instrumentation and Measurement*, vol. 57, no. 3, pp. 498-508, 2008.

[53]   R.E. Pedder, "Practical Quadrupole Theory: Graphical Theory," Extrel, Application Note RA-2010A, pp. 1-5.

[54]   D. J. Douglas, T. A. Glebova, N. V. Konenkov, and M. Y. Sudakov, "Spatial harmonics of the field in a quadrupole mass filter with circular electrodes," *Technical Physics*, vol. 44, no. 10, pp. 1215-1219, 1999.

[55]   P. H. Dawson, and N. R. Whetten, "Quadrupole Mass Filter: Circular Rods and Peak Shapes," *Journal of Vacuum Science and Technology*, vol. 7, no. 3, pp. 440-441, 1969.

[56]   J. R. Gibson, and S. Taylor, "Asymmetrical features of mass spectral peaks produced by quadrupole mass filters," *Rapid Communications in Mass Spectrometry*, vol. 17, pp. 1051-1055, 2003.

[57]   N. R. Whetten, and P. H. Dawson, "Some Causes of Poor Peak Shapes in Quadrupole Field Mass Analyzers," *Journal of Vacuum Science and Technology*, vol. 6, no. 1, pp. 100-103, 1968.

[58]   J. Wei, D. Lynch, R. E. Pedder, "Improving Abundance Sensitivity in Quadrupole Mass Spectrometers," Extrel, Application Note RA_2006B, pp. 1-4.

[59]   R. E. Pedder, "Practical Quadrupole Theory: Peak Shapes at Various Ion Energies," Extrel, Application Note RA_2011A, pp. 1-8.

[60] P. H. Dawson, "Fringing Fields in Quadrupole-Type Mass Analyzers," *Journal of Vacuum Science and Technology*, vol. 9, no. 1, pp. 487-491, 1971.

[61] Z. Du, D. J. Douglas, T. Glebova, and N. V. Konenkov, "Peak structure with a quadrupole mass filter operated in the third stability region," *International Journal of Mass Spectrometry*, vol. 197, pp. 113-121, 2000.

[62] P. H. Dawson, "The Acceptance of the Quadrupole Mass Filter," *International Journal of Mass Spectrometry and Ion Physics*, vol. 17, pp. 423-445, 1975.

[63] D. J. Douglas, and N. V. Konenkov, "Ion Source Emittance Influence on the Transmission of a Quadrupole Operated in the Second Stability Region," *Journal of the American Society for Mass Spectrometry*, vol. 9, pp. 1074-1080, 1998.

[64] P. H. Dawson, and N. R. Whetten, "Non-linear Resonances in Quadrupole Mass Spectrometers due to Imperfect Fields I. The Quadrupole Ion Trap," *International Journal of Mass Spectrometry and Ion Physics*, vol. 2, no. 1, pp. 45-49, 1969.

[65] W. Koczorowski, G. Szawiola, A. Walaszyk, A. Buczek, D. Stefanska, E. Stachowska, "Experimental investigation of the stability diagram for Paul traps in the case of praseodymium ions," *Hyperfine Interactions*, vol. 171, pp. 233-241, 2006.

[66] R. Alheit, S. Kleineidam, F. Vedel, M. Vedel, and G. Werth, "Higher order non-linear resonances in a Paul trap," *International Journal of Mass Spectrometry and Ion Processes*, vol. 154, pp. 155-169, 1996.

[67] T. Gudjons, P. Siebert, and G. Werth, "Influences of anharmonicities of a Paul trap potential on the motion of stored ions," *Applied Physics B*, vol. 65, pp. 57-62, 1997.

[68] A. Drakoudis, M. Söllner, and G. Werth, "Instabilities of ion motion in a linear Paul trap," *International Journal of Mass Spectrometry*, vol. 252, pp. 61-68, 2006.

[69] R. Takai, K. Nakayama, W. Saiki, K. Ito, and H. Okamoto, "Nonlinear Resonance Effects in a Linear Paul Trap," *Journal of the Physical Society of Japan*, vol. 76, no. 1, 014802, pp. 1-8, 2007.

[70] Y. Wang, J. Franzen, and K. P. Wanczek, "The non-linear resonance ion trap. Part 2. A general theoretical analysis," *International Journal of Mass Spectrometry and Ion Processes*, vol. 124, pp. 125-144, 1993.

[71] J. Schulte, P. V. Shevchenko, and A. V. Radchik, "Nonlinear field effects in quadrupole mass filters," *Review of Scientific Instruments*, vol. 71, no. 9, pp. 3566-3571, 1999.

[72] P. H. Dawson, "Higher zones of stability for the quadrupole mass filter," *Journal of Vacuum Science and Technology*, vol. 11, no. 6, pp. 1151-1153, 1974.

[73] S. Hiroki, T. Abe, Y. Murakami, K. Yanagishita, and S. Nakamura, "Development of a high-resolution quadrupole mass spectrometer capable of detecting ^{3}He and ^{4}He in a hydrogen isotope atmosphere," *Journal of Vacuum Science and Technology A*, vol. 12, no. 5, pp. 2711-2715, 1994.

[74] S. Hiroki, T. Abe, and Y. Murakami, "Detection of a 10^{-4} helium peak in a deuterium atmosphere using a modified high-resolution quadrupole mass spectrometer," *Review of Scientific Instruments*, vol. 65, no. 5. pp. 1912-1917, 1994.

[75] S. Hiroki, T. Abe, and Y, Murakami, "Separation of helium and deuterium peaks with a quadrupole mass spectrometer by using the second stability zone in the

Mathieu diagram," *Review of Scientific Instruments*, vol. 63, no. 8, pp. 3874-3876, 1992.

[76] P. H. Dawson, and Y. Bingqi, "The second stability region of the quadrupole mass filter I. Ion optical properties," *International Journal of Mass Spectrometry and Ion Processes*, vol. 56, pp. 25-39, 1984.

[77] Z. Du, D. J. Douglas, and N. Konenkov, "Elemental analysis with quadrupole mass filters operated in higher stability regions," *Journal of Analytical Atomic Spectrometry*, vol. 14, pp. 1111-1119, 1994.

[78] N. V. Konenkov, and J. T. Dowell, "Transmission of the quadrupole mass filter in the intermediate stability zone separation mode," *International Journal of Mass Spectrometry and Ion Processes*, vol. 164, pp. 201-206, 1997.

[79] S. Hiroki, T. Abe, and Y. Murakami, "Development of a quadrupole mass spectrometer using the second stable zone in Mathieu's stability diagram," *Review of Scientific Instruments*, vol. 62, no. 9, pp. 2121- 2124, 1991.

[80] P. Turner, S. Taylor, and J. R. Gibson, "Effect of ion entry acceptance conditions on the performance of a quadrupole mass spectrometer operated in upper and lower stability regions," *Journal of Vacuum Science and Technology A*, vol. 23, no. 3, pp. 480-487, 2005.

[81] R. R. A. Syms, L. Michelutti, and M. M. Ahma, "Two-dimensional microfabricated electrostatic einzel lens," *Sensor and Actuators A*, vol. 107, pp. 285-295, 2003.

[82] R. T. Short, D. P. Fries, G. P. G. Kibelka, M. L. Kerr, S. K. Toler, P. G. Wenner, and R. H. Byrne, "Field Chemical Analysis Using Real-Time In-Water Mass Spectrometry," in *Proceedings of OCEANS*, 2001, pp. 256-258.

[83] T. P. Griffin, J. A. Diaz, C. R. Arkin, C. Soto, C. H. Curley, and O. Gomez, "Three-Dimensional Concentration Mapping of Gases using a Portable Mass Spectrometer System," *Journal of the American Society for Mass Spectrometry*, vol. 19, pp. 1411-1418, 2008.

[84] J. H. Hoffman, R. C. Chaney, and H. Hammack, "Phoenix Mars Mission-The Thermal Evolved Gas Analyzer," *Journal of the American Society for Mass Spectrometry*, vol. 19. 1377-1383, 2008.

[85] K. Cheung, L. F. Velásquez-García, and A. I. Akinwande, "Fully Btach-Fabricated Linear Quadrupole Mass Filters," in *Technical Digest of Hilton Head*, 2008, pp. 316-319.

[86] G. E. Lee-Whiting, "Rounding Corners on Poles of Polygonal Profile," *Nuclear Instruments and Methods*, vol. 97, pp. 433-441, 1971.

[87] T. Hayashi, and N. Sakudo, "Quadrupole Field in Circular Concave Electrodes," *Review of Scientific Instruments*, vol. 39, no. 7, pp. 958-961, 1968.

[88] N. Sakudo, and T. Hayashi, "Quadrupole electrodes with flat faces," *Review of Scientific Instruments*, vol. 46, no. 8, pp. 1060-1062, 1975.

[89] G. Bosi, "Quadrupole fields in circular concave electrodes and poles," *Review of Scientific Instruments*, vol. 45, no. 10, pp. 1260-1262, 1974.

[90] R. R. A. Syms, T. J. Tate, M. M. Ahmad, and S. Taylor, "Design of a Microengineered Electrostatic Quadrupole Lens," *IEEE Transactions on Electron Devices*, vol. 45, no. 11, pp. 2304-2311, 1998.

[91]   T. J. Hogan, S. Taylor, K. Cheung, L. F. Velásquez-García, A. I. Akinwande, and R. E. Pedder, "Performance Characteristics of a MEMS Quadrupole Mass Filter with Square Electrodes – Experimental and Simulates Results," *submitted to IEEE Transactions on Instrumentation and Measurement*.

[92]   A. C. C. Voo, R. Ng, J. J. Tunstall, and S. Taylor, "Transmission through the quadrupole mass spectrometer mass filter: The effect of aperture and harmonics," *Journal of Vacuum Science and Technology A*, vol. 15, no. 4, pp. 2276-2281, 1997.

[93]   C. E. Pearson, D. R. Leibrandt, W. S. Bakr, W. J. Mallard, K. R. Brown, and I. L. Chuang, "Experimental investigation of planar ion traps," *Physical Review A*, vol. 73, no. 3, 032307, pp. 1-12, 2006.

[94]   D. Stick, W. K. Hensinger, S. Olmschenk, M. J. Madsen, K. Schwab, and C. Monroe, "Ion trap in a semiconductor chip," *Nature Physics*, vol. 2, pp. 36-39, 2006.

[95]   M. J. Madsen, W. K. Hensinger, D. Stick, J. A. Rabchuk, and C. Monroe, "Planar ion trap geometry for microfabrication," *Applied Physics B*, vol. 78, no. 5, pp. 639-651, 2004.

[96]   C. S. Trajber, M. Simon, and M Csatlos, "On the use of pre-filters in quadrupole mass spectrometers," *Measurement Science and Technology*, vol. 2, pp. 785-787, 1991.

[97]   S. Hiroki, K. Sakata, N. Sugiyama, S. Muramoto, T. Abe, and Y. Murakami, "Effects of a pre-filter on the sensitivity of a high-resolution quadrupole mass spectrometer," *Vacuum*, vol. 46, no. 7, pp. 681-683, 1995.

[98]   W. L. Fite, "Spatial separation of fringe fields in quadrupole mass filters," *Review of Scientific Instruments*, vol. 47, no. 3, pp. 326-330, 1976.

[99]   V. D. Berkout, and V. M. Doroshenko, "Improving the Quality of the Ion Beam Exiting a Quadrupole Ion Guide," *Journal of the American Society for Mass Spectrometry*, vol. 17, pp. 335-340, 2006.

[100] Z. Du, and D. J. Douglas, "A Novel Tandem Quadrupole Mass Analyzer," *Journal of the American Society for Mass Spectrometry*, vol. 10, pp. 1053-1066, 1999.

[101] N. V. Konenkov, and V. I. Kratenko, "Characteristics of a quadrupole mass filter in the separation mode of a few stability regions," *International Journal of Mass Spectrometry and Ion Processes*, vol. 108, pp. 115-136, 1991.

[102] R. A. Miller, E. G. Nazarov, G. A. Eiceman, and A. T. King, "A MEMS radio-frequency ion mobility spectrometer for chemical vapor detection," *Sensors and Actuators A*, vol. 91, pp. 301-312, 2001.

[103] A. B. Kanu, P. Dwivedi, M. Tam, L. Matz, and H. H. Hill Jr., "Ion mobility-mass spectrometry," *Journal of Mass Spectrometry*, vol. 43, pp. 1-22, 2008.

[104] M. Stubenrauch, M. Fischer, C. Kremin, S. Stoebenau, A. Albrecht, and O. Nagel, "Black silicon-new functionalities in microsystems," *Journal of Micromechanics and Microengineering*, vol. 16, pp. S82-S87, 2006.

[105] M. Huff, "Silicon Micromachined Wafer-Bonded Valves," Ph.D. Thesis, Massachusetts Institute of Technology, Cambridge, 1993.

[106] S. Taylor, J. J. Tunstall, J. H. Leck, R. F. Tindall, J. P. Jullien, J. Batey, R. R. A. Syms, T. Tate, and M. M. Ahmad, "Performance improvements for a miniature

quadrupole with a micromachined mass filter," *Vacuum*, vol. 53, pp. 203-206, 1999.

[107] H. Nakanishi, T. Nishimoto, R. Nakamura, A. Yotsumoto, T. Yoshida, and S. Shoji, "Studies on SiO_2-SiO_2 bonding with hydrofluoric acid. Room temperature and low stress bonding techniques for MEMS," *Sensors and Actuators*, vol. 79, pp. 237-244, 2000.

[108] Q.-Y. Tong, G. Fountain, and P. Enquist, "Room temperature SiO_2/SiO_2 covalent bonding," *Applied Physic Letters*, vol. 89, no. 042110, pp. 1-3, 2006.

[109] Q.-Y. Tong, Q. Gan, G. Fountain, G. Hudson, and P. Enquist, "Low-temperature bonding of silicon-oxide-covered wafers using diluted HF etching," *Applied Physics Letters*, vol. 85, no. 14, pp. 2762-2764, 2004.

[110] V. V. Titov, "Detailed Study of the Quadrupole Mass Analyzer Operating Within the First, Second, and Third (Intermediate) Stability Regions. II. Transmission and Resolution," *Journal of the American Society for Mass Spectrometry*, vol. 9, pp. 70-87, 1998.

[111] L. Jiang, G. Pandraud, P. J. French, S. M. Spearing, and M. Kraft, "Wafer bonding with nanoprecision alignment for micro/nano systems," in *Proceedings of Transducers*, 2007, pp. 2103-2106.

[112] I. Mizushima, T. Sato, S. Taniguchi, and Y. Tsunashima, "Empty-space-in-silicon technique for fabricating a silicon-on-nothing structure," *Applied Physics Letters*, vol. 77, no. 20, pp. 3290-3292, 2000.

[113] E. P. Sheretov, "Opportunities for optimization of the rf signal applied to electrodes of quadrupole mass spectrometers. Part I. General Theory," *International Journal of Mass Spectrometry*, vol. 198, pp. 83-96, 2000.

[114] N. V. Konenkov, L. M. Cousins, V. I. Baranov, and M. Yu. Sudakov, "Quadrupole mass filter operation with auxiliary Quadrupolar excitation: theory and experiment," *International Journal of Mass Spectrometry*, vol. 208, pp. 17-27, 2001.

[115] A. Moradian, and D. J. Douglas, "Experimental investigation of mass analysis using an island of stability with a quadrupole with 2.0% added octopole field," *Rapid Communications in Mass Spectrometry*, vol. 21. pp. 3306-3310, 2007.

[116] M. Takebe, and S. Kumashiro, "Computer simulation of the quadrupole mass filter," *Nuclear Instruments and Methods in Physics Research A*, vol. 363, pp. 411-415, 1995.

[117] J. R. Gibson, S. Taylor, and J. H. Leck, "Detailed simulation of mass spectra for quadrupole mass spectrometer systems," *Journal of Vacuum Science and Technology A*, vol. 18, no. 1, pp. 237-243, 2000.

[118] C. Ding, N. V. Konenkov, and D. J. Douglas, "Quadrupole mass filters with octopole fields," *Rapid Communications in Mass Spectrometry*, vol. 17. pp. 2495-2502, 2003.